

## Abstract

# Measurement of ( $\pi^-$ -Ar) and ( $K^+$ -Ar) total hadronic cross sections in the LArIAT experiment

Elena Gramellini

2018

The Liquid Argon Time Projection Chamber (LArTPC) represents one of the most advanced experimental technologies for physics at the Intensity Frontier due to its full 3D-imaging, excellent particle identification and precise calorimetric energy reconstruction. By deploying a LArTPC in a dedicated calibration test beam line at Fermilab, LArIAT (Liquid Argon In A Testbeam) aims to experimentally calibrate this technology in a controlled environment and to provide physics results key to the neutrino oscillation physics and proton decay searches of the Short Baseline Neutrino and Long Baseline Neutrino programs.

<sup>14</sup> LArIAT's physics program entails a vast set of topics with a particular focus on  
<sup>15</sup> the study of nuclear effects such as pion and kaon characteristic interaction modes.

This thesis presents two world's first measurements: the measurement of ( $\pi^-$ -Ar) total hadronic cross section in the 100-1000 MeV kinetic energy range and the measurement of the ( $K^+$ -Ar) total hadronic cross section in the 100-600 MeV kinetic energy range. The analyses devised for these measurements use both the core elements of LArIAT: beamline and TPC. The first step in each analysis is the development of an event selection based on beamline and TPC information geared towards the identification of the hadron of interest. We then proceed to match the beamline candidate to a suitable TPC track. Finally, we apply the “thin slice method” technique and measure the cross section, correcting for backgrounds and detector effects. The thin slice technique is a new method to measure hadron-argon cross sections possible only thanks to the combination of the tracking and calorimetry capability of

27 the LArTPC technology. Albeit never on argon, the hadronic cross section of pions  
28 has been measured before on several different elements in thin target experiments,  
29 leading to solid predictions in the argon case. Even through the use of a different  
30 technique, our measurement of the ( $\pi^-$ -Ar) total hadronic cross section is in general  
31 agreement with the prediction by the Geant4 Bertini Cascade model which are based  
32 on data from thin target experiments. On the contrary, cross section measurements  
33 for kaons are extremely rare, thus more difficult to model. Not surprisingly, our mea-  
34 surement of the ( $K^+$ -Ar) total hadronic cross section is mostly in disagreement with  
35 the Geant4 prediction.

36 This thesis also reports two ancillary detector physics measurements necessary  
37 for the cross section analyses: the measurements of the LArIAT electric field and  
38 calorimetry constants. We developed a technique to measure the LArIAT electric  
39 field using cathode to anode piercing tracks with cosmic data. We applied a new  
40 technique for the measurement of the calorimetry calibration constants based on the  
41 particles' momentum measurement.

42 The ( $\pi^-$ -Ar) and the ( $K^+$ -Ar) total hadronic cross measurements are the first  
43 physics results of the LArIAT experiment and will be the basis for the future LArIAT  
44 measurements of pion and kaon cross sections in the exclusive channels.

45

# Measurement of ( $\pi^-$ -Ar) and ( $K^+$ -Ar) total hadronic cross sections in the LArIAT experiment

46

47

48

A Dissertation  
Presented to the Faculty of the Graduate School  
of  
Yale University  
in Candidacy for the Degree of  
Doctor of Philosophy

49

50

51

52

53

54

55

by  
Elena Gramellini

56

Dissertation Director: Bonnie T. Fleming

57

Date you'll receive your degree

58

Copyright © 2018 by Elena Gramellini

59

All rights reserved.

60

*A mia mamma e mio babbo,*

61

*grazie per le radici e grazie per le ali.*

62

*To my mom and dad,*

63

*thank you for the roots and thank you for the wings.*

# <sup>64</sup> Contents

<sup>65</sup>	<b>Acknowledgements</b>	viii
<sup>66</sup>	<b>Introduction</b>	ix
<sup>67</sup>	<b>1 The theoretical framework</b>	1
<sup>68</sup>	1.1 The Standard Model . . . . .	1
<sup>69</sup>	1.2 Neutrinos: tiny cracks in the Standard Model . . . . .	4
<sup>70</sup>	1.2.1 Neutrinos in the Standard Model . . . . .	4
<sup>71</sup>	1.2.2 Neutrino Oscillations . . . . .	6
<sup>72</sup>	1.2.3 Make up of Neutrino Interactions . . . . .	7
<sup>73</sup>	1.3 Beyond the Standard Model . . . . .	9
<sup>74</sup>	1.3.1 Open Questions in Neutrino Physics . . . . .	11
<sup>75</sup>	1.3.2 Towards a more fundamental theory: GUTs . . . . .	15
<sup>76</sup>	1.4 Motivations for Hadronic Cross Sections in Argon . . . . .	18
<sup>77</sup>	1.4.1 Pion-Argon Total Hadronic Cross Section . . . . .	18
<sup>78</sup>	1.4.2 Kaon-Argon Total Hadronic Cross Section . . . . .	29
<sup>79</sup>	<b>2 Liquid Argon Detectors at the Intensity Frontier</b>	34
<sup>80</sup>	2.1 The Liquid Argon Time Projection Chamber Technology . . . . .	34
<sup>81</sup>	2.1.1 TPCs, Neutrinos & Argon . . . . .	35
<sup>82</sup>	2.1.2 LArTPC: Principles of Operation . . . . .	37

83	2.1.3	Liquid Argon: Ionization Charge . . . . .	40
84	2.1.4	Liquid Argon: Scintillation Light . . . . .	45
85	2.1.5	Signal Processing and Event Reconstruction . . . . .	49
86	2.2	The Intensity Frontier Program . . . . .	53
87	2.2.1	Prospects for LArTPCs in Neutrino Physics: SBN and DUNE	54
88	2.2.2	Prospects for LArTPCs in GUT Physics: DUNE . . . . .	55
89	2.2.3	Enabling the next generation of discoveries: LArIAT . . . . .	57
90	<b>3</b>	<b>LArIAT: Liquid Argon In A Testbeam</b>	<b>60</b>
91	3.1	The Particles' Path to LArIAT . . . . .	60
92	3.2	LArIAT Tertiary Beam Instrumentation . . . . .	62
93	3.2.1	Bending Magnets . . . . .	63
94	3.2.2	Multi-Wire Proportional Chambers . . . . .	65
95	3.2.3	Time-of-Flight System . . . . .	67
96	3.2.4	Punch-Through and Muon Range Stack Instruments . . . . .	68
97	3.2.5	LArIAT Cosmic Ray Paddle Detectors . . . . .	70
98	3.3	In the Cryostat . . . . .	71
99	3.3.1	Cryogenics and Argon Purity . . . . .	71
100	3.3.2	LArTPC: Charge Collection . . . . .	74
101	3.3.3	LArTPC: Light Collection System . . . . .	77
102	3.4	Trigger and DAQ . . . . .	80
103	3.5	Control Systems . . . . .	81
104	<b>4</b>	<b>Total Hadronic Cross Section Measurement Methodology</b>	<b>87</b>
105	4.1	Event Selection . . . . .	88
106	4.1.1	Selection of Beamline Events . . . . .	88
107	4.1.2	Particle Identification in the Beamline . . . . .	89
108	4.1.3	TPC Selection: Halo Mitigation . . . . .	89

109	4.1.4	TPC Selection: Shower Removal . . . . .	90
110	4.2	Beamline and TPC Handshake: the Wire Chamber to TPC Match . .	91
111	4.3	The Thin Slice Method . . . . .	93
112	4.3.1	Cross Sections on Thin Target . . . . .	93
113	4.3.2	Not-so-Thin Target: Slicing the Argon . . . . .	94
114	4.3.3	Corrections to the Raw Cross Section . . . . .	96
115	4.4	Procedure testing with truth quantities . . . . .	97
116	<b>5</b>	<b>Data and MC preparation for the Cross Section Measurements</b>	<b>100</b>
117	5.1	Cross Section Analyses Data Sets . . . . .	100
118	5.2	Construction of a Monte Carlo Simulation for LArIAT . . . . .	102
119	5.2.1	G4Beamline . . . . .	102
120	5.2.2	Data Driven MC . . . . .	107
121	5.3	Estimate of Backgrounds in the Pion Cross Section . . . . .	110
122	5.3.1	Background from Pion Capture and Decay . . . . .	110
123	5.3.2	Contributions from the Beamline Background . . . . .	113
124	5.4	Estimate of Energy Loss before the TPC . . . . .	116
125	5.5	Tracking Studies . . . . .	120
126	5.5.1	Angular Resolution . . . . .	120
127	5.6	Calorimetry Studies . . . . .	126
128	5.6.1	Kinetic Energy Measurement . . . . .	126
129	<b>6</b>	<b>Negative Pion Cross Section Measurement</b>	<b>129</b>
130	6.1	Raw Cross Section . . . . .	129
131	6.1.1	Statistical Uncertainty . . . . .	131
132	6.1.2	Treatment of Systematics . . . . .	133
133	6.2	Corrections to the Raw Cross Section . . . . .	134
134	6.2.1	Background subtraction . . . . .	134

<sup>135</sup>	6.2.2 Efficiency Correction . . . . .	137
<sup>136</sup>	6.3 Results . . . . .	141
<sup>137</sup>	<b>7 Positive Kaon Cross Section Measurement</b>	<b>143</b>
<sup>138</sup>	7.1 Raw Cross Section . . . . .	143
<sup>139</sup>	7.2 Corrections to the Raw Cross Section . . . . .	145
<sup>140</sup>	7.3 Results . . . . .	147
<sup>141</sup>	<b>8 Conclusions</b>	<b>150</b>
<sup>142</sup>	<b>A Measurement of LArIAT Electric Field</b>	<b>152</b>
<sup>143</sup>	<b>B Additional Tracking Studies for LArIAT Cross Section Analyses</b>	<b>160</b>
<sup>144</sup>	B.0.1 Study of WC to TPC Match . . . . .	161
<sup>145</sup>	B.0.2 Tracking Optimization . . . . .	163
<sup>146</sup>	<b>C Energy Calibration</b>	<b>166</b>

# <sup>147</sup> Acknowledgements

<sup>148</sup>

*“Dunque io ringrazio tutti quanti.*

<sup>149</sup>

*Specie la mia mamma che mi ha fatto così funky.”*

<sup>150</sup>

– Articolo 31, Tanqi Funky, 1996 –

<sup>151</sup>

*“At last, I thank everyone.*

<sup>152</sup>

*Especially my mom who made me so funky.”*

<sup>153</sup>

– Articolo 31, Tanqi Funky, 1996 –

<sup>154</sup>

A lot of people are awesome, especially you, since you probably agreed to read  
this when it was a draft.

<sup>156</sup>

“

# <sup>157</sup> Introduction

<sup>158</sup> This thesis work concerns the first measurement of the ( $\pi^-$ -Ar) total hadronic cross  
<sup>159</sup> section in the 100-1000 MeV kinetic energy range and the first measurement of the  
<sup>160</sup> ( $K^+$ -Ar) total hadronic cross section in the 100-650 MeV kinetic energy range. We  
<sup>161</sup> performed these measurements at the LArIAT experiment, a small (0.25 ton) Liquid  
<sup>162</sup> Argon Time Projection Chamber (LArTPC) on a beam of charged particles at the  
<sup>163</sup> Fermilab Test Beam Facility. Albeit particle and nuclear physics have a long history  
<sup>164</sup> of hadronic cross section measurements, the work outlined in this thesis presents a  
<sup>165</sup> new methodology – the “thin slice method” – for cross section measurements in argon,  
<sup>166</sup> possible only thanks to the detection capabilities of the LArTPC technology. The  
<sup>167</sup> combination of fine-grained tracking and excellent calorimetric information provided  
<sup>168</sup> by the LArTPC technology allows to see unprecedented details of particle interactions  
<sup>169</sup> in argon and, in LArIAT, to measure the kinetic energy of a hadron at each step  
<sup>170</sup> of the tracking. A renewed interest for precision measurements of hadronic cross  
<sup>171</sup> sections, particularly in argon, arises from the current panorama of experimental  
<sup>172</sup> particle physics at the intensity frontier.

<sup>173</sup> The discovery of the Higgs boson in 2012 marked the triumph of the Standard  
<sup>174</sup> Model of Particle Physics; exploring what lays beyond is the real challenge in our field  
<sup>175</sup> today. Since their formulation in 1930, neutrinos have been a source of surprises (and  
<sup>176</sup> Nobel Prizes) for particle physicists, tiny cracks in our understanding of Nature. In  
<sup>177</sup> particular, the discovery of neutrino oscillation represents the first evidence of physics

178 Beyond the Standard Model (BSM). From a theoretical point of view, the field is  
179 developing new theories to account for the small but non-zero mass of neutrinos,  
180 while trying to remain consistent with the rest of the Standard Model. From an  
181 experimental point of view, we are developing technologies and huge collaborations  
182 to probe these theories. As we enter the era of precision measurements of neutrino  
183 interaction, neutrinos might hold the key to the next generation of discoveries in  
184 particle physics.

185 Experimentally, precision measurements can be achieved only if the detector tech-  
186 nology is able to resolve the fine details of a neutrino interaction and to record a  
187 statistically relevant number of neutrinos. With “fine details” here we mean the abil-  
188 ity to distinguish the many products of the neutrino interaction, such as protons,  
189 pions, muons and electrons, and to measure their energy. Historically, bubble cham-  
190 ber neutrino detectors were the first revolution in neutrino detection: for example,  
191 the spatial resolution of Gargamelle allowed the discovery of neutrino neutral current  
192 interaction. Despite the high precision of bubble chambers images, this technology  
193 is hard to scale to massive size, making statistical analyses on neutrino interactions  
194 almost impossible to perform. To make up for the small neutrino interaction cross  
195 section, neutrino experiments moved to very large size, at the expenses of spatial  
196 precision. This is the case for the detectors which discovered neutrino oscillation:  
197 both Super-Kamiokande and SNO are massive Cherenkov detectors. With LArT-  
198 PCs, the field is gaining again bubble-chamber like precision but at massive scales.  
199 Following the recommendations of the latest Particle Physics Project Prioritization  
200 Panel [106], the US particle physics panorama is directing a substantial effort to-  
201 wards the exploration of the intensity frontier through the construction of massive  
202 LArTPCs. In particular, the near future will see the development of a Short Baseline  
203 Neutrino Program (SBN) and long baseline neutrino program (DUNE), both based  
204 on the LArTPC detector technology. The US liquid argon program has the potential

205 to answer many of the fundamental open questions in particle physics today, such  
206 as: is there a fourth generation neutrino? is CP violated in the lepton sector? are  
207 there any additional symmetries? and, can we find an indication of Grand Unified  
208 Theories?

209 The SBN program at Fermilab is tasked with conclusively addressing the existence  
210 of a fourth neutrino generation in the  $\Delta m^2 = \Delta m_{14}^2 \sim [0.1 - 10] \text{ eV}^2$  parameter space.  
211 The SBN program entails three surface LArTPCs positioned on the Booster Neutrino  
212 Beam at different distances from the neutrino production in oder to fully exploit the  
213 L/E dependence of the oscillation pattern: SBND (100 m from the decay pipe),  
214 MicroBooNE (450 m), and ICARUS (600 m). SBN will also perform an extensive  
215 program of neutrino cross section measurements, fundamental to abate systematics  
216 in the oscillation analyses in both SBN and DUNE.

217 DUNE has a vast neutrino and non-accelerator physics reach. For what it concerns  
218 neutrino physics, oscillation analyses in DUNE have the capability of solving the mass  
219 hierarchy and octant problem, and discovering CP violation in the neutrino sector.  
220 Besides its neutrino program, DUNE can open an experimental window on Grand  
221 Unified Theories (GUTs). GUTs could potentially answer fundamental questions  
222 such as the existence of non-zero neutrino masses and matter-antimatter asymmetry,  
223 explaining some “accidents” in the Standard Models, such as the exact cancellation of  
224 the proton and the electron charge. Directly probing GUTs at the unification energy  
225 scale is impossible by any foreseeable collider experiment. We then need an indirect  
226 proof such as baryon number violation, which is predicted by almost every GUT in the  
227 form of proton decay, bounded nucleon decay or  $n - \bar{n}$  oscillations on long time-scales.  
228 Historically, the main technology used in these searches has been water Cherenkov  
229 detectors, with Super-Kamiokande setting all the current experimental limits on the  
230 decay lifetimes at the order of  $\sim 10^{34}$  years. The DUNE far detector and its non-  
231 accelerator physics program is a interesting new actor on this stage. LArTPCs can in

fact complement nucleon decay searches in modes where water Cherenkov detectors are less sensitive, especially  $p \rightarrow K^+ \bar{\nu}$  [11].

Such a diverse physics program speaks to the versatility of the LArTPC technology. LArTPCs provide excellent electron/photon separation [9] lacking in Cherenkov detectors which can be leveraged to abate the photon background from neutral current interactions in  $\nu_e$  searches. LArTPCs also share superb tracking capability with bubble chamber detectors, with several additional benefits. They are electronically read out and self triggered detectors; they provide full 3D-imaging with millimeter resolution, precise calorimetric reconstruction and excellent particle identification.

The amount of information a LArTPC can provide makes these detectors rather complex: a series of dedicated measurements is necessary to obtain meaningful physics results from a LArTPC. The complexity of the LArTPC technology for neutrino detection is due to several reasons. Argon is a fairly heavy element, which means that nuclear effects play an important role in the looks of the interaction topology. For example, pions are one of the main products of neutrino interactions; yet, since data on charged particle interaction in argon is scarce, neutrino event generators have big uncertainties in the re-scattering simulation of pion in argon. The amount of details in an LArTPC event is easily parsed by human eye, but can make automatic event reconstruction rather challenging. Thus, reconstruction algorithms in LArTPC need to be tune to recognize the different topologies of the neutrino interaction products in argon. This is particularly true for pions, since they are an abundant product of the neutrino interactions: the occurrence of a pion interaction in argon can modify the topology of the neutrino event, causing a misidentification of the neutrino interaction.

The LArIAT [38] experiment is performing precise cross section measurements of charged particles in argon to bridge this gap of knowledge. The LArIAT LArTPC sits on a beam of charged particles at the Fermilab Test Beam Facility which provides charge particles of the type and energy range relevant for neutrino interaction of

259 both SBN and DUNE. The ( $\pi^-$ -Ar) hadronic cross section is a fundamental input for  
260 neutrino detectors in liquid argon, as pion interactions can modify the topology and  
261 energy reconstruction of neutrino events in the GeV range, where pion production  
262 is abundant. The ( $K^+$ -Ar) total hadronic differential cross section in LArIAT is  
263 particularly relevant for a high identification efficiency in the context of proton decay  
264 searches in DUNE in the  $p \rightarrow K^+ \bar{\nu}$  channel. In fact, the kaon-argon cross section  
265 affects the kaon topology by modifying the kaon tracking and energy reconstruction,  
266 impacting the basis for kaon identification in a LArTPC.

267 The cross section analyses exploit the totality of LArIAT’s experimental handles;  
268 they rely on beam line detector information as well as both calorimetry and tracking  
269 in the TPC. These analyses are LArIAT’s first physics results. In order to measure  
270 total hadronic argon cross sections, several steps are necessary. The analyses start by  
271 identifying a sample of the hadron of interest in the beam line and assessing the beam  
272 line contaminations. It proceeds with tracking the hadron candidates in the TPC and  
273 measuring their kinetic energy at each point in the tracking: the fine sampling of an  
274 hadron in the TPC forms the set of “incident” hadrons. Then, the hadronic interac-  
275 tion point is identified and the raw cross section is calculated. Two corrections are  
276 then applied to the raw cross section – a background subtraction and a correction  
277 for detector effects – to obtain the true cross section measurement.

278

279 This body of work is organized in 8 chapters. We provide a description of the  
280 theoretical framework for the measurements in Chapter 1. Chapter 2 outlines the  
281 LArTPC detector technology, while Chapter 3 describes LArIAT experimental setup.  
282 We present the event selection for both the pion and kaon analyses, as well as the  
283 “thin slice method” in Chapter 4. Chapter 5 describes the work done on the data  
284 and Monte Carlo samples in preparation of the cross section analyses. Chapter 6  
285 shows the results for the ( $\pi^-$ -Ar) total hadronic cross section measurement. Chapter

286 7 shows the results for the ( $K^+$ -Ar) total hadronic cross section measurement. We  
287 draw the final remarks on this work in Chapter 8

288 A series of additional studies and calibrations were necessary to perform the cross  
289 section analyses. Appendix A shows a measurement of the LArIAT LArTPC electric  
290 field using cosmic data. Appendix B shows an optimization of the tracking algorithms  
291 geared towards maximizing the efficiency of finding the hadronic interaction point.  
292 Appendix C shows the calorimetry calibration of the LArIAT LArTPC, which is a  
293 pivotal measurement to enable any physics analysis with TPC data.

<sup>294</sup> **Chapter 1**

<sup>295</sup> **The theoretical framework**



<sup>296</sup>

– J. S. Bach, 1720 ca. –

<sup>297</sup> In this chapter, we set the ( $\pi^-$ - Ar) and ( $K^+$ - Ar) total hadronic cross section  
<sup>298</sup> measurements into the greater theoretical and phenomenological framework. We start  
<sup>299</sup> by briefly describing the Standard Model (Section 1.1), with particular attention to  
<sup>300</sup> neutrinos and neutrino interactions (Section 1.2). We then describe some of the  
<sup>301</sup> open questions in neutrino physics today and Beyond Standard Model theories (1.3)  
<sup>302</sup> setting the stage for the measurements reported in this work (Section 1.4).

<sup>303</sup> **1.1 The Standard Model**

<sup>304</sup> The Standard Model (SM) of particle physics is the most accurate theoretical descrip-  
<sup>305</sup> tion of the subatomic world and, in general, one of the most precisely tested theories  
<sup>306</sup> in the history of physics. The SM describes the strong, electromagnetic and weak  
<sup>307</sup> interactions among elementary particles in the framework of quantum field theory,

308 accounting for the unification of electromagnetic and weak interactions for energies  
309 above the vacuum expectation value (VEV) of the Higgs field. The SM does not  
310 describe gravity or general relativity.

311 The Standard Model is a gauge theory based on the local symmetry group

$$G_{SM} = SU(3)_C \otimes SU(2)_L \otimes U(1)_Y \quad (1.1)$$

312 where the subscripts C indicates the conserved strong charge (color), and the  
313 subscripts Y indicates the conserved hypercharge. If we indicated with T the weak  
314 isospin T and with T3 its third component, hypercharge can be related to the electric  
315 charge Q through the Gell-Mann-Nishijima relation:

$$Q = \frac{Y}{2} + T_3. \quad (1.2)$$

316 In the quantum field framework, the SM fields correspond to the irreducible rep-  
317 resentations of the  $G_{SM}$  symmetry group. In particular, the particles are divided in  
318 two categories, fermions and bosons, according to their spin-statistics. Described by  
319 the Fermi-Dirac statistics, fermions have half-integer spin and are sometimes called  
320 “matter-particles”. Bosons or “force carriers” have integer spin, follow the Bose-  
321 Einstein statistics and mediate the interaction between fermions. The fundamental  
322 fermions and their quantum numbers are listed in Tab 1.1.

323 Quarks can interact via all three the fundamental forces; they are triplets of  
324  $SU(3)_C$ , that is they can exist in three different colors. If one chooses a base where  
325  $u$ ,  $c$  and  $t$  quarks are simultaneously eigenstates of both the strong and the weak  
326 interactions, the remaining eigenstates are usually written as  $d$ ,  $s$  and  $b$  for the strong  
327 interaction and  $d'$ ,  $s'$  and  $b'$  for the weak interaction, because the latter ones are  
328 the result of a CKM rotation on the first ones. Charged leptons interact via the  
329 weak and the electromagnetic forces, while neutrinos only interact via the weak force.

Generation	I	II	III	T	Y	Q
Leptons	$\begin{pmatrix} \nu_e \\ e \end{pmatrix}_L$	$\begin{pmatrix} \nu_\mu \\ \mu \end{pmatrix}_L$	$\begin{pmatrix} \nu_\tau \\ \tau \end{pmatrix}_L$	1/2 -1/2	-1 -1	0 -1
	$e_R$	$\mu_R$	$\tau_R$	0	-2	1
Quarks	$\begin{pmatrix} u \\ d' \end{pmatrix}_L$	$\begin{pmatrix} c \\ s' \end{pmatrix}_L$	$\begin{pmatrix} t \\ b' \end{pmatrix}_L$	1/2 -1/2	1/3 1/3	2/3 -1/3
	$u_R$ $d'_R$	$c_R$ $s'_R$	$t_R$ $b'_R$	0 0	4/3 -2/3	2/3 -1/3

Table 1.1: SM elementary fermionic fields. The subscripts L and R indicate respectively the negative chirality (left-handed) and the positive chirality (right-handed).

- 330 The gauge group univocally determines the number of gauge bosons that carry the  
 331 interaction; the gauge bosons correspond to the generators of the group: eight gluons  
 332 (g) for the strong interaction, one photon ( $\gamma$ ) and three bosons ( $W^\pm$ ,  $Z^0$ ) for the  
 333 electroweak interaction. A gauge theory by itself cannot provide a description of  
 334 massive particles, but it is experimentally well known that most of the elementary  
 335 particles have non-zero masses. The introduction of massive fields in the Standard  
 336 Model lagrangian would make the theory not gauge invariant, resulting ill-defined.  
 337 This problem is solved in the SM by the introduction of a scalar iso-doublet  $\Phi(x)$ , the  
 338 Higgs field, which gives mass to  $W^\pm$  and  $Z^0$  gauge bosons through the electroweak  
 339 symmetry breaking mechanism and to the fermions through Yukawa coupling [75, 76].  
 340 The discovery of the Higgs boson in 2012 by the LHC experiments [41, 42] marked  
 341 the ultimate confirmation of a long history of successful predictions by the SM.

## 342 1.2 Neutrinos: tiny cracks in the Standard Model

343 To our current knowledge, neutrinos are the most abundant fermion in the Universe.  
344 And yet, they are maybe the most mysterious particle in the SM: they generate  
345 theoretical puzzles and experimental challenges. In this section, we treat neutrinos  
346 within and beyond the SM and describe the make up of their interaction with matter.

### 347 1.2.1 Neutrinos in the Standard Model

348 Neutrino can be introduced in the SM as left-handed massless Weyl spinors. The  
349 Dirac equation of motion for a free field

$$(i\gamma^\mu \partial_\mu - m)\psi = 0 \quad (1.3)$$

350 for a fermionic field

$$\psi = \psi_L + \psi_R \quad (1.4)$$

351 is equivalent to the equations

$$i\gamma^\mu \partial_\mu \psi_L = m\psi_R \quad (1.5)$$

352

$$i\gamma^\mu \partial_\mu \psi_R = m\psi_L \quad (1.6)$$

353 for the chiral fields  $\psi_R$  and  $\psi_L$ , whose evolution in space and time is coupled  
354 through the mass  $m$ . If the fermion is massless, the chiral fields decouple and the  
355 fermion can be described by a single Weyl spinor with two independent compo-  
356 nents [116]. Pauli initially rejected the description of a physical particle through  
357 a single Weyl spinor because of its implication of parity violation. In fact, since  
358 the spatial inversion operator throws  $\psi_R \leftrightarrow \psi_L$ , parity is conserved only if both chi-  
359 ral components exist at the same time. For the neutrino introduction in the SM,  
360 experiments came in help of the theoretical description. The constraint of parity

<sup>361</sup> conservation weakened after Wu's experiment in 1957 [119]. Additionally, there was  
<sup>362</sup> no experimental indication for massive neutrinos, nor evidence of interaction via the  
<sup>363</sup> neutrino right-handed component.

<sup>364</sup> The symmetry group  $SU(2)_L \otimes U(1)_Y$  is the only group relevant for neutrino  
<sup>365</sup> interactions. The SM electroweak lagrangian is the most general renormalizable la-  
<sup>366</sup> grangian invariant under the local symmetry group  $SU(2)_L \otimes U(1)_Y$ . The lagrangian  
<sup>367</sup> couples the weak isotopic spin doublets and singlets described in Table 1.1 with the  
<sup>368</sup> gauge bosons  $A_a^\mu$  ( $a = 1, 2, 3$ ) and  $B^\mu$ , and Higgs doublet  $\Phi(x)$ :

$$\begin{aligned} \mathcal{L} = & i \sum_{\alpha=e,\mu,\tau} \bar{L}'_{\alpha L} \not{D} L'_{\alpha L} + i \sum_{\alpha=1,2,3} \bar{Q}'_{\alpha L} \not{D} Q'_{\alpha L} \\ & + i \sum_{\alpha=e,\mu,\tau} \bar{l}'_{\alpha R} \not{D} l'_{\alpha R} + i \sum_{\alpha=d,s,b} \bar{q}'^D_{\alpha R} \not{D} q'^D_{\alpha R} + i \sum_{\alpha=u,c,t} \bar{q}'^U_{\alpha R} \not{D} q'^U_{\alpha R} \\ & - \frac{1}{4} A_{\mu\nu} A^{\mu\nu} - \frac{1}{4} B_{\mu\nu} B^{\mu\nu} \\ & + (D_\rho \Phi)^\dagger (D^\rho \Phi) - \mu^2 \Phi^\dagger \Phi - \lambda (\Phi^\dagger \Phi)^2 \\ & - \sum_{\alpha,\beta=e,\mu,\tau} \left( Y_{\alpha\beta}^l \bar{L}'_{\alpha L} \Phi l'_{\beta R} + Y_{\alpha\beta}^{l*} \bar{l}'_{\beta R} \Phi^\dagger L'_{\alpha L} \right) \\ & - \sum_{\alpha=1,2,3} \sum_{\beta=d,s,b} \left( Y_{\alpha\beta}^D \bar{Q}'_{\alpha L} \Phi q'^D_{\beta R} + Y_{\alpha\beta}^{D*} \bar{q}'^D_{\beta R} \Phi^\dagger Q'_{\alpha L} \right) \\ & - \sum_{\alpha=1,2,3} \sum_{\beta=u,c,t} \left( Y_{\alpha\beta}^U \bar{Q}'_{\alpha L} \tilde{\Phi} q'^U_{\beta R} + Y_{\alpha\beta}^{U*} \bar{q}'^U_{\beta R} \tilde{\Phi}^\dagger Q'_{\alpha L} \right). \end{aligned} \quad (1.7)$$

<sup>369</sup> The first two lines of the lagrangian summarize the kinetic terms for the fermionic  
<sup>370</sup> fields and their coupling to the gauge bosons  $A_a^{\mu\nu}$ ,  $B^{\mu\nu}$ <sup>1</sup>. The third line describes  
<sup>371</sup> the kinetic terms and the self-coupling terms of the gauge bosons. The forth line is  
<sup>372</sup> the Higgs lagrangian, which results in the spontaneous symmetry breaking. The last  
<sup>373</sup> three lines describe the Yukawa coupling between fermions and the Higgs field, origin  
<sup>374</sup> of the fermions' mass.

---

1. In gauge theories the ordinary derivative  $\partial_\mu$  is substituted with the covariant derivative  $D_\mu$ . Here  $D_\mu = \partial_\mu + igA_\mu \cdot I + ig'B_\mu \frac{Y}{2}$ , where  $I$  and  $Y$  are the  $SU(2)_L$  and  $U(1)_Y$  generators, respectively.

375      The coupling between left-handed and right-handed field generates the mass term  
376 for fermions. The SM assumes only left-handed components for neutrinos, thus im-  
377 plying zero neutrino mass. Since any linear combination of massless fields results in a  
378 massless field, the flavor eigenstates are identical to the mass eigenstates in the SM.

### 379 1.2.2 Neutrino Oscillations

380      The determination of the flavor of a neutrino dynamically arises from the correspond-  
381 ing charged lepton associated in a change current interaction; for example, a  $\nu_e$  is a  
382 neutrino which produces an  $e^-$ , a  $\bar{\nu}_\mu$  is a neutrino which produces a  $\mu^+$ , *etc.* The  
383 neutrino flavor eigenstates  $|\nu_\alpha\rangle$ , with  $\alpha = e, \mu, \tau$ , are orthogonal to each other and  
384 form a base for the weak interaction matrix.

385      Overwhelming experimental data show that neutrinos change flavor during their  
386 propagation [101]. This phenomenon, called “neutrino oscillations”, was predicted  
387 first by Bruno Pontecorvo in 1957 [102]. Neutrino oscillations are possible only if  
388 the neutrino flavor eigenstate are not identical to the mass eigenstates. Thus, the  
389 observation of neutrino oscillation results in the first evidence of physics beyond the  
390 Standard Model. A minimal extension of the SM introduces three mass eigenstates,  
391  $|\nu_i\rangle$  ( $i = 1, 2, 3$ ), whose mass  $m_i$  is well defined. The unitary Pontecorvo-Maki-  
392 Nakagawa-Sakata matrix transforms the mass base into the flavor base as follows

$$|\nu_\alpha\rangle = U_{PMNS} |\nu_i\rangle, \quad (1.8)$$

393      with

$$U_{PMNS} = \begin{bmatrix} c_{12} & s_{12} & 0 \\ -s_{12} & c_{12} & 0 \\ 0 & 0 & 1 \end{bmatrix} \begin{bmatrix} c_{13} & 0 & s_{13}e^{-i\delta} \\ 0 & 1 & 0 \\ -s_{13}e^{-i\delta} & 0 & c_{13} \end{bmatrix} \begin{bmatrix} 1 & 0 & 0 \\ 0 & c_{23} & s_{23} \\ 0 & -s_{23} & c_{23} \end{bmatrix} \begin{bmatrix} e^{i\alpha_1} & 0 & 0 \\ 0 & e^{i\alpha_2} & 0 \\ 0 & 0 & 1 \end{bmatrix} \quad (1.9)$$

394 where  $c$  e  $s$  stand respectively for cosine and sine of the corresponding mixing  
 395 angles ( $\theta_{12}$ ,  $\theta_{23}$  and  $\theta_{13}$ ),  $\delta$  is the Dirac CP violation phase,  $\alpha_1$  and  $\alpha_2$  are the eventual  
 396 Majorana CP violation phases. Experimental results on neutrino oscillations are  
 397 generally reported in terms of the mixing angles and of the squared mass splitting  
 398  $\Delta m_{ab}^2 = m_a^2 - m_b^2$ , where  $a$  and  $b$  represent the mass eigenstates. A summary of the  
 399 current status of experimental results, albeit partial, is given in table 1.2.

Table 1.2: Summary of experimental results on neutrino oscillation parameters. **ADD CITATIONS**

	Value	Precision	Experiment
$\theta_{23}$	$45^\circ$	9.0%	Super Kamiokande, MINOS,
$-\Delta m_{32}^2$	$2.5 \cdot 10^{-3} \text{ eV}^2$	1.8%	Nova, MACRO
$\theta_{12}$	$34^\circ$	5.8%	SNO, Gallex,
$-\Delta m_{12}^2$	$7.4 \cdot 10^{-5} \text{ eV}^2$	2.8%	SAGE, KamLAND
$\theta_{13}$	$9^\circ$	4.7%	DAYA Bay,
$-\Delta m_{32}^2$	$2.5 \cdot 10^{-3} \text{ eV}^2$	1.8%	RENO

### 400 1.2.3 Make up of Neutrino Interactions

401 All neutrino experiments involving the detection of single neutrinos are concerned  
 402 with neutrino interactions (and neutrino cross sections) on nuclei. Given the invisible  
 403 nature of the neutrino, characterizing the products of its interaction is the only  
 404 method to a) assess the neutrino presence, b) detect its flavor in case of a charge  
 405 current interaction and c) eventually reconstruct its energy.

406 Historically, neutrino interactions with the nucleus in the GeV region are divided  
 407 into three categories into three categories whose contributions change as a function

408 of increasing neutrino energy:: quasi elastic (QE), resonant (RES), and deep inelastic  
409 (DIS) scattering. All current and forthcoming oscillation experiments on neutrino  
410 beams live in the 0.1-10 GeV transition region, which encompasses the energy where  
411 the QE neutrino-nucleus interaction transitions into RES and then into DIS. For  
412 scattering off free nucleons, neutrino and antineutrino QE charge current scattering  
413 refers to the process  $\nu_l n \rightarrow l^- p$  and  $\bar{\nu}_l p \rightarrow l^+ n$  where a charged lepton and single  
414 nucleon are ejected in the elastic interaction. Resonant scattering refers to an inelas-  
415 tic collision producing a nucleon excited state ( $\Delta, N^*$ ) – the resonance – which then  
416 quickly decays, most often to a nucleon and single-pion final state. DIS refers to the  
417 head-on collision between the neutrino and a parton inside the nucleon, producing  
418 hadronization and subsequent abundant production of mesons and nucleons. In addi-  
419 tion to such interactions between the neutrino and a single component of the nucleus,  
420 neutrinos can also interact with the nucleus as a whole, albeit more rarely, a well  
421 documented process called coherent meson production scattering [58]; the signature  
422 of such process is the production of a distinctly forward-scattered single meson final  
423 state, most often a pion. This simple picture of neutrino interactions works rather  
424 well for scattering off of light nuclear targets, such as the H<sub>2</sub> and D<sub>2</sub> of bubble cham-  
425 ber experiments [64], but the complexity of the nuclear structure for heavier nuclei  
426 such as argon complicates this model.

427 As we will discuss in Chapter 2, the properties of argon make it a good candidate  
428 for an interacting medium in neutrino experiments; in particular the density of its  
429 interaction centers increases the yield of neutrino interactions and allows for relatively  
430 compact detectors. Though, the choice of a relatively heavy nuclear target comes at  
431 the cost of enhancing nuclear effects which modify the kinematic and final state of  
432 the neutrino interaction products.

433 Nuclear effects can potentially affect neutrino event rates, final state particle emis-  
434 sion, neutrino energy reconstruction, and the neutrino/antineutrino ratios, carrying

435 deep implications for oscillation experiments. Even in the case of “simple” QE scat-  
436 tering, intra-nuclear hadron rescattering and correlation effects between the target  
437 nucleons can cause the ejection of additional nucleons in the final state, modifying  
438 the final state kinematics and topology. In the case of resonant and DIS scattering,  
439 the hadronic interactions of meson and nucleons produced in the decay of the res-  
440 onance or during hadronization complicate this picture even more. A large source  
441 of uncertainty in modeling nuclear effects in neutrino interactions come from mesons  
442 interactions (and re-interactions) in the nucleus, e.g., pion re-scattering, charge ex-  
443 change, and absorption.

444 A renewed interest for neutrino cross section measurements surged in recent years,  
445 along with a lively discussion on the data reporting; the historical method of reporting  
446 the neutrino cross section as a function of the neutrino energy or momentum trans-  
447 fered shakes under the weight of its dependency on the chosen nuclear model. On one  
448 hand, correcting for nuclear effects in neutrino interaction can introduce unwanted  
449 sources of uncertainty and model dependency especially due to the mis-modeling of  
450 the meson interactions. On the other, avoiding this correction makes a comparison  
451 between neutrino interactions on different target nuclei extremely difficult.

452 Data on neutrino scattering off many different nuclei are available for both charged  
453 current (CC) and neutral current (NC) channels, as summarized in [64]. A summary  
454 of the results on QE, resonant and DIS scattering for neutrinos and antineutrinos from  
455 accelerators on different target is reported in Figure 1.1, where the (NUANCE) [37]  
456 event generator is used as comparison with the theory.

### 457 1.3 Beyond the Standard Model

458 The discovery of neutrino oscillation and its implication of non-zero neutrino mass  
459 mark the beginning of a new, exciting era in neutrino physics: the era of physics Be-

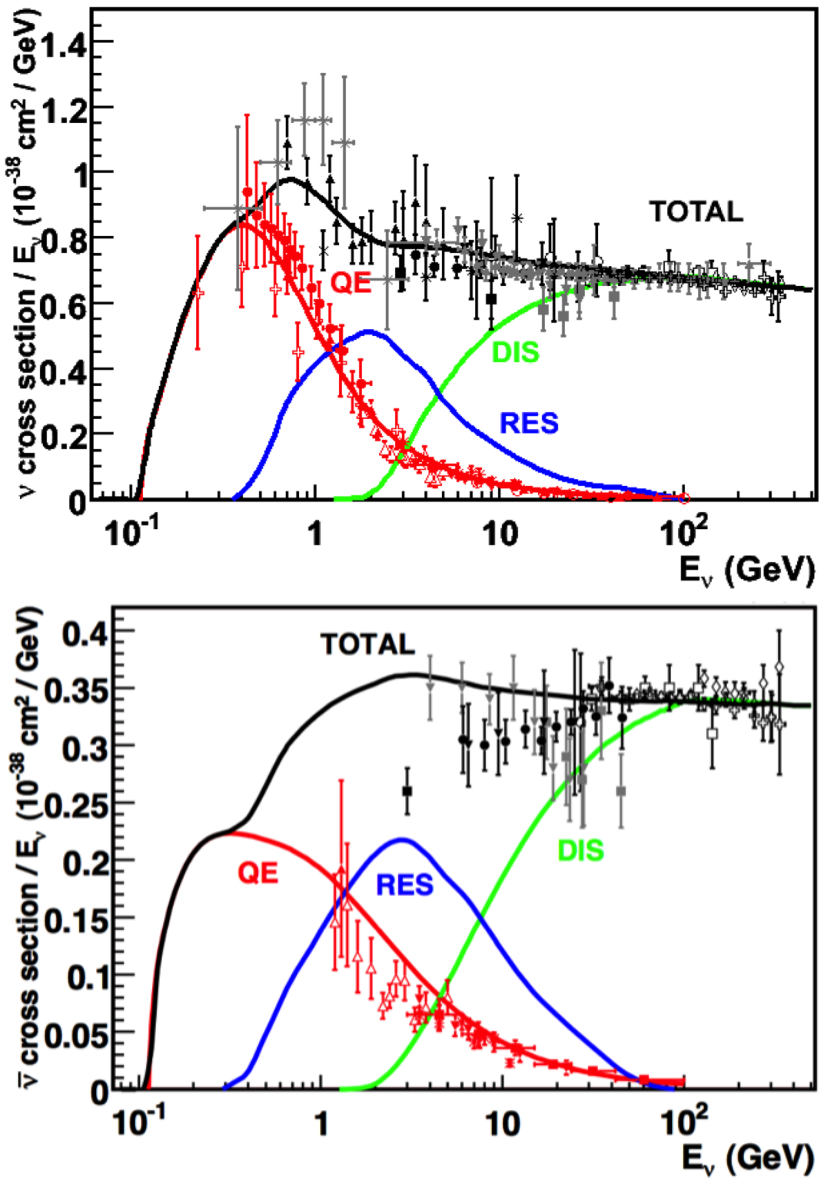


Figure 1.1: Total neutrino (top) and antineutrino (bottom) CC cross sections per nucleon divided by neutrino energy as a function of energy as reported in [64]. Predictions for the total (black), the QE (red), resonant (blue) and DIS (green) are provided by the NUANCE generator. The quasi-elastic scattering data and predictions have been averaged over neutron and proton targets (isoscalar target).

460 yond the Standard Model (BSM) at the intensity frontier. We are currently searching  
461 for new, deeper theories that can accommodate neutrinos with tiny but non-zero  
462 masses, while remaining consistent with the rest of the Standard Model.

463 **1.3.1 Open Questions in Neutrino Physics**

464 On one hand, the last three decades of experiments in neutrino oscillations brought  
465 spectacular advancements in the understanding of the oscillations pattern, measuring  
466 the neutrino mixing angles and mass splitting with a precision of less than 10%. On  
467 the other, they opened the field for a series of questions needing experimental answers.

468 **Sterile neutrinos.** Hints to the existence of at least one additional neutrino,  
469 in the form of various anomalies, have been puzzling physicists almost from the be-  
470 ginning of neutrino oscillation searches. Originally designed to look for evidence of  
471 neutrino oscillation, the Liquid Scintillator Neutrino Detector (LSND) [54] provided  
472 a first conflicting result with the Standard Model expectation of only three neutrinos.  
473 A second conflicting result has also been provided by the MiniBooNE experiment [50].

474 The LSND and MiniBooNE  $\nu_e$  and  $\bar{\nu}_e$  appearance results, known as the “LSND and  
475 MiniBooNE anomalies” [14, 15, 23], may be interpreted under the assumption of a new  
476 right-handed neutrino. The additional neutrino needs to be “sterile”, i.e needs not  
477 to couple with the electroweak force carriers, in order to meet the constraint imposed  
478 by the measurement of the width of the Z boson [2]. The new sterile neutrino would  
479 mainly be composed of a heavy neutrino  $\nu_4$  with mass  $m_4$  such that  $m_1, m_2, m_3 \ll m_4$   
480 and  $\Delta m^2 = \Delta m_{14}^2 \sim [0.1 - 10] \text{ eV}^2$ . The introduction of sterile neutrinos is an ap-  
481 pealing line of thinking, since this renormalizable generalization of the SM has the  
482 potential to impact long standing questions in high energy physics and cosmology:  
483 light sterile neutrinos are candidates for dark matter particles and there are ideas  
484 that the theory could be adjusted to explain the baryon asymmetry of the Universe  
485 via leptogenesis [71].

486       **CP Violation In Lepton Sector.** The measurement of non-zero value for the  
 487       oscillation parameter  $\theta_{13}$  allows the exploration of low-energy CP violation in the lep-  
 488       ton sector at neutrino long baseline oscillation experiments, enabling the possibility  
 489       to measure the Dirac CP-violating phase  $\delta$ . Exciting theoretical results tie  $\delta$  directly  
 490       to the generation of the baryon asymmetry of the Universe at the Grand Unified  
 491       Theory scale **a couple of cit would be nice**. According to the theoretical model de-  
 492       scribed in [100], for example, leptogenesis can be achieved if  $|\sin \theta_{13} \sin \delta| > 0.11$ , i.e.  
 493        $\sin \delta > 0.7$ .  
 494       The asymmetry in the oscillation probability of neutrinos and antineutrinos is the ob-  
 495       servable sensitive to the Dirac CP-violating phase  $\delta$  leveraged in neutrino oscillation  
 496       experiments. Using the parameterization of the PMNS matrix shown in Equation  
 497       1.9, the difference between the probability of  $\nu_e \rightarrow \nu_\mu$  oscillation and the probability  
 498       of  $\bar{\nu}_e \rightarrow \bar{\nu}_\mu$  oscillation can be parametrized as follows [39],

$$P_{\nu_e \rightarrow \nu_\mu} - P_{\bar{\nu}_e \rightarrow \bar{\nu}_\mu} = J \cos \left( \pm \delta - \frac{\Delta_{31} L}{2} \right) \sin \left( \frac{\Delta_{21} L}{2} \right) \sin \left( \frac{\Delta_{31} L}{2} \right) \quad (1.10)$$

499       where

$$J = \cos \theta_{13} \sin 2\theta_{13} \sin 2\theta_{12} \sin 2\theta_{23} \quad (1.11)$$

500       is the Jarlskog invariant [81],  $L$  the neutrino baseline, i.e. the distance between  
 501       the neutrino production and detection points, and  $\Delta_{ab}$  a factor proportional to the  
 502       sign and magnitude of the mass splitting. From these equations, it is clear how the  
 503       relative large value of  $\theta_{13}$  is a happy accident necessary not to completely suppress  
 504       the sensitivity to CP violation. The equations also show how the sensitivity to  $\delta$  is  
 505       tied to the measurement of the least precisely measured mixing angle,  $\theta_{23}$  (via the  
 506        $\sin 2\theta_{23}$  term) and to an other unknown quantity, the neutrino “mass hierarchy” (via  
 507       the  $\Delta_{ab}$  terms). The precise determination of  $\theta_{23}$  is often referred as to “the octant  
 508       problem”. Current experimental results [3, 12] are consistent with  $\theta_{23} = 45^\circ$ , which

509 would imply maximal mixing between  $\nu_\mu$  -  $\nu_\tau$ , hinting to an intriguing new symmetry.  
510 Therefore, a precise measurement of  $\theta_{23}$  is of great interest for theoretical models of  
511 quark-lepton universality [74, 92, 105], whose quark and lepton mixing matrices are  
512 proportional to the deviation of  $\theta_{23}$  from 45°.

513 **Neutrino mass hierarchy.** The “mass hierarchy” problem refers to the unknown  
514 ordering of the value of absolute mass of the neutrino mass eigenstates. Current  
515 oscillation experiments are sensitive only to the magnitude of the mass splitting, and  
516 not directly to its sign. In a framework where the lightest neutrino mass (arbitrarily)  
517 corresponds to the first eigenstate  $m_1$ , it is unknown whether  $m_2 - m_1 < m_3 - m_1$   
518 (Normal Hierarchy) or  $m_2 - m_1 > m_3 - m_1$  (Inverted Hierarchy). The mass hierarchy  
519 affects not only the sensitivity to CP violation searches in long baseline oscillation  
520 experiments, but also the sensitivity to determine whether neutrinos are Majorana  
521 particles in neutrinoless double beta decay experiments.

522 **Majorana or Dirac?** Evidence of neutrino oscillations demands the introduction  
523 of a mechanism which can give mass to the neutrinos. This mechanism should possibly  
524 also explain why neutrino masses are at least six orders of magnitude lower than the  
525 electron mass (the second lightest SM fermion). In a description of neutrinos as Dirac  
526 4-component spinors, the neutrino field acquires mass via the Higgs mechanism as  
527 any other fermion of the SM. In this case, the neutrino mass is given by  $m_a = \frac{y_a^\nu v}{\sqrt{2}}$ ,  
528 where  $v$  is the Higgs VEV and  $y_a^\nu$  is the Yukawa coupling between the Higgs and the  
529 neutrino. The smallness of neutrino masses can only be pinned on a tiny Yukawa  
530 coupling which is not justified by the theory.

531 In 1937, Majorana demonstrated that the introduction of a two components spinor is  
532 sufficient to describe a massive fermion [91]. The Dirac equations of motion for the  
533 chiral fields (equations 1.5 and 1.6) hold true in the case of two components spinor  
534 under the assumption that the chiral components  $\psi_R$  and  $\psi_L$  are correlated through  
535 the charge conjugation matrix  $\mathcal{C}$ ,  $\psi_R = \mathcal{C}\bar{\psi}_L$ . Therefore the theory is applicable only

536 to neutral fermions. Neutrinos are the only neutral elementary particles in the SM  
537 – the only possible Majorana particle candidate. This theory constructs a neutrino  
538 Majorana mass term  $\mathcal{L}_5$  of the following form in the Higgs unitary gauge

$$\mathcal{L}_5 = \frac{1}{2} \frac{gv^2}{\mathcal{M}} \nu_L^T \mathcal{C}^\dagger \nu_L, \quad (1.12)$$

539 where  $g$  is the coupling coefficient,  $v$  the Higgs VEV and  $\mathcal{M}$  a constant with the  
540 dimension of the mass proportional to the scale of new physics. The  $\mathcal{L}_5$  term would  
541 introduce a non-renormalizable term in the lagrangian, since it has dimensions of  
542 energy to the fifth power. This is not allowed in the SM lagrangian; however, the  
543 existence of such terms is plausible if we consider the SM as an effective theory  
544 at low energy, manifestation of the symmetry breaking of a more general theory at  
545 higher energy, e.g. a Grand Unified Theory (GUT), and not the definitive theory.  
546 The mass term in eq 1.12 implies the neutrino mass to be  $m = \frac{gv^2}{\mathcal{M}}$ . The coupling  
547 coefficient can be of the order of any other fermion's coupling coefficient, since the  
548 smallness of neutrino masses is achieved by the big value of the new physics mass  
549 scale alone. This vanilla formulation is the conceptual basis for many flavors of *see-*  
550 *saw mechanism* [121], which we will not discuss here in any detail. However, it is  
551 fascinating how the puzzle of the neutrino mass hints to the existence of a deeper and  
552 more complete theory.

553 From a kinematic point of view, Dirac and Majorana neutrinos satisfy the same  
554 energy-momentum dispersion relationship. Thus, it is impossible to discern the neu-  
555 trino nature through kinematic effects such as neutrino oscillations. Neutrinoless  
556 double beta decay searches are the most promising way to understand the nature of  
557 the neutrino and are therefore subject of great theoretical and experimental interest.  
558 Observation of the lepton number violating process  $0\nu\beta\beta$  would imply neutrinos have  
559 a Majorana component. Depending on the mass hierarchy, the theory also predicts

560  $0\nu\beta\beta$  exclusion regions and confirmation of the sole Dirac component for neutrinos [44].  
561  
562

### 563 1.3.2 Towards a more fundamental theory: GUTs

564 Despite its highly predictive power, a number of conceptual issues arise in the SM  
565 which disfavor it to be a good candidate for a fundamental theory.

566 The SM does not include a suitable dark matter candidate and a mechanisms  
567 that accounts for the baryon asymmetry of the universe. Additionally, up to a total  
568 of 25 parameters remain seemingly arbitrary and need to be fitted to data: 3 gauge  
569 couplings, 9 charged fermion masses, 3 mixing angles and one CP phase in the CKM  
570 matrix, the Higgs mass and quartic coupling,  $\theta_{QCD}$ , 3 neutrino mixing angles, 1 Dirac  
571 phase and, eventually, 2 Majorana phases.

572 From a group theory perspective, the SM has a rather complex group structure,  
573 where a gauge group is formed with the direct product of other three groups as shown  
574 in eq. 1.1. Drawing a parallel with the electroweak symmetry breaking mechanism,  
575 where the  $SU(2)_L \otimes U(1)_Y$  is recovered from  $U(1)_{EM}$ , an interesting line of simplification  
576 for the SM group structure would be to devise a similar mechanism where  
577  $SU(3)_C \otimes SU(2)_L \otimes U(1)_Y$  is recovered from an hypothetical larger group. IS THIS  
578 CORRECT? Just as the electroweak unification becomes evident at energies higher  
579 than the Higgs VEV, a direct manifestation of Grand Unification Theories (GUTs)  
580 would occur at even higher energies.

581 As the smallness of neutrino masses suggests the existence of a higher mass scale,  
582 an other, even stronger, hint to Grand Unification comes from the slope of running  
583 of the coupling constants. The coupling constants for the electromagnetic, weak and  
584 strong interactions in the SM vary as a function of the interaction energy as shown  
585 in figure 1.2; they do not exactly meet under the current experimental constraints,

<sup>586</sup> but their trend is interesting enough to push for the construction of theories where  
<sup>587</sup> perfect unification is achieved through the addition of new particles.

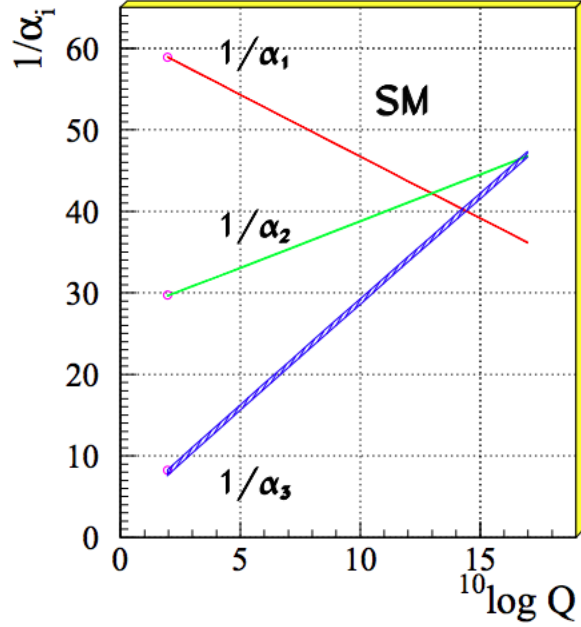


Figure 1.2: Evolution of the inverse of the three coupling constants in the Standard Model as a function of the momentum transferred, [85].

**SU(5).** The smallest simple group containing  $SU(3)_C \otimes SU(2)_L \otimes U(1)_Y$  is SU(5), as shown first by Georgi and Glashow in [68]. Quarks and leptons in this group fit the  $\bar{5}$  and 10 representations. The representation for left-handed fermions are the following

$$\bar{5} = (\nu_e, e^-)_L + \bar{d}_L \quad (1.13)$$

$$10 = e_L^+ + \bar{u}_L + (u, d)_L, \quad (1.14)$$

<sup>588</sup> while the boson structure gains a new couple of super heavy bosons (X,Y)

$$24 = \underbrace{(8, 1)}_{\text{gluons}} + \underbrace{(1, 3) + (1, 1)}_{W^\pm, Z, \gamma} + \underbrace{(3, 2) + (\bar{3}, 2)}_{X, Y \text{ bosons}}. \quad (1.15)$$

<sup>589</sup> Nice features such as charge quantization and the identity between the positron

590 and proton charge value come directly from the group structure. The new super  
591 heavy bosons are colored and form a weak doublet. Their are the mediator of the  
592 interaction that turns quarks into leptons, leading to predict the existence of processes  
593 that violate baryon number, such as  $p \rightarrow \pi^0 + e^+$  (see fig 1.8, right). The prediction  
594 for proton decay lifetime,  $\tau_p \sim \frac{M_X^4}{m_p^5} \sim 10^{30 \pm 1.5}$  years, is unfortunately experimentally  
595 disproved by IMB and Super-Kamiokande [4, 28].

596 **SO(10).** More complicated group structures, such as SO(10) are still viable  
597 candidates for GUT. SO(10) includes the same type of  $X$  and  $Y$  bosons as SU(5).  
598 Right-handed massive neutrinos are embedded in the construction of the irreducible  
599 representation of SO(10). Different patterns of SO(10) symmetry breaking to recover  
600 the SM are possible and lead to different predictions for the proton decay lifetime;  
601 some of these predictions are not excluded by the experiments [86].

602 **SUSY GUTs.** Supersymmetry theories allow for another family of GUTs. In  
603 SUSY, every fundamental particle in the SM has a “superpartner”, identical in each  
604 quantum number except for the spin-statistics: the fermion supersymmetric partners  
605 are bosons and vice versa. Collider experiments (mainly LHC) constrain the mass of  
606 the supersymmetric partners to be very heavy [?]. The SU(5), SU(10) groups with  
607 a SUSY twist are the basic groups for SUSY GUTs. From the phenomenology point  
608 of view, SUSY models tend to push the proton decay life time higher by a factor of  
609 four, they solve the “hierarchy problem”, and they also predict new channels for the  
610 proton decay. In particular they predict the presence of kaons in the final product,  
611 with a dominant mode of  $p \rightarrow K^+ \bar{\nu}$ . Predictions on the proton decay lifetime depend  
612 on the chosen SUSY model; again, some of the predictions are not excluded by the  
613 experiments [89, 90, 109].

614    **1.4 Motivations for Hadronic Cross Sections in Ar-**  
615    **gon**

616    Critical challenges await the next decade of high energy physics at the intensity  
617    frontier. Following the recommendation of the latest Particle Physics Project Priori-  
618    tization Panel [106], the US is dedicating substantial resources to the development of  
619    a short- and long- baseline neutrino program to address many of open questions in  
620    neutrino physics today. This program pivots on the Liquid Argon Time Projection  
621    Chamber (LArTPC) detector technology which will be described in Chapter 2.

622    The main goals of these research programs include:

- 623    - the assessment of the existence of right-handed sterile neutrinos via the study  
624       of accelerator neutrinos on a short baseline (SBN),
- 625    - the determination of the sign of  $\Delta m_{13}^2$  (or  $\Delta m_{23}^2$ ), i.e., the neutrino mass hier-  
626       archy via the study of accelerator neutrinos on a long baseline (DUNE),
- 627    - the determination of the octant, i.e. whether  $\theta_{23}$  is maximal, via the study of  
628       accelerator neutrinos on a long baseline (DUNE),
- 629    - the determination the status of CP symmetry in the lepton sector, via the study  
630       of accelerator neutrinos on a long baseline (DUNE),
- 631    - the search for observables predicted by GUTs, such as proton decay via the  
632       study of non accelerator physics in massive underground detectors (DUNE).

633    **1.4.1 Pion-Argon Total Hadronic Cross Section**

634    This section outlines the importance of the pion-argon total hadronic cross section in  
635    the context of the current and upcoming liquid argon neutrino experiments, SBN and  
636    DUNE. We describe the signal signature and historic measurements of pion-nucleus

637 cross section, as well as the implementation of these cross sections in the current  
638 version of the simulation package used by LArIAT.

639  **$\pi^-$ Ar Cross Section in the Context of Neutrino Searches**

640 As outlined in 1.2.3, neutrino experiments use the products of neutrino interactions  
641 to identify the energy and flavor of the incoming neutrino. Pions are a common  
642 product of neutrino interaction, especially in resonant scattering, DIS and coherent  
643 pion production. For neutrino experiments in argon, there are two main reasons  
644 why understanding pion hadronic interactions with argon is important: to model the  
645 behavior of the pion inside the target nucleus and to model the behavior of the pion  
646 during its propagation inside the detector medium.

647 Assumptions on the nuclear modeling and on the interaction of hadrons inside the  
648 nucleus performed at the level of the neutrino event generator bridge the measure-  
649 ment of the products of a neutrino interaction to the reconstruction of the neutrino  
650 energy and flavor. Thus, understanding pion hadronic interactions with the nucleus is  
651 particularly important to model correctly resonant, DIS and coherent pion production  
652 in neutrino interactions. For example, in case of resonant scattering,

$$\nu_l + N \rightarrow l + \Delta/N^* \rightarrow l + \pi + N', \quad (1.16)$$

653 the  $\Delta$  and  $N^*$  and excited states will decay hadronically in matters of  $\sim 10^{-24}$  s  
654 inside the nucleus producing pions which will have many chances to re-interact  
655 as they exit the target medium. The decay modes for the lower mass  $\Delta$  (1232) and  
656  $N^*(1440)$  are listed in table 1.3.

657 The key elements of a neutrino event generators for resonance and DIS events  
658 are the nuclear model and the hadron treatment (both production and transporta-  
659 tion). We illustrate here the conceptual basis of the GENIE Neutrino Generator [18]

660 as an example, since GENIE is one the most popular event generators for liquid ar-  
661 gon experiments. For example, the nuclear model used by GENIE for all processes  
662 is a Relativistic Fermi Gas (RFG) model modified to incorporate nucleon-nucleon  
663 correlations [30]. This means that the initial momentum and binding energy of the  
664 struck nucleon is determined by assuming nucleons inside the nucleus are quasi-free,  
665 acting independently in the mean field of the nucleus. For  $A > 20$  such as argon, the  
666 2-parameter Woods-Saxon shell model for density function is used. The GENIE mod-  
667 ule INTRANUKE [84] is used to simulate final-state interactions (FSI) which model  
668 hadron re-interactions inside the nucleus. This module places the outgoing parti-  
669 cles in the nucleus and propagates them using the “hA model”. In the INTRANUKE  
670 hA model, hadrons can undergo at most one FSI per event. When possible, external  
671 hadron-nucleus scattering data are used to tune INTRANUKE. Since no data is avail-  
672 able for Argon, GENIE uses an interpolation of data from heavier and lighter nuclei  
673 for the pion-argon cross section leading to large (10?s of %) resultant uncertainties in  
674 the INTRANUKE module.

675 Once the pion has left the target nucleus, the pion-argon hadronic cross section also  
676 plays an important role in the pion transportation inside the argon medium: processes  
677 such as pion absorption or pion charge exchange can greatly modify the topology of  
678 a neutrino interactions in the detector and lead to significant modifications in the  
679 event classification. Being able to reconstruct the details of pions inside the detector  
680 is an imperative for modern liquid argon neutrino experiment to achieve the design  
681 resolution for their key physics measurements.

## 682 $\pi^-$ -Ar Hadronic Interaction: Signal Signatures

683 Strong hadronic interaction models [49,69] predict the pion interaction processes with  
684 argon in the [100 - 1200] MeV energy range. The total hadronic  $\pi^-$ -Ar interaction  
685 cross section is defined as the one related to the single process driven only by the

686 strong interaction which is dominant in the considered energy range. In measuring  
687 the “total” cross section, we include both the elastic and reaction channels, regardless  
688 of the final state,

$$\sigma_{Tot} = \sigma_{Elastic} + \sigma_{Reaction}; \quad (1.17)$$

689 the reaction channel is further characterized by several exclusive channels with defined  
690 topologies,

$$\sigma_{Reaction} = \sigma_{Inelastic} + \sigma_{abs} + \sigma_{chex} + \sigma_{\pi prod}. \quad (1.18)$$

691 A summary of the pion final states in order of pion multiplicity for the reaction  
692 channel is given in table 1.4. Pion capture and pion decay at rest dominate the  
693 cross section under 100 MeV. We define pion capture as the process determining the  
694 formation of a pionic atom and the subsequent pion’s end of life. Stopping negative  
695 pions can form pionic argon, where the negative pion plays the role of an orbital  
696 electron. Since the pion mass is two orders of magnitude greater than the electron  
697 mass, the spatial wave form of the pion will overlap more with the nucleus compared  
698 to the electron case. After the electromagnetic formation of the pionic atom, the  
699 pion will get quickly absorbed by the nucleus, which is put in an excited state. The  
700 nucleus then de-excites with the emission of low energy nucleons and photons. Pion  
701 capture is dominant compared to pion decay, the other important process for very  
702 low energy pions. The decay of a pion is governed by the weak force; the pion decay  
703 life time is  $\tau_\pi = 2.6 \times 10^{-8}$  s and the main decay mode is  $\pi^- \rightarrow \mu^- + \bar{\nu}_\mu$  (BR 99.98%).  
704 Since pion capture can be considered an electromagnetic process and pion decay is a  
705 weak process, this energy region is purposely excluded from the hadronic cross section  
706 measurement.

707 **Previous measurements: Lighter and Heavier Nuclei**

708 Many experiments with pion beams have studied the hadronic interaction of pions on  
709 light and heavy materials, such as He, Li, C, Fe, Pb [36]. However, data on argon are  
710 rare: the total differential hadronic cross section has never been measured before on  
711 argon. Simulation packages such as Geant4 base their pion transportation for argon  
712 on data from lighter and heavier nuclei: the goal of LArIAT’s dedicated measurement  
713 on argon is to bridge this gap in data, thus reducing the uncertainties related to pion  
714 interactions in argon in both neutrino event generators and in simulation packages of  
715 pion transportation.

716 The shape of the pion-nucleus interaction cross section in the energy range con-  
717 sidered shows the distinct features indicating the presence of a resonance. In fact, the  
718 mean free path of a pion of kinetic energy between 100 and 400 MeV is much shorter  
719 than the average distance between nucleons (which is of the order of 1 fm). There-  
720 fore, the pion interacts with surface nucleons. A  $\Delta$  resonance is often produced in  
721 the interaction, which subsequently decays inside the nucleus. Experimental results  
722 on several nuclei as reported in [36] are shown in Figure 1.3; it is interesting to notice  
723 here how the shape of the  $\Delta$  resonance becomes less pronounced as a function of the  
724 mass number of the target nucleus. Pion interactions with heavier nuclei also shift the  
725 peak of the resonance at lower energy; this effect is due to kinematic considerations  
726 and to the difference in propagation of the  $\Delta$  inside the nucleus. Multiple scattering  
727 effect modify the resonance width, which is larger than the natural-decay width. As  
728 an example of a fairly well studied target, Figure 1.4 reports the negative pion cross  
729 section on Carbon for the elastic and reaction<sup>2</sup> channels, and their sum [55].

---

2. This paper calls “inelastic interaction” what we refer as to “reaction channel”.

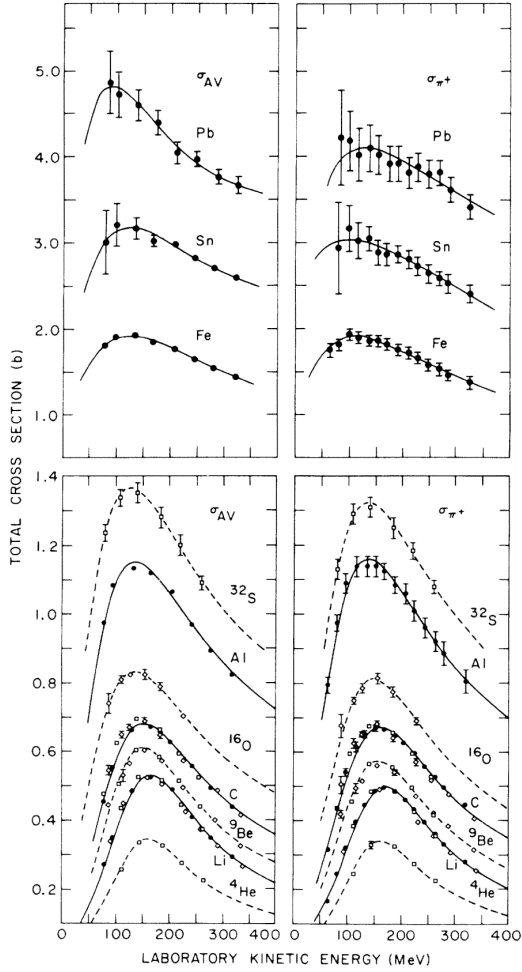


Figure 1.3: Pion-nucleus total cross sections:  $\sigma_{\pi^+}$  for positive pions (right) and  $\sigma_{AV}$  (left) for the average between positive and negative pions  $\sigma_{AV} = \frac{\sigma_{\pi^+} + \sigma_{\pi^-}}{2}$  in the  $\Delta$  resonance region. The error bars include estimates of systematic uncertainties. The curves are the results of fits to the data assuming a Breit-Wigner shape. This summary plot is reported in [36] and uses data from [52, 117].

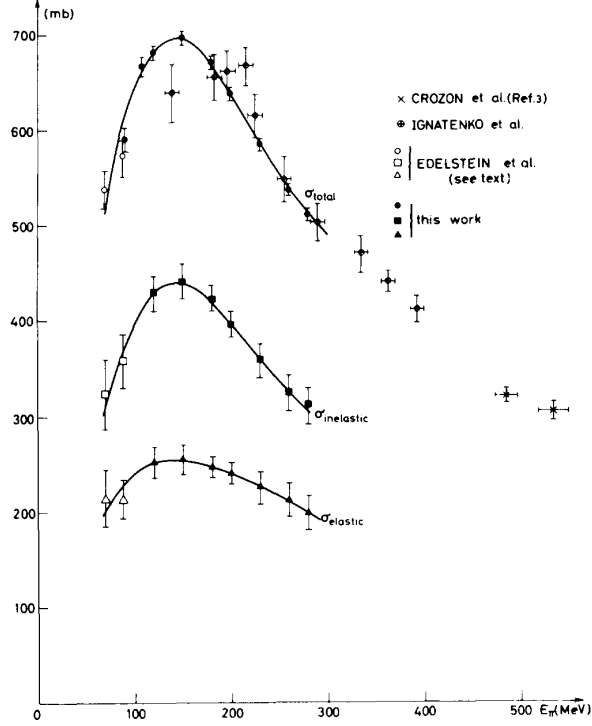


Figure 1.4: Negative pion nucleus total, elastic and reaction cross sections on  $^{12}\text{C}$  as from [55].

### 730 Negative Pion Interaction Cross Section in Simulation Packages

731 LArIAT uses Geant4 as the default simulation package. In particular, pions (and  
 732 kaons) transportation is achieved through the Geant4 FTFP\_BERT physics list. In  
 733 this physics list, Geant4 uses the Bertini cascade model [118] to simulate the products  
 734 of the pion-nucleus interaction as well as secondary hadronic re-interactions inside  
 735 the target nucleus (intra-nuclear cascade). The target nucleus is represented as a  
 736 continuous gas where the nuclear potential follows concentrical shells whose depths  
 737 approximate the Woods-Saxon shape. The CERN-HERA compilations [113, 114] of  
 738 hadron-nucleon interaction data is the data base used for the decision making process  
 739 after the cascade is invoked. The cross section model determines if the pion inter-  
 740 acts, the eventual type of interaction and the interaction multiplicity. For hadron  
 741 projectiles with energy less than 20 GeV, Geant4 reports the uncertainty on the cross

742 section model to be about the size of the error bars on the data used, or about 10%,  
743 increasing to 20-30% in energy regions where data is sparse.

744 The relevance of the GENIE generator for neutrino physics and its basic working  
745 principles have been outlined earlier in this section. Given GENIE's modularity,  
746 information on hadron-nucleus interactions can be extracted from the INTRANUKE  
747 module and directly compared against the Geant4 predictions. The work in [97]  
748 reviews the current status of negative and positive pion simulation in Geant4 and  
749 GENIE for  $^{12}\text{C}$ ,  $^{56}\text{Fe}$ , and  $^{40}\text{Ca}$ . From that work, we report the results for  $^{12}\text{C}$  in  
750 Figure 1.5 as it allows a direct comparison between Geant4, GENIE and and pion  
751 re-scattering data. Geant4 predictions for  $\pi^-$  on Carbon are in good agreement with  
752 data over the entire spectrum spectrum, while GENIE predictions seem to show some  
753 features at around 500 MeV and 900 MeV, maybe due to higher resonances in the hA  
754 model. From the same work, we also report the negative pion cross section on  $^{40}\text{Ca}$   
755 in Figure 1.6, since this is the nuclear medium closest to argon. The predictions from  
756 both Geant4 and GENIE agree with data in the high energy region; the Geant4 and  
757 GENIE predictions diverge in the resonance region, where data is not available. These  
758 few examples highlight how cross section data for the specific nucleus considered in  
759 the neutrino experiments is fundamental to inform the Monte Carlo simulation.

760 For the LArIAT simulation of the MC sample used in the  $\pi^-$  argon total hadronic  
761 cross section measurement we use the Geant4 Bertini Cascade model, whose predic-  
762 tions for the total, elastic and reaction hadronic cross sections are show in Figure  
763 1.7.

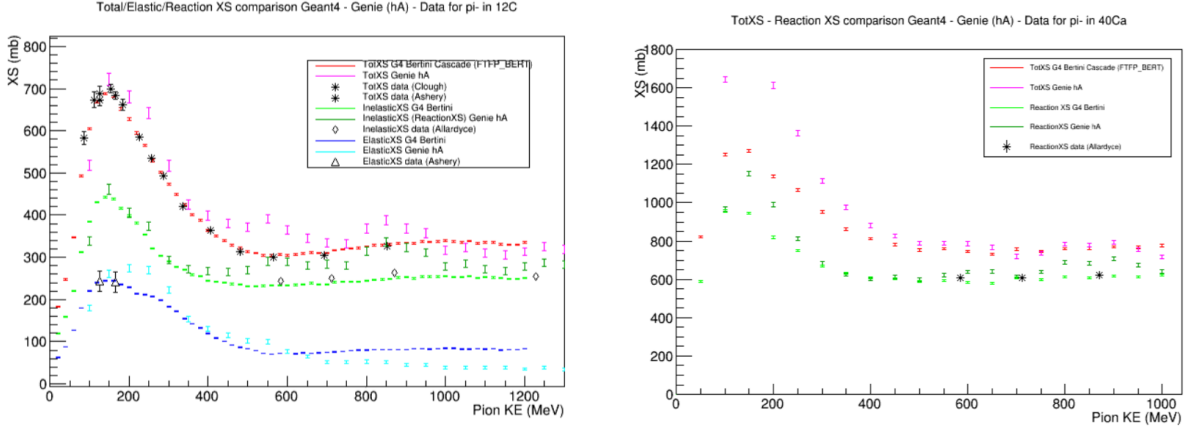


Figure 1.5: Total, elastic and reaction cross section for  $\pi^-$  on  $^{12}\text{C}$ . Comparison between results from Geant4 simulation (Bertini cascade model), Genie simulation (hA model), and experimental data [22, 52, 53, 108].

Figure 1.6: Total, elastic and reaction cross section for  $\pi^-$  on  $^{40}\text{Ca}$ . Comparison between results from Geant4 simulation (Bertini cascade model), Genie simulation (hA model), and experimental data [53].

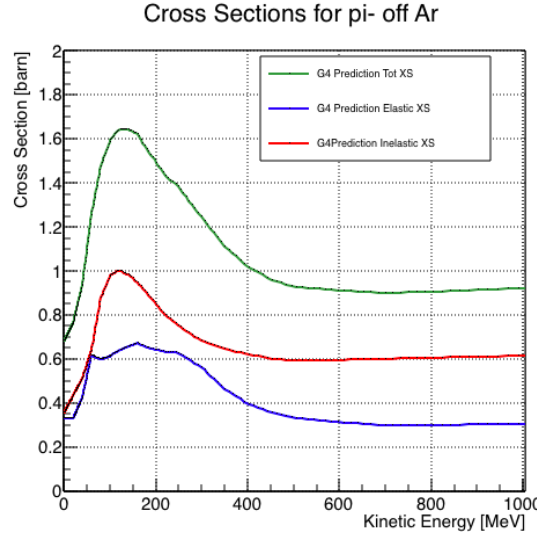


Figure 1.7: Total, elastic and reaction hadronic cross section for  $\pi^-$ -argon implemented in Geant4 10.01.p3.

Resonance	Decay Mode	Lifetime (s)
$\Delta$ (1232) $3/2^+$	$\Delta^{++}(\text{uuu}) \rightarrow p\pi^+$ $\Delta^+(\text{uud}) \rightarrow n\pi^+$ $\Delta^+(\text{uud}) \rightarrow p\pi^0$ $\Delta^0(\text{udd}) \rightarrow n\pi^0$ $\Delta^0(\text{udd}) \rightarrow p\pi^-$ $\Delta^-(\text{ddd}) \rightarrow n\pi^-$	$\sim 5.6 \times 10^{-24}$
$N^*$ (1440) $1/2^+$	$N^* \rightarrow N\pi$ $N^* \rightarrow N\pi\pi$	$\sim 2.2 \times 10^{-24}$

Table 1.3: Main decay modes of the lightest Delta resonance and Nucleon excited state.

N $\pi$ in FS	Channel Name	Reaction	Notes
0	Pion Absorption, $\sigma_{abs}$	$\pi^-(np) \rightarrow nn$ (2-body abs) $\pi^-(nnp) \rightarrow nnn$ (3-body abs) $\pi^-(npp) \rightarrow pnn$ (3-body abs) $\pi^-(nnpp) \rightarrow pmn$ (Multi-body abs)	Suppressed on single nucleon by energy conservation: the process occurs on at least two nucleons system.
1	Elastic Scattering, $\sigma_{el}$	$\pi^- + N \rightarrow \pi^- + N$	Scattering on nucleon or nucleus, the target is left in ground state
1	Charge Exchange, $\sigma_{chea}$	$\pi^- + p \rightarrow \Delta^0 \rightarrow \pi^0 + n$ $\pi^- + N \rightarrow \pi^+ +$ nucleons	Single charge exchange: charged pion converts into neutral pion  Double charge exchange: charged pion converts into opposite charge pion
1	Inelastic Scattering, $\sigma_{inel}$	$\pi^- + p \rightarrow \Delta^0 \rightarrow \pi^- + p$ (knock-out) $\pi^- + n \rightarrow \Delta^- \rightarrow \pi^- + n$ (knock-out)	Other possible reactions:  Pure Inelastic scattering: population of low energy bound excited states Nuclear break-up with nucleons or fragments knock-out
2+	Pion Production, $\sigma_{\pi prod}$	$\pi^- + N \rightarrow \geq 2\pi +$ nucleons	Possible if pion K.E $\geq 500$ MeV/c

Table 1.4: Summary of negative pion hadronic interactions of the reaction channel as a function of the pion multiplicity in the final state in the energy range [100-1200] MeV.

764 **1.4.2 Kaon-Argon Total Hadronic Cross Section**

765 This section outlines the importance of the kaon-argon total hadronic cross section.  
766 We start by discussing the measurement in the context of nucleon decay searches. We  
767 then describe the signal signature and historical measurements of kaon-nucleus cross  
768 section, as well as the implementation of this cross sections in the current version of  
769 the simulation package used by LArIAT.

770 **K<sup>+</sup>Ar Cross section in the Context of Nucleon Decay Searches**

771 Baryon number is accidentally conserved in the Standard Model. Even though no  
772 baryon number violation has been experimentally observed thus far, no underlying  
773 symmetry in line with the Noether paradigm [96] explains its conservation. As shown  
774 in section 1.3.2, almost all Grand Unified Theories predict at some level baryon num-  
775 ber violation in the form of nucleon decay on long time-scales. Given the impossibil-  
776 ity to reach grand unification energy scales with collider experiments (Energy Scale  
777 > 10<sup>15</sup> GeV), an indirect proof of GUTs is needed. The experimental observation of  
778 nucleon decay may be the only viable way to explore these theories.

779 In case of nucleon decay discovery, the dominant decay mode may uncover addi-  
780 tional information about the GUT type. Supersymmetric GUTs [24, 46] prefer the  
781 presence of kaons in the products of the decay, e.g.  $p \rightarrow K^+ \bar{\nu}$  (see fig 1.8, left).  
782 Gauge mediated GUTs, in which new gauge bosons are introduced that allow for the  
783 transformation of quarks into leptons, and vice versa, prefer the mode  $p \rightarrow e^+ \pi^0$  (see  
784 fig 1.8, right).

785 LArIAT tiny active volume makes it impossible for the experiment to place com-  
786 petitive limits on nucleon decay searches. However, LArIAT provides excellent data  
787 to characterize kaons in liquid argon for the “LAr golden mode”,  $p \rightarrow K^+ \bar{\nu}$ . The  
788 result of these studies will affect future proton decay searches in LArTPCs. Previous  
789 work has been done to assess the potential identification efficiency for different decay

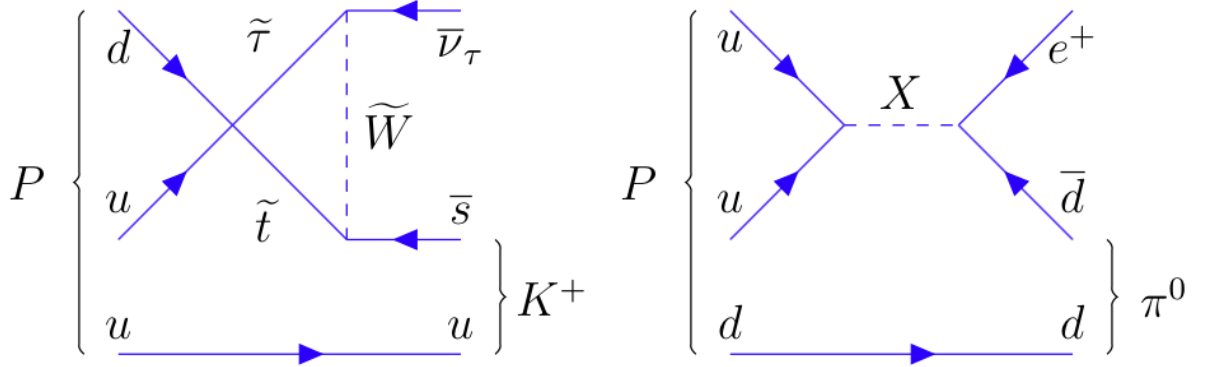


Figure 1.8: Feynman diagrams for proton decay “golden modes”:  $p \rightarrow K^+\bar{\nu}$  for supersymmetric GUTs on the left and  $p \rightarrow e^+\pi^0$  for gauge-mediated GUTs on the right.

790 modes in a LArTPC [51], but, as the time of this writing, no study of kaon selection  
 791 efficiency in LArTPCs has been performed on data. The  $K^+$ -Ar interaction cross  
 792 section has never been measured before and can affect the possibility of detecting  
 793 and measuring kaons when produced in a proton decay event. Kaon interactions with  
 794 argon can distort the kaon energy spectrum as well as change the topology of single  
 795 kaon events. In a LArTPC, non-interacting kaons appear as straight tracks with a  
 796 high ionization depositions at the end (Bragg peak). The topology of interacting  
 797 kaons can be quite different. In case of elastic scattering, a distinct kink will be  
 798 present in the track. In case of inelastic scattering the Bragg peak will not be present  
 799 and additional tracks will populate the event. Performing the total hadronic  $K^+$ -Ar  
 800 cross section measurement on data serves the double purpose of identifying the rate  
 801 of “unusual” topologies (kinks and additional tracks) and of developing tools for kaon  
 802 tracking in LAr.

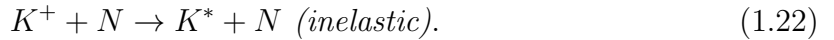
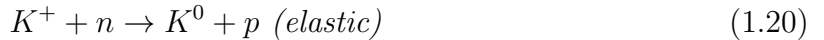
### 803 **$K^+$ Ar Hadronic Interaction: Signal Signatures**

The interaction of a mildly relativistic charged kaon with an argon nucleus is determined largely by the strong force. The total hadronic  $K^+$ -Ar interaction cross section

is defined as the one related to the single (hadronic) process driven only by the strong interaction. In this case, “total” indicates all strong interactions regardless of the final state. This condition purposefully includes both elastic and inelastic (reaction) channels. Indeed, the total cross section section can be then decomposed into

$$\sigma_{Tot} = \sigma_{Elastic} + \sigma_{Reaction}.$$

804 For the LArIAT cross section analysis, the kaons considered span a momentum  
 805 inside the TPC from 100 MeV/c to 800 MeV/c. In this energy range, the relevant  
 806 K-Nucleon interactions are according to [63]:



807 **Previous Measurements: Lighter and Heavier Nuclei**

808 In general, measurements on kaon cross sections are extremely scarce. The mea-  
 809 surement of the kaon interaction cross section would bring the additional benefit  
 810 of reducing the uncertainties associated with hadron interaction models adopted in  
 811 MC simulations for argon targets, beneficial for both proton decay studies and kaon  
 812 production from neutrino interaction studies, where the uncertainties for final state  
 813 interaction models are big [47].

814 Figure 1.9 shows a 1997 measurement on several elements as performed by Fried-  
 815 mann et al. [65]. As a reference, this paper measures a  $\sigma_{Tot}$  for Si of  $366.5 \pm 4.8$   
 816 mb and a  $\sigma_{Tot}$  for Ca of  $494.6 \pm 7.7$  mb at 488 MeV/c. The cross section for argon

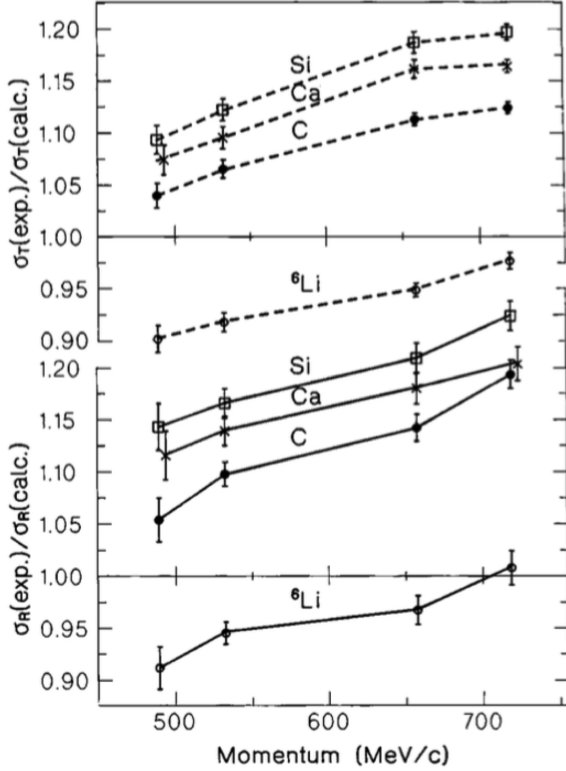


Figure 1.9: Ratios between experimental and calculated cross sections as from [65].  
Top: Total cross sections.  
Bottom: reaction cross sections.

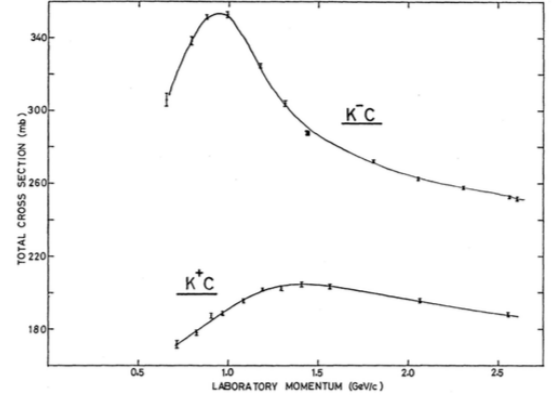


Figure 1.10: Total  $K^+$  and  $K^-$  cross sections on carbon as from [32].

is expected to lie in between these two measurements. Additional data on the kaon cross section are provided by Bugg et al. [32]. Bugg performs a measurement of the total  $K^+$  and  $K^-$  cross sections on protons and deuterons over the range of 0.6-2.65 GeV/c, as well as a measurement of the total  $K^+$  and  $K^-$  cross sections on carbon for a number of momenta; the results of this paper on carbon are reported in Figure 1.10.

### 823 Kaon Interaction Cross Section for thin target in Geant4

824 Since the kaon cross section in argon has never been measured before, simulation  
825 packages tune kaon transportation in argon by extrapolation from lighter and heavier  
826 nuclei. LArIAT uses the Geant4 suite for particle transportation. Since kaon data on

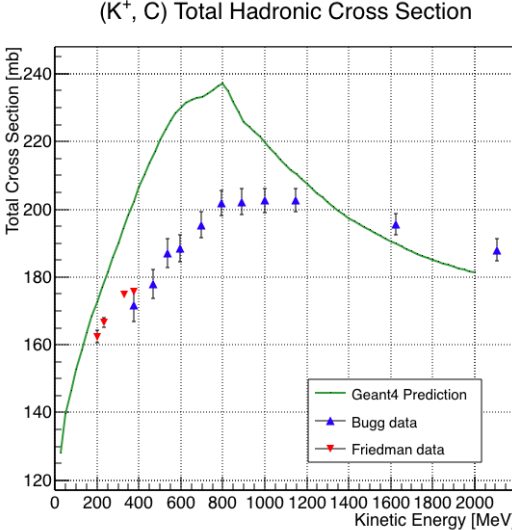


Figure 1.11: Total hadronic cross section for carbon implemented in Geant4 10.01.p3 with overlaid with the Bugg and Friedman data.

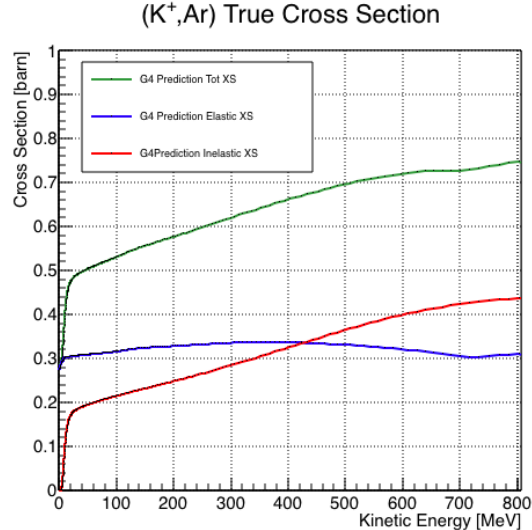


Figure 1.12: Total, elastic and reaction hadronic cross section for  $K^+$ -argon implemented in Geant4 10.01.p3.

carbon are available, we used it as a metric to evaluate the Geant4 prediction performances. Figure 1.11 shows the total hadronic cross section for carbon implemented in Geant4 10.01.p3 overlaid with the Bugg and Friedman data. Unfortunately, version 10.01.p3<sup>3</sup> of Geant4, which is the version used for the simulation in this work, does not reproduce the data for carbon closely. On one hand, this evidence makes us even more wary when using the Monte Carlo in simulating the kaon-argon interactions. On the other, it further highlights the importance of the kaon measurement. For the LArIAT simulation of the MC sample used in the  $K^+$  argon total hadronic cross section measurement we use the Geant4 Bertini Cascade model, whose predictions for the total, elastic and reaction hadronic cross sections are show in Figure 1.12.

3. It should be noted that the latest Geant4 version, 10.03.p3, uses a different parametrization for the kaon cross section and retrieves a better agreement with data.

<sup>837</sup> **Chapter 2**

<sup>838</sup> **Liquid Argon Detectors at the**  
<sup>839</sup> **Intensity Frontier**

<sup>840</sup>                             “*Don’t you know, honey,*  
<sup>841</sup>                             *Ain’t nobody ever gonna love you, the way I try to do?*”  
<sup>842</sup>                             – Janis Joplin, 1971 –

<sup>843</sup>       In the next few years, LArTPCs will be the tools to answer some of the burning  
<sup>844</sup>       questions in neutrino physics today. This chapter illustrates the operational principles  
<sup>845</sup>       of this detector technology, as well as the scope of the key detectors in the US liquid  
<sup>846</sup>       argon program – SBN, DUNE and LArIAT.

<sup>847</sup> **2.1 The Liquid Argon Time Projection Chamber**  
<sup>848</sup> **Technology**

<sup>849</sup>       In this section, we outline an extremely brief history of Time Projection Chambers  
<sup>850</sup>       as particle detectors, focusing on their incarnation as Argon detectors for neutrino  
<sup>851</sup>       physics. We further describe the working principles of Liquid Argon Time Projection

852 Chambers, leading to the description of the event reconstruction in LArTPC.

### 853 2.1.1 TPCs, Neutrinos & Argon

854 David Nygren designed the first Time Projection Chamber (TPC) in the late 1970s [98]  
855 for the PEP-4 experiment, a detector apt to study electron-positron collisions at the  
856 PEP storage ring at the SLAC National Accelerator Laboratory. From the original  
857 design in the seventies – a cylindrical chamber filled with methane gas – the TPC  
858 detector concept has seen many incarnations, the employment of several different  
859 active media and a variety of different particle physics applications, including, but  
860 not limited to the study of electron/positron storage rings (e.g. PEP4, TOPAZ,  
861 ALEPH and DELPHI), heavy ions collisions in fixed target and collider experiments  
862 (e.g. EOS/HISSL and ALICE ), dark matter (ArDM), rare decays and capture (e.g.  
863 TRIUMF, MuCap), neutrino detectors and nucleon decay (ICARUS, SBN, DUNE),  
864 and neutrino less double beta decay (Next). A nice review of the history of TPCs  
865 and working principles is provided in [77].

866 Several features of the TPC technology make these detectors a more versatile tool  
867 compared to other ionization detectors and explain such a wide popularity. TPCs are  
868 the only electronically read detector which deliver simultaneous three-dimensional  
869 track information and a measurement of the particle energy loss. Leveraging on both  
870 tracking and calorimetry, particle identification (PID) capabilities are enhanced over  
871 a wide momentum range.

872 Historically, the active medium in ionization detectors has been in the gaseous  
873 form. Carlo Rubbia first proposed the use of a Liquid Argon TPC for a neutrino  
874 experiment, ICARUS [107], in 1977. Using nobles elements in the liquid form for  
875 neutrino detectors is advantageous for several reasons. The density of liquids is  $\sim$ 1000  
876 times greater than gases, augmenting the number of targets for neutrino's interaction  
877 in the same volume, in a effort to balance the smallness of neutrino cross section. Since

Element	LAr	LXe
Atomic Number	18	54
Atomic weight A	40	131
Boiling Point Tb at 1 atm	87.3 K	165.0 K
Density	1.4 g/cm <sup>3</sup>	3.0 g/cm <sup>3</sup>
Radiation length	14.0 cm	2.8 cm
Moliere Radius	10.0 cm	5.7 cm
Work function	23.6 eV	15.6 eV
Electron Mobility at $E_{field} = 10^4$ V/m	0.047 m <sup>2</sup> /Vs	0.22 m <sup>2</sup> /Vs
Average dE/dx MIP	2.1 MeV/cm	3.8 MeV/cm
Average Scintillation Light Yield	40000 $\gamma$ /MeV	42000 $\gamma$ /MeV
Scintillation $\lambda$	128 nm	175 nm

Table 2.1: LAr, LXe summary of properties relevant for neutrino detectors.

the energy loss of charged particle is proportional to the target material density, as shown in the Bethe-Block equation (eq. 2.1), the increased density reflects into a proportionally higher energy loss, enhancing the calorimetry capability of detectors with a liquid active medium. Additionally, the ionization energy of liquids is smaller than gasses by the order of tens of eV. Thus, at the passage of charged particles, liquids generally produce more ionization electrons than gases for the same deposited energy, forcing the particles to deposit more energy in a shorter range. The downside of using noble liquid elements in experiments is that they require expensive cryogenic systems to cool the gas until it transitions to its the liquid form. The properties of liquid argon in comparison liquid xenon – a popular choice for dark matter and neutrinoless double beta decay detectors – are summarized in table 2.1. Albeit xenon would be more desirable than argon given some superior properties such as lower ionization energy and higher density and light yield, argon relative abundance abates the cost of argon compared to xenon, making argon a more viable choice for the construction of ton (and kilo-ton) scale neutrino detectors.

LArTPCs are some times referred as to “electronic” bubble-chambers, for the similarity in the tracking and energy resolution which is coupled with an electronic readout of the imaging information in LArTPCs. Compared to these historic detectors

896 however, LArTPC bestow tridimensional tracking and a self triggering mechanism  
897 provided by the scintillation light in the liquid argon. An event display of a  $\nu_\mu$  CC  
898 interaction candidate in the MicroBooNE detector is shown in picture 2.1 to display  
899 the level of spatial details these detectors are capable of; the color scale of the image  
900 is proportional to the energy deposited, hinting to these calorimetry capabilities of  
the detectors.



Figure 2.1: Event display of a  $\nu_\mu$  CC interaction candidate in the MicroBooNE detector.

901

### 902 2.1.2 LArTPC: Principles of Operation

903 To the bare bones, a LArTPC is a bulk of liquid argon sandwiched in a flat capacitor,  
904 equipped with a light collection system, as the cartoon in 2.2 shows. A uniform  
905 electric field of the order of 500 V/cm is maintained constant between the faces of the  
906 capacitor. The anode is sensitive to ionization charge and it is usually made of two  
907 or more planes segmented into several hundreds parallel sense wires a few millimeters  
908 apart; different geometries for the anode segmentation are under study [48].

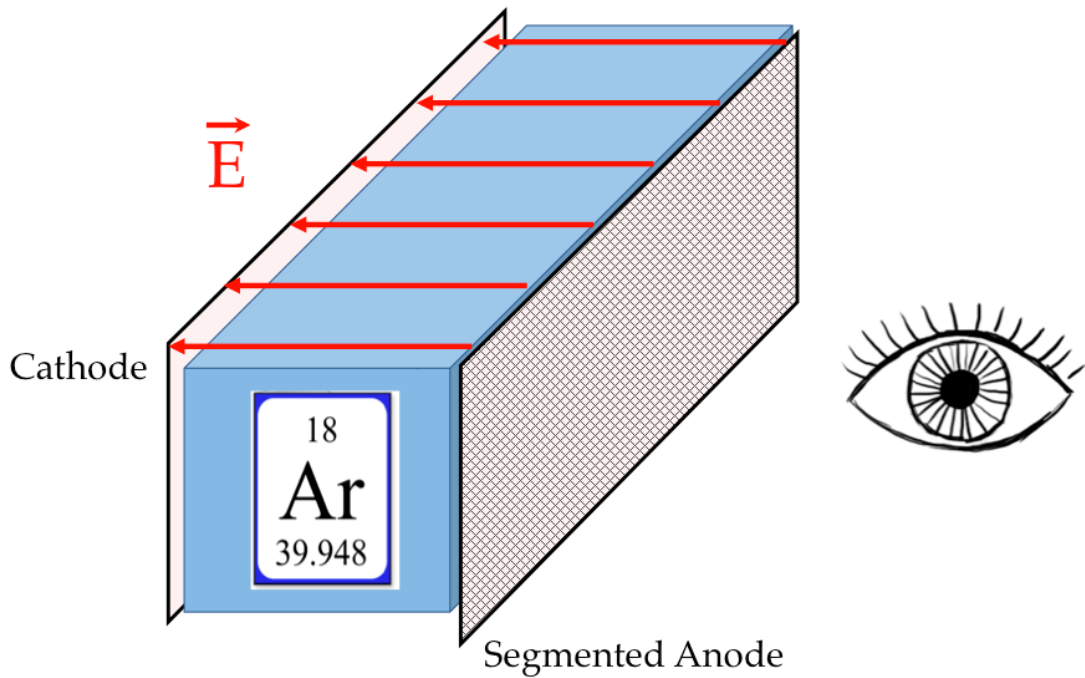


Figure 2.2: A cartoonish sketch of a LArTPC.

Argon ionization and scintillation are the processes leveraged to detect particles in the LArTPC active volume. When a ionizing radiation traverses the argon active volume it leaves a trail of ionization electrons along its trajectory and it excites the argon producing scintillation light – details on the production and detection of ionization charge and scintillation light are provided in 2.1.4 and 2.1.4 respectively. The optical detector sees the argon scintillation light in matters of nanoseconds. This flash of light determines the start time of an event in the chamber,  $t_0$ . The uniform electric field drifts the ionization electrons from the production point towards the anode in order of hundreds of microseconds or more depending on the chamber dimensions<sup>1</sup>. The anode sense wires see either an induced current by the drifting ionization charge (on induction planes) or an injection of such charge (collection

---

1. The ionized argon also drifts, but in the opposite directions compared to the electrons. Since the drift time is proportional to the particle mass, the ions' drift time is much longer than the electrons'. Ionized argon is collected on the cathode which is not instrumented, so it is not used to infer information about the interactions in the chamber.

920 plane). An appropriate choice of the voltage bias on each wire plane assures ideal  
921 charge transparency, so that all the ionization charge is collected on the collection  
922 plane and none on the induction planes.

923 The arrival time of the charge on the anode sense wires is used to measure the  
924 position of the original ionizing radiation in the drift direction. In fact, since the  
925 constant electric field implies that the drift velocity is also constant, the position of  
926 the original ionization is simply given by the multiplication of the drift velocity by the  
927 drift time, where the “drift time” is the difference between  $t_0$  and the charge arrival  
928 time on the wire planes. The spacial resolution on this dimension is limited by the  
929 time resolution of the electronics or by longitudinal diffusion of the electrons. The  
930 spatial information on the different wire planes maps a bi-dimensional projection of  
931 the interaction pattern in the plane perpendicular to the drift direction. The spacial  
932 resolution on this dimension is limited by the transverse electron diffusion in argon  
933 and by the grain of the anode segmentation, i.e. the spacing between the wires in  
934 the sense planes [45]. The off-line combination of the 2-D information on the wire  
935 planes with the timing information allows for the 3D reconstruction of the event in  
936 the chamber.

937 Since the charge deposited by the ionizing radiation is proportional to the de-  
938 posited energy and the charge collected on the sense plane is a function of the de-  
939 posited charge, LArTPCs allow the measurement of the energy deposit in the active  
940 volume. Effects due to the presence of free charge and impurities in the active vol-  
941 ume, such as a finite electron lifetime, recombination and space charge, complicate  
942 the relationship between deposited and collected charge affecting the measurement of  
943 the particle’s energy, as described in the next section.

944 **2.1.3 Liquid Argon: Ionization Charge**

945 The mean rate of energy loss by moderately relativistic elementary charge particles  
 946 heavier than electrons is well described by the modified Bethe-Bloch [101] equation

$$-\frac{dE}{dx} = K z^2 \frac{Z}{A} \varrho \frac{1}{\beta^2} \left[ \frac{1}{2} \ln \frac{2m_e c^2 \beta^2 \gamma^2 T_{max}}{I^2} - \beta^2 - \frac{\delta}{2} \right], \quad (2.1)$$

947 where  $z$  is the number of unit charge of the ionizing radiation,  $Z$ ,  $A$  and  $\varrho$  are the  
 948 atomic number, mass number and density of the medium,  $m_e$  is the electron mass,  
 949  $\gamma = \frac{\beta}{\sqrt{1-\beta^2}}$  is the Lorentz factor of the ionizing radiation,  $T_{max}$  is the maximum kinetic  
 950 energy which can be imparted to a free electron in a single collision,  $I$  is the mean  
 951 excitation energy on eV,  $\delta$  is the density correction and  $K = 0.307075 \text{ MeV g}^{-1} \text{ cm}^2$  is  
 952 a numerical conversion factor. The Bethe-Bloch treats the energy loss by an ionizing  
 953 radiation via quantum-mechanical collisions producing ionization or an excitation in  
 954 the medium as an uniform and continuous process. The density correction terms  
 955 becomes relevant for incident particle with high energy, where screening effects due  
 956 to the polarization of the medium by high energy particles occur.

957 Excitation and ionization of the detector medium occur in similar amounts. Since  
 958 the ionizing collisions occur randomly, we can parametrize their number  $k$  in a segment  
 959 of length  $s$  along the track with a Poissonian function

$$P(k) = \frac{s^k}{k! \lambda^k} e^{-s/\lambda}, \quad (2.2)$$

960 where  $\lambda = 1/N_e \sigma_i$ , with  $N_e$  being the electron density of  $\sigma_i$  the ionization cross-  
 961 section per electron. About 66% of the ionizing collisions in Argon produce only  
 962 a single electron/ion pair [77]; in the other cases, the transferred kinetic energy is  
 963 enough for the primary electron to liberate one or more secondary electrons, which  
 964 usually stay close to the original pair. Occasionally, electrons can receive enough

965 energy to be ejected with high energy, forming a so-called “ $\delta$ -ray”: a detectable short  
966 track off the particle trajectory, as shown in figure 2.3. The average number of  $\delta$ -ray  
967 with energy  $E > E_0$  per cm follows the empirical form

$$P(E > E_0) \sim \frac{y}{\beta^2 E_0}, \quad (2.3)$$

968 where  $y$  is an empirical factor depending on the medium (0.114 for gaseous Ar), and  
969  $\beta$  is  $v/c$ .

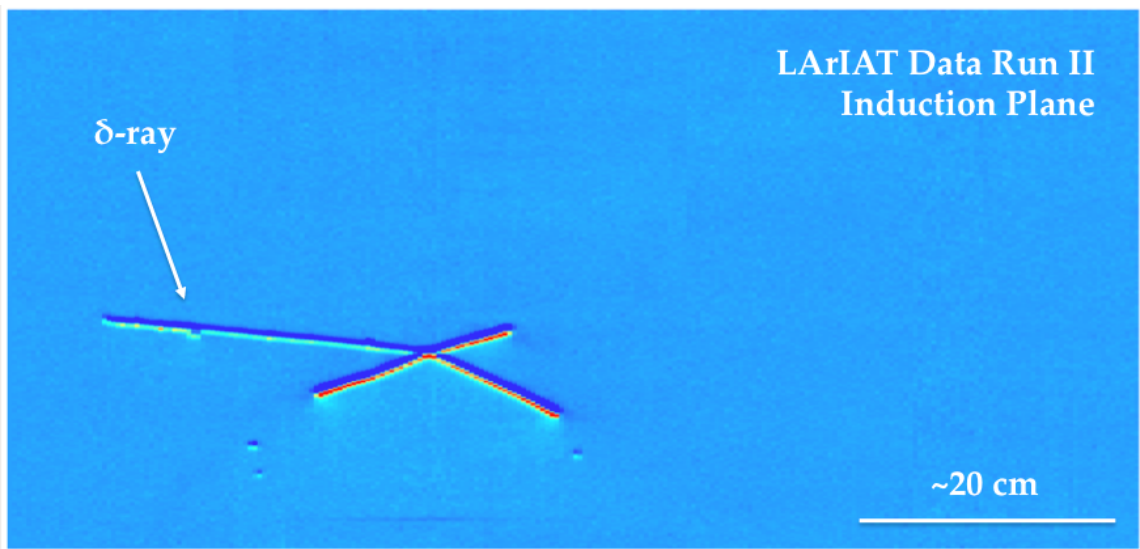


Figure 2.3: Events display for a LArIAT pion absorption candidate on the induction plane, with highlighted delta ray.

## 970 Purity & Electron Life Time

971 The presence of electronegative contaminants in liquid argon, such as oxygen  $O_2$   
972 and water  $H_2O$ , is particularly pernicious, since these molecules quench the charge  
973 produced by the ionizing radiation. Thus, amount of charge per unit of length  $dQ/dx$   
974 collected on the collection plane depends on the charge's production point in the  
975 detector: ionization produced close to the cathode will see more impurities along its  
976 journey to the collection plane than ionization produced close to the anode, resulting

977 in greater attenuation of its charge. As a result, the amount of charge collected on  
 978 the sense wires as a function of the traveled distance follows an exponential decay  
 979 trend. The traveled distance is generally measured in terms of drift time and the  
 980 characteristic time constant of the exponential decay is called electron lifetime  $\tau_e$ .  
 981 Figure 2.4 shows the typical life time for LArIAT data. The procedure to measure  
 982 the electron lifetime in LArIAT is outlined in [104]. LArIAT small drift distance (47  
 983 cm) allows for a relatively short electron life time. The life time for bigger detectors  
 984 such as MicroBooNE, whose drift distance is 2.6 m, needs to be of the order of  
 985 tens of milliseconds to allow a charge collection usable for physics analyses. Energy  
 986 reconstruction in LArTPC applies a correction for the finite lifetime to calibrate the  
 987 detector calorimetric response; details for LArIAT are provided in Section C.

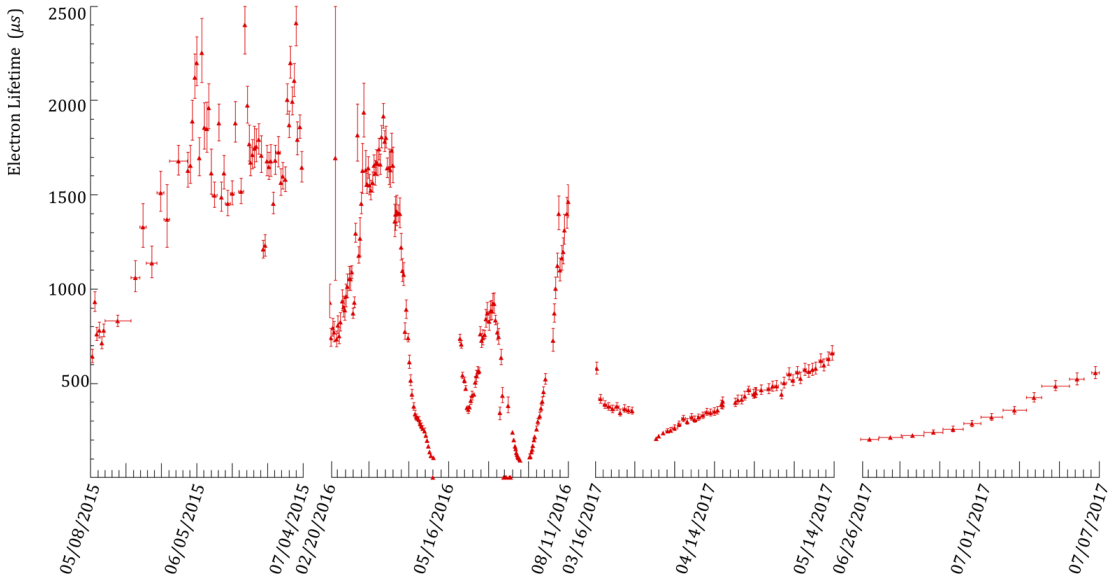


Figure 2.4: Electron lifetime during the LArIAT run period [43].

988 LArTPCs use hermetically sealed and leak-checked vessels to abate the leakage  
989 and diffusion of contaminants into the system. The liquid argon filling of the volume  
990 occurs after the vessel is evacuated or purged with gaseous argon [10] to reduce re-  
991 maining gases in the volume. Even so, the construction of a pure tank of argon is  
992 unviable, as several sources of impurity remain. In particular, impurities can come  
993 from the raw argon supply, the argon filtration system and from the outgassing from  
994 internal surfaces. Outgassing is a continuous diffusive process producing contami-  
995 nants, especially water, even after the vessel is sealed, particularly from materials in  
996 the ullage region<sup>2</sup>. Since research-grade argon comes from the industrial distillation  
997 of air, the impurities with the highest concentration are nitrogen, oxygen and water,  
998 generally maintained under the 1 part per million level by the vendor. Even so, a  
999 higher level of purity is necessary to achieve a free electron life time usable in meter  
1000 scale detectors. Thus, argon is constantly filtered in the cryogenic system, which  
1001 reduce the oxygen and water contamination to less than 100 parts per trillion. The  
1002 filtration system depends on the size and drift distance of the experiment and, for  
1003 experiments on several meters scale, it includes an argon recirculation system.

1004 **Recombination Effect**

1005 After production, ionization electrons thermalize with the surrounding medium and  
1006 may recombine with nearby ions. Recombination might occur either between the  
1007 electron and the parent ion through Coulomb attraction, as described in the geminate  
1008 theory [99], or thanks to the collective charge density of electrons and ions from  
1009 multiple ionizations in a cylindrical volume surrounding the particle trajectory, as  
1010 described in the columnar model [80]. Consideration on the average electron-ion  
1011 distance and the average ion-ion distance for argon show that the probability of

---

2. While the liquid argon low temperature reduces outgassing in the liquid, this process remains significant for absorptive material (such as plastic) above the surface of the liquid phase.

1012 geminate recombination is low; thus recombination in argon is mainly due to collective  
1013 effects [5]. Since protons, kaons and stopping particles present a higher ionization  
1014 compared to MIPs, recombination effects are more prominent when considering the  
1015 reconstruction of energy deposited by these particles.

1016       Theoretical descriptions of recombination based on the Birks model and the Box  
1017 model are provided in [29] and [112], respectively. The Birks model assumes a gaus-  
1018 sian spatial distribution around the particle trajectory during the entire recombina-  
1019 tion phase and identical charge mobility for ions and electrons. The Box model also  
1020 assumes that electron diffusion and ion mobility are negligible in liquid argon during  
1021 recombination. In these models, the fraction of ionization electrons surviving recom-  
1022 bination is a function of the number of ion-electron pairs per unit length, the electric  
1023 field, the average ion-electron separation distance after thermalization and the angle  
1024 of the particle with respect to the direction of the electric field – plus the diffusion  
1025 coefficient in the Birks model. Given the stringent assumptions, it is perhaps not sur-  
1026 prising that these models are in accordance to data only in specific regimes: the Birks  
1027 model is generally used to describe recombination for low  $dE/dx$ , the Box model for  
1028 high  $dE/dX$ . In LArTPC, the ICARUS and ArgoNeut experiments have measured  
1029 recombination in [16] and [5] respectively. Since LArIAT uses the refurbished Ar-  
1030 goNeut TPC and cryostat at the same electric field, LArIAT currently corrects for  
1031 recombination using the ArgoNeut measured recombination parameters in [5].

### 1032       **Space Charge Effect**

1033 Slow-moving positive argon ions created during ionization can build-up in LArTPC,  
1034 causing the distortion of the electric field within the detector. This effect, called  
1035 “space charge effect” leads to a displacement in the reconstructed position of the  
1036 signal ionization electrons. In surface LArTPCs the space charge effect is primarily  
1037 due to the rate of ionization produced by cosmic rays which is slowly drifting in the

1038 chamber at all times. Surface LArTPC of the size of several meters are expected  
1039 to be modestly impacted from the space charge effect, where charge build-up create  
1040 anisotropy of the electric field magnitude of the order of 5% at a drift field of 500  
1041 V/cm [93]. The smallness of the LArIAT drift volume and its relatively high electric  
1042 field are such that the effect of space charge is expected to be negligible.

### 1043 2.1.4 Liquid Argon: Scintillation Light

1044 Liquid argon emits scintillation light at the passage of charged particles. LArTPCs  
1045 leverage this property to determine when the ionization charge begins to drift towards  
1046 the anode plane.

#### 1047 Scintillation Process

1048 Scintillation light in argon peaks in the ultraviolet at a 128 nm, shown in comparison  
1049 to Xenon and Kypton in Figure 2.5, from [94]. The light yield collected by the optical  
1050 detector depends on the argon purity, the electric field, the dE/dx and particle type,  
1051 averaging at the tens of thousands of photons per MeV.

1052 The de-excitation of Rydberg dimers in the argon is responsible for the scintillation  
1053 light. Rydberg dimers exist in two states: singlets and a triplets. The time constant  
1054 for the singlet radiative decay is 6 ns, resulting in a prompt component for the scin-  
1055 tillation light. The decay of the triplet is delayed by intersystem crossing, producing  
1056 a slow component with a time constant of  $\sim$  1500 ns. “Self-trapped exciton lumines-  
1057 cence” and “recombination luminescence” are the two processes responsible for the  
1058 creation of the Rydberg dimers [83]. In the first process, a charged particle excites an  
1059 argon atom which becomes self-trapped in the surrounding bulk of argon, forming a  
1060 dimer; the dimer is in the singlet state 65% of the times and in the triplet state 35%  
1061 of the times. In case of recombination luminescence, the charged particle transfers  
1062 enough energy to ionize the argon. The argon ion forms a charged argon dimer state,

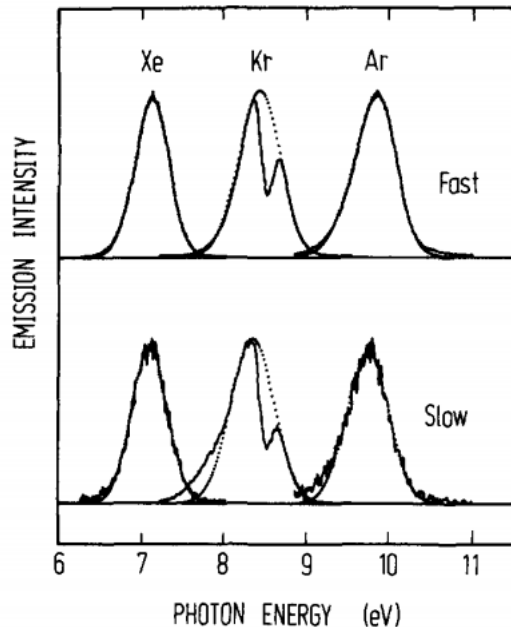


Figure 2.5: Emission spectra of the fast and slow emission components in Xenon, Krypton and Argon according to [94]. The dotted lines correspond to the Gaussian fits.

1063 which quickly recombines with the thermalized free electron cloud. Excimer states  
 1064 are produced in the recombination, roughly half in the singlet and half in the triplet  
 1065 state. The light yield dependency on the electric field, on the  $dE/dx$  and particle  
 1066 type derives from the role of free charge in the recombination luminescence process.  
 1067 The spacial separation between the argon ions and the free electron cloud depends on  
 1068 the electric field. On one hand, a strong electric field diminishes the recombination  
 1069 probability, leading to a smaller light yield; on the other, it increases the free charge  
 1070 drifting towards the anode plane. Hence, the amount of measurable charge and light  
 1071 anti-correlates as a function of the electric field. Ionizing particles in the argon mod-  
 1072 ify the local density of both free electrons and ions depending on their  $dE/dx$ . Since  
 1073 the recombination rate is proportional to the square of the local ionization density,  
 1074 highly ionizing particles boost recombination and the subsequent light yield compared  
 1075 to MIPs. The possibility to leverage this dependency for pulsedshape-based particle  
 1076 identification has been shown in [31, 88].

1077 **Effects Modifying the Light Yield**

1078 The production mechanism through emission from bound excimer states implies that  
1079 argon is transparent to its own scintillation light. In fact, the photons emitted from  
1080 these metastable states are not energetic enough to re-excite the argon bulk, greatly  
1081 suppressing absorption mechanisms. In a LArTPC however, several processes modify  
1082 the light yield in between the location where light is produced and the optical detector.  
1083 In a hypothetical pure tank of argon, Rayleigh scattering would be the most important  
1084 processes modifying the light yield. Rayleigh scattering changes the path of light  
1085 propagation in argon, prolonging the time between light production and detection.  
1086 The scattering length has been measured to be 66 cm [78] , shorter than the theoretical  
1087 prediction of  $\sim 90$  cm [111]; this value is short enough to be relevant for the current  
1088 size of LArTPCs detectors. In fact, Rayleigh scattering worsen the resolution on  $t_0$ ,  
1089 the start time for charge drifting, and alters the light directionality, complicating the  
1090 matching between light and charge coming from the same object in case of multiple  
1091 charged particles in the detector.

1092 Traces of impurities in argon such as oxygen, water and nitrogen also affect the  
1093 light yield, mainly via absorption and quenching mechanisms. Absorption occurs as  
1094 the interaction of a 128 nm photon directly with the impurity dissolved in the liquid  
1095 argon. Differently, quenching occurs as the interaction of an argon excimer and an  
1096 impurity, where the excimer transfers its excitation to the impurity and dissociates  
1097 non-radiatively. Given this mechanism, it is evident how quenching is both a function  
1098 of the impurity concentrations and the excimer lifetime. Since the triplet states  
1099 live much longer than the singlet states, quenching occurs mainly on triplet states,  
1100 affecting primarily the slow component of the light, reducing the scintillation yield  
1101 and a shortening of the scintillation time constants.

1102 The stringent constraints for the electron life time limit the presence of oxygen and  
1103 water to such a low level that both absorption and quenching on these impurity is not

1104 expected to be significant. Contrarily, the nitrogen level is not bound by the electron  
1105 life time constraints – nitrogen being an inert gas, expensive to filter. Thus, nitrogen  
1106 is often present at the level provided by the vendor. The effects of nitrogen on argon  
1107 scintillation light have been studied in the WArP R&D program and at several test  
1108 stands. The quenching process induced by nitrogen in liquid Ar has been measured  
1109 to be proportional to the nitrogen concentration, with a rate constant of  $\sim 0.11$   
1110  $\mu\text{s}^{-1}$  ppm $^{-1}$ ; appreciable decreasing in lifetime and relative amplitude of the slow  
1111 component have been shown for contamination as high as a few ppm of nitrogen [6].  
1112 For a nitrogen concentration of 2 parts per million, typical of the current generation  
1113 of LArTPC, the attenuation length due to nitrogen has been measured to be  $\sim 30$   
1114 meters [82].

## 1115 **Wavelength Shifting of LAr Scintillation Light**

1116 Liquid argon scintillation light is invisible for most optical detectors deployed in a  
1117 LArTPC, such as cryogenic PMTs and SiPMs, since a wavelength of 128 nm is gen-  
1118 erally too short to be absorbed from most in glasses, polymers and semiconductor  
1119 materials. Research on prototype SiPMs absorbing directly VUV light and their  
1120 deployment in noble gasses experiment is ongoing but not mature [120]. Thus, ex-  
1121 periments need to shift the wavelength of scintillation light to be able to detect it.  
1122 Albeit deployed in different ways, neutrinos and dark matter experiments commonly  
1123 use 1,1,4,4-tetraphenyl-butadiene (TPB) to shift the scintillation light. TPB absorbs  
1124 the vacuum ultraviolet (VUV) light and emits in the visible at  $\sim 425$  nm [33], with  
1125 a ratio of visible photon emitted per VUV photon absorbed of  $\sim 1.2:1$  [66].

1126 Neutrino experiments typically coat their optical detector system evaporating a  
1127 layer of TPB either directly on the PMTs glass surface or on acrylic plates mounted in  
1128 front of the PMTs [60]; this technique allows the fast detection light coming directly  
1129 from the neutrino interaction. Dark matter experiments typically evaporate TPB on

reflective foils mounted on the inside walls of the sensitive volume and detect the light after it has been reflected; this technique leads to a higher and more uniform light yield, though scattering effects for both the visible and VUV light augment the propagation time and hinder directionality information [61]. In order to take advantage of both these techniques, hybrid systems with PMT coating and foils are being considered for the next generation of large neutrino detectors.

### 2.1.5 Signal Processing and Event Reconstruction

In this section we illustrate the processing and reconstruction chain of the TPC signals, from the pulses on the sense wire to the construction of three dimensional objects with associated calorimetry. Different experiments can chose different software packages for their off line signal processing and event reconstruction, but a popular choice for US based LArTPCs is LArSoft [40]. Based on the Art framework [72], LArSoft is an event-based toolkit to perform simulation, analysis and reconstruction of LArTPCs events.

1144

LArTPC signal processing develops in several consecutive stages that we summarize here in the following categories: *Deconvolution*, *Hit Reconstruction*, *2D Clustering*, *3D Tracking*, *Calorimetry Reconstruction*. A visualization of the signal processing workflow is shown in figure 2.6.

1149

**Deconvolution.** Induction and collection planes have different field responses, given the different nature of the signals on these planes: the wires on the induction planes see the inductive signal of the drifting charge, while the wires on the collection planes see the current derived from the charge entering the conductor. Thus, signals on the induction plane are bi-polar pulse and signal on the collection plane are unipolar pulses, see Figure 2.6 panel a). The first step in signal processing is deconvolution,

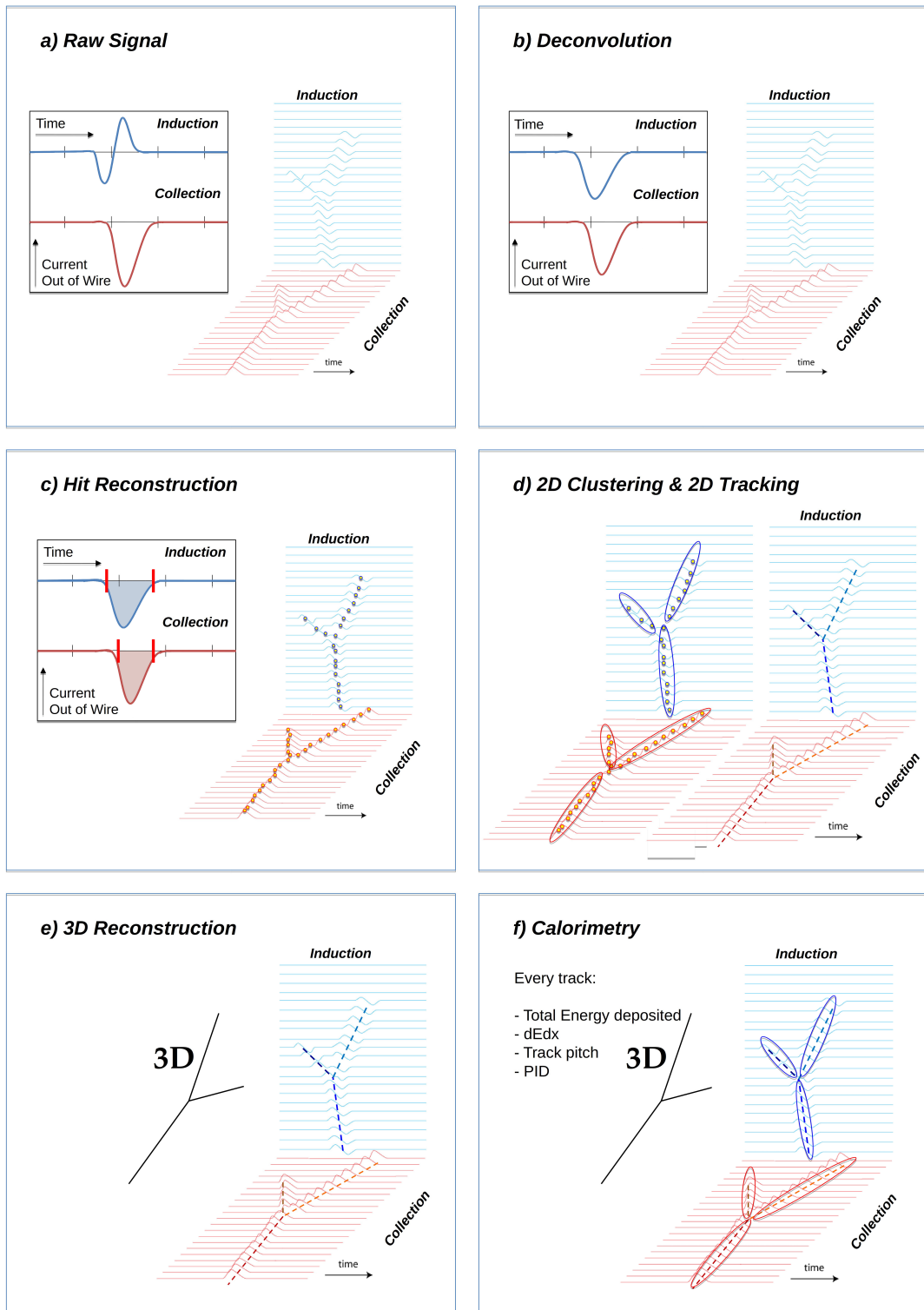


Figure 2.6: A scheme of a typical signal processing workflow in LArSoft.

1156 that is a series of off-line algorithms geared towards undoing the detector effects. The  
1157 result of the deconvolution step is the production of a comparable set waveforms on  
1158 all planes presenting unipolar, approximately gaussian-like pulses (Figure 2.6 panel  
1159 b). Signal from all planes are treated on equal footage beyond this point. Some  
1160 LArTPC apply noise filtering in the frequency domain just after the deconvolution  
1161 to clean up wire cross talk. Since signals from the LArIAT TPC are extremely clean,  
1162 noise filtering is not necessary.

1163

1164 **Hit Reconstruction.** The second stage of the signal processing is the recon-  
1165 struction of hits, indicating an energy deposition in the detector. A peak finder scans  
1166 the deconvolved TPC waveforms for each wire on the whole readout time looking for  
1167 spikes above the waveform’s baseline. It then fits these peaks with gaussian shapes  
1168 and stores the fit parameters such as the quality of the fit, the peak time, height and  
1169 area under the gaussian fit. The information resulting from this process on a single  
1170 spike form a single reconstructed “hit”, see Figure 2.6 panel c). The next steps in  
1171 the event reconstruction chain will then decide if rejecting hits with poor fits. It is  
1172 important to notice how the height and width of the hit depend on the topology of  
1173 the event: for example, a particle running parallel to the wire planes will leave a series  
1174 of sharp hits on many consecutive wires, while a particle traveling towards the planes  
1175 will leave a long, wide hit on very few wires. The height of the hits and their integral  
1176 is proportional to the charge collected on the wire, so it depends on the particle type.

1177

1178 The event reconstruction chain uses collection of hits to form more complex objects  
1179 associated with the particles in the detector. The development of different approaches  
1180 to accomplish this task is an extremely hot topic in LArTPC event reconstruction  
1181 which spans from more traditional approaches such as line-clustering [26] to the use of  
1182 machine learning tools [59]. Generally speaking, the scope of hit clustering and event

1183 reconstruction to provide shower-like or track like-objects with an associated energy  
1184 reconstruction. This is because different particles have different topology in the de-  
1185 tector – electrons and photon create electromagnetic showers, resulting in shower-like  
1186 topologies, while muons and hadrons leave track-like signals. For the scope of these  
1187 thesis, we will describe only LArIAT’s approach to track reconstruction even if we  
1188 recognize the breath of LArTPC event reconstruction is much wider. We are inter-  
1189 ested in the reconstruction of pions and kaons in the active volume, whose topology  
1190 is track-like.

1191

1192 **2D Clustering Reconstruction.** The LArIAT reconstruction of track-like ob-  
1193 jects starts by clustering hits on the collection and induction planes separately with  
1194 the use of the TrajCluster clustering package [25]. TrajCluster looks for a collection  
1195 of hits in the wire-time 2D space which can be described with a line-like 2D trajec-  
1196 tory. TrajCluster reconstructs trajectories by adding trajectory points to the leading  
1197 edge of the trajectory while stepping through the 2D space of hits. Several factors  
1198 determine whether a hit is added to the trajectory, including but not limited to

- 1199 1. the goodness of the fit of the single hit,
- 1200 2. the charge of the hit compared to the average charge and RMS of the hits  
1201 already forming the trajectory,
- 1202 3. the goodness of trajectory fit with and without the hit addition,
- 1203 4. the angle between the two lines formed by the collection of hits before and after  
1204 the considered hit in the trajectory.

1205 The final product of this reconstruction stage is the collection of bidimensional clusters  
1206 on each wire plane, see Figure 2.6 panel d).

1207 **3D Tracking.** The 3D tracking set of algorithms uses clusters close in time on  
1208 the induction and collection planes as starting point to form a 3D track. Firstly, it

1209 construct a tentative 3D trajectory using the edges of the clusters. Then, it projected  
1210 back the tentative trajectory on to the planes and adjusts the parameters of the 3D  
1211 track fit such that they minimize the distance between the fit projections and the  
1212 track hits in all wire planes simultaneously. Tridimensional tracking can use multiple  
1213 clusters in one plane, but it can never break them in smaller groups of hits. This  
1214 algorithm was first developed for the ICARUS collaboration [20]. The final product  
1215 of this reconstruction stage is the formation of tridimensional objects in the TPC  
1216 active volume, see Figure 2.6 panel e).

1217

1218 **Calorimetry.** The last step in the event reconstruction chain is to assign calorimetric  
1219 information to the track (or shower) objects. Calorimetry is performed separately on the different planes. A multi-step procedure is needed to retrieve the energy  
1220 deposited in the TPC from the charge seen by the wires. For each hit associated with  
1221 the track object, the calorimetry algorithms calculate the charge seen on every wire  
1222 using the area underneath the gaussian fit; then, they correct this raw charge by the  
1223 electron life time, the electronic noise on the considered wire and the recombination  
1224 effect. Lastly an overall calibration of the energy, explained in detail in section C,  
1225 is applied and the calorimetric information for the given track is assigned. Even if  
1226 calorimetry is done in 2D, it benefits from the 3D tracking information; typical information available after the calorimetric reconstruction are the total energy deposited  
1227 by the particle and its stopping power  $dE/dx$  at each “track pitch”, i.e. at each 2D  
1228 projection on the wire plane of the 3D trajectory.

## 1231 2.2 The Intensity Frontier Program

1232 This section highlights the role of Liquid Argon Time Projection Chambers at the  
1233 Intensity frontier. In particular, we show the prospects for the exploration of neutrino

1234 physics (Section 2.2.1) and GUT models (Section 2.2.2) in current and forthcoming  
1235 LAr experiments. In Section , we introduce LArIAT and its role in the Intensity  
1236 Frontier panorama.

1237 **2.2.1 Prospects for LArTPCs in Neutrino Physics: SBN and**  
1238 **DUNE**

1239 The ArgoNeut experiment [17] together the LAr R&D experiments TallBo and the  
1240 Yale TPC initiated the US LArTPC neutrino program. Following the success of the  
1241 ArgoNeut small TPC on the NuMI beam, a wide program of LArTPCs on neutrino  
1242 beams has flourished. The construction of LArTPCs as near and far detectors at  
1243 different baseline allows for the exploration of some of the fundamental questions in  
1244 neutrino physics today illustrated in section 1.3.1.

1245 The Short-Baseline Neutrino (SBN) [21] program at Fermilab is tasked with con-  
1246 clusively assess the nature of the “LSND and MiniBooNE anomalies” [14, 15, 23],  
1247 resolving the mystery of sterile neutrinos at the eV<sup>2</sup> scale. The SBN program entails  
1248 three surface LArTPCs positioned on the Booster Neutrino Beam at different dis-  
1249 tances from the neutrino production in oder to fully exploit the L/E dependence of  
1250 the oscillation pattern: SBND (100 m from the decay pipe), MicroBooNE (450 m),  
1251 and ICARUS (600 m). Within the oscillation context, the choice of the LArTPC tech-  
1252 nology for the SBN detectors changes the set of systematics with respect to LSND  
1253 and MiniBooNE, whose detection techniques were both based on Cherenkov light.  
1254 In particular, LArTPCs provide excellent electron/photon separation [9] lacking in  
1255 Cherenkov detectors which can be leveraged to abate the photon background from  
1256 neutral current interactions in  $\nu_e$  searches. MicroBooNE [8], the first detector of the  
1257 SBN program to be fully operational, started its first neutrino run in October 2015.  
1258 MicroBooNE is a 89 ton active volume LArTPC, single drift chamber with TPC di-  
1259 mensions of 2.6 m (drift) x 2.3 m (heigh) x 10.4 m (depth). MicroBooNE is positioned

at a very similar L/E on the Booster neutrino beam as MiniBooNE has the scope to directly cross check the MiniBooNE oscillation measurement. In case MicroBooNE confirms the presence of the “low energy excess” anomaly, SBND and ICARUS will provide the full measurement of the oscillation parameters. SBND and ICARUS are both dual drift chambers, whose active volume is respectively 112 ton and 600 ton. ICARUS is scheduled to become operational by the end of 2018 and SBND shortly after. Besides the oscillation analysis, the second main goals of SBN is to perform an extensive campaign of neutrino cross section measurements in argon. Given the importance of nuclear effects in (relatively) heavy materials, as discussed in section 1.2.3, both the oscillation analysis of the SBN program and the measurements of neutrino properties in DUNE will benefit from such a campaign.

On a different neutrino beam and baseline, the DUNE experiment, née LBNE [11], is the flagship experiment on the medium-long term of US-based neutrino physics, scheduled to start data taking in 2026. Shooting neutrinos from Fermilab for 800 miles to the SURF laboratory in South Dakota, DUNE is tasked with performing conclusive measurements of CP violation in the lepton sector, the neutrino mass ordering and the  $\theta_{23}$  octant. The DUNE far detector will count four 10 kton LArTPCs, roughly of dimensions of 19 m (horizontally) x 18 m (vertically) x 66 m (depth).

## 2.2.2 Prospects for LArTPCs in GUT Physics: DUNE

The experimental exploration of a manifestation of Grand Unified Theory is possible in DUNE thanks to its sheer mass. In particular, proton decay searches are a capital topic of DUNE’s wide non-accelerator physics program. The key elements for a rare decay experiment are: massive active volume, long exposure, high identification efficiency and low background. Figure 2.7 shows the current best experimental limits on nucleon decay lifetime over branching ratio (dots). Historically, the dominant technology used in these searches has been water Cherenkov detectors: all the best

1286 experimental limits on every decay mode are indeed set by Super-Kamiokande [?, ?].  
 1287 As shown in section 1.3.2, different family of GUTs predict the proton to decay in  
 1288 different modes. In particular, SUSY flavored GUTs prefer the presence of kaons  
 1289 in the decay products, e.g.  $p \rightarrow K^+ \bar{\nu}$ . It is particularly important to notice that  
 1290 the kaon energy for the proton decay mode  $p \rightarrow K^+ \bar{\nu}$  is under Cherenkov threshold  
 1291 in water. Thus, Super-Kamiokande set the limit on the lifetime for the  $p \rightarrow K^+ \bar{\nu}$   
 1292 mode by relying on photons from nuclear de-excitation and on the muon tagging in  
 1293 the kaon decay leptonic mode. For this reason, an attractive alternative approach to  
 1294 identifying nucleon decay is the use of a LArTPCs, where the kaon is directly visible  
 1295 in the detector. According to [11], DUNE will have an active volume large enough,  
 1296 have sufficient shielding from the surface, and will run for lengths of time sufficient  
 1297 to compete with Hyper-K, opening up the opportunity for the discovery of nucleon  
 1298 decay.

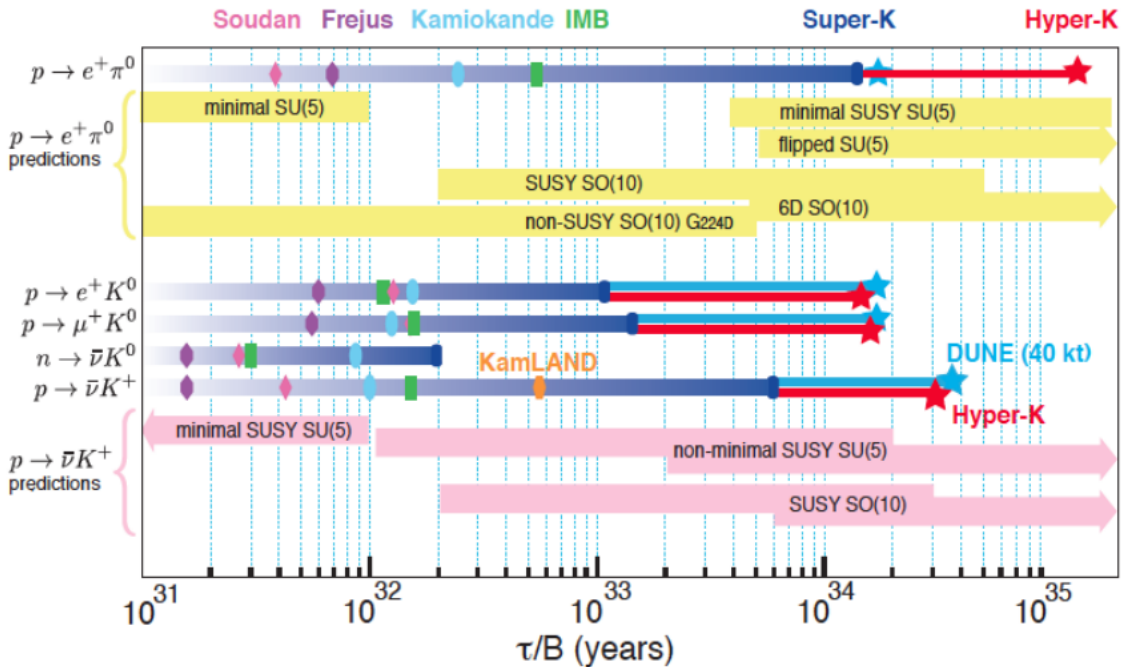


Figure 2.7: Proton decay lifetime limits from passed and future experiments.

1299 **2.2.3 Enabling the next generation of discoveries: LArIAT**

1300 LArIAT, a small LArTPC in a test beam, is designed to perform an extensive physics  
1301 campaign centered on charged particle cross section measurements while characteriz-  
1302 ing the detector performance for future LArTPCs. Since LArTPCs represent the most  
1303 advanced experiments for physics at the Intensity Frontier, their complex technology  
1304 needs a thorough calibration and dedicated measurements of some key quantities to  
1305 achieve the precision required for the next generation of discoveries. LArIAT’s goal  
1306 is to provide such calibration and dedicated measurements. The LArIAT LArTPC is  
1307 deployed in a dedicated calibration test beamline at Fermilab. We use the LArIAT  
1308 beamline to characterize the charge particles before they enter the TPC: the particle  
1309 type and initial momentum is known from beamline information. The precise calori-  
1310 metric energy reconstruction of the LArTPC technology enables the measurement of  
1311 the total differential cross section for tagged hadrons. The Pion-Nucleus and Kaon-  
1312 Nucleus total hadronic interaction cross section have never been measured before in  
1313 argon and they are a fundamental step to shed light on light meson interaction in nu-  
1314 clei per se, while providing a key input to neutrino physics and proton decay studies  
1315 in future LArTPC experiments like SBN and DUNE.

1316 In order to showcase LArIAT’s utility to SBN and DUNE, we illustrate briefly  
1317 two comparisons as examples: one regarding neutrino interactions and the second  
1318 regarding proton decay studies.

1319 The left side of figure 2.8 shows the distribution of products in momentum spectrum  
1320 and particle type as simulated in a  $\nu_e$  CC interaction in DUNE (according to [87]);  
1321 the range of these distribution is to compare with the momentum distribution of  
1322 light particles in the LArIAT beamline – shown on the right side of figure 2.8. The  
1323 momentum spectrum in the LArIAT beamline for electrons, muons and pions – the  
1324 most abundant particles produced in a  $\nu_e$  CC interaction – covers a wide range of the  
1325 expected momentum distribution in a neutrino event.

1326        The signature of a proton decay event in the “LAr golden mode” is the presence of  
 1327        a single kaon of about 400 MeV in the detector; the momentum spectrum of the kaon  
 1328        pre and post FSI in such an event as simulated by GENIE is shown on the left side  
 1329        of figure 2.9. The right side of figure 2.9 shows the momentum spectrum of kaons in  
 1330        the LArIAT beamline. Kaons arriving to the LArIAT TPC are ideal for proton decay  
 1331        studies, since their momentum in the beamline is just above the typical momentum  
 1332        for kaons in a proton decay event: the majority of LArIAT kaons slow down in the  
 1333        TPC enough to enter the desired momentum window.

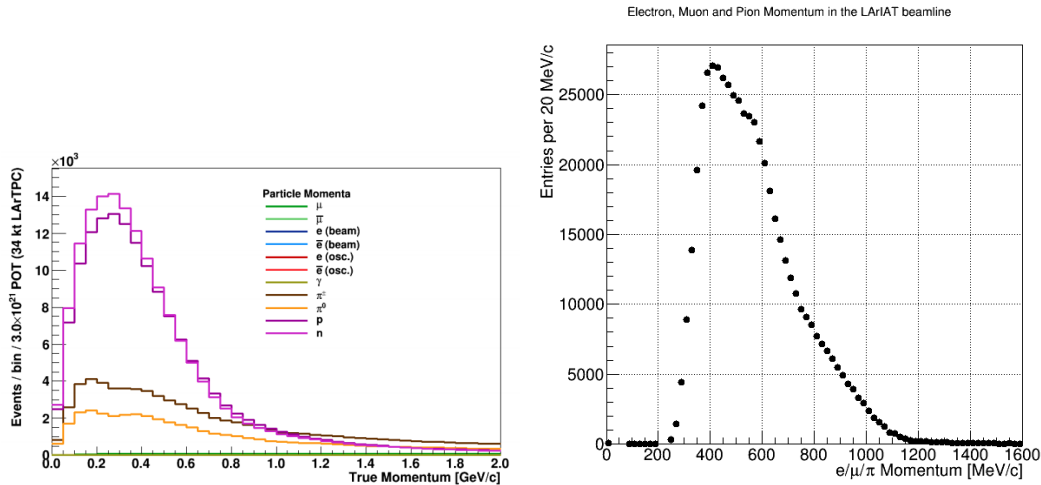


Figure 2.8: *Left.* Simulation of the products of a  $\nu_e$  CC interaction in DUNE, both in particles type and momentum.  
*Right.* Momentum spectrum for low mass particles ( $e, \mu, \pi$ ) in the LArIAT beamline, negative tune, Run II, Picky Tracks see section 3.2.2.

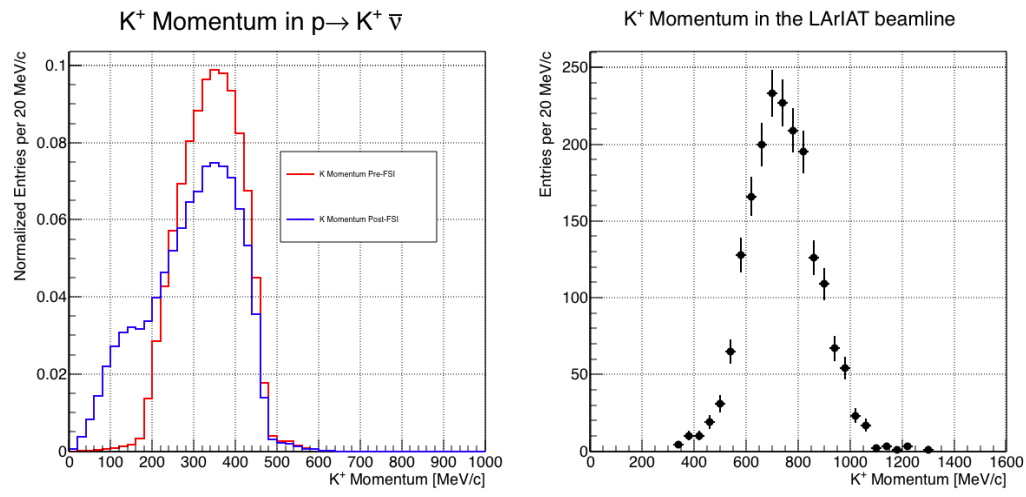


Figure 2.9: *Left.* Momentum of the kaon outgoing a proton decay  $p \rightarrow K^+ \bar{\nu}$  event as simulated by the Genie 2.8.10 event generator in argon. The red line represents the kaon momentum distribution before undergoing the simulated final state interaction inside the argon nucleus, while the blue line represents the momentum distribution after FSI.

*Right.* Positive Kaon momentum spectrum in the LArIAT beamline, positive tune, Run II, Picky Tracks see section 3.2.2.

<sup>1334</sup> **Chapter 3**

<sup>1335</sup> **LArIAT: Liquid Argon In A**

<sup>1336</sup> **Testbeam**

<sup>1337</sup> “*But, hey we need to be somewhat foolish...*”

<sup>1338</sup> – Agnes Obel, 2010 –

<sup>1339</sup> In this chapter, we describe the LArIAT experimental setup. We start by illus-  
<sup>1340</sup> trating the journey of the charged particles in the Fermilab accelerator complex, from  
<sup>1341</sup> the gaseous thermal hydrogen at the Fermilab ion source to the delivery of the LAr-  
<sup>1342</sup> IAT tertiary beam at MC7. We then describe the LArIAT beamline detectors, the  
<sup>1343</sup> LArTPC, the DAQ and the monitoring system.

<sup>1344</sup> **3.1 The Particles’ Path to LArIAT**

<sup>1345</sup> LArIAT’s particle history begins in the Fermilab accelerator complex with a beam of  
<sup>1346</sup> protons. The process of proton acceleration develops in gradual stages (see picture  
<sup>1347</sup> 3.1): gaseous hydrogen is ionized in order to form H<sup>-</sup> ions; these ions are boosted  
<sup>1348</sup> to 750 keV by a Cockcroft-Walton accelerator and injected into the linear accelerator  
<sup>1349</sup> (Linac) that increases their energy up to 400 MeV; then, H<sup>-</sup> ions pass through a

1350 carbon foil and lose the two electrons; the resulting protons are then injected into a  
1351 rapid cycling synchrotron, called the Booster; at this stage, protons reach 8 GeV of  
1352 energy and are compacted into bunches; the next stage of acceleration is the Main  
1353 Injector, a synchrotron which accelerates the bunches up to 120 GeV; in the Main  
1354 Injector, several bunches are merged into one and are ready for delivery.

1355 The Fermilab accelerator complex works in supercycles of 60 seconds in duration.  
1356 A 120 GeV primary proton beam with variable intensity is extracted in four-second  
1357 “spills” and sent to the Meson Center beam line.

1358 LArIAT’s home at Fermilab is the Fermilab Test Beam Facility (FTBF), where  
1359 the experiment characterizes a beam of charged particles in the Meson Center beam  
1360 line. At FTBF, the primary beam is focused onto a tungsten target to create LAr-  
1361 IAT’s secondary beam. The secondary beamline is set such that the composition of  
1362 the secondary particle beam is mainly positive pions. The momentum peak of the  
1363 secondary beam was fixed at 64 GeV/c for the LArIAT data considered in this work,  
1364 although the beam is tunable in momentum between 8-80 GeV/c; this configuration  
1365 of the secondary beamline assured a stable beam delivery at the LArIAT experimental  
1366 hall.

1367 The secondary beam impinges then on a copper target within a steel collimator  
1368 inside the LArIAT experimental hall (MC7) to create the LArIAT tertiary beam,  
1369 (shown in Fig. 3.2). The steel collimator selects particles produced with a 13° pro-  
1370 duction angle. The particles are then bent by roughly 10° through a pair of dipole  
1371 magnets. By configuring the field intensity of the magnets we allow the particles of  
1372 LArIAT’s tertiary beam to span a momentum range from 0.2 to 1.4 GeV/c. The  
1373 polarity of the magnet is also configurable and determines the sign of the beamline  
1374 particles which are focused on the LArTPC. If the magnet polarity is positive the  
1375 tertiary beam composition is mostly pions and protons with a small fraction of elec-  
1376 trons, muons, and kaons. It is the job of the LArIAT beamline equipment to select the

## Fermilab Accelerator Complex

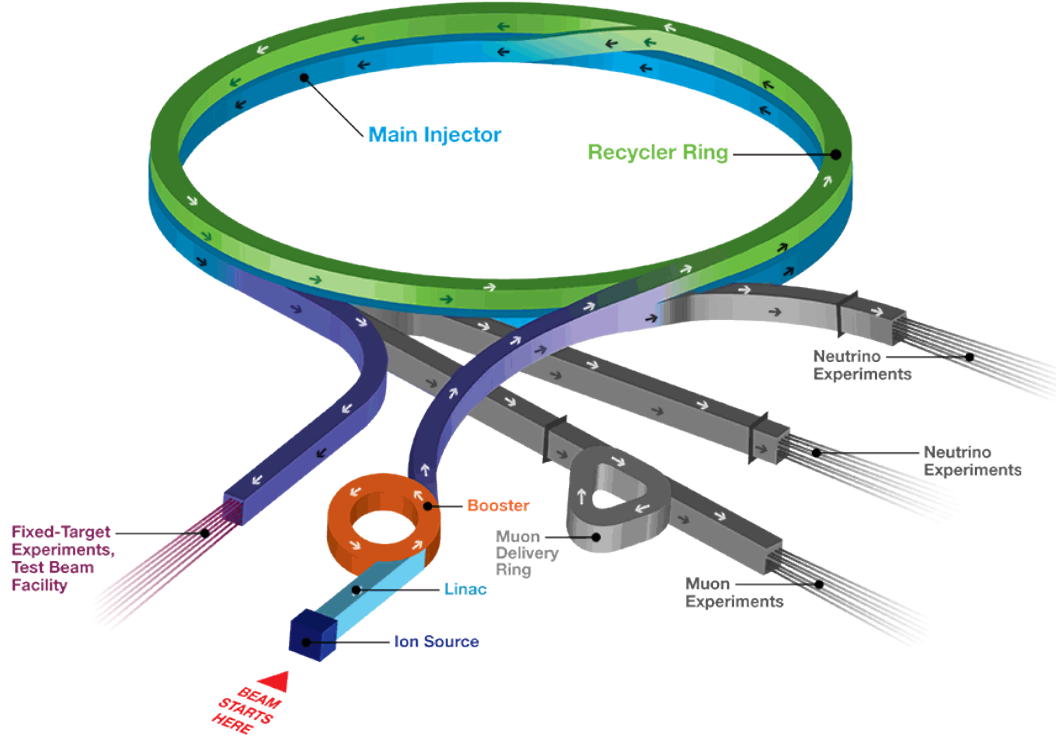


Figure 3.1: Layout of Fermilab Accelerator complex.

1377 particles polarity, to perform particle identification in the beamline and to measure  
1378 the momentum of the tertiary beam particles before they get to the LArTPC. The  
1379 LArIAT detectors are described in the following paragraphs.

### 1380 3.2 LArIAT Tertiary Beam Instrumentation

1381 The instrumentation of LArIAT tertiary beam and the TPC components have changed  
1382 several times during the three years of LArIAT data taking. The following paragraphs  
1383 describe the components operational during “Run II”, the data taking period relevant  
1384 to the hadron cross section measurements considered in this thesis.

1385 The key components of the tertiary beamline instrumentation for the hadron cross  
1386 section analyses are the two bending magnets, a set of four wire chambers (WCs)

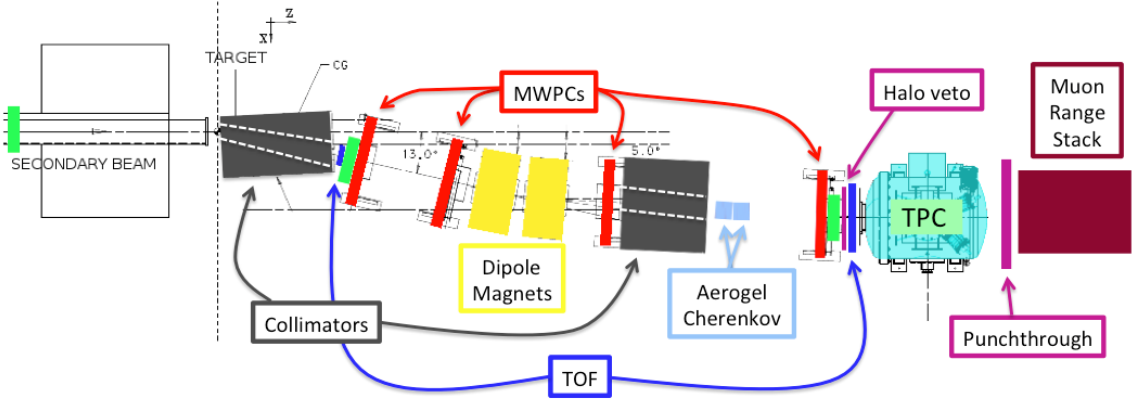


Figure 3.2: Bird’s eye view of the LArIAT tertiary beamline. In grey: upstream and downstream collimators; in yellow: bending magnets; in red: multi wire proportional chambers; in blue: time of flight; in green: liquid argon TPC volume; in maroon: muon range stack.

and two time-of-flight scintillating paddles (TOF) and, of course, the LArTPC. The magnets determine the polarity of the particles in the tertiary beam; the combination of magnets and wire chambers determines the particles’ momenta, which is used to determine the particle species in conjunction with the TOF. A muon range stack downstream from the TPC and two sets of cosmic paddles configured as a telescope surrounding the TPC are also used for calibration purposes. A couple of Aerogel Cherenkov counters, which we will not describe here as they are not used in the hadron cross section measurements, completes the beamline instrumentation.

### 3.2.1 Bending Magnets

LArIAT uses a pair of identical Fermilab type “NDB” electromagnets, recycled from the Tevatron’s anti-proton ring, in a similar configuration used for the MINERvA T-977 test beam calibration [56]. The magnets are a fundamental piece of the LArIAT beamline equipment, as they are used for the selection of the particle polarity and for the momentum measurement before the LArTPC. The sign of the current in the magnets allows us to select either positively or negatively charged particles; the value

1402 of the magnetic field is used in the momentum determination and in the subsequent  
1403 particle identification.

1404 We describe here the characteristics and response of one magnet, as the second one  
1405 has a similar response, given its identical shape and history. Each magnet is a box with  
1406 a rectangular aperture gap in the center to allow for the particle passage. The magnet  
1407 aperture measures 14.22 cm in height, 31.75 cm in width, and 46.67 cm in length.  
1408 Since the wire chambers aperture ( $\sim 12.8 \text{ cm}^2$ ) is smaller than the magnet aperture,  
1409 only the central part of the magnet gap is utilized. The field is extremely uniform  
1410 over this limited aperture and was measured with two hall probes, both calibrated  
1411 with nuclear magnetic resonance probes. The probes measured the excitation curve  
1412 shown in Figure 3.3.

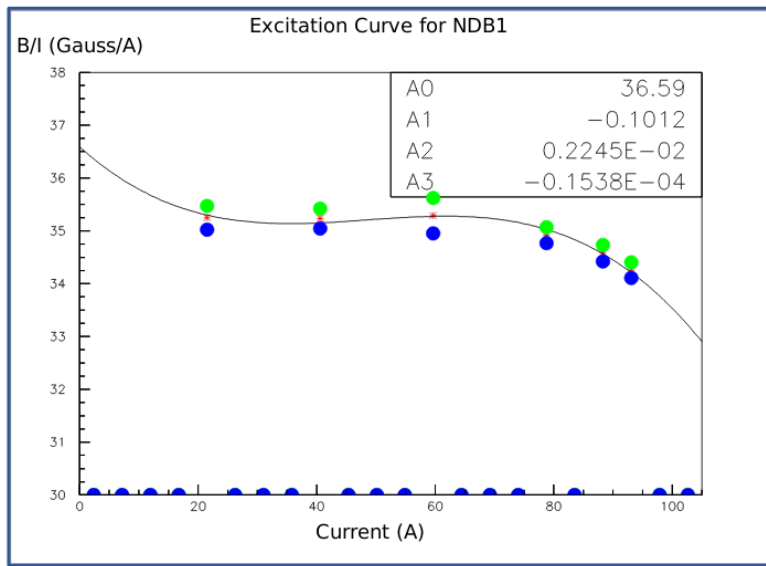


Figure 3.3: Magnetic field over current as a function of the current, for one NDB magnet (excitation curve). The data was collected using two hall probes (blue and green). We fit the readings with a cubic function (black) to average of measurements (red) given in the legend [43].

1413 The current through the magnets at a given time is identical in both magnets.  
1414 For the Run II data taking period, the current settings explored were 60A ( $B \sim 0.21$   
1415 T) and 100A ( $B \sim 0.35$  T) in both polarities. Albeit advantageous to enrich the  
1416 tertiary beam composition with high mass particles such as kaons, we never pushed

1417 the magnets current over 100 A, not to incur in overheating. During operation, we  
1418 operated an air and water cooling system on the magnets and we remotely monitored  
1419 the magnet temperatures.

1420 **3.2.2 Multi-Wire Proportional Chambers**



Figure 3.4: One of the four Multi Wire Proportional Chambers (WC) used in the LArIAT tertiary beamline and related read-out electronics.

1421 LArIAT uses four multi-wire proportional chambers, or wire chambers (WC) for  
1422 short, two upstream and two downstream from the bending magnets. The geometry of  
1423 one chamber is shown in Figure 3.4: the WC effective aperture is a square of 12.8 cm  
1424 perpendicular to the beam direction. Inside the chamber, the 128 horizontal and 128  
1425 vertical wires strung at a distance of 1 mm from each other in a mixture of 85% Argon  
1426 and 15% isobutane gas. The WC operating voltage is between 2400 V and 2500 V.  
1427 The LArIAT wire chambers are an upgraded version of the Fenker Chambers [62],  
1428 where an extra grounding improves the signal to noise ratio of the electronic readout.

1429 Two ASDQ chips [95] mounted on a mother board plugged into the chamber serve  
1430 as front end amplifier/discriminator. The chips are connected to a multi-hit TDC [73]  
1431 which provides a fast OR output used as first level trigger. The TDC time resolution  
1432 is 1.18 ns/bin and can accept 2 edges per 9 ns. The maximum event rate acceptable  
1433 by the chamber system is 1 MHz: this rate is not a limiting factor considering that

1434 the rate of the tertiary particle beam at the first wire chamber is estimated to be less  
1435 than 15 kHz. A full spill of data occurring once per supercycle is stored on the TDC  
1436 board memory at once and read out by a specially designed controller. We use LVDS  
1437 cables to carry both power and data between the controller and the TDCs and from  
1438 the controller to the rest of the DAQ.

### 1439 Multi-Wire Proportional Chambers functionality

1440 We use the wire chamber system together with the bending magnets to measure the  
1441 particle's momentum.

1442 In the simplest scenario, only one hit on each and every of the four wire chambers  
1443 is recorded during a single readout of the detector systems. Thus, we use the hit  
1444 positions in the two wire chambers upstream of the magnets to form a trajectory  
1445 before the bend, and the hit positions in the two wire chambers downstream of the  
1446 magnets to form a trajectory after the bend. We use the angles in the XZ plane  
1447 between the upstream and downstream trajectories to calculate the  $Z$  component of  
1448 the momentum as follows:

$$P_z = \frac{B_{eff}L_{eff}}{3.3(\sin(\theta_{DS}) - \sin(\theta_{US}))}, \quad (3.1)$$

1449 where  $B_{eff}$  is the effective maximum field in a square field approximation,  $L_{eff}$   
1450 is the effective length of both magnets (twice the effective length of one magnet),  
1451  $\theta_{US}$  is the angle off the  $z$  axis of the upstream trajectory,  $\theta_{DS}$  is the angle off the  
1452  $z$  axis of the downstream trajectory and  $3.3 c^{-1}$  is the conversion factor from [T·m]  
1453 to [MeV/c]. By using the hit positions on the third and fourth wire chamber, we  
1454 estimate the azimuthal and polar angles of the particle trajectory, and we are able to  
1455 calculate the other components of the momentum.

1456 The presence of multiple hits in a single wire chamber or the absence of hits in one  
1457 (or more) wire chambers can complicate this simple scenario. The first complication

is due to beam pile up, while the latter is due to wire chamber inefficiency. In the case of multiple hits on a single WC, at most one wire chamber track is reconstructed per event. Since the magnets bend particles only in the X direction, we assume the particle trajectory to be roughly constant in the YZ plane, thus we keep the combination of hits which fit best with a straight line. It is still possible to reconstruct the particle’s momentum even if the information is missing in either of the two middle wire chambers (WC2 or WC3), by constraining the particle trajectory to cross the plane in between the magnets.

Events satisfying the simplest scenario of one single hit in each of the four wire chambers form the “Picky Track” sample. We construct another, higher statistics sample, where we loosen the requirements on single hit and wire chamber efficiency: the “High Yield” sample. For LArIAT Run II, the High Yield sample is about three times the Picky Tracks statistics. We assume an uncertainty of 2% for four-point WC track, momentum uncertainty as reported for the same beamline in [56].

### 3.2.3 Time-of-Flight System

Two scintillator paddles, one upstream of the first set of WCs and one downstream of the second set of WCs form LArIAT time-of-flight (TOF) detector system.

The upstream paddle is made of a 10 x 6 x 1 cm scintillator piece, read out by two PMTs mounted on the beam left side which collect the light from light guides mounted on all four edges of the scintillator. The downstream paddle is a 14 x 14 x 1 cm scintillator piece read out by two PMTs on the opposite ends of the scintillator, as shown in figure 3.5. The relatively thin width in the beamline direction minimizes energy loss of beam particles traveling through the scintillator material.

The CAEN 1751 digitizer is used to digitize the TOF PMTs signals at a sampling rate of 1 GHz. The 12 bit samples are stored in a circular memory buffer. At trigger time, data from the TOF PMTs are recorded to output in a 28.7  $\mu$ s windows starting

1484 approximately 8.4  $\mu$ s before the trigger time.

1485 **TOF functionality**

1486 The TOF signals rise time (10-90%) is 4 ns and a full width, half-maximum of 9 ns  
1487 consistent in time. The signal amplitudes from the upstream TOF and downstream  
1488 TOF are slightly different: 200 mV for the upstream PMTs but only 50 mV for  
1489 downstream PMTs. The time of the pulses was calculated utilizing an oversampled  
1490 template derived from the data itself. We take the pulse pedestal from samples  
1491 far from the pulse and subtract it from the pulse amplitude. We then vertically  
1492 stretch a template to match the pedestal-subtracted pulse amplitude and we move  
1493 it horizontally to find the time. With this technique, we find a pulse time-pickoff  
1494 resolution better than 100 ps. The pulse pile up is not a significant problem given  
1495 the TOF timing resolution and the rate of the particle beam. Leveraging on the  
1496 pulses width uniformity of any given PMT, we flag events where two pulses overlap  
1497 as closely in time as 4 ns with a 90% efficiency according to simulation.

1498 We combine the pulses from the two PMTs on each paddle to determine the  
1499 particles' arrival time by averaging the time measured from the single PMT, so to  
1500 minimize errors due to optical path differences in the scintillator. However, a time  
1501 spread of approximately 300 ps is present in both the upstream and downstream  
1502 detectors, likely due to transit time jitter in the PMTs themselves.

1503 **3.2.4 Punch-Through and Muon Range Stack Instruments**

1504 The punch-through and the muon range stack (MuRS) detectors are located down-  
1505 stream of the TPC. These detectors provide a sample of TPC crossing tracks without  
1506 relying on TPC information and can be used to improve particle ID for muons and  
1507 pions with momentum higher than 450 MeV/c.

1508 The punch-through is simple sheet of scintillator material, read out by two PMTs.



Figure 3.5: Image of the down stream time of flight paddle, PMTs and relative support structure before mounting.

1509 The MuRS is a segmented block of steel with four slots instrumented with scintillation  
1510 bars. The four steel layers in front of each instrumented slot are 2 cm, 2 cm, 14 cm  
1511 and 16 cm deep in the beam direction. Each instrumented slot is equipped with  
1512 four scintillation bars each, positioned horizontally in the direction orthogonal to the  
1513 beam. Each scintillator bar measures ? x ? x 2 cm and it is read out by one PMT.

1514 The signals from both the punch-thorough and the MuRS PMTs are sent to a  
1515 NIM discriminator. If the signal crosses the discriminator threshold, it is digitized in  
1516 the CAEN V1740, same as the TPC. The sampling time of the CAEN V1740 is slow  
1517 (of the order of 128 ns) and that the pulse shape information from the PMT is lost.  
1518 A Punch-thorough and MuRS signal will then be simply a “hit” at a given time in  
1519 the beamline event.

1520 It is worth mentioning here the presence of an additional scintillation paddle  
1521 between WC4 and the downstream paddle of the TOF system, called halo. The  
1522 halo is a 39x38x1 cm<sup>3</sup> paddle with a 6.5 cm radius hole in the center, whose original  
1523 function was to reject beam particles slightly offset from the beamline center. Data

1524 from this paddle turned out to be unusable, so our data events include both particle  
1525 going through the halo scintillation material or through the halo hole.

### 1526 **3.2.5 LArIAT Cosmic Ray Paddle Detectors**

1527 LArIAT triggers both on beam events and on cosmic rays events. We perform this  
1528 latter trigger by using two sets of cosmic ray paddle detectors (a.k.a. “cosmic towers”.)  
1529 The cosmic towers frame the LArIAT cryostat, as one sits in the downstream left  
1530 corner and the other sits in the upstream right corner of the cryostat. Two paddle  
1531 sets of four scintillators pieces each make up each cosmic tower, an upper set and a  
1532 lower set per tower. Of the four paddles, a couple of two matched paddles stands  
1533 upright while the a second matched pair lies across the top of the assembly in the top  
1534 sets (or across the bottom of the assembly in the bottom sets). The horizontal couple  
1535 is used as a veto for particles traveling from inside the TPC out. The four signals  
1536 from the vertical paddles along one of the body diagonals of the TPC are combined  
1537 in a logical “AND”. This allows to select track due to cosmic muons at the ground  
1538 level crossing the TPC along one of its diagonals. Cosmic ray muons whose average  
1539 energy is in the few GeV range crossing both anode and cathode populate the events  
1540 triggered this way. This particularly useful sample of tracks is associated can be used  
1541 for many tasks; for example, we use anode-cathode piercing tracks to cross check  
1542 the TPC electric field on data (see Appendix A), to calibrate the charge response of  
1543 the TPC wires for the full TPC volume and to measure the electron lifetime in the  
1544 chamber [104].

1545 We retrieved the scintillation paddles from the decommissioning of the CDF de-  
1546 tector at Fermilab and we used only the paddles with a counting efficiency greater  
1547 than 95% and low noise at working voltage. The measured trigger rate of the whole  
1548 system is 0.032 Hz, corresponding to  $\sim 2$  muons per minute.



Figure 3.6: Photograph of one of the scintillation counters used in the cosmic towers.

### **1549 3.3 In the Cryostat**

1550 The heart of the LArIAT experiment lives in the LArIAT cryostat. In this section,  
1551 we describe the cryogenic system and the argon purity (Section 3.3.1), the LArIAT  
1552 TPC (Section 3.3.2) and light collection system (3.3.3).

#### **1553 3.3.1 Cryogenics and Argon Purity**

1554 LArIAT repurposed the ArgoNeuT cryostat [17] in order to use it in a beam of charged  
1555 particles, and added a new process piping and a new liquid argon filtration system in  
1556 FTBF. Inside the LArIAT experimental hall, the cryostat sits in the beam of charged  
1557 particles with its horizontal main axis oriented parallel to the secondary beam,  $3^\circ$   
1558 off axis from the tertiary beam

1559 Two volumes make up LArIAT cryostat, shown in Figure 3.7: the inner vessel and  
1560 the outer vessel. Purified liquid argon fills the inner vessel, while the outer volume  
1561 provides insulation through a vacuum jacket equipped with layers of aluminized mylar  
1562 superinsulation. The inner vessel is a cylinder of 130 cm length and 76.2 cm diameter,  
1563 containing about 550 L of LAr, corresponding to a mass of 0.77 ton. We run the signal  
1564 cables for the LArTPC and the high voltage feedthrough through a “chimney” at the  
1565 top and mid-length of the cryostat.

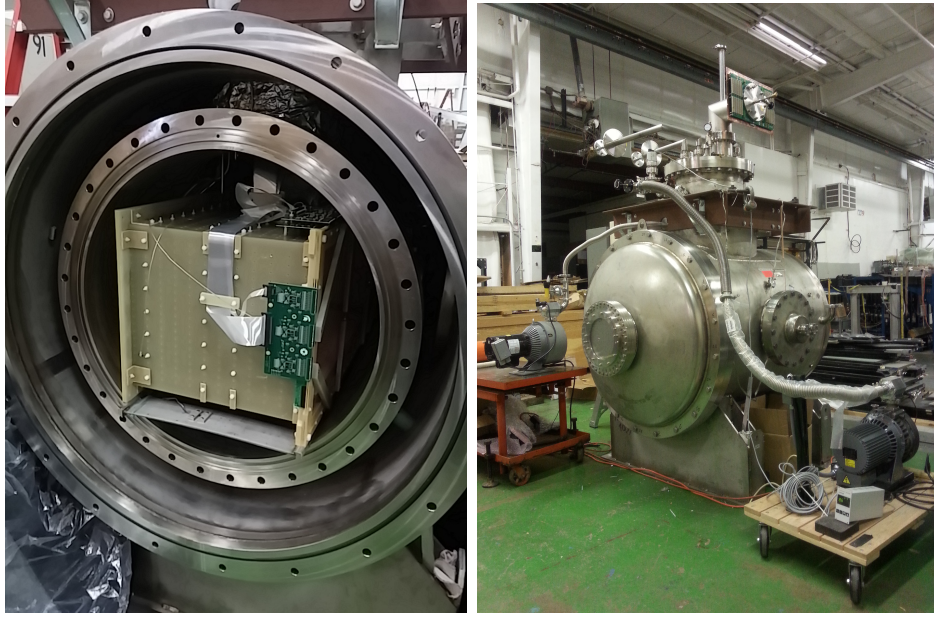


Figure 3.7: Left: the LArIAT TPC in the inner volume of the open cryostat. Right: cryostat fully sealed ready to be transported to FTBF.

Given the different scopes of the ArgoNeuT and LArIAT detectors, we made several modifications to the ArgoNeuT cryostat in order to use it in LArIAT. In particular, the modifications shown in Figure 3.8 were necessary to account for the beam of charged particles entering the TPC and to employ the new FTBF liquid argon purification system. We added a “beam window” on the front outer end cap and an “excluder” on the inner endcap, with the purpose of minimizing the amount of non-instrumented material upstream of the TPC’s active volume. The amount of non-instrumented material in front of the TPC for LArIAT corresponds to  $\sim 0.3$  electron radiation lengths ( $X_0$ ), to compare against the  $\sim 1.6X_0$  of ArgoNeuT. To allow studies of the scintillation light, we added a side port feedthrough which enables the mounting of the light collection system, as well as the connections for the corresponding signal and high-voltage cables (see Section 3.3.3). We modified the bottom of the cryostat adding Conflat and ISO flange sealing to connect the liquid argon transfer line to the new argon cooling and purification system.

As in any other LArTPC, argon purity is a crucial parameter for LArIAT. Indeed,



Figure 3.8: Main modifications to the ArgoNeuT cryostat: 1) outlet for connection to the purification system at the bottom of the cryostat; 2) the “beam-window” on the outer endcap and “excluder” which reduces the amount of non-instrumented material before the TPC; 3) the side port to host the light collection system.

1581 the presence of contaminants affects both the basic working principles of a LArTPC,  
 1582 as shown in section 2.1.2: electronegative contaminants such as oxygen and water de-  
 1583 crease the number of ionization electrons collected on the wires after drifting through  
 1584 the volume. In addition, contaminants such as Nitrogen decrease the light yield  
 1585 from scintillation light, especially in its slow component. In LArIAT, contaminations  
 1586 should not exceed the level of 0.2 parts per billion (ppb). We achieve this level of  
 1587 purity in several stages. The specifics required for the commercial argon bought for  
 1588 LArIAT are 2 parts per million (ppm) oxygen, 3.5 ppm water, and 10 ppm nitrogen.  
 1589 This argon is monitored with the use of commercial gas analyzer. Argon is stored in  
 1590 a dewar external to LArIAT hall and filtered before filling the TPC. LArIAT uses a  
 1591 filtration system designed for the Liquid Argon Purity Demonstrator (LAPD) [57]:  
 1592 half of a 77 liter filter contains a 4A molecular sieve (Sigma-Aldrich [110]) able to re-  
 1593 move mainly water, while the other half contains BASF CU-0226 S, a highly dispersed  
 1594 copper oxide impregnated on a high surface area alumina, apt to remove mainly oxy-

1595 gen [27]. A single pass of argon in the filter is sufficient to achieve the necessary  
1596 purity, unless the filter is saturated. In case the filter saturates, the media needs to  
1597 be regenerated by using heated gas; this happened twice during the Run II period<sup>1</sup>.  
1598 The electron lifetime during the full LArIAT data taking are shown in Figure 2.4.  
1599 The filtered argon reaches the inner vessel via a liquid feedthrough which is routed to  
1600 the bottom of the cryostat. Argon is not recirculated in the system; rather, it boils  
1601 off and vents to the atmosphere. During data taking, we replenish the argon in the  
1602 cryostat every 6 hours to keep the TPC high voltage feedthrough and cold electronics  
1603 always submerged. In fact, we constantly monitor the level, temperature, and pres-  
1604 sure of the argon both in the commercial dewar and inside the cryostat during data  
1605 taking.

### 1606 **3.3.2 LArTPC: Charge Collection**

1607 The LArIAT Liquid Argon Time Projection Chamber is a rectangular box of dimen-  
1608 sions 47 cm (drift) x 40 cm (height) x 90 cm (length), containing 170 liters of Liquid  
1609 Argon. The LArTPC three major subcomponents are

- 1610 1) the cathode and field cage,
- 1611 2) the wire planes,
- 1612 3) the read-out electronics.

#### 1613 **Cathode and field cage**

1614 A G10 plain sheet with copper metallization on one of the 40 x 90 cm inner surfaces  
1615 forms the cathode. A high-voltage feedthrough on the top of the LArIAT cryostat  
1616 delivers the high voltage to the cathode; the purpose of the high voltage system

---

1. We deemed the filter regeneration necessary every time the electron lifetime dropped under 100  $\mu\text{s}$ .

1617 (Figure 3.9) is to drift ionization electrons from the interaction of charged particles  
1618 in the liquid argon to the wire planes. The power supply used in this system is a  
1619 Glassman LX125N16 [70] capable of generating up to -125 kV and 16 mA of current,  
1620 but operated at -23.5kV during LArIAT Run-II. The power supply is connected via  
1621 high voltage cables to a series of filter pots before finally reaching the cathode.

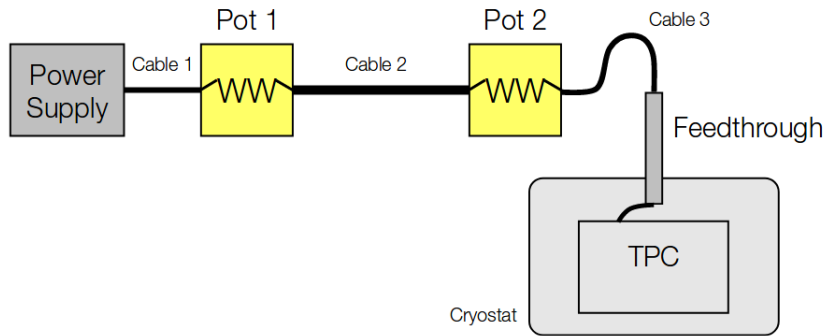


Figure 3.9: Schematic of the LArIAT high voltage system.

1622 The field cage is made of twenty-three parallel copper rings framing the inner walls  
1623 of the G10 TPC structure. A network of voltage-dividing resistors connected to the  
1624 field cage rings steps down the high voltage from the cathode to form a uniform electric  
1625 field. The electric field over the entire TPC drift volume is 486 V/cm, as measured  
1626 in appendix A. The maximum drift length, i.e. the distance between cathode and  
1627 anode planes, is 47 cm.

## 1628 Wire planes

1629 LArIAT Run-II has three wire planes separated by 4 mm spaces: in order of increasing  
1630 distance from the cathode, they are the shield, the induction and the collection plane.  
1631 The “wire pitch”, i.e., the distance between two adjacent wires in a given plane, is  
1632 4 mm. The shield plane counts 225 parallel wires of equal length oriented vertically.  
1633 This plane is not connected with the read-out electronics; rather it shields the outer  
1634 planes from extremely long induction signals due to the ionization in the whole drift

volume. As the shield plane acts almost like a Faraday cage, the resulting shape of signals in the first instrumented plane (induction) is easier to reconstruct. Both the induction and collection planes count 240 parallel wires of different length oriented at  $60^\circ$  from the vertical with opposite signs. Electrons moving past the induction plane will induce a bipolar pulse on its wires; the drifting electrons will be then collected on the collection plane's wires, forming a unipolar pulse.

The three wire planes and the cathode form three drift volumes, as shown in Figure 3.10. The main drift volume is defined as the region between the cathode plane and the shield plane (C-S). The other two drift regions are those between the shield plane and the induction plane (S-I), and between the induction plane and the collection plane (I-C). The electric field in these regions is chosen to satisfy the charge transparency condition and allow for 100% transmission of the drifting electrons through the shield and the induction planes.

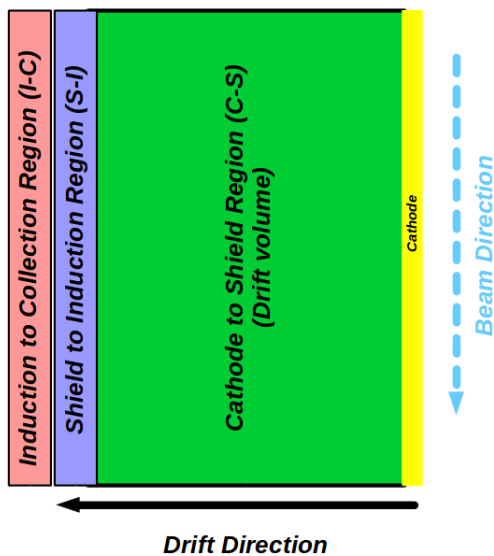


Figure 3.10: Schematic of the three drift regions inside the LArIAT TPC: the main drift volume between the cathode and the shield plane (C-S) in green, the region between the shield plane and the induction plane (S-I) in purple, and the region between the induction plane and the collection plane (I-C) in pink.

Table 3.1 provides the default voltages applied to the cathode and the shield,

1649 induction, and collection plane.

Table 3.1: Cathode and anode planes default voltages

Cathode	Shield	Induction	Collection
-23.17 kV	-298.8 V	-18.5 V	338.5 V

1650 **Electronics**

1651 Dedicated electronics read the induction and collection plane wires, for a total of  
1652 480-channel analog signal path from the TPC wires to the signal digitizers. A digital  
1653 control system for the TPC-mounted electronics, a power supply, and a distribution  
1654 system complete the front-end system. Figure 3.11 shows a block diagram of the  
1655 overall system. The direct readout of the ionization electrons in liquid argon forms  
1656 typically small signals on the wires, which need amplification in oder to be processed.  
1657 LArIAT performs the amplification stage directly in cold with amplifiers mounted  
1658 on the TPC frame inside the liquid argon. The BNL ASICs adopted in LArIAT are  
1659 designated as LArASIC, version 4-star and are the same used by the MicroBooNE  
1660 experiment [60]. The signal from the ASICs are driven to the other end of the readout  
1661 chain, to the CAEN V1740 digitizers [35]. The CAEN V1740 has a 12 bit resolution  
1662 and a maximum input range of 2 VDC, resulting in about 180 ADC count for a  
1663 crossing MIP.

1664 **3.3.3 LArTPC: Light Collection System**

1665 The collection of scintillation photons is the second mechanism of particle detection  
1666 in argon other than the ionization electrons. Over the course of LArIAT's three years  
1667 of data taking, the light collection system changed several times. We describe here  
1668 the light collection system for Run II. Two PMTs, a 3-inch diameter Hamamatsu  
1669 R-11065 and 2-inch diameter ETL D757KFL [7], as well as three SiPMs arrays (two  
1670 Hamamatsu S11828-3344M 4x4 arrays and one single-channel SensL MicroFB-60035)

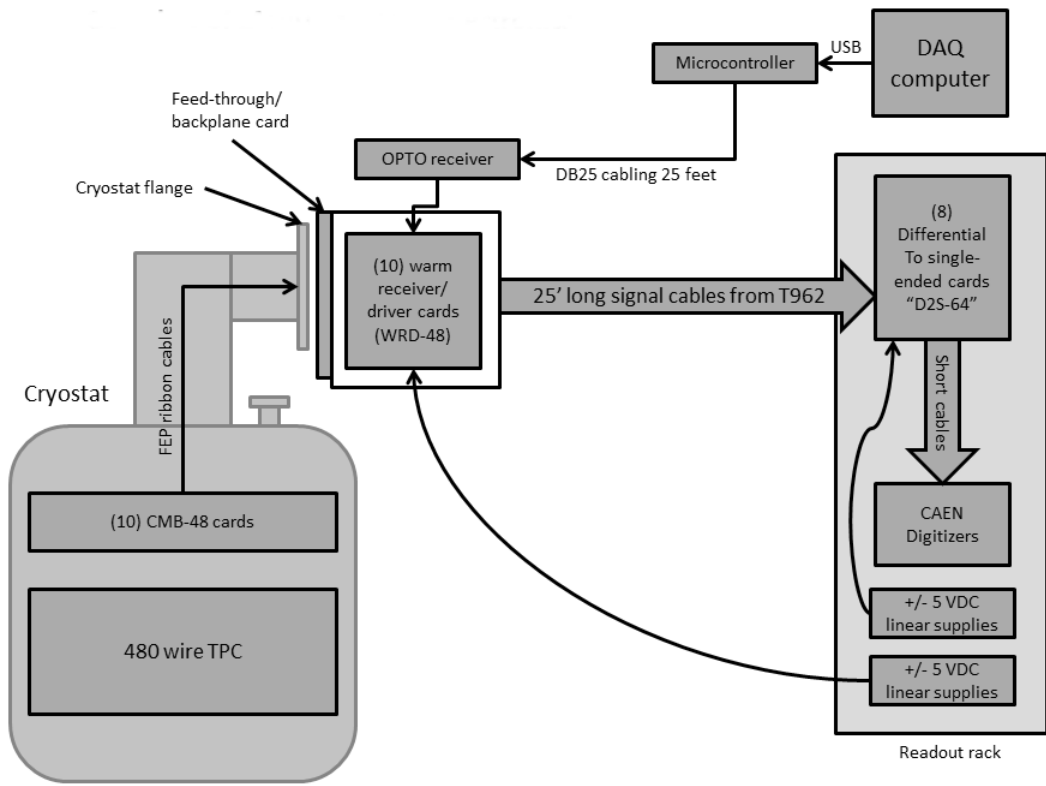


Figure 3.11: Overview of LArIAT Front End electronics.

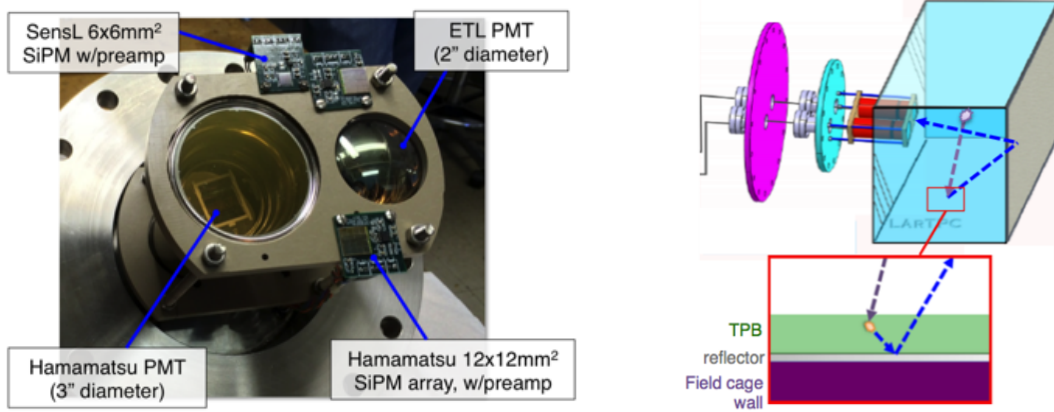


Figure 3.12: LArIAT’s photodetector system for observing LAr scintillation light inside the TPC (left), and a simplified schematic of VUV light being wavelength-shifting along the TPB-coated reflecting foils (right).

1671 are mounted on the PEEK support structure. PEEK screws into an access flange  
 1672 as shown in Figure 3.12, on the anode side, leaving approximately 5 cm of clearance  
 1673 from the collection plane.

1674 Liquid argon scintillates in vacuum-ultraviolet (VUV) range at 128 nm; since  
 1675 cryogenic PMTs are not sensitive to VUV wavelengths, we need to shift the light to a  
 1676 range that is visible to the PMTs. In LArIAT, the wavelength shifting is achieved by  
 1677 installing highly-reflective 3M VIKUITI dielectric substrate foils coated with a thin  
 1678 layer of tetraphenyl-butadiene (TPB) on the four unbiased walls of the TPC. The  
 1679 scintillation light interaction with the TPB emits one or more visible photons, which  
 1680 are then reflected into the chamber. Thus, the light yield increases and results in  
 1681 higher uniformity of light across the TPC active volume, allowing the possibility of  
 1682 light-based calorimetry, currently under study.

1683 For Run II, we coated the windows of the ETL PMT and the SensL SiPM with  
 1684 a thin layer of TPB. In doing so, some of the VUV scintillation light converts into  
 1685 visible right at the sensor faces, keeping information on the direction of the light  
 1686 source. Information about the light directionality is hindered for the light reflected  
 1687 on foils, as the reflection is uniform in angle.

## 1688 3.4 Trigger and DAQ

1689 The LArIAT DAQ and trigger system governs the read out of all the many subsystems  
1690 forming LArIAT. The CAEN V1495 module [34] and its user-programmable FPGA  
1691 are the core of this system. Every 10 ns, this module checks for matches between  
1692 sixteen logical inputs and user-defined patterns in the trigger menu; if it finds a match  
1693 for two consecutive clock ticks, that trigger fires.

1694 LArIAT receives three logic signals from the Fermilab accelerator complex related  
1695 to the beam timing which we use as input triggers: a pulse just before the beam, a  
1696 pulse indicating beam-on, and a beam-off pulse.

1697 The beam instruments, the cosmic ray taggers, and the light collection system  
1698 provide the other NIM-standard logic pulse inputs to the trigger decision. We auto-  
1699 matically log the trigger inputs configuration with the rest of the DAQ configuration  
1700 at the beginning of each run.

1701 Fundamental inputs to the trigger card come from the TOF (see section 3.2.3)  
1702 and the wire chambers (see section 3.2.2), as activity in these systems points to the  
1703 presence of a charged particle in tertiary beam line. In particular, the discriminated  
1704 pulses from the TOF PMTs form a NIM logic pulse for the trigger logic. We ask  
1705 for a coincidence within a 20 ns window for all the pulses from the PMTs looking at  
1706 the same scintillator block and use a delayed coincidence between the upstream and  
1707 downstream paddle to inform the trigger decision. In order to form a coincidence  
1708 between the upstream and downstream paddles, we delay the upstream paddle coin-  
1709 cidence by 20 ns and widen it by 100 ns. The delay and widening are necessary to  
1710 account for both lightspeed particles and slower particles (high-mass) to travel the  
1711 6.5 m between the upstream and the downstream paddles. For the read out of the  
1712 wire chambers, we use a total of sixteen multi-hit TDCs [73], four per chamber: two  
1713 TDC per plane (horizontal and vertical), sixty-four wires per TDC. In each TDC, we  
1714 keep the logical “OR” for any signal over threshold from the sixty-four wires. We

1715 then require a coincidence between the “OR” for the horizontal TDCs and the “OR”  
1716 for the vertical TDCs: with this logic we make sure that at least one horizontal wire  
1717 and one vertical wire saw significant signal in one wire chamber. The single logical  
1718 pulse from each of the four wire chambers feeds into the first four inputs to the V1495  
1719 trigger card. We require a coincidence within 20 ns of at least three logical inputs to  
1720 form a trigger.

1721 The cosmic towers (see Section 3.2.5) provide another primary input to the trigger,  
1722 in order to capture long tracks from cosmic muons crossing the TPC. We use NIM  
1723 modules to require coincidences between one upper and one lower paddle set of any  
1724 opposite cosmic towers. The OR all the opposite towers’ coincidences is fed as an  
1725 input to the trigger card.

1726 We use the signal from the cryogenic PMTs (see Section 3.3.3) to form several  
1727 interesting triggers. The coincidence of signals from all the PMT pulses within  $\sim$ 20 ns  
1728 is an indication of ionizing radiation in the TPC and forms a trigger input. The  
1729 coincidence of two subsequent scintillation logic pulses delayed by a maximum of  $7 \mu\text{s}$   
1730 forms the Michel electron trigger.

## 1731 **3.5 Control Systems**

1732 LArIAT is a complex ensemble of systems which needed to be monitored simultane-  
1733 ously during data taking. We performed the monitoring of the systems operations  
1734 with a slow control system, a DAQ monitoring system and a low level data quality  
1735 monitoring described in the following sections.

### 1736 **Slow Control**

1737 We used the Synoptic Java Web Start framework [19] as a real-time display of subsys-  
1738 tem conditions. Synoptic provides a Graphical User Interface that talks to the Fer-

milab Accelerator Control System via the ACNET protocol. Its simple GUI allowed us to change the operating parameters and to graph the trends of several variables of interest for all of the tertiary beam detectors. Among the most important quantities monitored by Synoptic there are the level of argon in both the inner vessel and the external dewar, the operating voltages of cathode and wire planes, of the PMTs and SiPMs, and of the four wire chambers, as well as the magnet temperatures. Figure 3.13 shows an example of the monitoring system. LArIAT uses the Accelerator Control NETwork system (ACNET) to monitor the beam conditions of the MCcenter beamline. For example, the horizontal and vertical position of the beam at the first two wire chambers (WC1 and WC2) are shown in 3.14 as seen by the shifter during data taking.

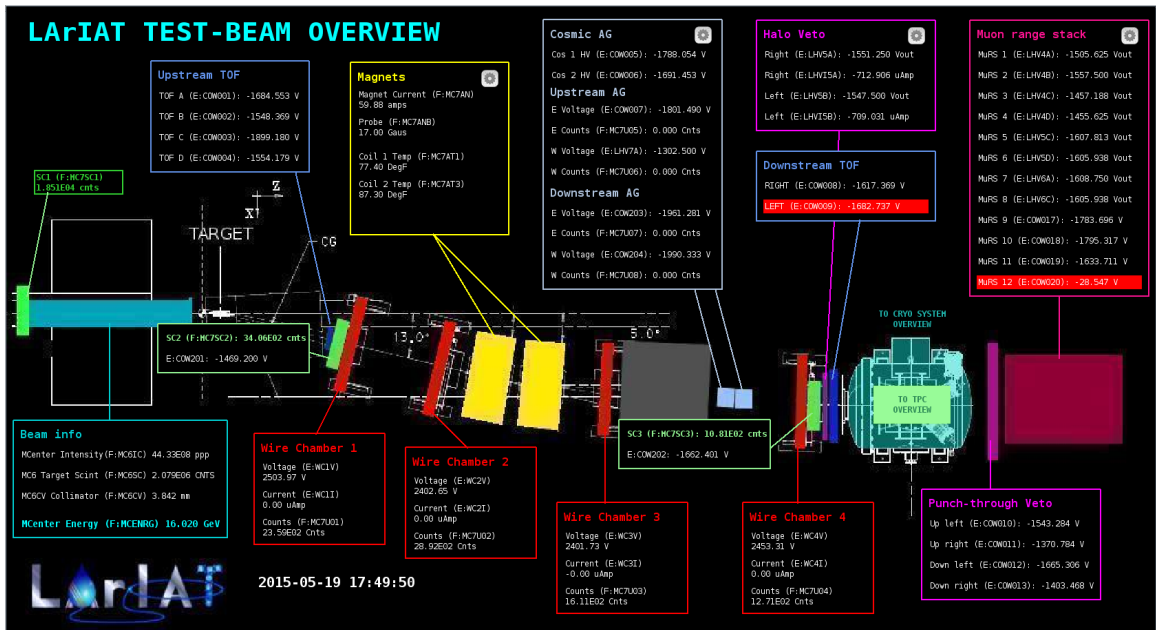


Figure 3.13: Interface of the Synoptic slow control system

## 1750 DAQ Monitoring

We monitor the data taking and the run time evolution with the Run Status Webpage (<http://lariat-wbm.fnal.gov/lariat/run.html>), a webpage updated in real-time. The

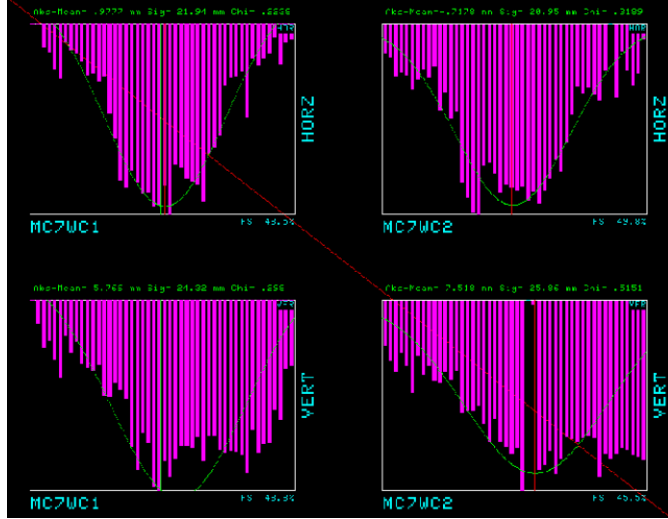


Figure 3.14: Beam position at the upstream wire chambers monitored with ACNET.

1753 page displays, among other information, the total number of triggers in the event,  
 1754 the total number of detectors triggered during a beam spill, the trigger patterns, the  
 1755 number of times a particular trigger pattern was satisfied during a beam spill, and  
 1756 the current time relative to the Fermilab accelerator complex supercycle. A screen  
 1757 shot of the page is show in figure 3.15.

### 1758 Data Quality Monitoring

1759 We employ two systems to ensure the quality of our data during data taking: the  
 1760 Near-Real-Time Data Quality Monitoring and the Event Viewer.

1761 The Near-Real-Time Data Quality Monitoring (DQM) is a webpage which receives  
 1762 updates from all the VME boards in the trigger system and displays the results of  
 1763 a quick analysis of the DAQ stream of raw data on a spill-by-spill basis. The DQM  
 1764 allows the shifter to monitor almost in real time (typically with a 2-minute delay)  
 1765 a series of low level-quantities and compare them to past collections of beam spills.  
 1766 Some of the variables monitored in the DQM are the pedestal mean and RMS on  
 1767 CAEN digitizer boards of the TPC wires and PMTs of the beamline detectors, the  
 1768 hit occupancy and timing plots on the wire chambers, and number of data fragments

1769 recorded that are used to build a TPC event. Abnormal values for low-level quantity  
1770 in the data activates a series of alarms in the DQM; this quick feedback on the DAQ  
1771 and beam conditions is fundamental to assure a fast debugging of the detector and a  
1772 very efficient data taking during beam uptime.

1773 The online Event Viewer displays a two dimensional representation (Wire vs Time)  
1774 of LArIAT TPC events on both the Induction and the Collection planes in near real  
1775 time. The raw pulses collected by the DAQ on each wire are plotted as a function  
1776 of drift time, resulting in an image of the TPC event easily readable by the shifter.  
1777 This tool guarantees a particularly good check of the TPC operation which activate  
1778 an immediate feedback for troubleshooting a number of issues. For example, it is  
1779 easy for the shifter to spot high occupancy events and request a reduction of the  
1780 primary beam intensity, or to spot a decrease of the argon purity which requires the  
1781 regeneration of filters, or to catch the presence of electronic noise and reboot the  
1782 ASICs. An example of high occupancy event is shown in 3.16.

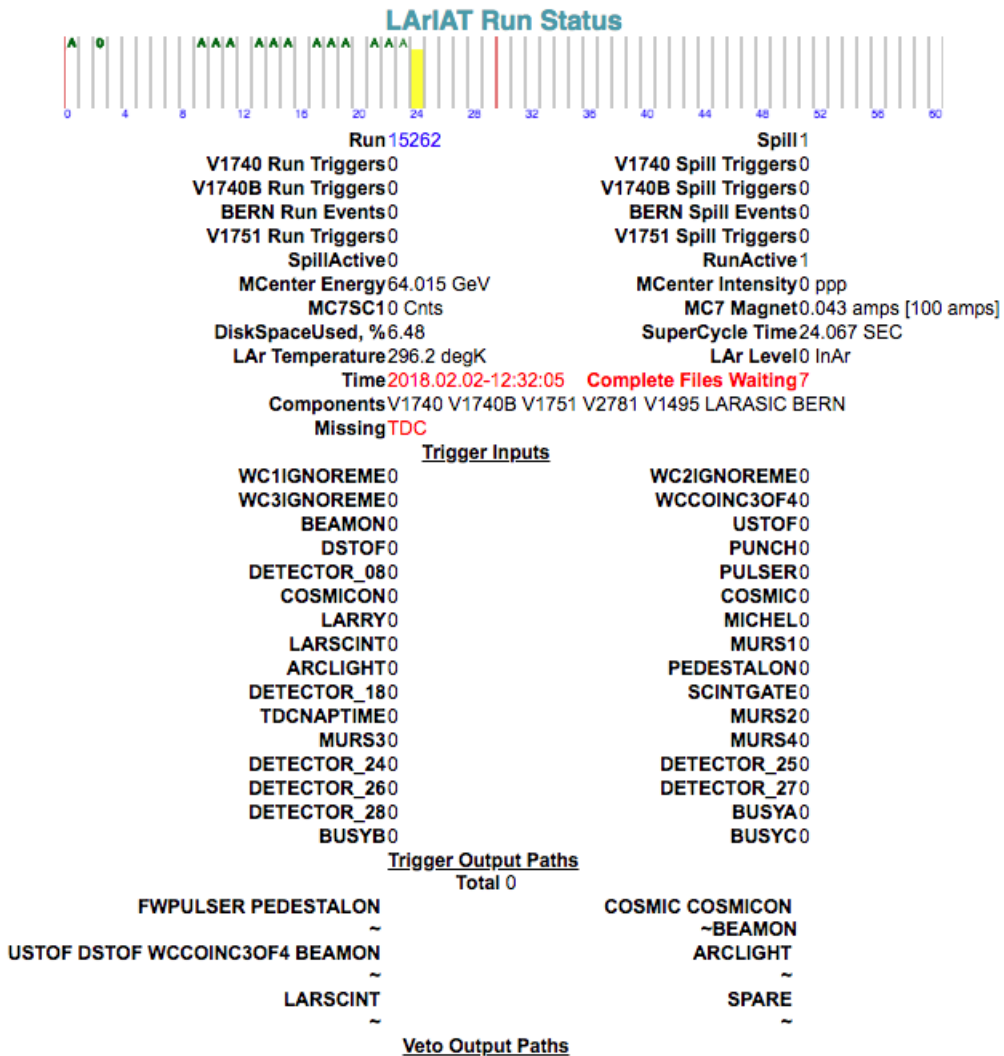


Figure 3.15: Run Status page at LArIAT downtime. At the top the yellow bar displays the current position in the Fermilab supercycle. Interesting information to be monitored by the shifter were the run number and number of spills, time elapsed from data taking (here in red), the energy of the secondary beam and the trigger paths.

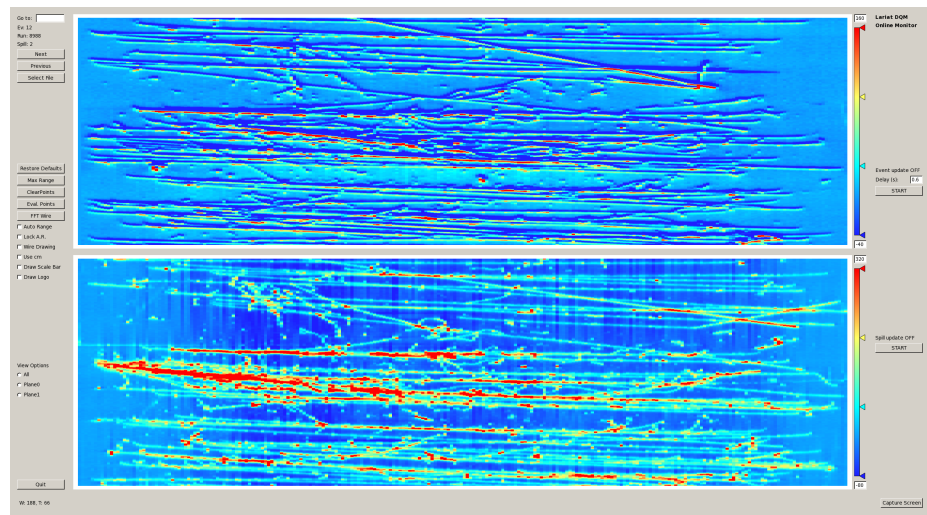


Figure 3.16: High occupancy event display: induction plane (top) and collection plane (bottom).

<sup>1783</sup> **Chapter 4**

<sup>1784</sup> **Total Hadronic Cross Section**

<sup>1785</sup> **Measurement Methodology**

<sup>1786</sup> “Like a lemon to the lime and the bubble to the bee”

<sup>1787</sup> – Eazy-E, 1993 –

<sup>1788</sup> This chapter describes the general procedure employed to measure a total hadronic  
<sup>1789</sup> differential cross section in LArIAT. Albeit with small differences, both the ( $\pi^-$ ,Ar)  
<sup>1790</sup> and ( $K^+$ ,Ar) total hadronic cross section measurements rely on the same procedure.  
<sup>1791</sup> We start by selecting the particle of interest using a combination of beamline detectors  
<sup>1792</sup> and TPC information (Section 4.1). We then perform a handshake between the  
<sup>1793</sup> beamline information and the TPC tracking to assure the selection of the correct  
<sup>1794</sup> TPC track (Section 4.2). Finally, we apply the “thin slice” method and measure the  
<sup>1795</sup> “raw” hadronic cross section (Section 4.3). A series of corrections are then evaluated  
<sup>1796</sup> to obtain the “true” cross section (Section 4.3.3).

<sup>1797</sup> At the end of this chapter, we show a sanity check of the methodology by applying  
<sup>1798</sup> the thin slice method employing only MC truth information and retrieving the Geant4  
<sup>1799</sup> tabulated cross section for pions and kaons (Section 4.4).

## 1800 4.1 Event Selection

1801 The measurement of the ( $\pi^-$ ,Ar) and ( $K^+$ ,Ar) total hadronic cross section in LArIAT  
1802 starts by selecting the pool of pion or kaon candidates and measuring their momen-  
1803 tum. This is done through the series of selections on beamline and TPC information  
1804 described in the next sections. The summary of the event selection in data is reported  
1805 in Table 4.1.

### 1806 4.1.1 Selection of Beamline Events

1807 As shown in equation 4.5, we leverage the beamline particle identification and mo-  
1808 mentum measurement before entering the TPC as an input to evaluate the kinetic  
1809 energy for the hadrons used in the cross sections measurements. Thus, we select the  
1810 LArIAT data to keep only events whose wire chamber and time of flight information  
1811 is registered (line 1 in Table 4.1). Additionally, we perform a check of the plausi-  
1812 bility of the trajectory inside the beamline detectors: given the position of the hits  
1813 in the four wire chambers, we make sure the particle's trajectory does not cross any  
1814 impenetrable material such as the collimator and the magnets steel (line 2 in Table  
1815 4.1).

	Run-II Neg Pol	Run-II Pos Pol
1. Events Reconstructed in Beamline	158396	260810
2. Events with Plausible Trajectory	147468	240954
3. Beamline $\pi^-/\mu^-/e^-$ Candidate	138481	N.A.
4. Beamline $K^+$ Candidate	N.A	2837
5. Events Surviving Pile Up Filter	108929	2389
6. Events with WC2TPC Match	41757	1081
7. Events Surviving Shower Filter	40841	N.A.
8. Available Events For Cross Section	40841	1081

Table 4.1: Number of data events for Run-II Negative and Positive polarity

1816 **4.1.2 Particle Identification in the Beamline**

1817 In data, the main tool to establish the identity of the hadron of interest is the LArIAT  
1818 tertiary beamline, in its function of mass spectrometer. We combine the measurement  
1819 of the time of flight,  $TOF$ , and the beamline momentum,  $p_{Beam}$ , to reconstruct the  
1820 invariant mass of the particles in the beamline,  $m_{Beam}$ , as follows

$$m_{Beam} = \frac{p_{Beam}}{c} \sqrt{\left(\frac{TOF * c}{l}\right)^2 - 1}, \quad (4.1)$$

1821 where  $c$  is the speed of light and  $l$  is the length of the particle's trajectory between  
1822 the time of flight paddles.

1823 Figure 4.1 shows the mass distribution for the Run II negative polarity runs on  
1824 the left and positive polarity runs on the right. We perform the classification of events  
1825 into the different samples as follows:

- 1826 •  $\pi/\mu/e$ : mass  $< 350 \text{ MeV}/c^2$   
1827 • kaon:  $350 \text{ MeV} < \text{mass} < 650 \text{ MeV}/c^2$   
1828 • proton:  $650 \text{ MeV} < \text{mass} < 3000 \text{ MeV}/c^2$ .

1829 Lines 3 and 4 in Table 4.1 show the number of negative  $\pi/\mu/e$  and positive  $K$   
1830 candidates which pass the mass selection for LArIAT Run-II data.

1831 **4.1.3 TPC Selection: Halo Mitigation**

1832 The secondary beam impinging on LArIAT secondary target produces a plethora of  
1833 particles which propagates downstream. The presence of upstream and downstream  
1834 collimators greatly abates the number of particles tracing down the LArIAT tertiary  
1835 beamline. However, it is possible that more than one particle sneaks into the LArTPC  
1836 during its readout time: the TPC readout is triggered by the particle firing the

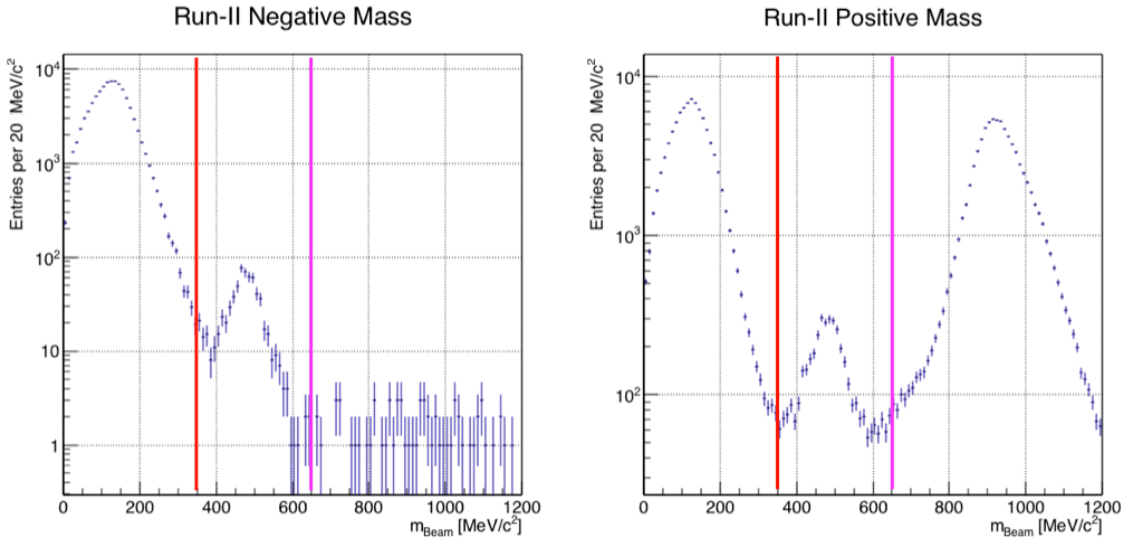


Figure 4.1: Distribution of the beamline mass as calculated according to equation 4.1 for the Run-II events reconstructed in the beamline, negative polarity runs on the left and positive polarity runs on the right. The classification of the events into  $\pi^\pm/\mu^\pm/e^\pm$ ,  $K^\pm$ , or (anti)proton is based on these distributions, whose selection cut are represented by the vertical colored lines.

1837 beamline detectors, but particles from the beam halo might be present in the TPC at  
1838 the same time. We call “pile up” the additional traces in the TPC. We adjusted the  
1839 primary beam intensity between LArIAT Run I and Run II to reduce the presence of  
1840 events with high pile up particles in the data sample. For the cross section analyses,  
1841 we remove events with more than 4 tracks in the first 14 cm upstream portion of the  
1842 TPC from the sample (line 5 in in Table 4.1).

1843 **4.1.4 TPC Selection: Shower Removal**

1844 In the case of the  $(\pi^-,\text{Ar})$  cross section, the resolution of beamline mass spectrometer  
1845 is not sufficient to select a beam of pure pions. In fact, muons and electrons survive  
1846 the selection on the beamline mass. It is important to notice that the composition of  
1847 the negative polarity beam is mostly pions, as will be discussed in section 5.2.1. Still,  
1848 we devise a selection on the TPC information to mitigate the presence of electrons

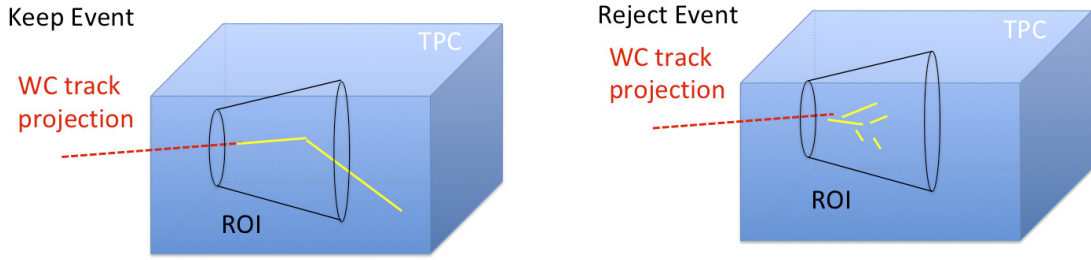


Figure 4.2: Visual rendering of the shower filter. The ROI is a cut cone, with a small radius of 4 cm, a big radius of 10 cm and an height of 42 cm (corresponding to 3 radiation lengths for electrons in Argon).

1849 in the sample used for the pion cross section. The selection relies on the different  
 1850 topologies of a pion and an electron event in the argon: while the former will trace  
 1851 a track inside the TPC active volume, the latter will tend to “shower”, i.e. interact  
 1852 with the medium, producing bremsstrahlung photons which pair convert into several  
 1853 short tracks. In order to remove the shower topology, we create a region of interest  
 1854 (ROI) around the TPC track corresponding to the beamline particle. We look for  
 1855 short tracks contained in the ROI, as depicted in figure 4.4: if more than 5 tracks  
 1856 shorter than 10 cm are in the ROI, we reject the event. Line 7 in Table 4.1 shows  
 1857 the number of events surviving this selection.

## 1858 4.2 Beamline and TPC Handshake: the Wire Cham- 1859 ber to TPC Match

1860 For each event passing the selection on its beamline information, we need to identify  
 1861 the track inside the TPC corresponding to the particle which triggered the beamline  
 1862 detectors, a procedure we refer to as “WC to TPC match” (WC2TPC for short).  
 1863 In general, the TPC tracking algorithm will reconstruct more than one track in the  
 1864 event, partially due to the fact that hadrons interact in the chamber and partially  
 1865 because of pile up particles during the triggered TPC readout time, as shown in

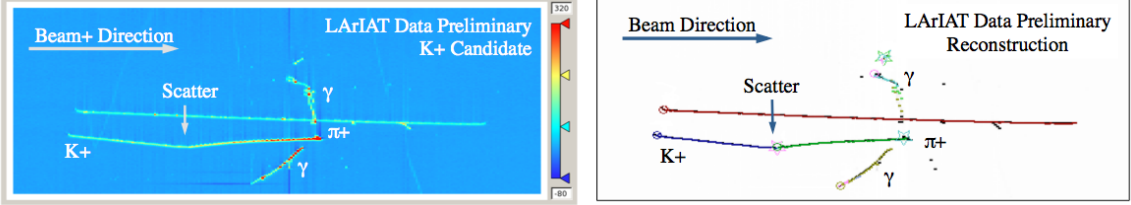


Figure 4.3: Kaon candidate event: on the right, event display showing raw quantities; on the left, event display showing reconstructed tracks. In the reconstructed event display, different colors represent different track objects. A kink is visible in the kaon ionization, signature of a hadronic interaction: the tracking correctly stops at the kink position and two tracks are formed. An additional pile-up track is so present in the event (top track in red).

1866 figure 4.3.

1867 We attempt to uniquely match one wire chamber track to one and only one recon-  
 1868 structed TPC track. In order to determine if a match is present, we apply a geomet-  
 1869 rical selection on the relative the position of the wire chamber and TPC tracks. We  
 1870 start by considering only TPC tracks whose first point is in the first 2 cm upstream  
 1871 portion of the TPC for the match. We project the wire chamber track to the TPC  
 1872 front face where we define the coordinates of the projected point as  $x_{FF}$  and  $y_{FF}$ . For  
 1873 each considered TPC track, we define  $\Delta X$  as the difference between the  $x$  position of  
 1874 the most upstream point of the TPC track and  $x_{FF}$ .  $\Delta Y$  is defined analogously. We  
 1875 define the radius difference,  $\Delta R$ , as  $\Delta R = \sqrt{\Delta X^2 + \Delta Y^2}$ . We define as  $\alpha$  the angle  
 1876 between the incident WC track and the TPC track in the plane that contains them.  
 1877 If  $\Delta R < 4$  cm,  $\alpha < 8^\circ$ , a match between WC-track and TPC track is found. We de-  
 1878 scribe how we determine the value for the radius and angular selection in Section ??.  
 1879 We discard events with multiple WC2TPC matches. We use only those TPC tracks  
 1880 that are matched to WC tracks in the cross section calculation. Line 6 in Table 4.1  
 1881 shows the number of events where a unique WC2TPC match was found.  
 1882 In MC, we mimic the matching between the WC and the TPC track by construct-  
 1883 ing a fake WC track using truth information at wire chamber four. We then apply  
 1884 the same WC to TPC matching algorithm as in data.

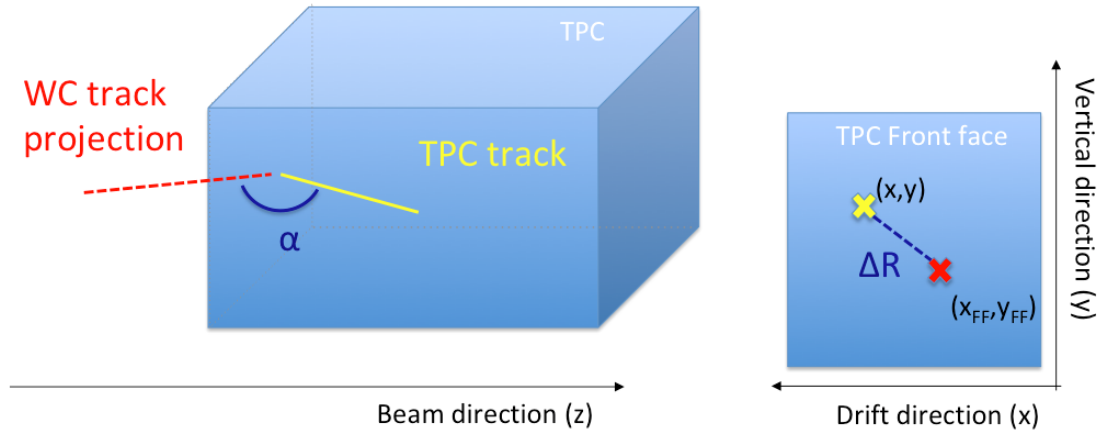


Figure 4.4: Visual rendering of the wire chamber to TPC match.

## 1885 4.3 The Thin Slice Method

1886 Once we have selected the pool of hadron candidates and we have identified the TPC  
1887 track corresponding to the beamline event, we apply the thin slice method to measure  
1888 the cross section, as the following sections describe.

### 1889 4.3.1 Cross Sections on Thin Target

1890 Cross section measurements on a thin target have been the bread and butter of  
1891 nuclear and particle experimentalists since the Geiger-Marsden experiments [67]. At  
1892 their core, this type of experiments consists in shooting a beam of particles with a  
1893 known flux on a thin slab of material and recording the outgoing flux.

1894 In general even in the case of thin target, the target is not a single particle,  
1895 but rather a slab of material containing many diffusion centers. The so-called “thin  
1896 target” approximation assumes that the target centers are uniformly distributed in  
1897 the material and that the target is thin compared to the projectile interaction length,  
1898 so that no center of interaction sits in front of another. In this approximation, the  
1899 ratio between the number of particles interacting in the target  $N_{\text{Int}}$  and the number of  
1900 incident particles  $N_{\text{Inc}}$  on the target determines the interaction probability  $P_{\text{Interacting}}$ ,

1901 which is the complementary to one of the survival probability  $P_{Survival}$ . Equation 4.2

$$P_{Survival} = 1 - P_{Interacting} = 1 - \frac{N_{Int}}{N_{Inc}} = e^{-\sigma_{TOT} n \delta X} \quad (4.2)$$

1902 describes the probability for a particle to survive the thin target. This formula relates  
1903 the interaction probability to the total hadronic cross section ( $\sigma_{TOT}$ ), the density of  
1904 the target centers ( $n$ )<sup>1</sup> and the thickness of the target along the incident hadron  
1905 direction ( $\delta X$ ). If the target is thin compared to the interaction length of the process  
1906 considered, we can Taylor expand the exponential function in equation 4.2 and find  
1907 a simple proportionality relationship between the cross section and the number of  
1908 incident and interacting particles, as shown in equation 4.3:

$$1 - \frac{N_{Int}}{N_{Inc}} = 1 - \sigma_{TOT} n \delta X + O(\delta X^2). \quad (4.3)$$

1909 Solving for the cross section, we find:

$$\sigma_{TOT} = \frac{1}{n \delta X} \frac{N_{Int}}{N_{Inc}}. \quad (4.4)$$

### 1910 4.3.2 Not-so-Thin Target: Slicing the Argon

1911 The interaction length of pions and kaons in argon is expected to be of the order  
1912 of 50 cm for pions and 100 cm for kaons. Thus, the LArIAT TPC, with its 90 cm  
1913 of length, is not a thin target. However, the fine-grained tracking of the LArIAT  
1914 LArTPC allows us to treat the argon volume as a sequence of many adjacent thin  
1915 targets.

1916 As described in Chapter 3, LArIAT wire planes consist of 240 wires each. The  
1917 wires are oriented at +/- 60° from the vertical direction at 4 mm spacing, while the

---

1. The scattering center density in the target,  $n$ , relates to the argon density  $\rho$ , the Avogadro number  $N_A$  and the argon molar mass  $m_A$  as  $n = \frac{\rho N_A}{m_A}$ .

1918 beam direction is oriented 3 degrees off the  $z$  axis in the  $XZ$  plane. The wires collect  
 1919 signals proportional to the energy loss of the hadron along its path in a  $\delta X = 4$   
 1920 mm/(sin(60°)cos(3°))  $\approx 4.7$  mm slab of liquid argon. Thus, one can think to slice  
 1921 the TPC into many thin targets of  $\delta X = 4.7$  mm thickness along the direction of the  
 1922 incident particle, making a measurement at each wire along the path.

1923 Considering each slice  $j$  a “thin target”, we can apply the cross section calculation  
 1924 from Equation 4.4 iteratively, evaluating the kinetic energy of the hadron as it enters  
 1925 each slice,  $E_j^{kin}$ . For each WC2TPC matched particle, the energy of the hadron  
 1926 entering the TPC is known thanks to the momentum and mass determination by the  
 1927 tertiary beamline,

$$E_{FrontFace}^{kin} = \sqrt{p_{Beam}^2 - m_{Beam}^2} - m_{Beam} - E_{loss}, \quad (4.5)$$

1928 where  $E_{loss}$  is a correction for the energy loss in the uninstrumented material between  
 1929 the beamline and the TPC front face. The energy of the hadron at each slab is  
 1930 determined by subtracting the energy released by the particle in the previous slabs.  
 1931 For example, at the  $j^{th}$  point of a track, the kinetic energy will be

$$E_j^{kin} = E_{FrontFace}^{kin} - \sum_{i < j} E_{Dep,i}, \quad (4.6)$$

1932 where  $E_{Dep,i}$  is the energy deposited at each argon slice before the  $j^{th}$  point as mea-  
 1933 sured by the calorimetry associated with the tracking.

1934 If the particle enters a slice, it contributes to  $N_{Inc}(E^{kin})$  in the energy bin corre-  
 1935 sponding to its kinetic energy in that slice. If it interacts in the slice, it also contributes  
 1936 to  $N_{Int}(E^{kin})$  in the appropriate energy bin. The cross section as a function of kinetic  
 1937 energy,  $\sigma_{TOT}(E^{kin})$  will then be proportional to the ratio  $\frac{N_{Int}(E^{kin})}{N_{Inc}(E^{kin})}$ .

1938 Our goal is to measure the total interaction cross section, independently from the  
 1939 topology of the interaction. Thus, we determine that a hadron interacted simply by

	min	max
X	1 cm	46 cm
Y	-15 cm	15 cm
Z	0 cm	86 cm

Table 4.2: Fiducial volume boundaries used to determine cross section interaction point.

requiring that the last point of the WC2TPC matched track lies inside the fiducial volume, whose boundaries are defined in Table 4.2. If the TPC track stops within the fiducial volume, its last point will be the interaction point; if the track crosses the boundaries of the fiducial volume, the track will be considered “through going” and no interaction point will be found. The only points of the hadronic candidate track considered to fill the  $N_{\text{Inc}}$ ) and  $N_{\text{Inc}}$  plots are the ones contained in the fiducial volume.

### 4.3.3 Corrections to the Raw Cross Section

Equation 4.4 is a prescription for measuring the cross section in case of a pure beam of the hadron of interest and 100% efficiency in the determination of the interaction point. For example, if LArIAT had a beam of pure pions and were 100% efficient in determining the interaction point within the TPC, the pion cross section in each energy bin would be given by

$$\sigma_{TOT}^{\pi^-}(E_i) = \frac{1}{n\delta X} \frac{N_{\text{Int}}^{\pi^-}(E_i)}{N_{\text{Inc}}^{\pi^-}(E_i)}. \quad (4.7)$$

Unfortunately, this is not the case. In fact, the selection used to isolate pions in the LArIAT beam allows for the presence of some muons and electrons as background, while the kaon selection allows for a small percentage of protons (see Section 5.2.1). Also, the LArIAT TPC is not 100% efficient in determining the interaction point. Therefore we need to apply two corrections evaluated on the MC in order to

1958 extract the true cross section from LArIAT data: the background subtraction and  
 1959 the efficiency correction. Still using the pion case as example, we estimate the pion  
 1960 cross section in each energy bin changing Equation 4.7 into

$$\sigma_{TOT}^{\pi^-}(E_i) = \frac{1}{n\delta X} \frac{N_{Int}^{\pi^-}(E_i)}{N_{Inc}^{\pi^-}(E_i)} = \frac{1}{n\delta X} \frac{\epsilon^{Inc}(E_i)[N_{Int}^{TOT}(E_i) - B_{Int}(E_i)]}{\epsilon^{Int}(E_i)[N_{Inc}^{TOT}(E_i) - B_{Inc}(E_i)]}, \quad (4.8)$$

1961 where  $N_{Int}^{TOT}(E_i)$  and  $N_{Inc}^{TOT}(E_i)$  is the measured content of the interacting and  
 1962 incident histograms for events that pass the event selection,  $B_{Int}(E_i)$  and  $B_{Inc}(E_i)$   
 1963 represent the contributions from the background to the interacting and incident his-  
 1964 tograms respectively, and  $\epsilon^{Int}(E_i)$  and  $\epsilon^{Inc}(E_i)$  are the efficiency corrections for said  
 1965 histograms.

1966 As we will show in section 5.3, the background subtraction for the interacting  
 1967 and incident histograms can be translated into a corresponding relative pion content  
 1968  $C_{Interacting}^{\pi MC}(E_i)$  and  $C_{Incident}^{\pi MC}(E_i)$  and the cross section re-written as follows

$$\sigma_{TOT}^{\pi^-}(E_i) = \frac{1}{n\delta X} \frac{\epsilon^{Inc}(E_i)}{\epsilon^{Int}(E_i)} \frac{C_{Int}^{\pi MC}(E_i)}{C_{Inc}^{\pi MC}(E_i)} \frac{N_{Int}^{TOT}(E_i)}{N_{Inc}^{TOT}(E_i)}. \quad (4.9)$$

## 1969 4.4 Procedure testing with truth quantities

1970 The  $(\pi^-, \text{Ar})$  and  $(K^+, \text{Ar})$  total hadronic cross section implemented in Geant4 can be  
 1971 used as a tool to validate the measurement methodology. We describe here a closure  
 1972 test done on Monte Carlo to prove that the methodology of slicing the TPC retrieves  
 1973 the underlying cross section distribution implemented in Geant4 within the statistical  
 1974 uncertainty.

1975 For pions and kaons in the considered energy range, the Geant4 inelastic model  
 1976 adopted is “BertiniCascade”; the pion elastic cross sections are tabulated from on  
 1977 Chips, while the kaon elastic cross sections are tabulated on Gheisha and Chips.

1978 For the validation test, we fire a sample of pions and a sample of kaons inside the

1979 LArIAT TPC active volume using the Data Driven Monte Carlo (see section 5.2.2).  
1980 We apply the thin-sliced method using only true quantities to calculate the hadron  
1981 kinetic energy at each slab in order to decouple reconstruction effects from possible  
1982 issues with the methodology. For each slab of 4.7 mm length along the path of the  
1983 hadron, we integrate the true energy deposition as given by the Geant4 transportation  
1984 model. Then, we recursively subtracted it from the hadron kinetic energy at the TPC  
1985 front face to evaluate the kinetic energy at each slab until the true interaction point is  
1986 reached. Since the MC is a pure beam of the hadron of interest and truth information  
1987 is used to retrieve the interaction point, no correction is applied. Doing so, we obtain  
1988 the true interacting and incident distributions for the considered hadron, from which  
1989 we derive the true MC cross section as a function of the hadron true kinetic energy.

1990 Figure 4.5 shows the total hadronic cross section for argon implemented in Geant4  
1991 10.03.p1 (solid lines) overlaid with the true MC cross section as obtained with the  
1992 sliced TPC method (markers) for pions on the left and kaons on the right; the total  
1993 cross section is shown in green, the elastic cross section in blue and the inelastic  
1994 cross section in red. The nice agreement with the Geant4 distribution and the cross  
1995 section obtained with the sliced TPC method gives us confidence in the validity of  
1996 the methodology.

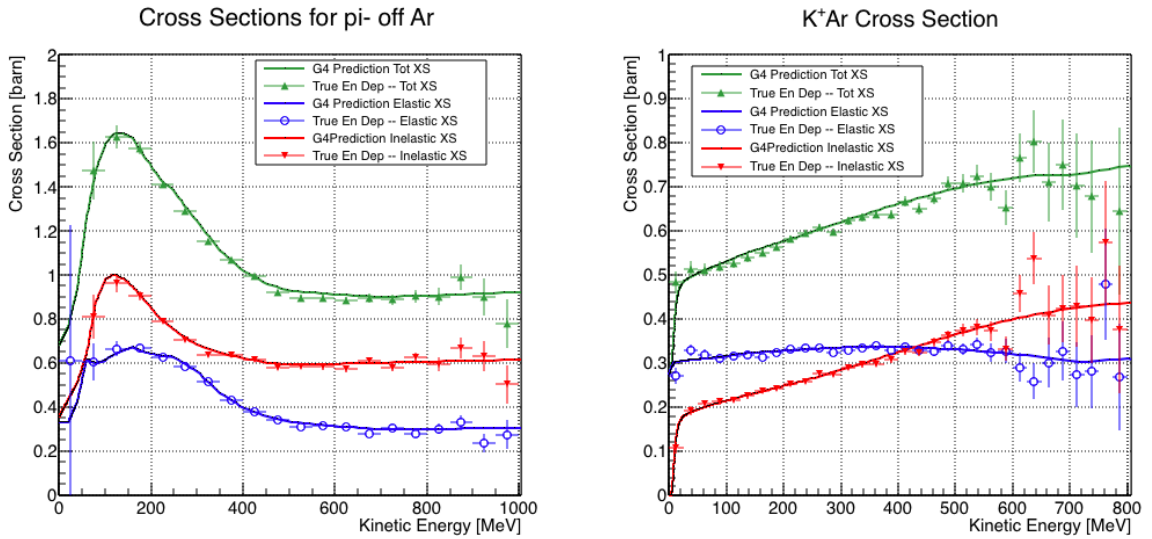


Figure 4.5: Hadronic cross sections for ( $\pi^-$ ,Ar) on the left and ( $K^+$ ,Ar) on the right as implemented in Geant4 10.03.p1 (solid lines) overlaid the true MC cross section as obtained with the sliced TPC method (markers). The total cross section is shown in green, the elastic cross section in blue and the inelastic cross section in red.

1997 **Chapter 5**

1998 **Data and MC preparation for the**  
1999 **Cross Section Measurements**

2000 “*Il dolce non lo mangi mai, ma qualche volta ti rifai.*  
2001 *Abbracciami”*  
2002 – Pietro Ciampi, 1971 –

2003 This chapter describes the work done on the data and Monte Carlo samples in  
2004 preparation for the cross section analyses. This entails the choice of the datasets  
2005 and the production of the information needed to construct the Monte Carlo Simula-  
2006 tion (Section 5.1), the construction and use of said Monte Carlo simulation (section  
2007 5.2), the study of backgrounds for the pion cross section (Section 5.3), the study of  
2008 the energy loss between WC4 and TPC (Section 5.4), the study of the tracking in the  
2009 TPC (Section 5.5), and study of the calorimetry response (Section 5.6).

2010 **5.1 Cross Section Analyses Data Sets**

2011 We choose LArIAT Run-II as the data period for the ( $\pi^-$ ,Ar) and ( $K^+$ ,Ar) total  
2012 hadronic cross section analyses. Data taking for the this period started on 03/15/2016

2013 and ended on 07/31/2016. Since we are interested in beamline and TPC information,  
2014 we ask basic requirements on the operational status of the time of flight, wire chambers  
2015 and TPC to form the good run list for this period, which we informally call “lovely  
2016 runs”.

2017 The subset of lovely runs chosen for the  $(\pi^-, \text{Ar})$  total hadronic cross section  
2018 analysis includes only the -60A and -100A magnet configurations in negative polarity,  
2019 even if LArIAT explored several other beamline configurations during Run-II. The -  
2020 60A and -100A combined data set accounts for approximately 90% of the total Run-II  
2021 negative polarity runs. The choice of the main two beamline settings limits the need  
2022 for the production of many different MC sets and related corrections, still maintaining  
2023 a high number of events.

2024 Similarly, the subset of lovely runs chosen for the  $(K^+, \text{Ar})$  total hadronic cross  
2025 section analysis includes only the +60A and +100A magnet configurations in positive  
2026 polarity. It should be noted that kaons are extremely rare in the +60A sample, thus  
2027 the data sample for the  $(K^+, \text{Ar})$  cross section after the mass selection is about 90%  
2028 +100A runs, as shown in Table 5.1.

2029 For the first measurements in LArIAT that uses both beamline and TPC infor-  
2030 mation, we choose strict requirements on the reconstruction of the WC tracks, the  
2031 so-called “Picky Track” sample (see Section 3.2.2). This choice presents two ad-  
2032 vantages: the uncertainty on the momentum reconstruction for the “Picky Tracks”  
2033 sample is smaller compared to the “High Yield” sample, and the comparison with  
2034 the beamline MC results is straightforward. A possible future update and cross check  
2035 of these analysis would be the use of the High Yield sample, where the statistics is  
2036 about three times higher.

2037 The breakdown of beamline events as a function of the magnets settings is shown  
2038 in Table 5.1. The choice of the data sets determines the production of beamline MC  
2039 and serves as basis for the production of Data Driven MC, as shown in the next

2040 sections.

## 2041 5.2 Construction of a Monte Carlo Simulation for 2042 LArIAT

2043 For the simulation of LArIAT events and for the simulation of the datasets' particle  
2044 make up, we use a combination of two MC generators: the G4Beamline Monte Carlo  
2045 and the Data Driven single particle Monte Carlo (DDMC). We use the G4Beamline  
2046 MC to simulate the particle transportation in the beamline and calculate the particle  
2047 composition of the beam just after the fourth Wire Chamber (WC4). In order to  
2048 simulate the beamline particles after WC4 and in the TPC, we use the DDMC.

### 2049 5.2.1 G4Beamline

2050 G4Beamline simulates the beam collision with the LArIAT secondary target, the  
2051 energy deposited by the particles in the LArIAT beamline detectors, and the action  
2052 of the LArIAT magnets, effectively accounting for particle transportation through the  
2053 beamline from the LArIAT target until “Big Disk”, a fictional, void detector located  
2054 just before the LArIAT cryostat. At the moment of this writing, G4Beamline does  
2055 not simulated the responses of the beamline detectors. It is possible to interrogate the  
2056 truth level information of the simulated particles in several points of the geometry.  
2057 In order to ease the handshake between G4Beamline and the DDMC, we ask for  
2058 the beam composition just after WC4. Since LArIAT data are taken under different

	I = 60 A	I = 100 A	Total
Data Events after $\pi/\mu/e$ Mass Selection	67068	71413	138481
Data Events after $K$ Mass Selection	274	2563	2837

Table 5.1: Number of data events which fit the  $\pi/\mu/e$  or  $K$  mass hypothesis as a function of magnet settings.

beam conditions, we need to simulate separately the beam composition according to the magnets' settings and the secondary beam intensity with G4Beamline. For the pion cross section analysis the relevant beam conditions are secondary beam energy of 64 GeV, negative polarity magnet with current of 100 A and 60 A. For the kaon cross section analysis the relevant beam conditions is a secondary beam energy of 64 GeV, positive polarity magnet with current of 100 A.

## Beam Composition for Negative Pion Cross Section

Even if pions are by far the biggest beam component in negative polarity runs, the LArIAT tertiary beam is not a pure pion beam. While useful to discriminate between pions, kaons, and protons, the beamline detectors are not sensitive enough to discriminate among the lighter particles in the beam: electrons, muons and pions fall under the same mass hypothesis. Thus, we need to assess the contamination from beamline particles other than pions in the event selections used for the pion cross section analysis and correct for its effects. The first step of this process is assessing the percentage of electrons and muons in the  $\pi/\mu/e$  beamline candidates via the G4Beamline MC. Since the beamline composition is a function of the magnet settings, we simulate separately events for magnet current of -60A and -100A. Figure 5.1 shows the momentum predictions from G4Beamline overlaid with data for the 60A runs (left) and for the 100A runs (right). The predictions for electrons, muons and pions have been staggered and their sum is area normalized to data. Albeit not perfect, these plots show a reasonable agreement between the momentum shapes in data and MC. We attribute the difference in shape to a two approximations performed in the MC. Firstly, G4Beamline lacks the simulation of the WC efficiency which is momentum dependent and leads to enhance the number events in the center of the momentum distribution. Secondly, G4Beamline stop tracking pions and their products if they decay in after WC1; in data, pion decays in flight can still create a

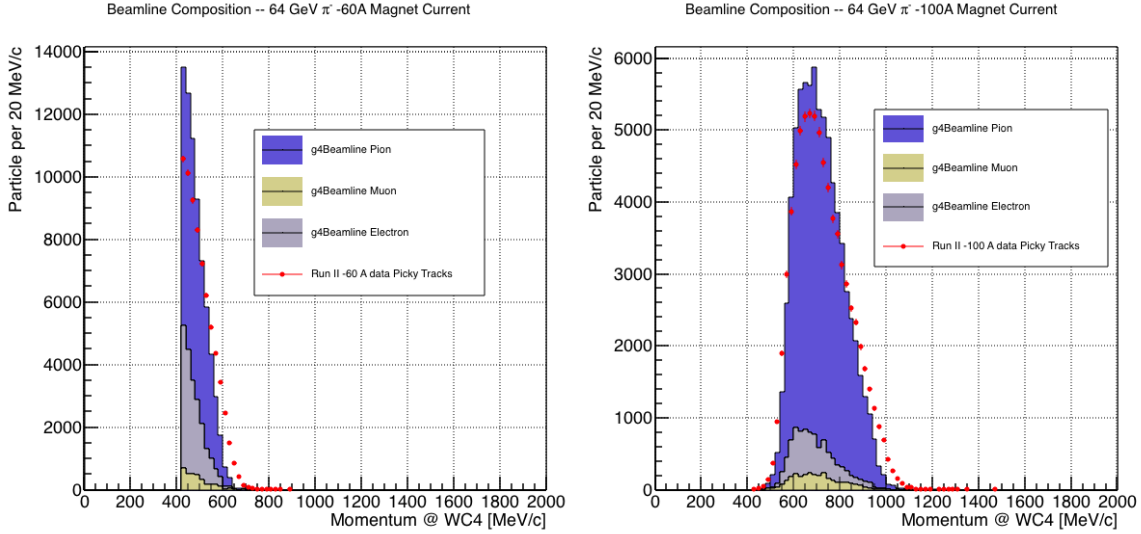


Figure 5.1: Beam composition for the -60A runs (left) and -100A runs (right). The solid blue plot represents the simulated pion content, the yellow plot represents the simulated muon content and the grey plot represents the simulated electron content. The plots are area normalized to the number of data events, shown in red.

	I = -60 A	I = -100 A
G4Pions	68.8 %	87.4 %
G4Muons	4.6 %	3.7 %
G4Electrons	26.6 %	8.9 %

Table 5.2: Simulated beamline composition per magnet settings

2085 trigger if the produced muon travels thought the beamline detectors. In the pion cross  
 2086 section analysis, these differences between data and G4Beamline are accounted for as  
 2087 a systematic uncertainty related to the beam composition (see Section 6.2.1).

2088 Table 5.2 shows the beam composition per magnet setting after the mass selection  
 2089 according to the G4Beamline simulation.

2090 The estimated beam composition is used as a basis to estimate the background  
 2091 contamination in the  $(\pi^-, \text{Ar})$  cross section measurement, whose full treatment is  
 2092 described in section 5.3.

2093 **Beam Composition for Positive Kaon Cross Section**

2094 In the positive polarity runs, the tertiary beam composition is mainly pions and  
2095 protons. The left side of Figure 5.2 shows the predictions for the momentum spectra  
2096 for the 100A positive runs according to G4Beamline (solid colors) overlaid with data  
2097 (black points). Since the LArIAT beamline detectors can discriminate between kaons  
2098 and other particles, we do not rely on the G4Beamline simulation to estimate the  
2099 beamline contamination in the pool of kaon candidates (as in the case of the pion  
2100 cross section), but rather we use a data driven approach. The basic idea of this data  
2101 driven approach is to estimate the bleed over from high and low mass peaks under  
2102 the kaon peak by fitting the tails of the  $\pi/\mu/e$  and proton mass distributions, as  
2103 shown in Figure 5.2 right side. Since the shape of the tails is unknown, the estimate  
2104 is done multiple times varying the range and shape for reasonable functions. For  
2105 example, to estimate the proton content under the kaon peak, we start by fitting the  
2106 left tail of the proton mass distribution with a gaussian function between  $650 \text{ MeV}/c^2$   
2107 and  $750 \text{ MeV}/c^2$ . We extend the fit function under the kaon peak and integrate the  
2108 extended fit function between  $350-650 \text{ MeV}/c^2$ . We integrate the mass histogram  
2109 in the same range and calculate the proton contamination as the ratio between the  
2110 two integrals. We repeat this procedure for several fit shapes (gaussian, linear and  
2111 exponential functions) and tail ranges. Finally, we calculate the contamination as  
2112 the weighted average of single estimates, where the weights are calculated to be the  
2113  $1./|1 - \chi^2|$  of the tail fits. The procedure is repeated for lighter particles mass peak  
2114 independently. With 12 iterations of this method we find a proton contamination of  
2115  $5.0 \pm 2.0 \%$  and a contamination from the lighter particles of  $0.2 \pm 0.5 \%$ . The  
2116 estimate of the proton background is currently not used in the kaon cross section  
2117 analysis, but it is a fundamental step to retrieve the true kaon cross section which  
2118 will be implemented in the further development of the analysis.

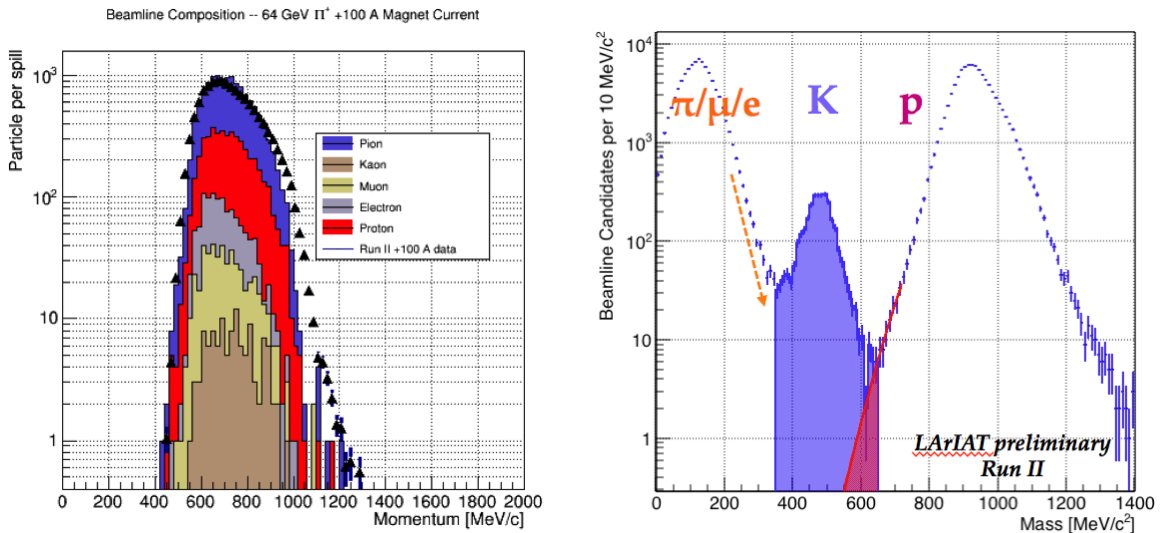


Figure 5.2: *Left:* Beam composition for the +100A runs after WC4 (no mass selection applied). The solid colors represent the contributions from the G4Beamline simulated particles: blue plot represents the simulated pion content, the yellow plot represents the simulated muon content and the grey plot represents the simulated positron content, the red the proton content and the mustard the kaon content. The plots are area normalized to the number of data events, shown in black. *Right:* Mass distribution for the Run-II positive runs, where the area under the kaon mass peak is highlighted in purple. The area under the extension of a possible fit for the proton tail is highlighted in red.

2119 **5.2.2 Data Driven MC**

2120 The Data Driven single particle Monte Carlo (DDMC) is a single particle gun which  
2121 simulates the particle transportation from WC4 into the TPC leveraging on the beam-  
2122 line data information. The DDMC uses the data momentum and position at WC4  
2123 to derive the event generation: a general sketch of the DDMC workflow is shown in  
2124 Figure 5.3.

2125 When producing a DDMC sample, beamline data from a particular running pe-  
2126 riod and/or running condition are selected first. For example, data for the negative  
2127 60A runs and for the negative 100A runs inform the event generation stage of two  
2128 different DDMC samples. Figure 5.4 schematically shows the data quantities of in-  
2129 terest leveraged from data: the momentum ( $P_x, P_y, P_z$ ) and position ( $X, Y$ ) at WC4.  
2130 For each data event, we obtain the particle position ( $X, Y$ ) at WC4 directly from the  
2131 data measurement; we calculate the components of the momentum using the beam-  
2132 line measurement of the momentum magnitude in conjunction with the hits on WC3  
2133 and WC4 to determine the direction of the momentum vector, as described in section  
2134 3.2.2. The momentum and position of the selected data form a 5-dimensional tuple,  
2135 which we sample thousands of times through a 5-dimensional hit-or-miss sampling  
2136 procedure to generate the MC events. This sampling generates MC events with the  
2137 same momentum and position distributions as data, with the additional benefit of  
2138 accounting for the correlations between the  $P_x, P_y, P_z, X, Y$  variables. As an example,  
2139 the results of the DDMC generation compared to data for the kaon +100A sample  
2140 are shown in figure 5.5 for the  $P_z, X$  and  $Y$  distributions; as expected, MC and data  
2141 agree within the statistical uncertainty by construction. A LArSoft simulation mod-  
2142 ule then launches single particle MC from  $z = -100$  cm (the location of the WC4)  
2143 using the generated events. The particles are free to decay and interact in their path  
2144 from WC4 to the TPC according to the Geant4 simulation.

2145 Using the DDMC technique ensures that the MC and data particles have very

2146 similar momentum, position and angular distributions at WC4 and allows us to use  
 2147 the MC sample in several occasions: to estimate the background contamination to  
 2148 the pion cross section (see Section 5.3), to calibrate the energy loss upstream of the  
 2149 TPC (see Section 5.4), or to study the tracking and the calorimetric performance  
 2150 (sections 5.5 and 5.6). A small caveat is in order here: the DDMC is a single particle  
 2151 Monte Carlo, which means that the beam pile-up is not simulated.

2152 We generate six samples for the pion cross section measurement: three samples  
 2153 of  $\sim 330000$  pions, muons and electrons to simulate the negative 60A runs, and three  
 2154 samples of  $\sim 340000$  pions, muons and electrons for the negative 100A runs. We  
 2155 generate a sample of 195000 kaons for the kaon cross section analysis.

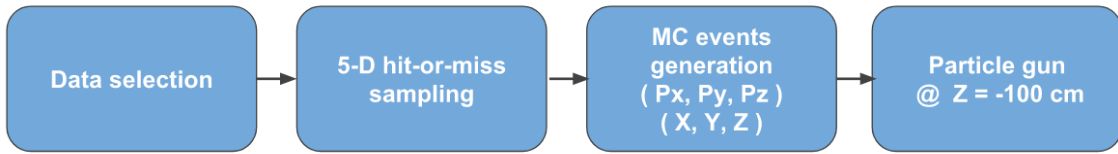


Figure 5.3: Workflow for Data Driven single particle Monte Carlo production.

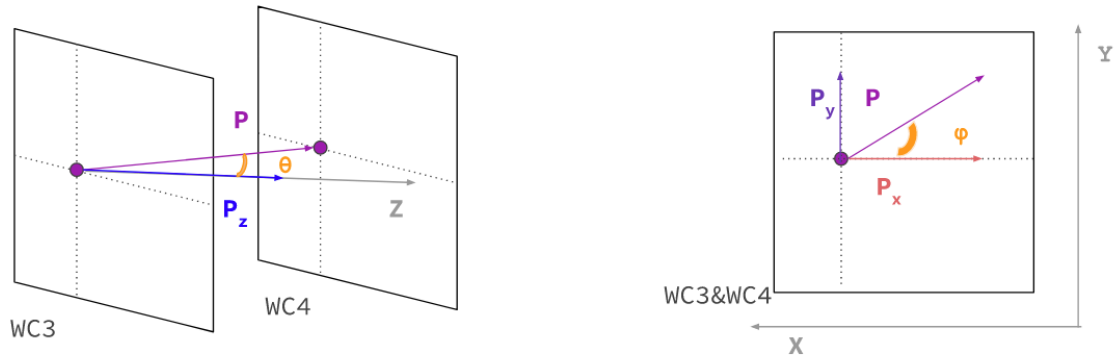


Figure 5.4: Scheme of the quantities of interest for the DDMC event generation:  $P_x, P_y, P_z, X, Y$  at WC4.

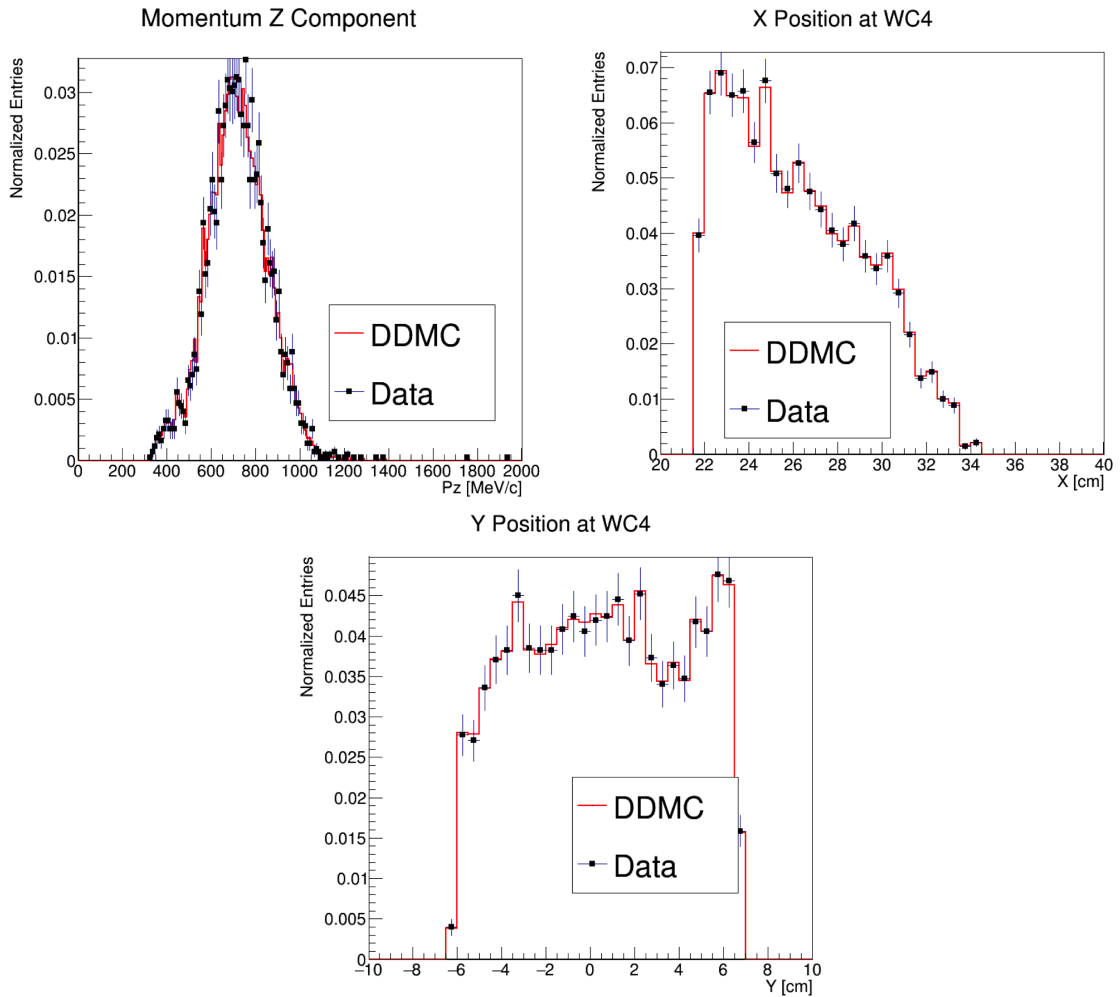


Figure 5.5: Comparison between generated quantities and data distributions for the 100A kaon sample: Z component of the momentum at WC4 (top left), X position at Wire Chamber 4 (top right), Y position at Wire Chamber 4 (bottom).

2156 **5.3 Estimate of Backgrounds in the Pion Cross  
2157      Section**

2158 We use the beamline simulation and the DDMC simulation to estimate the back-  
2159 ground in the total hadronic pion cross section. Two categories of background exists  
2160 for the negative pion cross section measurement: the one related to the pion interac-  
2161 tion in the chamber, discussed in Section 5.3.1 and the one related to the beamline  
2162 contamination, discussed in Section 5.3.2.

2163 **5.3.1 Background from Pion Capture and Decay**

2164 Our goal is to measure the total hadronic cross section for negative pions in argon.  
2165 Since pion capture can be classified as an electromagnetic process and pion decay is a  
2166 weak process, capture and decay represent unwanted interactions. We present here a  
2167 study of capture and decay in Monte Carlo and the solution we adopted to mitigate  
2168 their occurrence in the data sample.

2169 For this MC study, we use a sample of MC pions generated according to the  
2170 –60A beam profile with the DDMC (see Section 5.2.2). It is important to notice  
2171 that capture occurs predominantly at rest, while decay may occur both in flight and  
2172 at rest. Thus, we can highly mitigate capture and decay at rest by removing pions  
2173 which would release all their energy in the TPC and stop. This translates into a  
2174 momentum selection, where we keep only events whose WC momentum is above a  
2175 certain threshold. Figure 5.6 shows the true momentum distribution for the primary  
2176 pions<sup>1</sup> that arrive to the TPC (pink), that capture (green) or decay (blue) inside the  
2177 TPC, on a linear scale (left) and on a log scale (right) vertical axis.

---

1. We use here the Geant4 denomination “primary” to indicate that the pion considered does not undergo interactions modifying its energy before getting to the TPC. In fact, not every pion shot from wire chamber four will arrive to the TPC as primary, some will decay or interact before the TPC.

2178 In order to choose the selection value for the wire chamber momentum, it is  
2179 beneficial to estimate the ratio of events which capture or decay that survive the  
2180 selection in MC as a function of the momentum threshold, and compare it with the  
2181 survival ratio for all the 60A events. This is done in figure 5.7. We define the survival  
2182 ratio simply as the number of events surviving the true momentum selection divided  
2183 by the number of events of that category. We calculate the survival ratio separately  
2184 for the three event categories explained above: total (pink), capture (green) and decay  
2185 (blue). Selecting pions with momentum greater than 420 MeV/c reduces the capture  
2186 events by 99% while maintaining about 80% of the 60A data sample and almost  
2187 the entire 100A sample. Figure 5.8 shows the ratio of events which end their life in  
2188 capture (green) or decay (blue) over the total number of events as a as a function of  
2189 the true momentum at wire chamber four. This ratio is slightly dependent on the  
2190 inelastic cross section implemented in Geant4, as we are able to register a pion capture  
2191 (or decay) only if it did not interact inelastically in the TPC. We choose a momentum  
2192 threshold of 420 MeV/c because the percentage of capture events drops below 1% and  
2193 the percentage of decays is never above 2% for momenta greater than 420 MeV/c.  
2194 After the momentum selection, we evaluate the contribution of capture and decay to  
2195 be a negligibly small background to the cross section measurement compared to the  
2196 background related to the beamline which we will address in the next section.

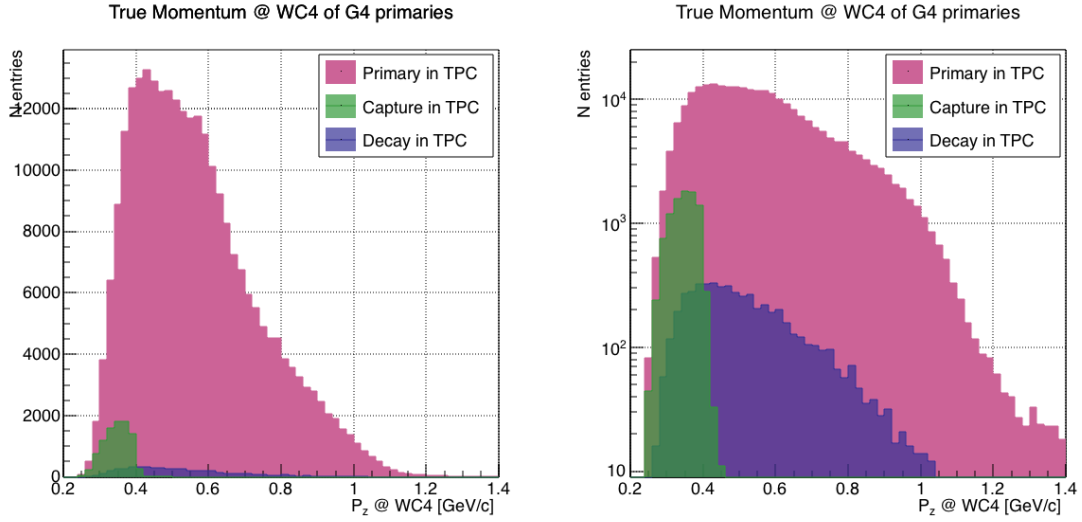


Figure 5.6: True momentum distribution at wire chamber 4 for every simulated pion arriving in the TPC (pink), ending its life in capture (green) or in decay (blue) in the TPC, linear vertical axis on the left, logarithmic on the right.

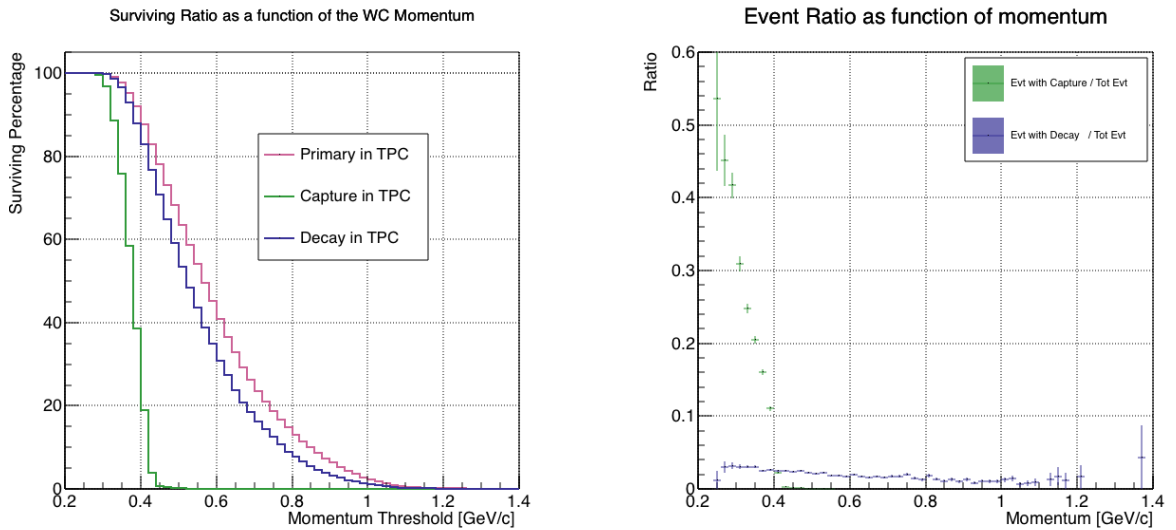


Figure 5.7: Survival ratio as a function of selection threshold on true momentum at wire chamber four for every simulated pion arriving in the TPC (pink), capture (green) or in decay (blue).

Figure 5.8: Ratio between the capture (green) and decay (blue) events over the total number of events as a function of the true momentum at wire chamber four.

2197    **5.3.2 Contributions from the Beamline Background**

2198    We define beamline background every TPC track matched to the WC track which is  
2199    not a primary pion. Potentially, there are 4 different types of beamline background:

2200            1) electrons,

2201            2) muons,

2202            3) secondaries from pion events,

2203            4) matched pile up events.

2204        The first step to quantify the effect of the beamline background on the pion cross  
2205    section is to estimate what percentage of events used in the cross section calculation  
2206    is not a primary pion. We start by noting that the last type of background, the  
2207    “matched pile up” events, is a negligible fraction, because of the definition of the  
2208    WC2TPC match: we deem the probability of a single match with a halo particle in  
2209    the absence of a beamline particle<sup>2</sup> negligibly small. As shown in Section 5.2.1, we  
2210    use G4Beamline to estimate the percentage of pions, muons and electrons at WC4,  
2211    obtaining the composition shown in Table 5.2. The next step is to simulate those  
2212    pions, muons and electrons from WC4 to the TPC with the DDMC and evaluate their  
2213    contribution to the cross section. To do so, we start by simulating the same number  
2214    of electrons, muons and pions with the DDMC and we apply the same selection chain  
2215    (i.e. track multiplicity rejection, WC2TPC acceptance and shower rejection) on the  
2216    three samples. The number of events per particle species surviving this selection is  
2217    shown on table 5.3. In order to reproduce the closest make up of the beam to data,  
2218    we weight each event of a given particle species according to the estimated beam  
2219    composition. In case of 60A runs, for example, the weights are 0.688 for pions, 0.046  
2220    for muons and 0.266 for electrons.

---

2. Events with multiple WC2TPC matches are always rejected.

	Magnet Current -60A			Magnet Current -100 A		
	MC $\pi^-$	MC $\mu^-$	MC $e^-$	MC $\pi^-$	MC $\mu^-$	MC $e^-$
Total Initial events	334500	334500	334500	344500	344500	344500
After Multiplicity Rejection	330668	333420	198065	326576	344208	201380
After WC2TPC Selection	218239	296333	91139	230418	300228	98834
Evts After Shower Rejection	208063	288914	20293	219882	293585	17780
Selection Survival Rate	62.3%	86.6%	6.1%	63.8%	85.5%	5.2%
Beam Composition @WC4	68.8%	4.6 %	26.6 %	87.4 %	3.7 %	8.9 %
Beam Composition @TPC FF	88.5%	8.2%	3.3 %	94.0%	5.3%	0.7%

Table 5.3: MC selection flow per particle species.

2221 It should be noted that pions may interact hadronically in the steel or in the  
 2222 non-instrumented argon upstream to the TPC front face while travelling the length  
 2223 of between WC4 and the TPC. Or, they could decay in flight between WC4 and the  
 2224 TPC. One of the interaction products can leak into the TPC and be matched with the  
 2225 WC track, contributing to the pool of events used for the cross section calculation. We  
 2226 call this type of particles “secondaries” from pion events, with a terminology inspired  
 2227 by Geant4. We estimate the number of secondaries using the DDMC pion sample.  
 2228 The percentage of secondaries is given by the number of matched WC2TPC tracks  
 2229 whose corresponding particle is not flagged as primary by Geant4. The secondary to  
 2230 pion ratio is 4.9% in the 60A sample and 4.3% in the 100A sample.

2231 We evaluate the beamline background contribution to the cross section by pro-  
 2232 ducing the interacting and incident histograms for the events surviving the selection,  
 2233 staggering the contributions for each particle species, as shown in Figure 5.9. From  
 2234 those histograms, we are able to evaluate the contribution of pions and beamline  
 2235 backgrounds to each bin of the interacting and incident histograms separately and  
 2236 obtain the relative pion content. The relative pion content in each bin for the inter-  
 2237 acting and incident histograms represents the correction applied to data. We take

here the interacting histogram as example, noting that the derivation of the correction for the incident histogram is identical. The number of entries in each bin of the interacting plot (Figure 5.9 left) is  $N_{\text{Int}}^{\text{TOT}}(E_i)$ , equal to the sum of the pions and beamline backgrounds in that bin, namely

$$N_{\text{Int}}^{\text{TOT}}(E_i) = N_{\text{Int}}^{\pi}(E_i) + \underbrace{N_{\text{Int}}^{\mu}(E_i) + N_{\text{Int}}^e(E_i) + N_{\text{Int}}^{\text{Secondary}}(E_i)}_{B_{\text{Int}}(E_i)}. \quad (5.1)$$

Thus, the relative pion content to each bin in MC can be calculated as follows

$$C_{\text{Int}}^{\pi MC}(E_i) = \frac{N_{\text{Int}}^{\pi MC}}{N_{\text{Int}}^{\text{TOTMC}}(E_i)} = \frac{N_{\text{Int}}^{\text{TOTMC}}(E_i) - B_{\text{Int}}^{MC}(E_i)}{N_{\text{Int}}^{\text{TOTMC}}(E_i)}. \quad (5.2)$$

In order to evaluate the pion content of each bin in data, we scale the measured bin by the corresponding relative pion content found in MC, as follows

$$N_{\text{Int}}^{\pi RecoData} = N_{\text{Int}}^{\text{TOTData}}(E_i) - B_{\text{Int}}^{\text{Data}}(E_i) = C_{\text{Int}}^{\pi MC}(E_i)N_{\text{Int}}^{\text{TOTData}}(E_i). \quad (5.3)$$

The pion content is evaluated separately in the interacting and incident histograms. Their ratio determines a correction to the measured raw cross section. For example, the measured raw cross section of a sample with enhanced muons content will tend to be lower than the raw cross section of a muon free sample. This is because most of the muons will cross the TPC without stopping, thus contributing almost exclusively to the incident histogram, forcing the pion content to be lower in the incident histogram than in the interacting; thus, the correction will tend to enhance the cross section.

2253 **5.4 Estimate of Energy Loss before the TPC**

2254 The beamline particles travel a path from where their momentum is measured in  
2255 the beamline until they are tracked again inside the TPC. In the LArIAT geometry,  
2256 a particle leaving the WC4 will encounter the materials listed in Table 5.4 before  
2257 being registered again. The energy lost by the particle in this non-instrumented  
2258 material modifies the particle's kinetic energy and directly affects the cross section  
2259 measurement, as shown in equation 4.5.

Material	density [g/cm <sup>3</sup> ]	width [cm]
Fiberglass laminate (G10)	1.7	1.28
Liquid Argon	1.4	3.20
Stainless Steel	7.7	0.23
Titanium	4.5	0.04
Air	$1.2 \cdot 10^{-3}$	89.43
Plastic Scintillator	1.03	1.20 (+ 1.30)

Table 5.4: LArIAT material budget from WC4 to the TPC Front Face.

We derive an estimate of the energy loss between the beamline momentum measurement and the TPC ( $E_{loss}$ ) from the pion and kaon DDMC samples, since this quantity is not measurable directly on data. The  $E_{loss}$  distribution for the 60A and 100A pion sample is shown in figure 5.10, left and right respectively. The  $E_{loss}$  distribution for the whole kaon sample is shown in figure 5.11. A clear double peaked structure is visible, which is due to the particles either missing or hitting the HALO paddle: a schematic rendering of this occurrence is shown in figure 5.12. The kinematic at WC4 determines the trajectory of a particle and whether or not it will hit the halo paddle. In figure 5.13 , we plot the true horizontal component of the momentum  $P_x$  versus the true  $X$  position at WC4 for pions missing the halo paddle (left) and for pions hitting the halo paddle (right) for the -60A MC simulation runs – analogous plots are obtained with the -100A pion simulation and with the kaon simulation. These distributions can be separated drawing a line in this position-momentum space.

We use a logistic regression [13] as a classifier to find the best separating line, shown in both plots as the red line. We classify as “hitting the halo paddle” all pions whose  $P_x$  and  $X$  are such that

$$P_x + 0.02 * X - 0.4 < 0$$

and as “missing the halo paddle” all pions whose  $P_x$  and  $X$  are such that

$$P_x + 0.02 * X - 0.4 > 0,$$

where the coefficients of the line are empirically found by the logistic regression estimation. Overall, this simple method classifies in the right category (hit or miss) about 86% of the pion events. In MC, we assign  $E_{loss} = 32 \pm 4$  MeV for pion events classified as “hitting the halo paddle”; we assign  $E_{loss} = 24 \pm 3$  MeV for pion events classified as “missing the halo paddle”. We apply the same classifier on data.

A scan of the simulated geometry showed an excess of 3 cm of uninstrumented argon compared with the surveyed detector geometry. We account for this difference by assigning in data  $E_{loss} = 24 \pm 6$  MeV for pion events classified as “hitting the halo paddle” and  $E_{loss} = 17 \pm 6$  MeV for pion events classified as “missing the halo paddle”, where the uncertainty is derived as the standard deviation of the double peaked distribution.

The summary of the values for used for  $E_{Loss}$  for the pion sample is listed in table 5.5 with the analogous results for the study on the kaon case.

	$E_{loss}$ [MeV]	
	Hitting Halo	Missing Halo
Pion MC	$32 \pm 4$	$24 \pm 3$
Pion Data	$25 \pm 6$	$17 \pm 6$
Kaon MC	$38 \pm 6$	$31 \pm 5$
Kaon Data	$26 \pm 7$	$22 \pm 7$

Table 5.5: Energy loss for pions and kaons.

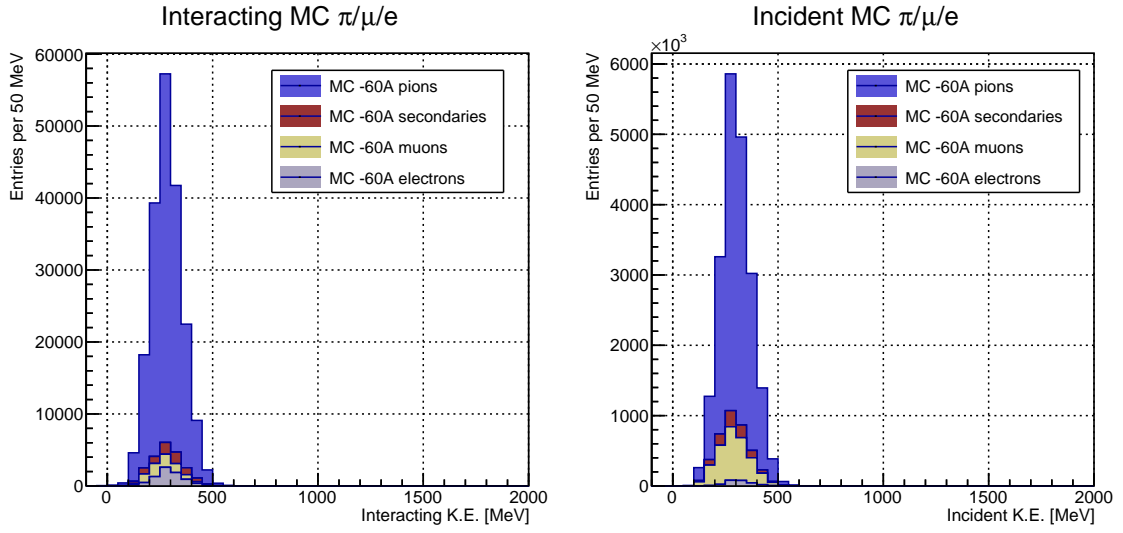


Figure 5.9: Left: staggered contributions to the interacting kinetic energy distribution for electron (grey), muons (yellow) and pion (blue) in the 60A simulation sample. Right: staggered contributions to the incident kinetic energy distribution for electron (grey), muons (yellow) and pion (blue) in the 60A simulation sample.

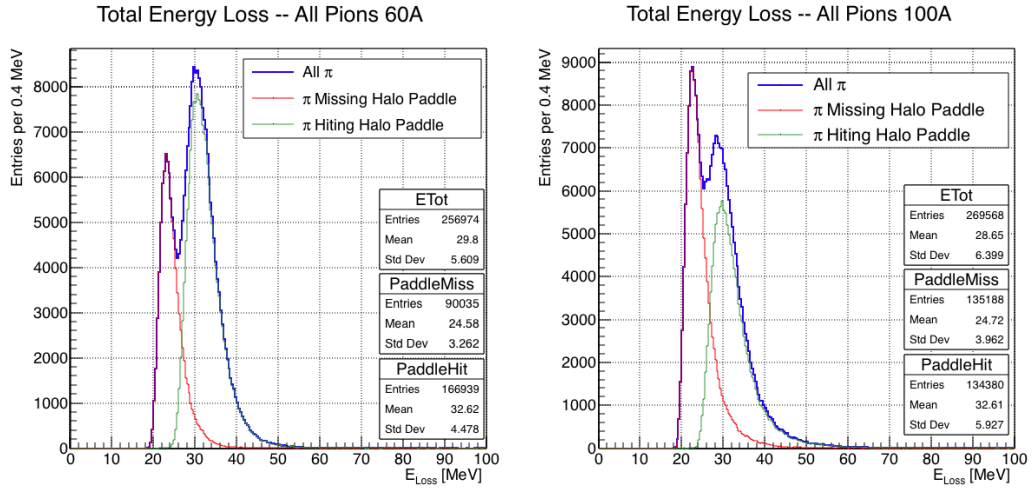


Figure 5.10: True energy loss between WC4 and the TPC front face according to the MC simulation of negative pions of the 60A runs (left) and of the 100A runs (right). The distribution for the whole data sample is shown in blue, the distribution for the pions missing the halo is shown in red, and the distribution for the pions hitting the halo is shown in green.

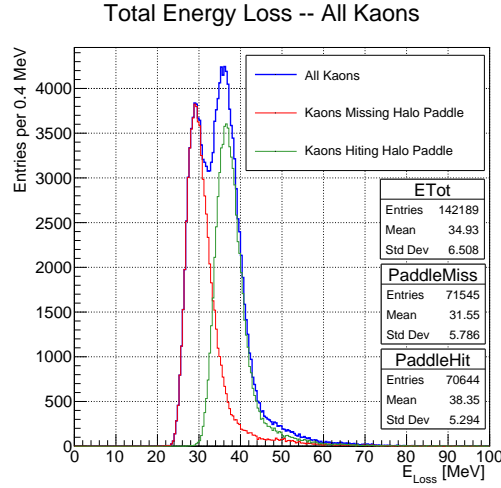


Figure 5.11: True energy loss between WC4 and the TPC front face according to the MC simulation of positive kaons in the 60A and 100A combined sample. The distribution for the whole data sample is shown in blue, the distribution for the kaons missing the halo is shown in red, and the distribution for the kaons hitting the halo is shown in green.

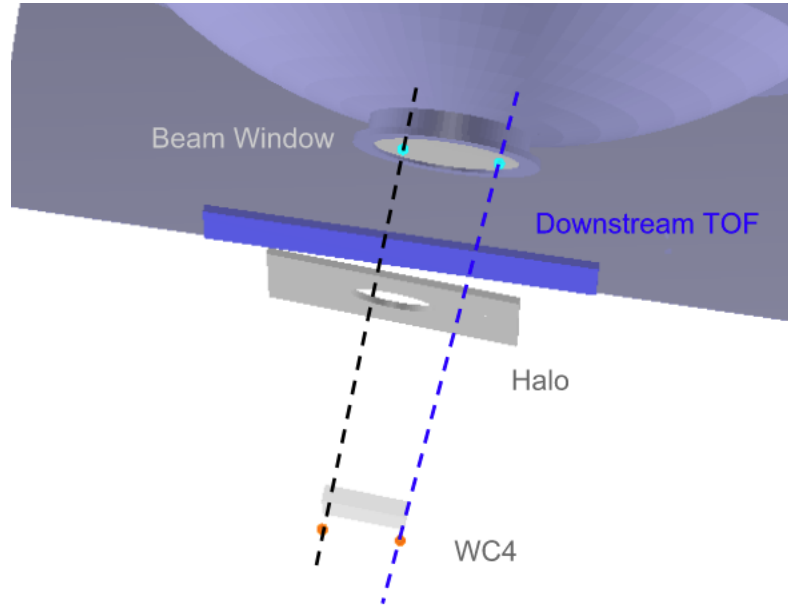


Figure 5.12: Schematic rendering of the particle path between WC4 and the TPC front face. The paddle with the hollow central circle represents the Halo paddle. We illustrate two possible trajectories: in black, a trajectory that miss the paddle and goes through the hole in the Halo, in blue a trajectory that hits the Halo paddle and goes through the scintillation material.

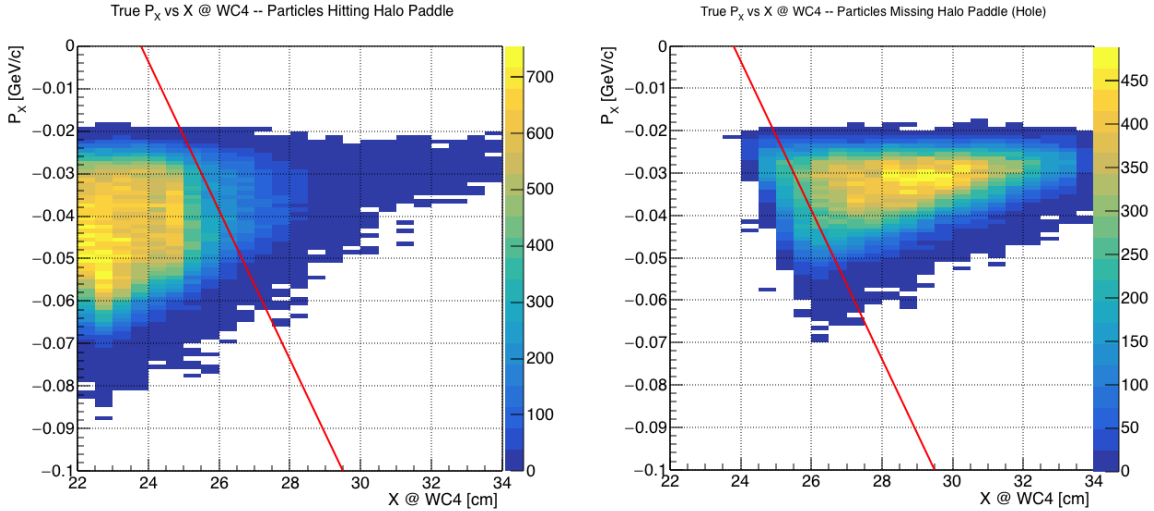


Figure 5.13: Horizontal component of the true momentum vs the horizontal position at WC4 for MC simulated pions of the 60A runs. The plot on the left shows the distribution for pion that miss the halo paddle and the plot on the right shows the distributions for pions that hit the halo. The form of the classifier is overlaid to both plots (red line).

## 2273 5.5 Tracking Studies

2274 The tracking of hadrons in the TPC determines both the beamline to TPC hand-  
 2275 shake and the identification of the interaction point within the TPC. Thus, it plays  
 2276 a fundamental role in the cross section measurements. We performed several studies  
 2277 geared towards the optimization of the package for tracking in the TPC. In particular,  
 2278 we studied a suitable set of parameters for the WC2TPC match and we optimized  
 2279 the clustering algorithm to maximize the efficiency of finding the interaction point on  
 2280 MC. Given the technical nature of these studies, we report them in Appendix B. We  
 2281 report here the evaluation of the angular resolution of the tracking algorithm in data  
 2282 and MC, due to its implication on the physics measurement.

### 2283 5.5.1 Angular Resolution

2284 Scope of this study is to understand and compare the tracking performances and  
 2285 angular resolution of the TPC tracking on data and MC. We use the angular resolution

2286 of the tracking to determine the value of smallest angle that we can reconstruct with  
2287 a non-zero efficiency, effectively determining a selection on the angular distribution  
2288 of the cross section measurement due to the tracking performance.

2289 We start by selecting all the WC2TPC matched tracks used for the cross section  
2290 analysis. These tracks can contain from a minimum of 3 3D-space points to a maxi-  
2291 mum of 240 3D-space points. We fit a line to all the 3D-space points associated with  
2292 the track. For each track we calculate the average distance between each point in  
2293 space and the fit line as follows

$$\bar{d} = \frac{\sum_i^N d_i}{N}, \quad (5.4)$$

2294 where  $N$  is the number of 3D-space points of the track and  $d_i$  is the distance of the  
2295  $i$ -th space point to the line fit. Several tests to compare the goodness of fit between  
2296 data and MC have been considered. We decided to use  $\bar{d}$  for its straightforward  
2297 interpretation. The  $\bar{d}$  distribution for data and MC is shown in Figure 5.16 for pions  
2298 and in Figure 5.18 for kaons and shows a relatively good agreement between data and  
2299 MC.

2300 A visual representation of the procedure used to evaluate the angular resolution  
2301 is shown in Figure 5.14. For each track, we order the space points according to their  
2302 Z position along the positive beam direction (panel a) and we split them in two sets:  
2303 the first set contains all the points belonging to the first half of the track and the  
2304 second set contains all the points belonging the second half of the track. We remove  
2305 the last four points in the first set and the first four points in the second set, so to  
2306 have a gap in the middle of the original track (panel b). We fit the first and the second  
2307 set of points with two lines (panel c). We then calculate the angle between the fit of  
2308 the first and second half  $\alpha$  (panel d). The angle  $\alpha$  determines the spatial resolution  
2309 of the tracking. The distributions for data and MC for  $\alpha$  are given in Figure 5.17 for  
2310 pions and in Figure 5.19 for kaons. The mean of the data and MC angular resolution  
2311 are reported in Table tab:AngRes for pions and kaons in data and MC.

2312     Interaction angles smaller than the angle resolution are indistinguishable for the  
 2313     reconstruction. Therefore, we assess our ability to measure the cross section to be  
 2314     limited to interaction angles greater than 5.0 deg. More accurate studies of the angular  
 2315     resolution as a function of the kinetic energy and track length, albeit interesting, are  
 2316     left for an improvement of the analysis.

2317     It is beneficial to take a moment to describe the definition of interaction angle.  
 2318     In case of elastic scattering, the definition is straightforward: the interaction angle is  
 2319     the angle between the incoming and outgoing hadron, i.e.

$$\theta = \cos^{-1} \left( \frac{\vec{p}_{\text{incoming}} \cdot \vec{p}_{\text{outgoing}}}{|\vec{p}_{\text{incoming}}| |\vec{p}_{\text{outgoing}}|} \right). \quad (5.5)$$

2320     In case of inelastic scattering, the presence of several topologies requires a more  
 2321     complex definition, as shown in figure 5.15. We define the scattering angle as the  
 2322     biggest of the angles between the incoming hadron and the visible daughters, where  
 2323     the visible daughters are charged particles that travel more than 0.47 cm in the  
 2324     detector (see panel a); in case all the daughters are invisible, the angle is assigned  
 2325     to be 90 deg (see panel b). We chose this working definition of scattering angle  
 2326     for inelastic scattering keeping in mind how our tracking reconstruction works: the  
 2327     tracking will stop correctly non of the daughters are is visible in the detector and it  
 2328     is likely to stop correctly if multiple daughters form an interaction vertex. The only  
 2329     “dangerous” case is the production of one charged daughter plus neutrals, which we  
 2330     can study with this working definition of scattering angle (see panel c).

2331     We can see the effects of the angular resolution on the cross section by plotting the  
 2332     true Geant4 cross section for interaction angles greater than a minimum interaction

	Data	MC
Pions	$\bar{\alpha}_{Data} = (5.0 \pm 4.5) \text{ deg}$	$\bar{\alpha}_{MC} = (4.5 \pm 3.9) \text{ deg}$
Kaons	$\bar{\alpha}_{Data} = (4.3 \pm 3.7) \text{ deg}$	$\bar{\alpha}_{MC} = (4.4 \pm 3.6) \text{ deg}$

Table 5.6: Angular resolution for Pion and Kaon tracking in both data and MC.

angle. Figure 5.20 shows the true Geant4 cross section for interaction angles greater than 0 deg (green), 4.5 deg (red), 5.0 deg (blue) and 9.0 deg (yellow). A small 0.5 deg systematic shift between the mean of the data and MC angular resolution is present.

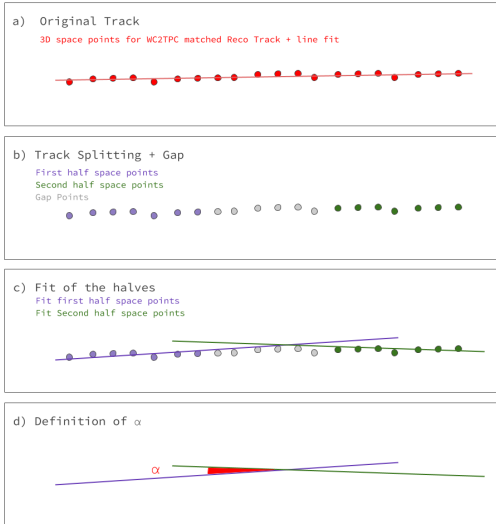


Figure 5.14: A visual representation of the procedure used to evaluate the angular resolution.

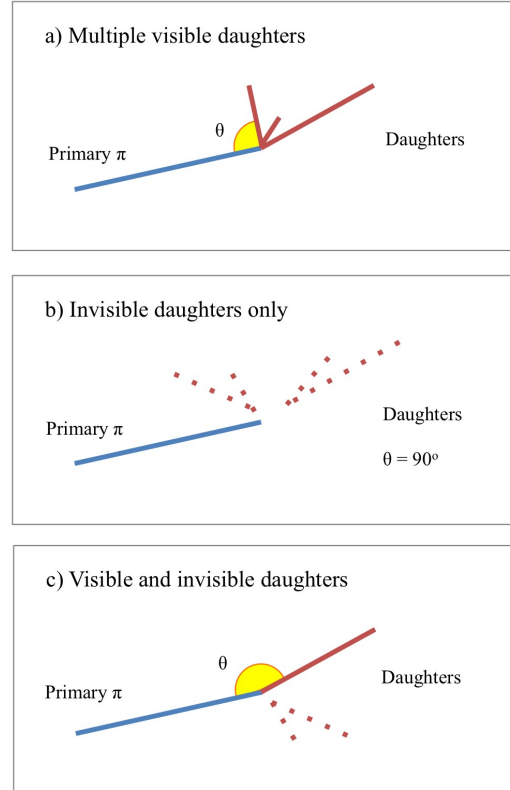


Figure 5.15: A visual representation of the scattering angle definition in case of inelastic scattering.

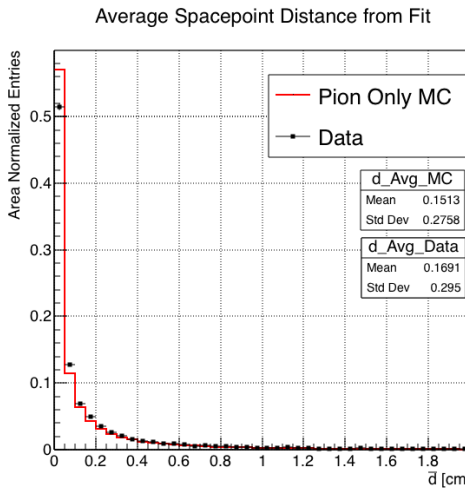


Figure 5.16: Distributions of the average distance between each 3D point in space and the fit line,  $\bar{d}$  for the data used in the pion cross section analysis and the pion only DDMC. The distributions are area normalized.

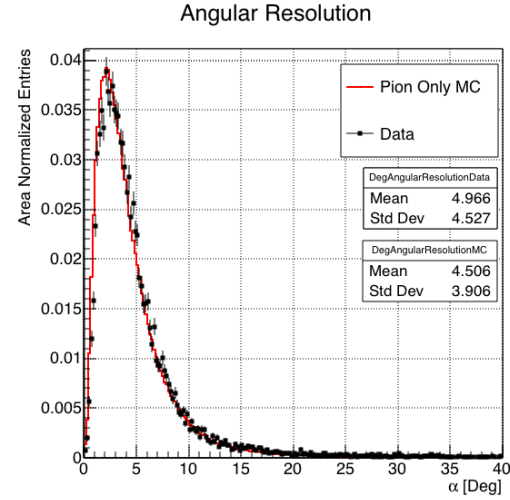


Figure 5.17: Distributions of angular resolution  $\alpha$  for data used in the pion cross section analysis and pion only DDMC. The distributions are area normalized.

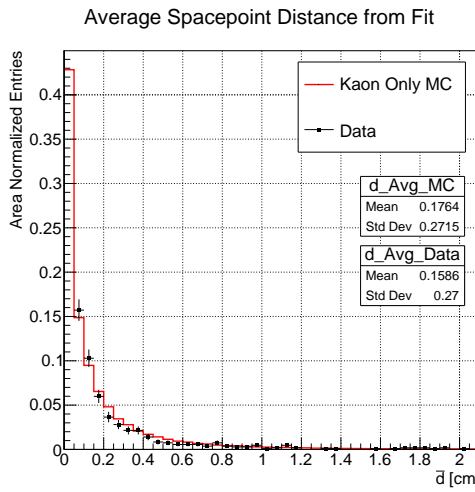


Figure 5.18: Distributions of the average distance between each 3D point in space and the fit line,  $\bar{d}$  for the data used in the kaon cross section analysis and the kaon only DDMC. The distributions are area normalized.

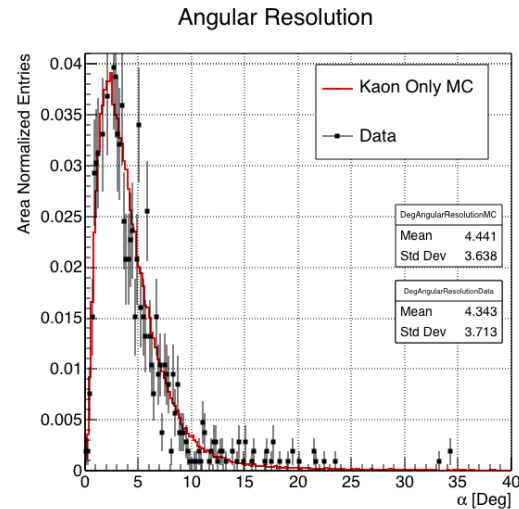


Figure 5.19: Distributions of angular resolution  $\alpha$  for data used in the kaon cross section analysis and kaon only DDMC. The distributions are area normalized.

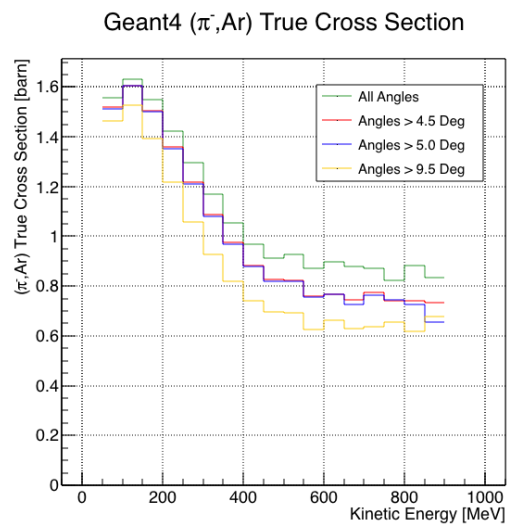


Figure 5.20: True ( $\pi^-$ , Ar) cross section for interaction angles greater than 0 deg (green), 4.5 deg (red), 5.0 deg (blue) and 9.0 deg (yellow).

2336 **5.6 Calorimetry Studies**

2337 The measured kinetic energy of a hadron candidate at each argon slab determines  
2338 which bins of the interacting and incident histograms a selected event is going to fill.  
2339 Thus, the energy measurement provided by the LArTPC is fundamental for the cross  
2340 section analysis. In Appendix C, we describe how we calibrate the TPC calorimetric  
2341 response. In the following section, we describe how we measure the kinetic energy of  
2342 the hadrons in the TPC.

2343 **5.6.1 Kinetic Energy Measurement**

2344 In this section, we define the measurement on the kinetic energy and determine the  
2345 related uncertainty. We will propagate this uncertainty into the cross section mea-  
2346 surement, as discussed in Section 6.1.2 for the pion cross section and in Section ??  
2347 for the kaon cross section.

2348 The kinetic energy of a hadron at the  $j^{\text{th}}$  slice of argon in the TPC is given by

$$KE_j = \sqrt{p_{\text{Beam}}^2 + m_{\text{Beam}}^2} - m_{\text{Beam}} - E_{\text{Loss}} - E_{\text{FF-j}}, \quad (5.6)$$

2349 where  $p_{\text{Beam}}$  is the momentum measured by the beamline detectors,  $m_{\text{Beam}}$  is the  
2350 mass of the hadron as reported in the PDG,  $E_{\text{Loss}}$  is the energy loss between the  
2351 beamline and the TPC, and  $E_{\text{FF-j}}$  is the energy that the hadron deposited from the  
2352 TPC front face until the  $j^{\text{th}}$  slice. The uncertainty on  $KE_j$  is then given by

$$\delta KE_j = \sqrt{\delta p_{\text{Beam}}^2 + \delta E_{\text{Loss}}^2 + \delta E_{\text{dep FF-j}}^2}, \quad (5.7)$$

2353 where we have dropped the uncertainty on the mass, since it is orders of magnitude  
2354 smaller than the other uncertainties. We assume the relative uncertainty on  $p_{\text{Beam}}$  to  
2355 be 2%, and the uncertainty on the energy loss upstream to be 7 MeV, as calculated

2356 in Section 5.4. We describe the estimate of the uncertainty on  $E_{\text{FF-j}}$  in the rest of  
2357 this section.

2358 The energy deposited by the hadron from the TPC front face until the  $j^{\text{th}}$  slice is  
2359 the sum of the measured energy deposited in each previous slabs  $E_i$ , i.e.

$$E_{\text{FF-j}} = \sum_{i < j} E_i, \quad (5.8)$$

2360 where  $E_i$  is measured in each slab as the product of the stopping power,  $dE/dX_i$ ,  
2361 and the track pitch,  $\text{Pitch}_i$ , for that point. If we assume conservatively that the  
2362 measurements of  $E_i$  are not independent from one another, the uncertainty on  $E_{\text{FF-j}}$   
2363 becomes

$$\delta E_{\text{FF-j}} = (j - 1)\delta E_i, \quad (5.9)$$

2364 where  $\delta E_i$  is the uncertainty on the energy loss in one slab of argon.

2365 The left side of Figure 5.21 shows the distribution of the energy deposited in each  
2366 slab of argon, for the 60A negative pion dataset in black and for the pion only MC  
2367 in blue. The analogous plot for the -100A negative pion data set is show on the right  
2368 side of Figure 5.21. The distributions are fitted with a landau displayed in red for  
2369 data and in teal for MC. The uncertainty on  $E_i$  is given by the width of the Landau  
2370 fit to the data. A small systematic uncertainty is given by a 1.0% difference between  
2371 the most probable value of the landau fits in data and MC.

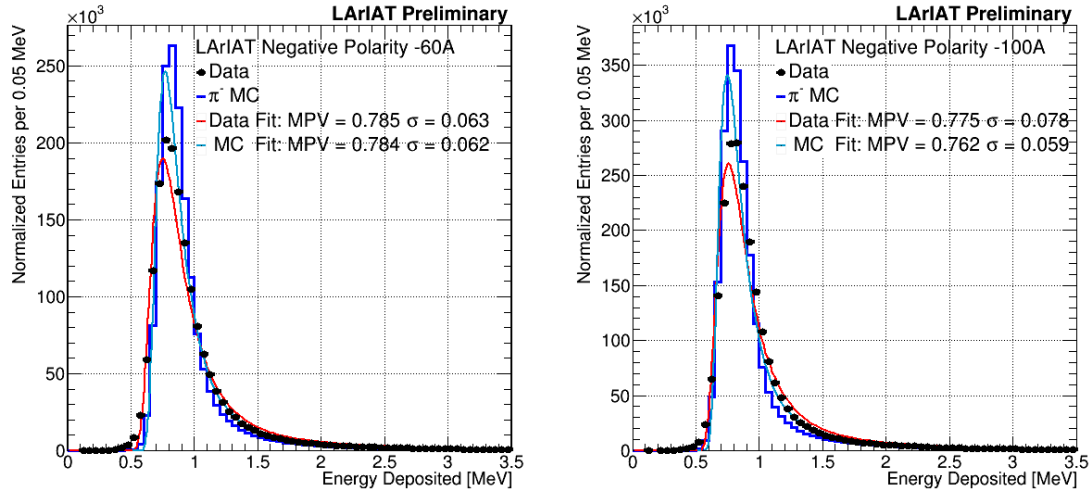


Figure 5.21: Energy deposited  $E_i$  in a single slab of argon for the pion -60A runs (left) and -100A runs (right). The data is shown in black, the MC in blue. The distributions are fitted with a landau displayed in red for data and in teal for MC.

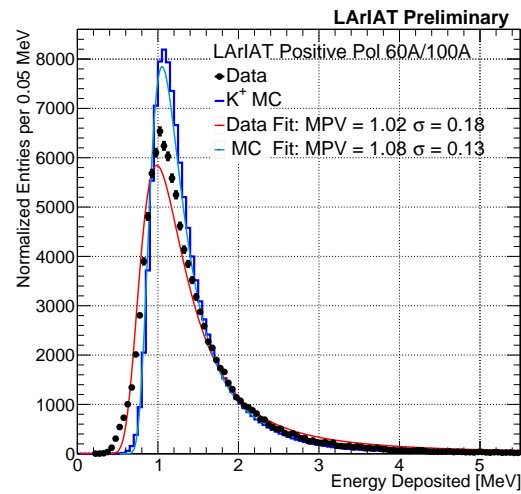


Figure 5.22: Energy deposited  $E_i$  in a single slab of argon for the kaons of the +60A runs and +100A runs. The data is shown in black, the MC in blue. The distributions are fitted with a landau displayed in red for data and in teal for MC.

2372 **Chapter 6**

2373 **Negative Pion Cross Section**  
2374 **Measurement**

2375 “*Y ella es flama que se eleva, Y es un pájaro a volar.*  
2376 *En la noche que se incendia, estrella de oscuridad*  
2377 *que busca entre la tiniebla, la dulce hoguera del beso.*”  
2378 – Lila Downs, 2002 –

2379 In this chapter, we show the result of the thin slice method to measure the ( $\pi^-$ -  
2380 Ar) total hadronic cross section. In Section 6.1, we start by measuring the raw  
2381 cross section, i.e. the cross section obtained exclusively using data reconstruction,  
2382 without any additional corrections. In Section 6.2, we apply a statistical subtraction  
2383 of the background contributions based on simulation and a correction for detection  
2384 inefficiency. The final results are presented in Section 6.3.

2385 **6.1 Raw Cross Section**

2386 We measure the raw ( $\pi^-$ -Ar) total hadronic cross section as a function of the kinetic  
2387 energy in the two chosen data sets, the -60A and -100A negative runs. As we will

clarify in Section 6.2, the corrections to the raw cross section depend on the beam conditions and need to be calculated independently for the two datasets. Thus, we present here the measurement of the raw cross section on the two datasets separately.

As stated in section 4.3.2, the raw cross section is given by the equation 4.4

$$\sigma_{TOT}(E_i) = \frac{1}{n\delta X} \frac{N_{Int}^{TOT}(E_i)}{N_{Inc}^{TOT}(E_i)}, \quad (6.1)$$

where  $N_{Int}^{TOT}$  is the measured number of particles interacting at kinetic energy  $E_i$ ,  $N_{Inc}^{TOT}$  is the measured number of particles incident on an argon slice at kinetic energy  $E_i$ ,  $n$  is the density of the target centers and  $\delta X$  is the thickness of the argon slice. The density of the target centers and the slab thickness are  $n = 0.021 \cdot 10^{24} \text{ cm}^{-3}$  and  $\delta X = 0.47 \text{ cm}$ , respectively.

Figure 6.1 shows the distribution of  $N_{Int}^{TOT}$  as a function of the kinetic energy for the 60A dataset on the left and for the 100A dataset on the right. The data central points are represented by black dots, the statistical uncertainty is shown in black, while the systematic uncertainty is shown in red. Data is displayed over the  $N_{Int}^{TOT}$  distribution obtained with a MC mixed sample of pions, muon and electrons (additional details on the composition will be provided in Section ??). The contribution from the simulated pions is shown in blue, the one from secondaries in red, the one from muons in yellow and the ones from electrons in gray. The simulated pion's and backgrounds' contributions are stacked; the sum of the integrals from each particle species is normalized to the integral of the data.

Figure 6.2 shows the distribution of  $N_{Inc}^{TOT}$  for the 60A dataset on the left and for the 100A dataset on the right. Data is displayed over the MC. The same color scheme and normalization procedure is used for both the interacting and incident histograms.

Figure 6.3 shows the raw cross section for the 60A dataset on the left and for the 100A dataset on the right, statistical uncertainty in black and systematic uncertainty

2412 in red. The raw data cross section is overlaid to the reconstructed cross section for  
 2413 the MC mixed sample, displayed in azure. Since the background contributions and  
 2414 the detector effects for the 60A and 100A sample are different, it is premature to  
 2415 compare the raw cross sections obtained from the two samples at this point.

2416 We describe the calculation of the statistical uncertainty for the interacting, in-  
 2417 cident and cross section distributions in Section 6.1.1; we describe the procedure to  
 2418 calculate the corresponding systematics uncertainty on Section 6.1.2.

### 2419 6.1.1 Statistical Uncertainty

2420 The statistical uncertainty for a given kinetic energy bin of the cross section is cal-  
 2421 culated by error propagation from the statistical uncertainty on  $N_{\text{Inc}}^{\text{TOT}}$  and  $N_{\text{Int}}^{\text{TOT}}$   
 2422 correspondent bin. Since the number of incident particles in each energy bin is given  
 2423 by a simple counting, we assume that  $N_{\text{Inc}}^{\text{TOT}}$  is distributed as a poissonian with mean  
 2424 and variance equal to  $N_{\text{Inc}}^{\text{TOT}}$  in each bin. On the other hand,  $N_{\text{Int}}^{\text{TOT}}$  follows a bino-  
 2425 mial distribution: a particle in a given energy bin might or might not interact. The  
 2426 variance for the binomial is given by

$$\text{Var}[N_{\text{Int}}^{\text{TOT}}] = \mathcal{N}P_{\text{Interacting}}(1 - P_{\text{Interacting}}). \quad (6.2)$$

2427 Since the interaction probability  $P_{\text{Interacting}}$  is  $\frac{N_{\text{Int}}^{\text{TOT}}}{N_{\text{Inc}}^{\text{TOT}}}$  and the number of tries  $\mathcal{N}$  is  
 2428  $N_{\text{Inc}}^{\text{TOT}}$ , equation 6.2 translates into

$$\text{Var}[N_{\text{Int}}^{\text{TOT}}] = N_{\text{Inc}}^{\text{TOT}} \frac{N_{\text{Int}}^{\text{TOT}}}{N_{\text{Inc}}^{\text{TOT}}} \left(1 - \frac{N_{\text{Int}}^{\text{TOT}}}{N_{\text{Inc}}^{\text{TOT}}}\right) = N_{\text{Int}}^{\text{TOT}} \left(1 - \frac{N_{\text{Int}}^{\text{TOT}}}{N_{\text{Inc}}^{\text{TOT}}}\right). \quad (6.3)$$

2429  $N_{\text{Inc}}^{\text{TOT}}$  and  $N_{\text{Int}}^{\text{TOT}}$  are not independent. The statistical uncertainty on the cross  
 2430 section is thus calculated as

$$\delta\sigma_{\text{TOT}}(E) = \sigma_{\text{TOT}}(E) \left( \frac{\delta N_{\text{Int}}^{\text{TOT}}}{N_{\text{Int}}^{\text{TOT}}} + \frac{\delta N_{\text{Inc}}^{\text{TOT}}}{N_{\text{Inc}}^{\text{TOT}}} \right) \quad (6.4)$$

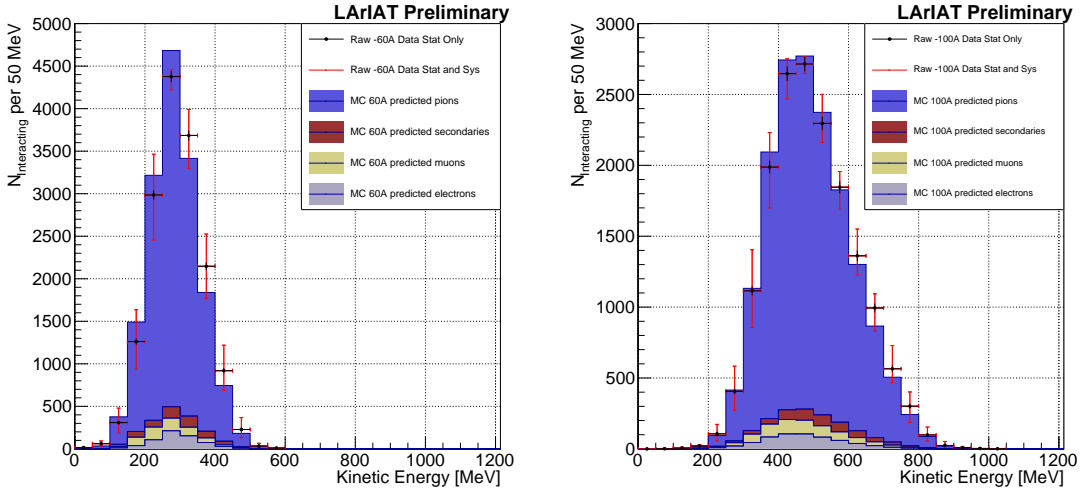


Figure 6.1: Raw number of interacting pion candidates as a function of the reconstructed kinetic energy for the 60A runs (left) and for the 100A runs (right). The statistical uncertainties are shown in black, the systematic uncertainties in red.

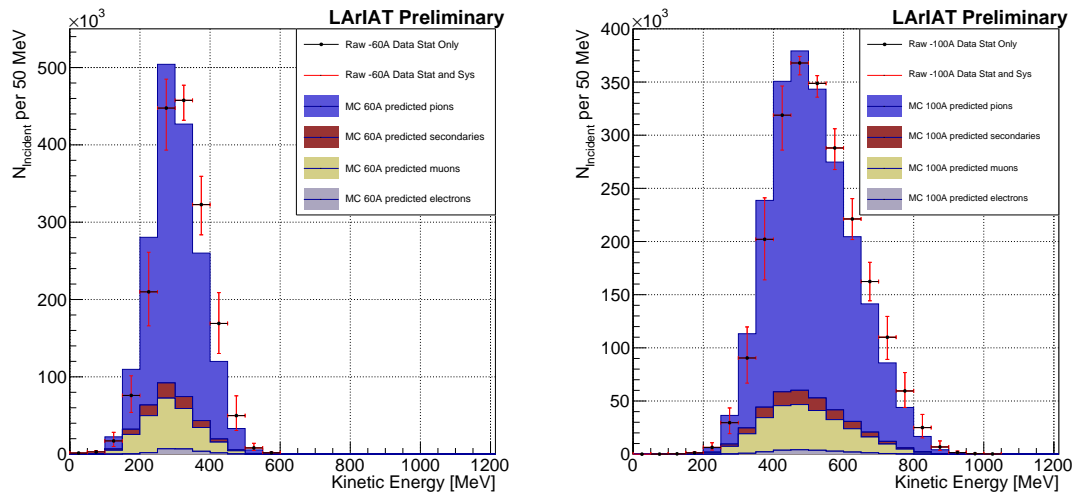


Figure 6.2: Raw number of incident pion candidates as a function of the reconstructed kinetic energy for the 60A runs (left) and for the 100A runs (right). The statistical uncertainty is shown in black, the systematic uncertainties in red.

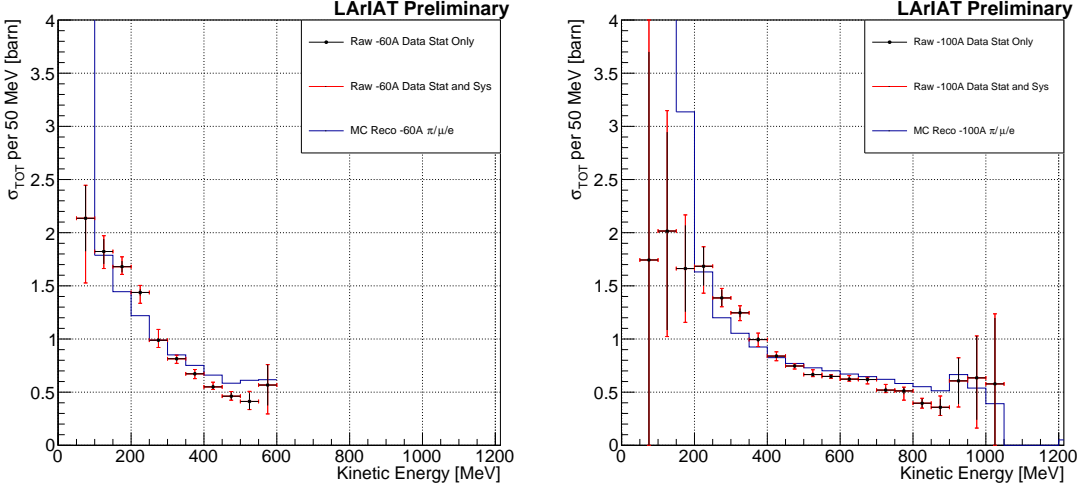


Figure 6.3: Raw ( $\pi^-$ -Ar) total hadronic cross section for the 60A runs (left) and for the 100A runs (right). The statistical uncertainty is shown in black, the systematic uncertainties in red. The raw cross section obtained with a MC mixed sample of pions, muon and electrons in the percentage predicted by G4Beamline is shown in azure.

2431 where:

$$\delta N_{\text{Inc}}^{\text{TOT}} = \sqrt{N_{\text{Inc}}^{\text{TOT}}} \quad (6.5)$$

$$\delta N_{\text{Int}}^{\text{TOT}} = \sqrt{N_{\text{Int}}^{\text{TOT}} \left(1 - \frac{N_{\text{Int}}^{\text{TOT}}}{N_{\text{Inc}}^{\text{TOT}}}\right)}. \quad (6.6)$$

### 2432 6.1.2 Treatment of Systematics

2433 The only systematic effect considered in the measurement of the raw cross section  
 2434 results from the propagation of the uncertainty associate with the measurement of  
 2435 the kinetic energy at each argon slab. As shown in Section 5.6.1, the uncertainty on  
 2436 the kinetic energy of a pion candidate at the  $j^{\text{th}}$  slab of argon is given by

$$\delta KE_j = \sqrt{\delta p_{\text{Beam}}^2 + \delta E_{\text{Loss}}^2 + \delta E_{\text{dep FF-j}}^2} \quad (6.7)$$

$$= \sqrt{(2\% p_{\text{Beam}})^2 + (6 \text{ [MeV]})^2 + (j - 1)^2 (\sim 0.08 \text{ [MeV]})^2}. \quad (6.8)$$

2437 We propagate this uncertainty by varying the energy measurement  $KE_j$  at each  
 2438 argon slab. We measure  $N_{\text{Inc}}^{\text{TOT}}$ ,  $N_{\text{Int}}^{\text{TOT}}$  and the cross section in three cases: first  
 2439 assigning the measured  $KE_j$  at each kinetic energy sampling, then assigning  $KE_j +$   
 2440  $\delta KE_j$ , and finally assigning  $KE_j - \delta KE_j$ . The difference between the values obtained  
 2441 using the  $KE_j$  sampling and the maximum and minimum values in each kinetic energy  
 2442 bin determines the systematic uncertainty.

## 2443 **6.2 Corrections to the Raw Cross Section**

2444 As described in section 4.3.3, we need to apply a background correction and an  
 2445 efficiency correction in order to derive the true pion cross section from the raw cross  
 2446 section. The true cross section is given in equation 4.9,

$$\sigma_{\text{TOT}}^{\pi^-}(E_i) = \frac{1}{n\delta X} \frac{\epsilon^{\text{Inc}}(E_i)}{\epsilon^{\text{Int}}(E_i)} \frac{C_{\text{Int}}^{\pi MC}(E_i)}{C_{\text{Inc}}^{\pi MC}(E_i)} \frac{N_{\text{Int}}^{\text{TOT}}(E_i)}{N_{\text{Inc}}^{\text{TOT}}(E_i)}. \quad (4.9)$$

2447 Section 6.2.1 describes the evaluation of pion content in the interacting and inci-  
 2448 dent histograms, ( $C_{\text{Int}}^{\pi MC}(E_i)$  and  $C_{\text{Inc}}^{\pi MC}(E_i)$ ) and the propagation to the cross section  
 2449 measurement of the relative systematic uncertainties.

2450 Section 6.2.2 describes the procedure employed to obtain the efficiency corrections  
 2451  $\epsilon^{\text{Int}}(E_i)$  and  $\epsilon^{\text{Inc}}(E_i)$  and the propagation to the cross section measurement of the  
 2452 relative uncertainties.

### 2453 **6.2.1 Background subtraction**

2454 We use the procedure described in 5.3.2 to evaluate the relative pion content in  
 2455 the interacting histogram  $C_{\text{Int}}^{\pi MC}(E_i)$  and the relative pion content in the incident  
 2456  $C_{\text{Inc}}^{\pi MC}(E_i)$ . We start by evaluating the relative pion content assuming the beamline  
 2457 composition simulated by G4Beamline, whose pion, muon and electron percentages  
 2458 per beam condition are reported again in the first line of Table 6.1. The left side of

2459 Figure 6.4 shows the MC estimated relative pion content for the interacting histogram  
2460 as function of kinetic energy for the 60A runs (top) and 100A runs (bottom). The  
2461 right side of the same figure shows the MC estimated relative pion content for the  
2462 incident histogram as function of kinetic energy for the 60A runs (top) and 100A  
2463 runs (bottom). In Figure 6.4 the central curves displayed in light blue are obtained  
2464 using the beamline composition as predicted by G4Beamline: these are the correction  
2465 curves for the relative pion content applied to data.

2466 So, the question now becomes: how well do we know the beamline composition?  
2467 In absence of additional data constraints, we take a 100% systematic uncertainty on  
2468 the electron content, reported in lines 3 and 4 of Table 6.1. The effect of doubling or  
2469 halving the electron percentage in the beam on the pion relative content is displayed  
2470 in red in Figure 6.4. We reserve a slightly different treatment for the muon content.  
2471 Since G4Beamline tracks only particles which cross all the wire chambers, pion events  
2472 that decay in flight from WC1 to WC4 are not recorded by G4Beamline. Pion decays  
2473 in the beamline could be trigger the beamline detectors in data, if the produced muon  
2474 proceeds in the beamline. Thus, we take the G4Beamline prediction for muons as a  
2475 lower bound in the composition: the effect of doubling the muon content (line 2 in  
2476 Table 6.1) is shown in blue on Figure 6.4. A future study of data from additional  
2477 beamline detectors such as the Aerogel Chernkov detectors [43] or the muon range  
2478 stack (see Section 3.2.4) has the potential of a narrowing the systematics uncertainty  
2479 coming from the beamline composition.

2480 We propagate the uncertainty on the beamline composition as a systematic un-  
2481 certainty to the cross section by varying the beam composition for all the cases listed  
2482 in Table 6.1 and evaluating variation of obtained data cross sections in each bin. This  
2483 systematic uncertainty is summed in quadrature with the statistical uncertainty and  
2484 the systematic uncertainty related to the kinetic energy measurement.

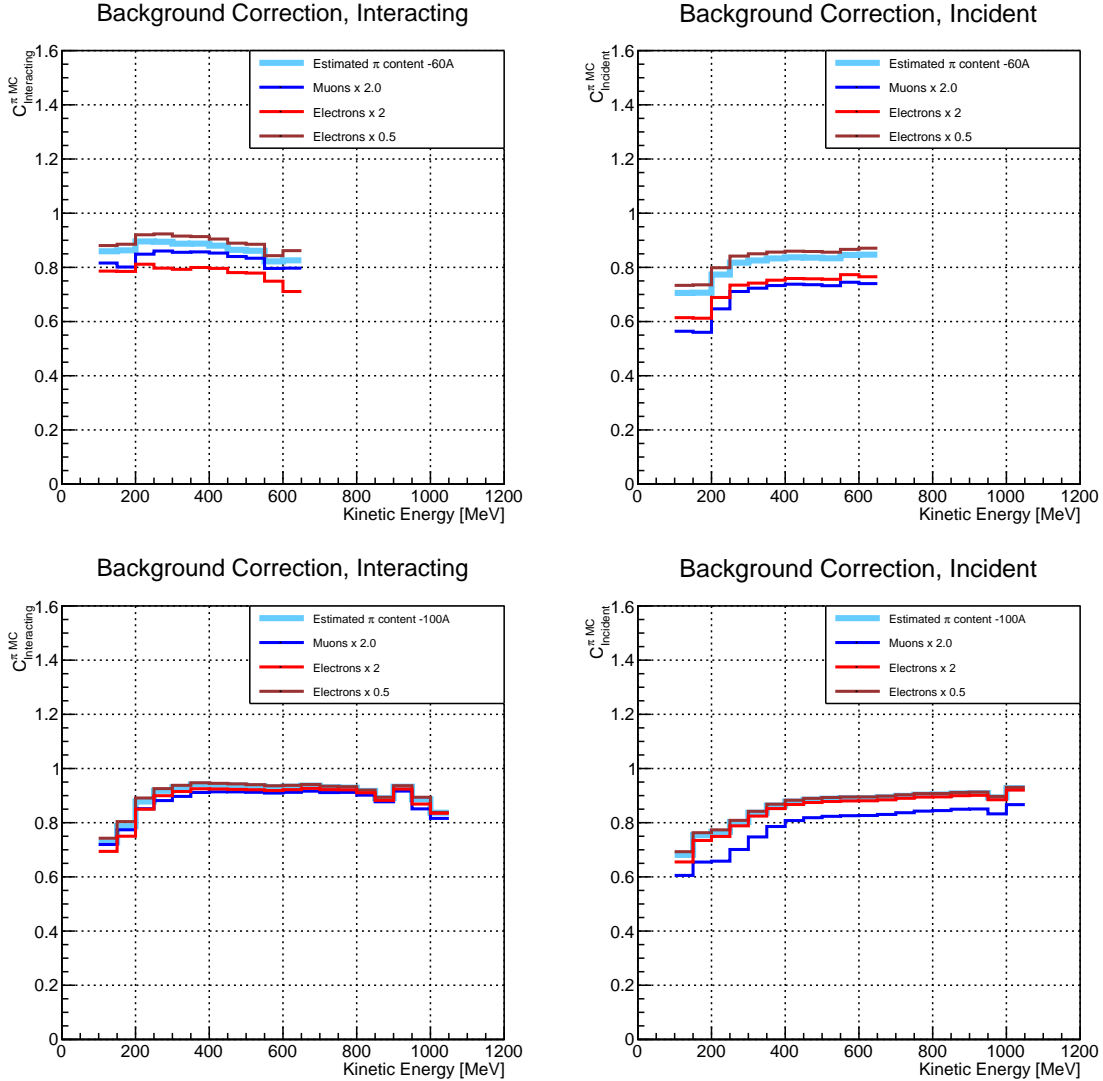


Figure 6.4: *Left:* MC estimated relative pion content for interacting histogram a function of kinetic energy for the 60A runs (top) and 100A runs (bottom), predicted background content in azure and muon and electron content variation in blue and red. *Right:* MC estimated relative pion content for incident histogram a function of kinetic energy for the 60A runs (top) and 100A (bottom), predicted background content in azure and muon and electron content variation in blue and red

2485 **6.2.2 Efficiency Correction**

2486 The interaction point for a track used in the total hadronic cross section analysis  
2487 is defined to be the last point of the WC2TPC matched track which lies inside the  
2488 fiducial volume. This definition is independent from the topology of the interaction.  
2489 If the TPC track stops within the fiducial volume, its last point will be the interaction  
2490 point, no matter what the products of the interaction look like; if the track crosses the  
2491 boundaries of the fiducial volume, the track will be considered “through going” and no  
2492 interaction point will be found. Given this definition, it is evident that we rely on the  
2493 tracking algorithm to discern where the interaction occurred in the TPC and correctly  
2494 stop the tracking. The tracking algorithm has an intrinsic angle resolution as shown  
2495 in section 5.5.1, which limits its efficiency, especially in the case of elastic scattering  
2496 occurring at low angles. Thus, we need to apply an efficiency correction to data in order  
2497 to retrieve the true cross section. The efficiency correction is evaluated separately for  
2498 the interacting and incident histograms, namely  $\epsilon_i^{\text{int}}$  and  $\epsilon_i^{\text{inc}}$ , and propagated to the  
2499 cross section as shown in equation 4.9.

2500 **Efficiency Correction: Procedure**

2501 We describe here the procedure to calculate the efficiency correction taking the in-  
2502 teracting histogram as example and noting that the procedure is identical for the  
2503 incident histogram.

2504 We derive the correction on a set of pure pion MC, calculating its value bin by  
2505 bin as the ratio between the true bin content and the correspondent reconstructed  
2506 bin content. The correction is then applied to the relevant bin in data. In formulae,  
2507 the efficiency correction is calculated to be

$$\epsilon^{\text{Int}}(E_i) = \frac{N_{\text{Interacting}}^{\pi \text{ Reco MC}}(E_i)}{N_{\text{Interacting}}^{\pi \text{ True MC}}(E_i)}, \quad (6.9)$$

2508 where  $N_{\text{Int}}^{\pi \text{ True MC}}(E_i)$  is the content of the  $i$ -th bin in for the true interacting  
 2509 histogram, and  $N_{\text{Int}}^{\pi \text{ Reco MC}}(E_i)$  is the content of the  $i$ -th bin in for the reconstructed  
 2510 interacting histogram. The correction is applied to data as follows

$$N_{\text{Int}}^{\pi \text{ True Data}}(E_i) = \frac{N_{\text{Int}}^{\pi \text{ Reco Data}}(E_i)}{\epsilon^{\text{Int}}(E_i)} = N_{\text{Int}}^{\pi \text{ Reco Data}}(E_i) \frac{N_{\text{Int}}^{\pi \text{ True MC}}(E_i)}{N_{\text{Int}}^{\pi \text{ Reco MC}}(E_i)}. \quad (6.10)$$

2511 where  $N_{\text{Int}}^{\pi \text{ Reco Data}}(E_i)$  is the background subtracted bin content of the  $i$ -th bin in  
 2512 for the reconstructed interacting histogram for data, i.e.

$$N_{\text{Int}}^{\pi \text{ Reco Data}}(E_i) = N_{\text{Int}}^{\text{TOT Data}}(E_i) - B_{\text{Int}}^{\text{Data}}(E_i) = C_{\text{Int}}^{\pi \text{ MC}}(E_i) N_{\text{Int}}^{\text{TOT Data}}(E_i). \quad (6.11)$$

2513 In section 5.5.1, we estimated the angular resolution for data and MC to be  
 2514  $\bar{\alpha}_{\text{Data}} = (5.0 \pm 4.5)$  deg and  $\bar{\alpha}_{\text{MC}} = (4.5 \pm 3.9)$  deg, respectively. Most interaction  
 2515 angles smaller than the angular resolution will thus be indistinguishable for the re-  
 2516 construction. Thus, we claim we are able to measure the cross section for interaction  
 2517 angles greater than 5.0 deg. Geant4 simulates interactions at all angles, as shown in  
 2518 figure 6.7. In order to calculate the efficiency correction, we select events which have  
 2519 an interaction angle greater than a given  $\alpha_{\text{res}}$  to construct the true interacting and  
 2520 incident histograms (the denominator of the efficiency correction). The systematics  
 2521 on the efficiency correction is estimated by varying the value of  $\alpha_{\text{res}}$  between 0 deg  
 2522 and 4.5 deg and propagating the uncertainty on the cross section.

2523 Figure 6.5 shows  $\epsilon^{\text{Int}}(E_i)$  in the left side and  $\epsilon^{\text{Inc}}(E_i)$  on the right as a function of  
 2524 the kinetic energy for the 60A runs and their systematic uncertainty. Similarly, figure  
 2525 6.6 shows  $\epsilon^{\text{Int}}(E_i)$  in the left side and  $\epsilon^{\text{Inc}}(E_i)$  on the right as a function of the kinetic  
 2526 energy for the 100A runs and their systematic uncertainty.

	Magnet Current -60A			Magnet Current -100 A		
	MC $\pi^-$	MC $\mu^-$	MC $e^-$	MC $\pi^-$	MC $\mu^-$	MC $e^-$
Expected Composition	68.8 %	4.6 %	26.6 %	87.4 %	3.7 %	8.9 %
Composition 2x Muons	64.2 %	9.2 %	26.6 %	83.7 %	7.4 %	8.9 %
Composition 2x Electrons	42.2 %	4.6 %	53.2 %	78.5 %	3.7 %	17.8 %
Composition 0.5x Electrons	82.1 %	4.6 %	13.3 %	91.9 %	3.7 %	4.4 %

Table 6.1: Beam composition variation for the study of systematics due to beam contamination.

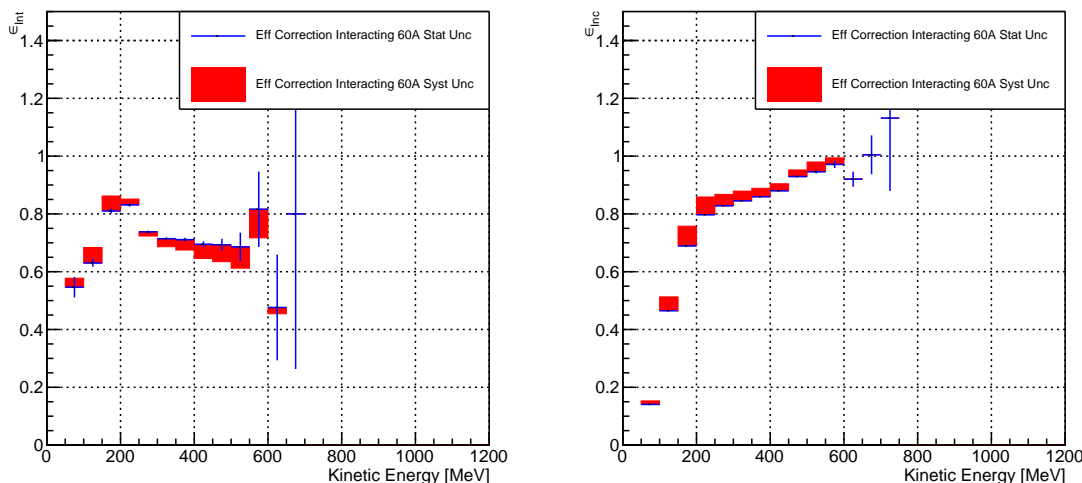


Figure 6.5: *Left:* Efficiency correction on the 60A interacting histogram, statistical uncertainty in blue, systematic uncertainty in red. *Right:* Efficiency correction on the 60A incident histogram, statistical uncertainty in blue, systematic uncertainty in red.

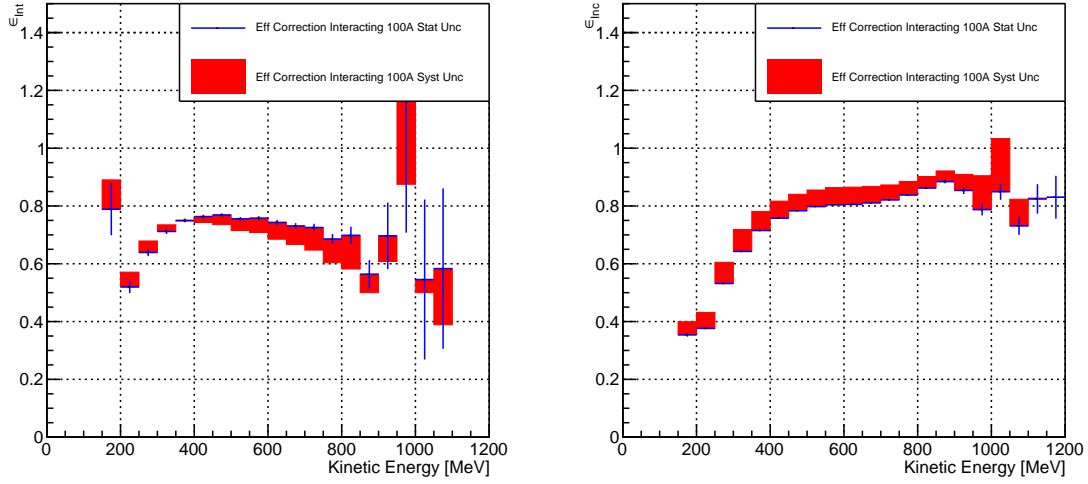


Figure 6.6: *Left*: Efficiency correction on the 100A interacting histogram, statistical uncertainty in blue, systematic uncertainty in red. *Right*: Efficiency correction on the 100A incident histogram, statistical uncertainty in blue, systematic uncertainty in red.

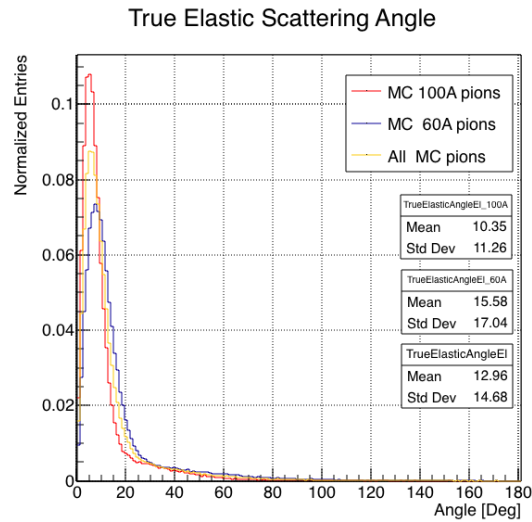


Figure 6.7: Distribution of the true scattering angle for a pion elastic scattering off the argon nucleus as simulated by Geant4.

2527 **6.3 Results**

2528 Figure 6.8 show the measurement of the ( $\pi^-$ -Ar) total hadronic cross section for  
2529 scattering angles greater than  $5^\circ$ , as the result of the background subtraction and  
2530 efficiency correction to the raw cross section. The top left plot is the measurement  
2531 obtained on the 60A data, statistical uncertainty in black and systematic uncertainty  
2532 in red. The top right plot is the measurement obtained on the 100A data, statistical  
2533 uncertainty in black and systematic uncertainty in blue. The bottom plot shows the  
2534 two measurements overlaid. In all three plot, the Geant4 prediction for the total  
2535 hadronic cross section for angle scattering greater than  $5^\circ$  is displayed in green.

2536 The systematic uncertainty on the cross section is the sum in quadrature of the  
2537 statistical uncertainty, the systematic uncertainty related to the kinetic energy mea-  
2538 surement, the systematic uncertainty related to the beam composition and the sys-  
2539 tematic uncertainty related to the efficiency correction.

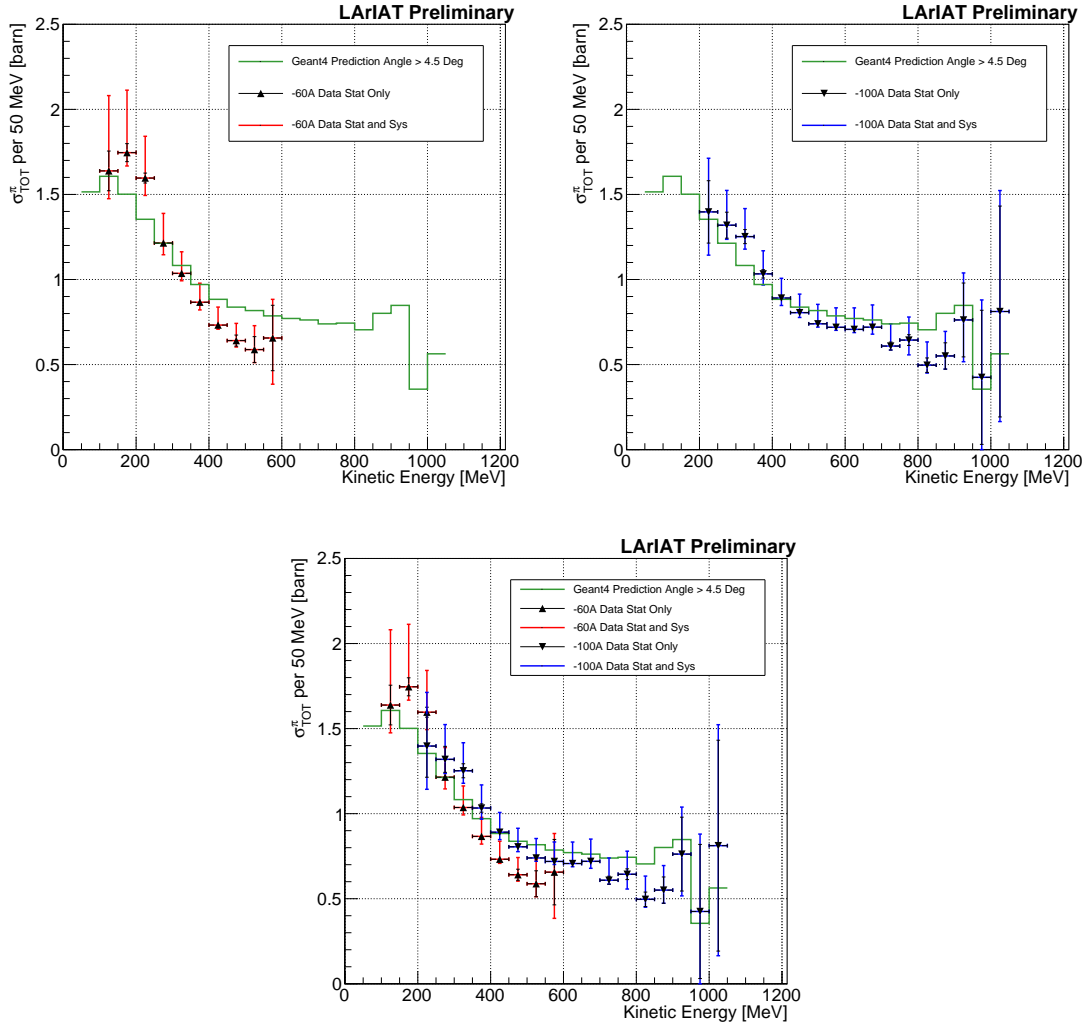


Figure 6.8: *Top Left:* ( $\pi^-$ -Ar) total hadronic cross section for scattering angles greater than  $5^\circ$  measured in the 60A sample, statistical uncertainty in black and systematic uncertainty in red. The Geant4 prediction for the total hadronic cross section for angle scattering greater than  $5^\circ$  is displayed in green.

*Top Right:* ( $\pi^-$ -Ar) total hadronic cross section for scattering angles greater than  $5^\circ$  measured in the 100A sample, statistical uncertainty in black and systematic uncertainty in blue. The Geant4 prediction for the total hadronic cross section for angle scattering greater than  $5^\circ$  is displayed in green.

*Bottom:* ( $\pi^-$ -Ar) total hadronic cross section measurements in the 60A and 100A samples overlaid with the Geant4 prediction (green).

2540 **Chapter 7**

2541 **Positive Kaon Cross Section**  
2542 **Measurement**

2543 “Beat-up little seagull, on a marble stair  
2544 Tryin’ to find the ocean, lookin’ everywhere.”  
2545 – Nina Simone, 1978 –

2546 In this chapter, we show the result of the thin slice method to measure the ( $K^+$ -  
2547 Ar) total hadronic cross section. In Section 7.1, we start by measuring the raw  
2548 cross section. In Section 7.2, we apply a statistical subtraction of the background  
2549 contributions based on simulation and a correction for detection inefficiency. The  
2550 final results are presented in Section 7.3.

2551 **7.1 Raw Cross Section**

2552 We measure the raw ( $K^+$ -Ar) total hadronic cross section as a function of the kinetic  
2553 energy in the combined +60A and +100A dataset.

2554 Similar to the pion case, the raw cross section is given by the equation 4.4

$$\sigma_{TOT}(E_i) = \frac{1}{n\delta X} \frac{N_{Int}^{TOT}(E_i)}{N_{Inc}^{TOT}(E_i)}, \quad (7.1)$$

2555 where  $N_{Int}^{TOT}$  is the measured number of particles interacting at kinetic energy  $E_i$ ,  
2556  $N_{Inc}^{TOT}$  is the measured number of particles incident on an argon slice at kinetic energy  
2557  $E_i$ ,  $n$  is the density of the target centers and  $\delta X$  is the thickness of the argon slice.  
2558 The density of the target centers and the slab thickness are  $n = 0.021 \cdot 10^{24} \text{ cm}^{-3}$  and  
2559  $\delta X = 0.47 \text{ cm}$ , respectively.

2560 As in the case of pions, kaons might decay or interact between WC4 and the TPC  
2561 front face. Some of the interaction products may be wrongly matched to the WC  
2562 track, forming the “secondary” particle’s background in the kaon sample. We estimate  
2563 the effect of the contamination of secondaries through the DDMC kaon sample. Figure  
2564 7.1 shows the distribution of  $N_{Int}^{TOT}$  as a function of the kinetic energy. The data  
2565 central points are represented by black dots, the statistical uncertainty is shown in  
2566 black, while the systematic uncertainty is shown in red. Data is displayed over the  
2567  $N_{Int}^{TOT}$  distribution obtained with a DDMC sample of kaons shot from WC4. The  
2568 contribution from the simulated kaons which interact hadronically is shown in pink,  
2569 the contributions from kaon decay is shown in orange and the one from secondaries  
2570 in red. The simulated kaon’s and secondaries’ contributions are stacked; the sum of  
2571 their integrals is normalized to the integral of the data.

2572 Figure 7.2 shows the distribution of  $N_{Inc}^{TOT}$ . Data is displayed over the MC. For the  
2573  $N_{Inc}^{TOT}$  distribution we do not make a distinction between kaons that decay or interact  
2574 hadronically because any kaon independently from its final interaction contributes  
2575 to the flux of incident particles at given kinetic energy. The same normalization  
2576 procedure is used for both the interacting and incident histograms.

2577 Figure 7.3 shows the raw cross section, statistical uncertainty in black and system-

atic uncertainty in red. The raw data cross section is overlaid to the reconstructed cross section for the MC mixed sample, displayed in azure. We calculate the statistical uncertainty for the interacting, incident and cross section distributions in a similar fashion to the pion case as described in Section 6.1.1.

As in the pion case, the only systematic effect considered in the measurement of the raw cross section results from the propagation of the uncertainty associate with the measurement of the kinetic energy at each argon slab. For kaons, the uncertainty on the kinetic energy of a candidate at the  $j^{th}$  slab of argon is given by

$$\delta KE_j = \sqrt{\delta p_{Beam}^2 + \delta E_{Loss}^2 + \delta E_{dep\ FF-j}^2} \quad (7.2)$$

$$= \sqrt{(2\% p_{Beam})^2 + (7\text{ [MeV]})^2 + (j - 1)^2(\sim 0.18\text{ [MeV]})^2}. \quad (7.3)$$

We propagate this uncertainty by varying the energy measurement  $KE_j$  at each argon slab. We measure  $N_{Inc}^{TOT}$ ,  $N_{Int}^{TOT}$  and the cross section in three cases: first assigning the measured  $KE_j$  at each kinetic energy sampling, then assigning  $KE_j + \delta KE_j$ , and finally assigning  $KE_j - \delta KE_j$ . The difference between the values obtained using the  $KE_j$  sampling and the maximum and minimum values in each kinetic energy bin determines the systematic uncertainty.

## 7.2 Corrections to the Raw Cross Section

As described in section 4.3.3, we need to apply a background correction and an efficiency correction in order to derive the true Kaon cross section from the raw cross section. The true cross section is given in equation 4.9,

$$\sigma_{TOT}^{K^+}(E_i) = \frac{1}{n\delta X} \frac{\epsilon^{Inc}(E_i)}{\epsilon^{Int}(E_i)} \frac{C_{Int}^{KMC}(E_i)}{C_{Inc}^{KMC}(E_i)} \frac{N_{Int}^{TOT}(E_i)}{N_{Inc}^{TOT}(E_i)}. \quad (4.9)$$

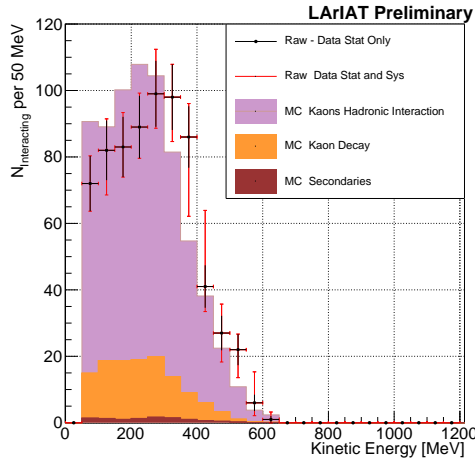


Figure 7.1: Raw number of interacting kaon candidates as a function of the reconstructed kinetic energy. The statistical uncertainties are shown in black, the systematic uncertainties in red.

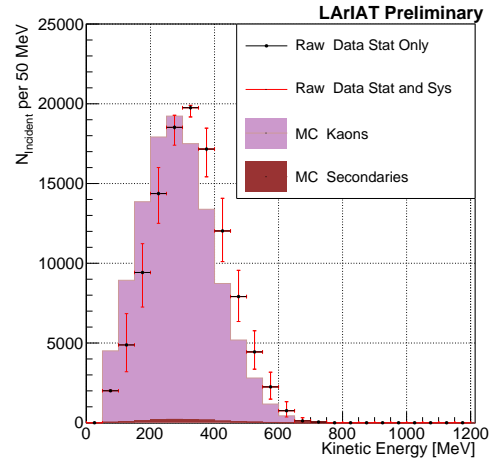


Figure 7.2: Raw number of incident kaon candidates as a function of the reconstructed kinetic energy. The statistical uncertainty is shown in black, the systematic uncertainties in red.

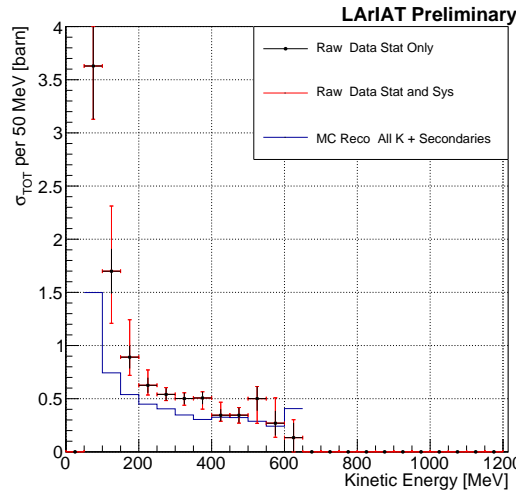


Figure 7.3: Raw ( $K^+$ -Ar) total hadronic cross section. The statistical uncertainty is shown in black, the systematic uncertainties in red. The raw cross section obtained with a MC sample of kaons is shown in blue. For the MC cross section, we include the contributions from secondaries.

2596 Currently, the only background considered for the kaon hadronic cross section  
2597 comes from the presence of secondaries. A further development of the analysis will  
2598 need to account for the presence of a small proton contamination. Figure 7.4 shows  
2599 the relative kaon content for the interacting and incident histograms.

2600 As described in 6.2.2 for the pion case, we derive the correction on a set of pure  
2601 kaon MC, calculating its value bin by bin as the ratio between the true bin content  
2602 and the correspondent reconstructed bin content. The correction is then applied to  
2603 the relevant bin in data. The efficiency correction is evaluated separately for the  
2604 interacting and incident histograms, namely  $\epsilon_i^{\text{int}}$  and  $\epsilon_i^{\text{inc}}$ , and propagated to the cross  
2605 section as shown in equation 4.9.

2606 In section 5.5.1, we estimated the angular resolution for data and MC to be  
2607  $\bar{\alpha}_{\text{Data}} = (4.3 \pm 3.7)$  deg and  $\bar{\alpha}_{\text{MC}} = (4.4 \pm 3.6)$  deg, respectively. Most interaction  
2608 angles smaller than the angular resolution will thus be indistinguishable for the re-  
2609 construction. Thus, we claim we are able to measure the cross section for interaction  
2610 angles greater than 4.5 deg. Geant4 simulates interactions at all angles: in order to  
2611 calculate the efficiency correction, we select events which have an interaction angle  
2612 greater than a  $\alpha_{\text{res}}$  to construct the true interacting and incident histograms (the de-  
2613 nominator of the efficiency correction). The systematics on the efficiency correction  
2614 is estimated by varying the value of  $\alpha_{\text{res}}$  between 0 deg and 4.5 deg and propagating  
2615 the uncertainty on the cross section.

2616 Figure 7.5 shows  $\epsilon^{\text{Int}}(E_i)$  in the left side and  $\epsilon^{\text{Inc}}(E_i)$  on the right as a function of  
2617 the kinetic energy for the kaon sample and their systematic uncertainty.

## 2618 7.3 Results

2619 Figure 7.6 show the measurement of the ( $K^+$ -Ar) total hadronic cross section for  
2620 scattering angles greater than  $5^\circ$ , as the result of the background subtraction and

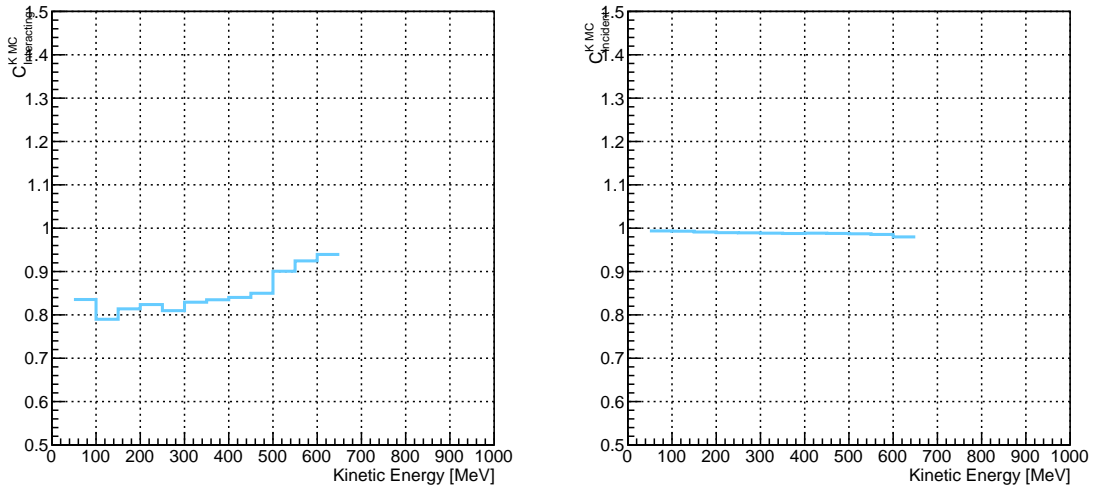


Figure 7.4: *Left:* MC estimated relative kaon content for kaons interacting hadronically as function of kinetic energy. *Right:* MC estimated relative kaon content for incident histogram a function of kinetic energy.

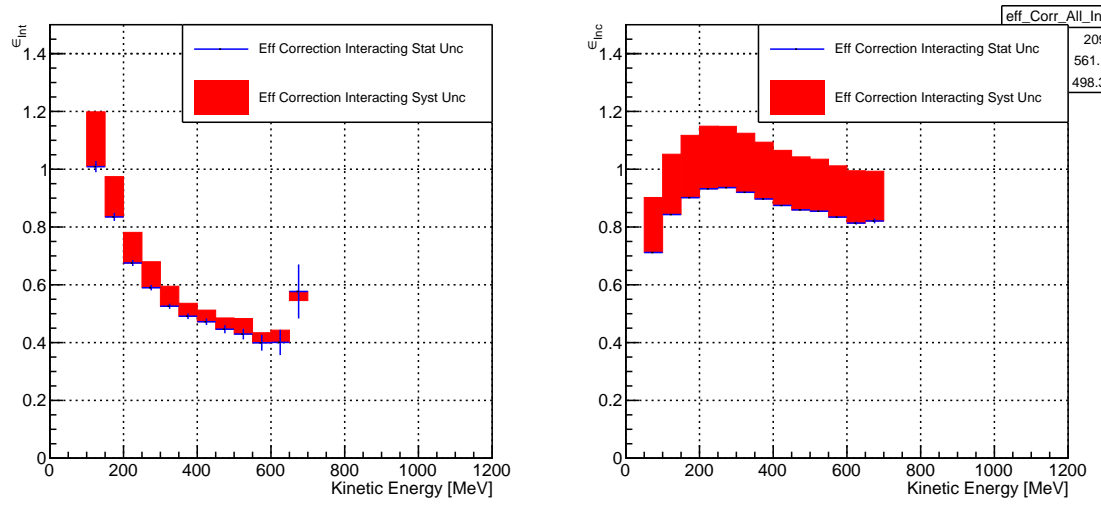


Figure 7.5: *Left:* Efficiency correction on the interacting histogram, statistical uncertainty in blue, systematic uncertainty in red. *Right:* Efficiency correction on the incident histogram, statistical uncertainty in blue, systematic uncertainty in red.

2621 efficiency correction to the raw cross section. The plot shows the measurement ob-  
 2622 tained on the full dataset, statistical uncertainty in black and systematic uncertainty  
 2623 in red. The Geant4 prediction for the total hadronic cross section for angle scattering  
 2624 greater than  $5^\circ$  is displayed in green.

2625 The systematic uncertainty on the cross section is the sum in quadrature of the  
 2626 statistical uncertainty, the systematic uncertainty related to the kinetic energy mea-  
 2627 surement and the systematic uncertainty related to the efficiency correction.

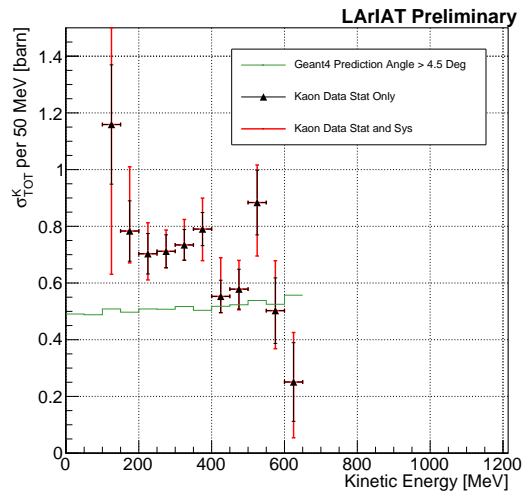


Figure 7.6: ( $K^+$ -Ar) total hadronic cross section for scattering angles greater than  $5^\circ$  measured in the 60A sample, statistical uncertainty in black and systematic uncertainty in red. The Geant4 prediction for the total hadronic cross section for angle scattering greater than  $5^\circ$  is displayed in green.

2628 **Chapter 8**

2629 **Conclusions**

2630 In the era of neutrino precision measurements, of huge liquid argon detectors and  
2631 of massive amount of information from LArTPCs, a renewed interest for an ancient  
2632 measurement arises: the measurement of hadronic interactions with matter. With  
2633 this work, we presented the first ever ( $\pi^-$ -Ar) and ( $K^+$ -Ar) total hadronic cross  
2634 section measurements as a function of the hadron kinetic energy. These analyses are  
2635 the first physics analyses developed by the LArIAT experiment. Both the analysis  
2636 follow a similar workflow and they rely on beam line detector information as well as  
2637 both calorimetry and tracking in the TPC.

2638 In order to measure ( $\pi^-$ -Ar) total hadronic argon cross sections, we start by  
2639 selecting pion beamline candidates through a series of selections on the beamline  
2640 and TPC information apt to maximize the number of pions in the selection over  
2641 the number of muons and electrons. We use the LArIAT beamline MC to estimate  
2642 the beam composition of the selected beamline candidates and we propagate them  
2643 to the LArIAT TPC constructing a properly weighted sample with the DDMC. We  
2644 apply the thin slice method on the pion candidates and obtain the raw cross section  
2645 measurement. From the simulated sample, we obtain two corrections accounting for  
2646 the beamline background contamination and for detector effects. Finally, we apply

2647 the corrections to data and measure the true cross section.

2648 In order to measure ( $K^+$ -Ar) total hadronic argon cross sections, we follow a  
2649 similar procedure, i.e. we apply the thin slice method on kaon candidates identified  
2650 in the beamline to obtain the raw cross section. We apply a background correction and  
2651 a correction for detector effects to the raw cross section. The background correction  
2652 accounts for the presence of secondary particles in both the interacting and incident  
2653 histograms and for the presence of decay events in the interacting plot.

2654 The final results for the ( $\pi^-$ -Ar) and ( $K^+$ -Ar) total hadronic cross section are  
2655 shown side by side in figure 8.1.

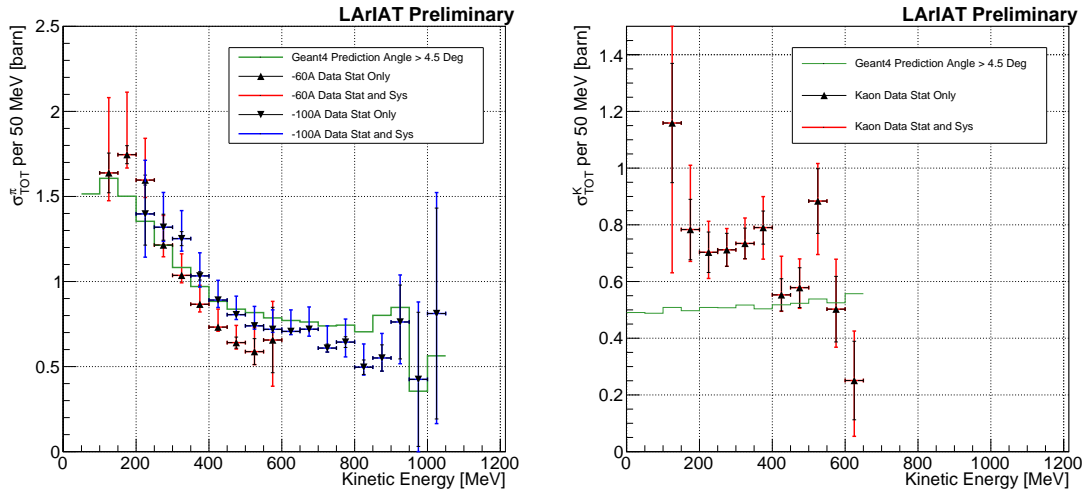


Figure 8.1: *Left:* ( $\pi^-$ -Ar) total hadronic cross section measurements in the 60A and 100A samples overlaid with the Geant4 prediction (green). *Right:* ( $K^+$ -Ar) total hadronic cross section for scattering angles greater than  $5^\circ$  measured in the 60A sample, statistical uncertainty in black and systematic uncertainty in red. The Geant4 prediction for the total hadronic cross section for angle scattering greater than  $5^\circ$  is displayed in green.

2656 These analyses' will serve as a basis for the future cross section measurements of  
2657 pions and kaons for the exclusive channels in LArIAT.

2658 **Appendix A**

2659 **Measurement of LArIAT Electric  
2660 Field**

2661 The electric field of a LArTPC in the drift volume is a fundamental quantity for  
2662 the proper functionality of this technology, as it affects almost every reconstructed  
2663 quantity such as the position of hits or their collected charge. Given its importance,  
2664 we calculate the electric field for LArIAT with a single line diagram from our HV  
2665 circuit and we cross check the obtained value with a measurement relying only on  
2666 TPC data.

2667 Before getting into the details of the measurement procedures, it is important to  
2668 explicit the relationship between some quantities in play. The electric field and the  
2669 drift velocity ( $v_{drift}$ ) are related as follows

$$v_{drift} = \mu(E_{field}, T)E_{field}, \quad (\text{A.1})$$

2670 where  $\mu$  is the electron mobility, which depends on the electric field and on the  
2671 temperature (T). The empirical formula for this dependency is described in [115]  
2672 and shown in Figure A.1 for several argon temperatures.

2673 The relationship between the drift time ( $t_{drift}$ ) and the drift velocity is trivially

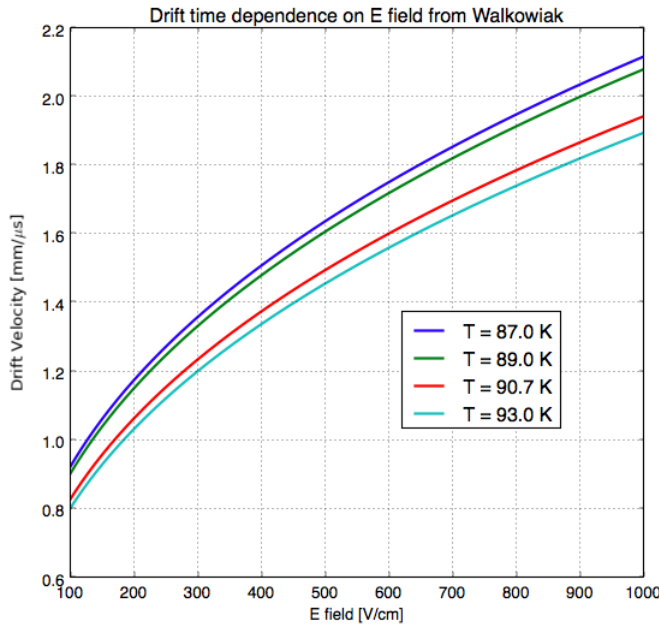


Figure A.1: Drift velocity dependence on electric field for several temperatures. The slope of the line at any one point represents the electron mobility for that given temperature and electric field.

Table A.1: Electric field and drift velocities in LArIAT smaller drift volumes

	Shield-Induction	Induction-Collection
$E_{field}$	700.63 V/cm	892.5 V/cm
$v_{drift}$	1.73 mm/μs	1.90 mm/μs
$t_{drift}$	2.31 μs	2.11 μs

2674 given by

$$t_{drift} = \Delta x / v_{drift}, \quad (\text{A.2})$$

2675 where  $\Delta x$  is the distance between the edges of the drift region. Table A.1 reports the  
2676 values of the electric field, drift velocity, and drift times for the smaller drift volumes.

2677 With these basic parameters established, we can now move on to calculating the  
2678 electric field in the main drift region (between the cathode and the shield plane).

## 2679 Single line diagram method

2680 The electric field strength in the LArIAT main drift volume can be determined know-  
 2681 ing the voltage applied to the cathode, the voltage applied at the shield plane, and the  
 2682 distance between them. We assume the distance between the cathode and the shield  
 2683 plane to be 470 mm and any length contraction due to the liquid argon is negligibly  
 2684 small ( $\sim 2$  mm).

2685 The voltage applied to the cathode can be calculated using Ohm's law and the  
 2686 single line diagram shown in Figure A.2. A set of two of filter pots for emergency  
 2687 power dissipation are positioned between the Glassman power supply and the cathode,  
 2688 one at each end of the feeder cable, each with an internal resistance of  $40 \text{ M}\Omega$ .

2689 Given the TPC resistor chain, the total TPC impedance is  $6 \text{ G}\Omega$ . Since the total  
 2690 resistance on the circuit is driven by the TPC impedance, we expect the resulting  
 2691 current to be

$$I = V_{PS}/R_{tot} = -23.5 \text{ kV}/6 \text{ G}\Omega \sim 4 \mu\text{A}, \quad (\text{A.3})$$

2692 which we measure with the Glassman power supply, shown in Figure A.3.

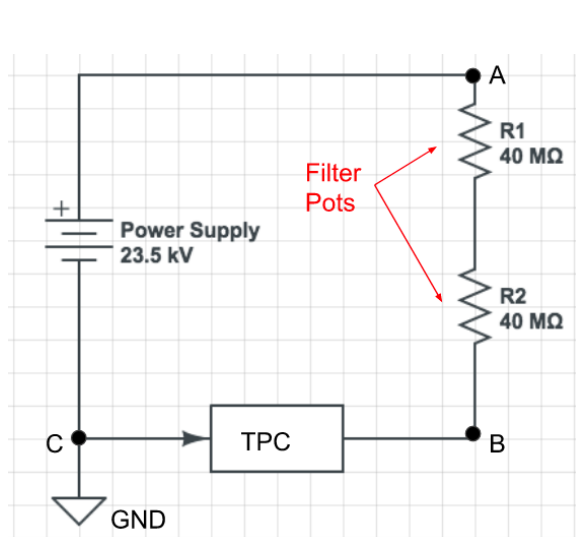


Figure A.2: LArIAT HV simple schematics.

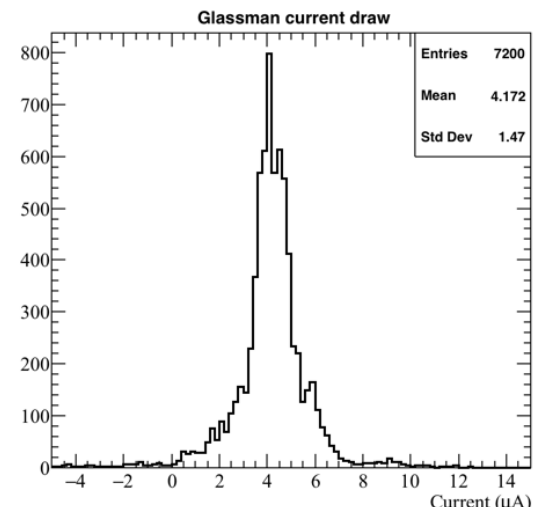


Figure A.3: Current reading from the Glassman between May 25th and May 30th, 2016 (typical Run-II conditions).

2693 Using this current, the voltage at the cathode is calculated as

$$V_{BC} = V_{PS} - (I \times R_{eq}) = -23.5 \text{ kV} + (0.00417 \text{ mA} \times 80 \text{ M}\Omega) = -23.17 \text{ kV}, \quad (\text{A.4})$$

2694 where  $I$  is the current and  $R_{eq}$  is the equivalent resistor representing the two filter  
2695 pots. The electric field is then calculated to be

$$E_{\text{field}} = \frac{V_{BC} - V_{\text{shield}}}{\Delta x} = 486.54 \text{ V/cm}. \quad (\text{A.5})$$

2696 **E field using cathode-anode piercing tracks**

2697 We devise an independent method to measure the drift time (and consequently drift  
2698 velocity and electric field) using TPC cathode to anode piercing tracks. We use this  
2699 method as a cross check to the single line method. The basic idea is simple:

- 2700 0. Select cosmic ray events with only 1 reconstructed track
- 2701 1. Reduce the events to the one containing tracks that cross both anode and cath-  
2702 ode
- 2703 2. Identify the first and last hit of the track
- 2704 3. Measure the time difference between these two hits ( $\Delta t$ ).

2705 This method works under the assumptions that the time it takes for a cosmic particle  
2706 to cross the chamber ( $\sim \text{ns}$ ) is small compared to the charge drift time ( $\sim \text{hundreds}$   
2707 of  $\mu\text{s}$ ).

2708 We choose cosmic events to allow for a high number of anode to cathode piercing  
2709 tracks (ACP tracks), rejecting beam events where the particles travel almost perpen-  
2710 dicularly to drift direction. We select events with only one reconstructed track to  
2711 maximize the chance of selecting a single crossing muon (no-michel electron). We  
2712 utilize ACP tracks because their hits span the full drift length of the TPC, see figure

2713 A.4, allowing us to define where the first and last hit of the tracks are located in space  
2714 regardless of our assumption of the electric field.

2715 One of the main features of this method is that it doesn't rely on the measurement  
2716 of the trigger time. Since  $\Delta t$  is the time difference between the first and last hit of a  
2717 track and we assume the charge started drifting at the same time for both hits, the  
2718 measurement of the absolute beginning of drift time  $t_0$  is unnecessary. We boost the  
2719 presence of ACP tracks in the cosmic sample by imposing the following requirements  
2720 on tracks:

- 2721 • vertical position (Y) of first and last hits within  $\pm 18$  cm from TPC center  
2722 (avoid Top-Bottom tracks)
- 2723 • horizontal position (Z) of first and last hits within 2 and 86 cm from TPC front  
2724 face (avoid through going tracks)
- 2725 • track length greater than 48 cm (more likely to be crossing)
- 2726 • angle from the drift direction (phi in figure A.5) smaller than 50 deg (more  
2727 reliable tracking)
- 2728 • angle from the beam direction (theta in figure A.5) greater than 50 deg (more  
2729 reliable tracking)

2730 Tracks passing all these selection requirements are used for the  $\Delta t$  calculation.

2731 For each track passing our selection, we loop through the associated hits to retrieve  
2732 the timing information. The analysis is performed separately on hits on the collection  
2733 plane and induction plane, but lead to consistent results. As an example of the time  
2734 difference, figures A.6 and A.7 represent the difference in time between the last and  
2735 first hit of the selected tracks for Run-II Positive Polarity sample on the collection  
2736 and induction plane respectively. We fit with a Gaussian to the peak of the  $\Delta t$   
2737 distributions to extract the mean drift time and the uncertainty associated with it.

2738 The long tail at low  $\Delta t$  represents contamination of non-ACP tracks in the track  
2739 selection. We apply the same procedure to Run-I and Run-II, positive and negative  
2740 polarity alike.

2741 To convert  $\Delta t$  recorded for the hits on the induction plane to the drift time we  
2742 employ the formula

$$t_{drift} = \Delta t - t_{S-I} \quad (\text{A.6})$$

2743 where  $t_{drift}$  is the time the charge takes to drift in the main volume between the  
2744 cathode and the shield plane and  $t_{S-I}$  is the time it takes for the charge to drift from  
2745 the shield plane to the induction plane. In Table A.1 we calculated the drift velocity  
2746 in the S-I region, thus we can calculate  $t_{S-I}$  as

$$t_{S-I} = \frac{l_{S-I}}{v_{S-I}} = \frac{4mm}{1.73mm/\mu s} \quad (\text{A.7})$$

2747 where  $l_{S-I}$  is the distance between the shield and induction plane and  $v_{S-I}$  is the drift  
2748 velocity in the same region. A completely analogous procedure is followed for the hits  
2749 on the collection plane, taking into account the time the charge spent in drifting from  
2750 shield to induction as well as between the induction and collection plane. The value  
2751 for  $\Delta t_{drift}$ , the calculated drift velocity ( $v_{drift}$ ), and corresponding drift electric field  
2752 for the various run periods is given in Table A.2 and are consistent with the electric  
2753 field value calculated with the single line diagram method.

### Delta $t_{drift}$ , drift v and E field with ACP tracks

Data Period	$\Delta t_{Drift}$ [ $\mu s$ ]	Drift velocity [mm/ $\mu s$ ]	E field [V/cm]
RunI Positive Polarity Induction	$311.1 \pm 2.4$	$1.51 \pm 0.01$	$486.6 \pm 21$
RunI Positive Polarity Collection	$310.9 \pm 2.6$	$1.51 \pm 0.01$	$487.2 \pm 21$
RunII Positive Polarity Induction	$315.7 \pm 2.8$	$1.49 \pm 0.01$	$467.9 \pm 21$
RunII Positive Polarity Collection	$315.7 \pm 2.7$	$1.49 \pm 0.01$	$467.9 \pm 21$
RunII Negative Polarity Induction	$315.9 \pm 2.6$	$1.49 \pm 0.01$	$467.1 \pm 21$
RunII Negative Polarity Collection	$315.1 \pm 2.8$	$1.49 \pm 0.01$	$470.3 \pm 21$
Average Values	314.1	$1.50 \pm 0.01$	$474.3 \pm 21$

Table A.2:  $\Delta t$  for the different data samples used for the Anode-Cathode Piercing tracks study.

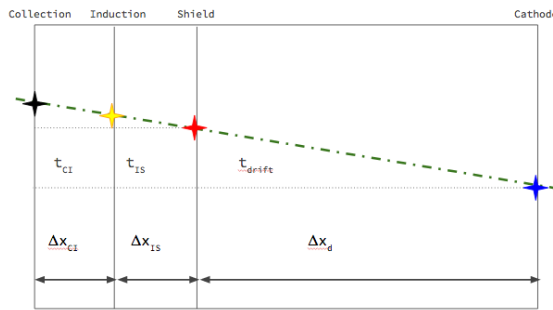


Figure A.4: Pictorial representation of the YX view of the TPC. The distance within the anode planes and between the shield plane and the cathode is purposely out of proportion to illustrate the time difference between hits on collection and induction. An ACP track is shown as an example.

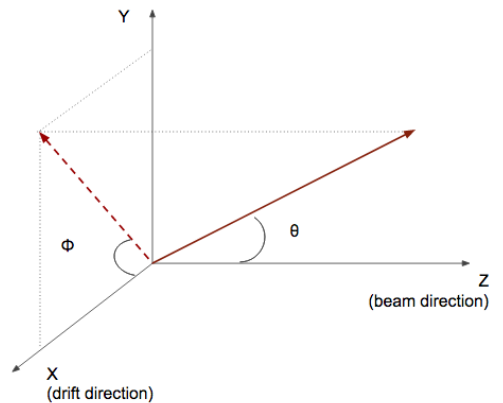


Figure A.5: Angle definition in the context of LArIAT coordinate system.

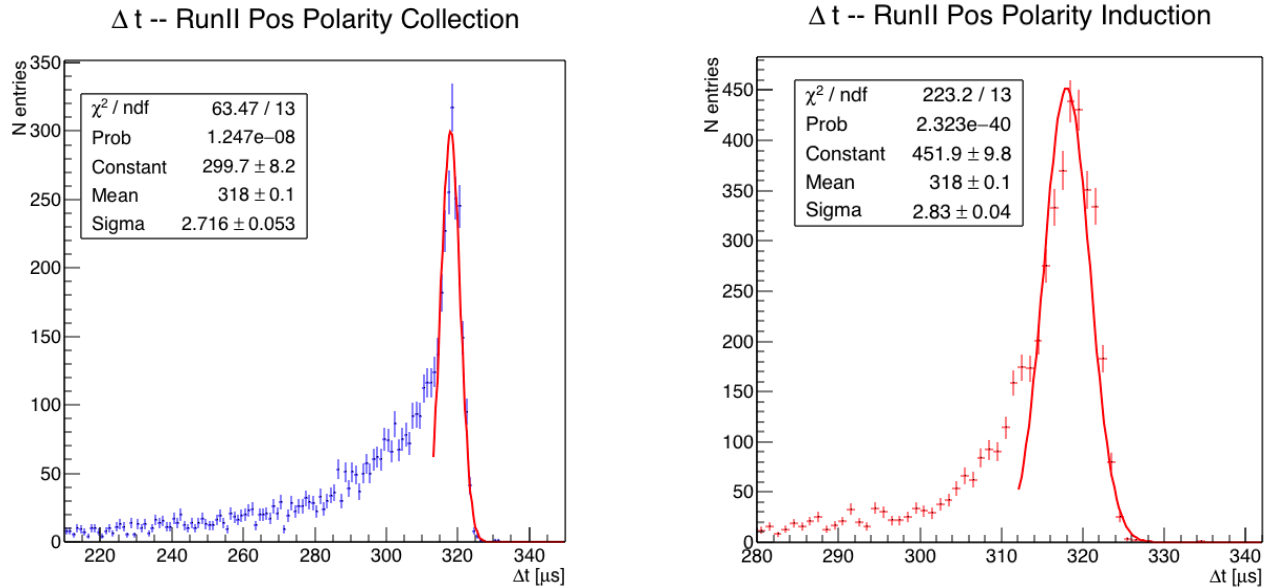


Figure A.6: Collection plane  $\Delta t$  fit for Run II positive polarity ACP data selected tracks.

Figure A.7: Induction plane  $\Delta t$  fit for Run II positive polarity ACP data selected tracks.

2754 **Appendix B**

2755 **Additional Tracking Studies for**  
2756 **LArIAT Cross Section Analyses**

2757 In this section, we describe two studies. The first is a justification of the selection  
2758 criteria for the beamline handshake with the TPC information. We perform this  
2759 study to boost the correct identification of the particles in the TPC associated with  
2760 the beamline information, while maintaining sufficient statistics for the cross section  
2761 measurement. The second study is an optimization of the tracking algorithm, with  
2762 the scope of maximizing the identification of the hadronic interaction point inside the  
2763 TPC. These two studies are related, since the optimization of the tracking is per-  
2764 formed on TPC tracks which have been matched to the wire chamber track; in turn,  
2765 the tracking algorithm for TPC tracks determines the number of reconstructed tracks  
2766 in each event used to try the matching with the wire chamber track. Starting with  
2767 a sensible tracking reconstruction, we perform the WC2TPC matching optimization  
2768 first, then the tracking optimization. The WC2TPC match purity and efficiency are  
2769 then calculated again with the optimized tracking.

2770 **B.0.1 Study of WC to TPC Match**

2771 Scope of this study is assessing the performances of the WC2TPC match on Monte  
2772 Carlo (see Section 4.2 ) and decide the selection values we will use on data. A  
2773 word of caution is necessary here. With this study, we want to minimize pathologies  
2774 associated with the presence of the primary hadron itself, e.g. the incorrect association  
2775 between the beamline hadron and its decay products inside the TPC. Assessing the  
2776 contamination from pile-up<sup>1</sup>, albeit related, is beyond the scope of this study.

2777 In MC, we are able to define a correct WC2TPC match using the Geant4 truth  
2778 information. We are thus able to count how many times the WC tracks is associated  
2779 with the wrong TPC reconstructed track.

2780 We define a correct match if the all following conditions are met:

- 2781 - the length of the true primary Geant4 track in the TPC is greater than 2 cm,  
2782 - the length of the reconstructed track length is greater than 2 cm,  
2783 - the Z position of the first reconstructed point is within 2 cm from the TPC  
2784 front face  
2785 - the distance between the reconstructed track and the true entering point is the  
2786 minimum compared with all the other reconstructed tracks.

2787 In order to count the wrong matches, we consider all the reconstructed tracks  
2788 whose Z position of the first reconstructed point lies within 2 cm from the TPC front  
2789 face. Events with true length in TPC < 2 cm are included. Since hadrons are shot  
2790 100 cm upstream from the TPC front face, the following two scenarios are possible  
2791 from a truth standpoint:

2792 [Ta ] the primary hadron decays or interact strongly before getting to the TPC,

---

1. We remind the reader that the DDMC is a single particle Monte Carlo, where the beam pile up is not simulated.

2793 [Tb ] the primary hadron enters the TPC.

2794 As described in Section 4.2, we define a WC2TPC match according to the relative  
2795 position of the WC and TPC track parametrized with  $\Delta R$  and the angle between  
2796 them, parametrized with  $\alpha$ . Once we choose the selection values  $r_T$  and  $\alpha_T$  to de-  
2797 termine a reconstructed WC2TPC match, the following five scenarios are possible in  
2798 the truth to reconstruction interplay :

- 2799 1) only the correct track is matched  
2800 2) only one wrong track is matched  
2801 3) the correct track and one (or more) wrong tracks are matched  
2802 4) multiple wrong tracks matched.  
2803 5) no reconstructed tracks are matched

2804 Since we keep only events with one and only one match, we discard cases 3), 4)  
2805 and 5) from the events used in the cross section measurement. For each set of  $r_T$  and  
2806  $\alpha_T$  selection value, we define purity and efficiency of the selection as follows:

$$\text{Efficiency} = \frac{\text{Number of events correctly matched}}{\text{Number of events with primary in TPC}}, \quad (\text{B.1})$$

$$\text{Purity} = \frac{\text{Number of events correctly matched}}{\text{Total number of matched events}}. \quad (\text{B.2})$$

2807 Figure B.1 shows the efficiency (left) and purity (right) for WC2TPC match as  
2808 a function of the radius,  $r_T$ , and angle,  $\alpha_T$ , selection value. It is apparent how both  
2809 efficiency and purity are fairly flat as a function of the radius selection value at a  
2810 given angle. This is not surprising. Since we are studying a single particle gun Monte  
2811 Carlo sample, the wrong matches can occur only for mis-tracking of the primary or

2812 for association with decay products; decay products will tend to be produced at large  
 2813 angles compared to the primary, but could be fairly close to the in  $x$  and  $y$  projection  
 2814 of the primary. The radius cut would play a key role in removing pile up events.

2815 For LArIAT cross section measurements, we generally prefer purity over efficiency,  
 2816 since a sample of particles of a pure species will lead to a better measurement. Ob-  
 2817 viously, purity should be balanced with a sensible efficiency to avoid rejecting the  
 2818 whole sample.

2819 We choose  $(\alpha_T, r_T) = (8 \text{ deg}, 4 \text{ cm})$  and get a MC 85% efficiency and 98% purity  
 2820 for the kaon sample and a MC 95% efficiency and 90% purity for the pion sample.

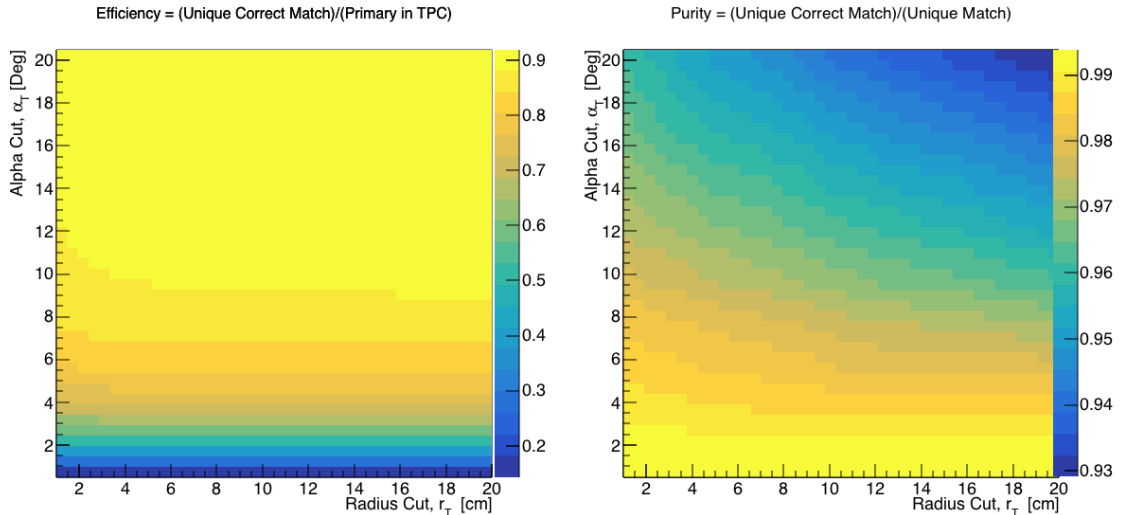


Figure B.1: Efficiency (left) and purity (right) for WC2TPC match as a function of the radius and angle selections for the kaon sample.

### 2821 B.0.2 Tracking Optimization

2822 We perform an optimization of the clustering algorithm (see Section 2.1.5) with  
 2823 the scope of maximizing the efficiency of finding the interaction point for the to-  
 2824 tal hadronic cross section measurements. We define as the interaction point the most  
 2825 downstream point of a WC2TPC matched TPC tracks within the TPC fiducial vol-  
 2826 ume. Since all the WC2TPC tracks are by definition beam particles, tracks travel

2827 from upstream to downstream in the TPC; thus, identifying the interaction point  
2828 means to stop the tracking correctly.

2829 TrajCluster is the package used to cluster hits in LArIAT; this package counts more  
2830 than 20 tunable parameters. A standard method to develop clustering algorithms and  
2831 checking their performances is to “hand scan”, which means recognizing the effect of  
2832 parameters tuning by looking at a series of data event displays. Albeit we recognize  
2833 the importance of hand scanning as a great diagnosis tool, we developed a fully  
2834 automated optimization package which compares MC reconstructed information to  
2835 MC truth.

2836 We start by defining a figure of merit in order to discern what makes a parameter  
2837 configuration better than an other. We chose the percentage of events whose recon-  
2838 structed and true length differ less than 2 cm. We then identify the parameters in  
2839 TrajCluster that are most important to correctly stop the tracking and an appropriate  
2840 range of values for each of them. We chose to optimize the parameters that leverage  
2841 on the angle between consecutive groups of hits, the number of hits use in the cluster  
2842 fit and the average hit charge to stop the tracking. We define a configuration space  
2843 with all possible combination of values for the chosen parameters and we perform  
2844 reconstruction one combination at a time: the combination with the highest figure of  
2845 merit determines the optimized tracking reconstruction.

2846 We chose construct the combination space using a total of 5 parameters, 3 values  
2847 each and two iterations of the method (for a total of 486 combinations). We run the  
2848 combinations on a sample of 100000 pion events. After the optimization, the most  
2849 upstream point of the tracking is correctly identified 99.5% of the times, the most  
2850 downstream point is correctly identified 62.5% of the times, the tracking stops short  
2851 about 15% of the times and misses the interaction point 22.5% of the times. Hand  
2852 scanning confirmed that the missed interaction points happen in the vast majority of  
2853 cases for very shallow angles, as shown in the event display in Figure, or in the case

2854 of angles visible only in one projection plane. We also noticed that the premature  
2855 stopping of the tracks is often related to the presence of delta rays parallel to the  
2856 track. We see room of improvement, such as the delta ray removal and a forced track  
2857 breaking in case of a kink present in a single plane, for a future analysis. **ADD evd**

2858 The procedure behind this optimization package is virtually applicable to any  
2859 LArSoft module where it is possible to define figure of merit.

2860 **Appendix C**

2861 **Energy Calibration**

2862 Scope of the energy calibration is to identify the factors which convert the charge  
2863 collected ( $dQ$ ) to energy deposited in the chamber ( $dE$ ). As described in section  
2864 2.1.5, this is a multi-step procedure. In LArIAT, we first correct the raw charge by  
2865 the electronic noise on the considered wire [103], then by the electron lifetime [104],  
2866 and then by the recombination using the ArgoNeut recombination values. Lastly, we  
2867 apply overall calibration of the energy, i.e. we determine the “calorimetry constants”  
2868 using the procedure described in this section.

2869 We independently determine the calorimetry constants for Data and Monte Carlo  
2870 in the LArIAT Run-II Data samples using a parametrization of the stopping power  
2871 (a.k.a. energy deposited per unit length,  $dE/dX$ ) as a function of momentum. This is  
2872 done by comparing the stopping power measured on reconstructed quantities against  
2873 the Bethe-Bloch theoretical prediction for various particle species (see Equation 2.1).  
2874 We obtain the theoretical expectation for the  $dE/dX$  most probable value of pions  
2875 ( $\pi$ ), muons ( $\mu$ ), kaons ( $K$ ), and protons ( $p$ ) in the momentum range most relevant  
2876 for LArIAT (Figure C.1) using the tables provided by the Particle Data Group [101]  
2877 for liquid argon [1].

2878 The basic idea of this calibration technique is to utilize a sample of beamline

2879 events with known particle species and momentum to measure the  $dE/dX$  of the  
2880 corresponding tracks in the TPC. In particular, we decided to use positive pions as  
2881 calibration sample and samples from all the other particle species as cross check. Once  
2882 the  $dE/dX$  of the positive pion sample has been measured at various momenta, we  
2883 tune to calorimetry constants within the reconstruction software to align the measured  
2884 values to match the theoretical ones found in Figure C.1.

2885 In data, we start by selecting a sample of beamline positive pion beamline can-  
2886 didates without any restriction on their measured momentum<sup>1</sup>. We then apply the  
2887 WC2TPC match and subtract the energy loss upstream to the TPC front face, de-  
2888 termining the momentum at the TPC front face. For each surviving pion candidate,  
2889 we measure the  $dE/dx$  at each of the first 12 spacepoints associated the 3D recon-  
2890 structed track, corresponding to a  $\sim 5$  cm portion. These  $dE/dX$  measurements are  
2891 then put into a histogram that corresponds to measured momentum of the track.  
2892 The  $dE/dX$  histograms are sampled every 50 MeV/c in momentum (e.g. 150 MeV/c  
2893  $< P < 200$  MeV/c, 200 MeV/c  $< P < 250$ /c MeV, etc...). This process of selecting,  
2894 sampling, and recording the  $dE/dX$  for various momentum bins is repeated over the  
2895 entire sample of events, allowing us to collect sufficient statistic in most of the mo-  
2896 mentum bins between 150 MeV/c and 1100 MeV/c. On average, pions and muons  
2897 only lose  $\sim 10$  MeV in this 5 cm section of the track and protons lose  $\sim 20$  MeV. Thus  
2898 choosing 50 MeV/c size bins for our histograms covers the energy spread within those  
2899 bins due to energy loss from ionization for all the particle species identifiable in the  
2900 beamline. Each 50 MeV/c momentum binned  $dE/dX$  histogram is now fit with a  
2901 simple Landau function. The most probable value (MPV) and the associated error  
2902 on the MPV from the fit are extracted and plotted against the theoretical prediction  
2903 Figure C.1. Depending on the outcome of the data-prediction comparison, we modify  
2904 the calorimetry constants and we repeat the procedure until a qualitative agreement

---

2904 1. it should be noted that some muon and position contamination is present in the  $\pi^+$  sample

2905 is achieved. We perform this tuning for the collection and induction plane separately.  
 2906 As a cross check to the calorimetry constants determined using the positive pions,  
 2907 we lock the constants and plot the  $dE/dx$  versus momentum distribution of all the  
 2908 other particle species identifiable in the beamline data ( $\pi/\mu/e$ , K , p, in both polarities)  
 2909 against the corresponding Beth-Bloch prediction. The agreement between data  
 2910 from the other particle species and the predictions is the expected result of this cross  
 2911 check. The results of the tuning and cross check for Run-II data on the collection  
 2912 plane is shown in Figure C.2 negative polarity data on top, positive polarity data on  
 2913 the bottom.

2914 In MC, we simulate the corresponding positive pion sample with the DDMC (see  
 2915 section 5.2.2) and follow the same steps as in data. More details on the calorimetry  
 2916 tuning can be found in [79].

2917 **Add agreement between data and MC for dedx for pions**

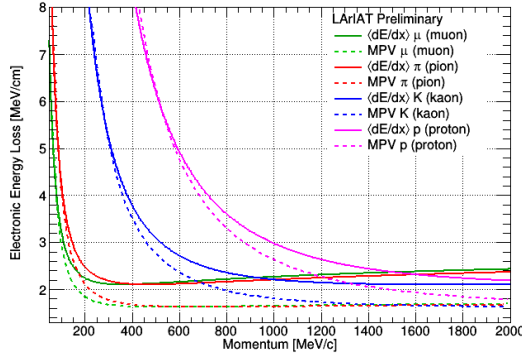


Figure C.1: Stopping power for pions, muons, kaons, and protons in liquid argon over the momentum range most relevant for LArIAT according to the Beth-Bloch equation. The solid lines represent the prediction for the mean energy  $dE/dX$ , while the dashed lines are the predictions for the MPV.

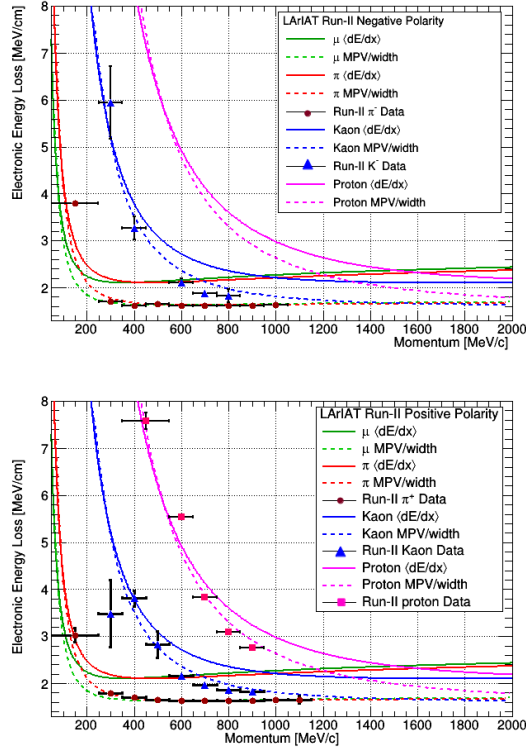


Figure C.2: Stopping power versus Momentum for Run-II negative (top) and positive (bottom) polarity data. We achieve the agreement between the Bethe-Bloch predictions and the distribution obtained with of the positive pions (top plot, red dots) by tuning the calorimetry constants. Once the calorimetry constants are locked in, the agreement between the other particle species and the Bethe-Bloch predictions follows naturally.

2918 **Bibliography**

- 2919 [1] PDG Tables for Liquid Argon. . Technical report.
- 2920 [2] Precision electroweak measurements on the  $Z$  resonance. *Physics Reports*,  
2921 427(5):257 – 454, 2006.
- 2922 [3] K. Abe, J. Amey, C. Andreopoulos, M. Antonova, S. Aoki, A. Ariga, D. Au-  
2923 tiero, S. Ban, M. Barbi, G. J. Barker, G. Barr, C. Barry, P. Bartet-Friburg,  
2924 M. Batkiewicz, V. Berardi, S. Berkman, S. Bhadra, S. Bienstock, A. Blondel,  
2925 S. Bolognesi, S. Bordoni, S. B. Boyd, D. Brailsford, A. Bravar, C. Bronner,  
2926 M. Buizza Avanzini, R. G. Calland, T. Campbell, S. Cao, S. L. Cartwright,  
2927 M. G. Catanesi, A. Cervera, C. Checchia, D. Cherdack, N. Chikuma,  
2928 G. Christodoulou, A. Clifton, J. Coleman, G. Collazuol, D. Coplowe, A. Cudd,  
2929 A. Dabrowska, G. De Rosa, T. Dealtry, P. F. Denner, S. R. Dennis, C. Densham,  
2930 D. Dewhurst, F. Di Lodovico, S. Di Luise, S. Dolan, O. Drapier, K. E. Duffy,  
2931 J. Dumarchez, M. Dziewiecki, S. Emery-Schrenk, A. Ereditato, T. Feusels,  
2932 A. J. Finch, G. A. Fiorentini, M. Friend, Y. Fujii, D. Fukuda, Y. Fukuda,  
2933 V. Galymov, A. Garcia, C. Giganti, F. Gizzarelli, T. Golan, M. Gonin, D. R.  
2934 Hadley, L. Haegel, M. D. Haigh, D. Hansen, J. Harada, M. Hartz, T. Hasegawa,  
2935 N. C. Hastings, T. Hayashino, Y. Hayato, R. L. Helmer, A. Hillairet, T. Hiraki,  
2936 A. Hiramatsu, S. Hirota, M. Hogan, J. Holeczek, F. Hosomi, K. Huang, A. K.  
2937 Ichikawa, M. Ikeda, J. Imber, J. Insler, R. A. Intonti, T. Ishida, T. Ishii, E. Iwai,  
2938 K. Iwamoto, A. Izmaylov, B. Jamieson, M. Jiang, S. Johnson, P. Jonsson,

2939 C. K. Jung, M. Kabirnezhad, A. C. Kaboth, T. Kajita, H. Kakuno, J. Kameda,  
2940 D. Karlen, T. Katori, E. Kearns, M. Khabibullin, A. Khotjantsev, H. Kim,  
2941 J. Kim, S. King, J. Kisiel, A. Knight, A. Knox, T. Kobayashi, L. Koch, T. Koga,  
2942 A. Konaka, K. Kondo, L. L. Kormos, A. Korzenev, Y. Koshio, K. Kowalik,  
2943 W. Kropp, Y. Kudenko, R. Kurjata, T. Kutter, J. Lagoda, I. Lamont, M. Lam-  
2944 oureux, E. Larkin, P. Lasorak, M. Laveder, M. Lawe, M. Licciardi, T. Lindner,  
2945 Z. J. Liptak, R. P. Litchfield, X. Li, A. Longhin, J. P. Lopez, T. Lou, L. Ludovici,  
2946 X. Lu, L. Magaletti, K. Mahn, M. Malek, S. Manly, A. D. Marino, J. F. Martin,  
2947 P. Martins, S. Martynenko, T. Maruyama, V. Matveev, K. Mavrokordis, W. Y.  
2948 Ma, E. Mazzucato, M. McCarthy, N. McCauley, K. S. McFarland, C. McGrew,  
2949 A. Mefodiev, C. Metelko, M. Mezzetto, P. Mijakowski, A. Minamino, O. Mi-  
2950 neev, S. Mine, A. Missent, M. Miura, S. Moriyama, Th. A. Mueller, J. Myslik,  
2951 T. Nakadaira, M. Nakahata, K. G. Nakamura, K. Nakamura, K. D. Nakamura,  
2952 Y. Nakanishi, S. Nakayama, T. Nakaya, K. Nakayoshi, C. Nantais, C. Nielsen,  
2953 M. Nirko, K. Nishikawa, Y. Nishimura, P. Novella, J. Nowak, H. M. O'Keeffe,  
2954 K. Okumura, T. Okusawa, W. Oryszczak, S. M. Oser, T. Ovsyannikova, R. A.  
2955 Owen, Y. Oyama, V. Palladino, J. L. Palomino, V. Paolone, N. D. Patel,  
2956 P. Paudyal, M. Pavin, D. Payne, J. D. Perkin, Y. Petrov, L. Pickard, L. Pick-  
2957 ering, E. S. Pinzon Guerra, C. Pistillo, B. Popov, M. Posiadala-Zezula, J.-M.  
2958 Poutissou, R. Poutissou, P. Przewlocki, B. Quilain, T. Radermacher, E. Radi-  
2959 cioni, P. N. Ratoff, M. Ravonel, M. A. Rayner, A. Redij, E. Reinherz-Aronis,  
2960 C. Riccio, P. A. Rodrigues, E. Rondio, B. Rossi, S. Roth, A. Rubbia, A. Rychter,  
2961 K. Sakashita, F. Sánchez, E. Scantamburlo, K. Scholberg, J. Schwehr, M. Scott,  
2962 Y. Seiya, T. Sekiguchi, H. Sekiya, D. Sgalaberna, R. Shah, A. Shaikhiev,  
2963 F. Shaker, D. Shaw, M. Shiozawa, T. Shirahige, S. Short, M. Smy, J. T.  
2964 Sobczyk, H. Sobel, M. Sorel, L. Southwell, J. Steinmann, T. Stewart, P. Stowell,  
2965 Y. Suda, S. Suvorov, A. Suzuki, S. Y. Suzuki, Y. Suzuki, R. Tacik, M. Tada,

- 2966 A. Takeda, Y. Takeuchi, H. K. Tanaka, H. A. Tanaka, D. Terhorst, R. Terri,  
2967 T. Thakore, L. F. Thompson, S. Tobayama, W. Toki, T. Tomura, C. Touramani,  
2968 T. Tsukamoto, M. Tzanov, Y. Uchida, M. Vagins, Z. Vallari, G. Vasseur,  
2969 T. Vladislavljevic, T. Wachala, C. W. Walter, D. Wark, M. O. Wascko, A. We-  
2970 ber, R. Wendell, R. J. Wilkes, M. J. Wilking, C. Wilkinson, J. R. Wilson, R. J.  
2971 Wilson, C. Wret, Y. Yamada, K. Yamamoto, M. Yamamoto, C. Yanagisawa,  
2972 T. Yano, S. Yen, N. Yershov, M. Yokoyama, K. Yoshida, T. Yuan, M. Yu, A. Za-  
2973 lewska, J. Zalipska, L. Zambelli, K. Zaremba, M. Ziembicki, E. D. Zimmerman,  
2974 M. Zito, and J. Źmuda. Combined analysis of neutrino and antineutrino oscil-  
2975 lations at t2k. *Phys. Rev. Lett.*, 118:151801, Apr 2017.
- 2976 [4] K. Abe, Y. Haga, Y. Hayato, M. Ikeda, K. Iyogi, J. Kameda, Y. Kishimoto,  
2977 M. Miura, S. Moriyama, M. Nakahata, T. Nakajima, Y. Nakano, S. Nakayama,  
2978 A. Orii, H. Sekiya, M. Shiozawa, A. Takeda, H. Tanaka, T. Tomura, R. A. Wen-  
2979 dell, R. Akutsu, T. Irvine, T. Kajita, K. Kaneyuki, Y. Nishimura, E. Richard,  
2980 K. Okumura, L. Labarga, P. Fernandez, J. Gustafson, C. Kachulis, E. Kearns,  
2981 J. L. Raaf, J. L. Stone, L. R. Sulak, S. Berkman, C. M. Nantais, H. A.  
2982 Tanaka, S. Tobayama, M. Goldhaber, W. R. Kropp, S. Mine, P. Weatherly,  
2983 M. B. Smy, H. W. Sobel, V. Takhistov, K. S. Ganezer, B. L. Hartfiel, J. Hill,  
2984 N. Hong, J. Y. Kim, I. T. Lim, R. G. Park, A. Himmel, Z. Li, E. O’Sullivan,  
2985 K. Scholberg, C. W. Walter, T. Wongjirad, T. Ishizuka, S. Tasaka, J. S. Jang,  
2986 J. G. Learned, S. Matsuno, S. N. Smith, M. Friend, T. Hasegawa, T. Ishida,  
2987 T. Ishii, T. Kobayashi, T. Nakadaira, K. Nakamura, Y. Oyama, K. Sakashita,  
2988 T. Sekiguchi, T. Tsukamoto, A. T. Suzuki, Y. Takeuchi, T. Yano, S. V. Cao,  
2989 T. Hiraki, S. Hirota, K. Huang, T. Kikawa, A. Minamino, T. Nakaya, K. Suzuki,  
2990 Y. Fukuda, K. Choi, Y. Itow, T. Suzuki, P. Mijakowski, K. Frankiewicz, J. Hig-  
2991 night, J. Imber, C. K. Jung, X. Li, J. L. Palomino, M. J. Wilking, C. Yanag-  
2992 isawa, D. Fukuda, H. Ishino, T. Kayano, A. Kibayashi, Y. Koshio, T. Mori,

- 2993 M. Sakuda, C. Xu, Y. Kuno, R. Tacik, S. B. Kim, H. Okazawa, Y. Choi,  
2994 K. Nishijima, M. Koshiba, Y. Totsuka, Y. Suda, M. Yokoyama, C. Bronner,  
2995 M. Hartz, K. Martens, Ll. Marti, Y. Suzuki, M. R. Vagins, J. F. Martin, A. Kon-  
2996 aka, S. Chen, Y. Zhang, and R. J. Wilkes. Search for proton decay via  $p \rightarrow e^+ \pi^0$   
2997 and  $p \rightarrow \mu^+ \pi^0$  in 0.31 megaton · years exposure of the super-kamiokande water  
2998 cherenkov detector. *Phys. Rev. D*, 95:012004, Jan 2017.
- 2999 [5] R Acciarri, C Adams, J Asaadi, B Baller, T Bolton, C Bromberg, F Ca-  
3000 vanna, E Church, D Edmunds, A Ereditato, S Farooq, B Fleming, H Greenlee,  
3001 G Horton-Smith, C James, E Klein, K Lang, P Laurens, D McKee, R Mehdiyev,  
3002 B Page, O Palamara, K Partyka, G Rameika, B Rebel, M Soderberg, J Spitz,  
3003 A M Szelc, M Weber, M Wojcik, T Yang, and G P Zeller. A study of electron  
3004 recombination using highly ionizing particles in the argoneut liquid argon tpc.  
3005 *Journal of Instrumentation*, 8(08):P08005, 2013.
- 3006 [6] R Acciarri, M Antonello, B Baibussinov, M Baldo-Ceolin, P Benetti,  
3007 F Calaprice, E Calligarich, M Cambiaghi, N Canci, F Carbonara, F Cavanna,  
3008 S Centro, A G Cocco, F Di Pompeo, G Fiorillo, C Galbiati, V Gallo, L Grandi,  
3009 G Meng, I Modena, C Montanari, O Palamara, L Pandola, G B Piano Mortari,  
3010 F Pietropaolo, G L Raselli, M Roncadelli, M Rossella, C Rubbia, E Segreto,  
3011 A M Szelc, S Ventura, and C Vignoli. Effects of nitrogen contamination in  
3012 liquid argon. *Journal of Instrumentation*, 5(06):P06003, 2010.
- 3013 [7] R. Acciarri et al. Demonstration and Comparison of Operation of Photomulti-  
3014 plier Tubes at Liquid Argon Temperature. *JINST*, 7:P01016, 2012.
- 3015 [8] R. Acciarri et al. Design and Construction of the MicroBooNE Detector. *JINST*,  
3016 12(02):P02017, 2017.

- 3017 [9] R. Acciarri et al. First Observation of Low Energy Electron Neutrinos in a  
3018 Liquid Argon Time Projection Chamber. *Phys. Rev.*, D95(7):072005, 2017.  
3019 [Phys. Rev.D95,072005(2017)].
- 3020 [10] M Adamowski, B Carls, E Dvorak, A Hahn, W Jaskierny, C Johnson, H Jostlein,  
3021 C Kendziora, S Lockwitz, B Pahlka, R Plunkett, S Pordes, B Rebel, R Schmitt,  
3022 M Stancari, T Tope, E Voirin, and T Yang. The liquid argon purity demon-  
3023 strator. *Journal of Instrumentation*, 9(07):P07005, 2014.
- 3024 [11] C. Adams et al. The Long-Baseline Neutrino Experiment: Exploring Funda-  
3025 mental Symmetries of the Universe. 2013.
- 3026 [12] P. Adamson, L. Aliaga, D. Ambrose, N. Anfimov, A. Antoshkin, E. Arrieta-  
3027 Diaz, K. Augsten, A. Aurisano, C. Backhouse, M. Baird, B. A. Bambah,  
3028 K. Bays, B. Behera, S. Bending, R. Bernstein, V. Bhatnagar, B. Bhuyan,  
3029 J. Bian, T. Blackburn, A. Bolshakova, C. Bromberg, J. Brown, G. Brunetti,  
3030 N. Buchanan, A. Butkevich, V. Bychkov, M. Campbell, E. Catano-Mur, S. Chil-  
3031 dress, B. C. Choudhary, B. Chowdhury, T. E. Coan, J. A. B. Coelho, M. Colo,  
3032 J. Cooper, L. Corwin, L. Cremonesi, D. Cronin-Hennessy, G. S. Davies, J. P.  
3033 Davies, P. F. Derwent, R. Dharmapalan, P. Ding, Z. Djurcic, E. C. Dukes,  
3034 H. Duyang, S. Edayath, R. Ehrlich, G. J. Feldman, M. J. Frank, M. Gabrielyan,  
3035 H. R. Gallagher, S. Germani, T. Ghosh, A. Giri, R. A. Gomes, M. C. Goodman,  
3036 V. Grichine, R. Group, D. Grover, B. Guo, A. Habig, J. Hartnell, R. Hatcher,  
3037 A. Hatzikoutelis, K. Heller, A. Himmel, A. Holin, J. Hylen, F. Jediny, M. Judah,  
3038 G. K. Kafka, D. Kalra, S. M. S. Kasahara, S. Kasetti, R. Keloth, L. Kolupaeva,  
3039 S. Kotelnikov, I. Kourbanis, A. Kreymer, A. Kumar, S. Kurbanov, K. Lang,  
3040 W. M. Lee, S. Lin, J. Liu, M. Lokajicek, J. Lozier, S. Luchuk, K. Maan, S. Mag-  
3041 ill, W. A. Mann, M. L. Marshak, K. Matera, V. Matveev, D. P. Méndez, M. D.  
3042 Messier, H. Meyer, T. Miao, W. H. Miller, S. R. Mishra, R. Mohanta, A. Moren,

- 3043 L. Mualem, M. Muether, S. Mufson, R. Murphy, J. Musser, J. K. Nelson,  
3044 R. Nichol, E. Niner, A. Norman, T. Nosek, Y. Oksuzian, A. Olshevskiy, T. Ol-  
3045 son, J. Paley, P. Pandey, R. B. Patterson, G. Pawloski, D. Pershey, O. Petrova,  
3046 R. Petti, S. Phan-Budd, R. K. Plunkett, R. Poling, B. Potukuchi, C. Principato,  
3047 F. Psihas, A. Radovic, R. A. Rameika, B. Rebel, B. Reed, D. Rocco, P. Rojas,  
3048 V. Ryabov, K. Sachdev, P. Sail, O. Samoylov, M. C. Sanchez, R. Schroeter,  
3049 J. Sepulveda-Quiroz, P. Shanahan, A. Sheshukov, J. Singh, J. Singh, P. Singh,  
3050 V. Singh, J. Smolik, N. Solomey, E. Song, A. Sousa, K. Soustruznik, M. Strait,  
3051 L. Suter, R. L. Talaga, M. C. Tamsett, P. Tas, R. B. Thayyullathil, J. Thomas,  
3052 X. Tian, S. C. Tognini, J. Tripathi, A. Tsaris, J. Urheim, P. Vahle, J. Vasel,  
3053 L. Vinton, A. Vold, T. Vrba, B. Wang, M. Wetstein, D. Whittington, S. G. Wo-  
3054 jcicki, J. Wolcott, N. Yadav, S. Yang, J. Zalesak, B. Zamorano, and R. Zwaska.  
3055 Constraints on oscillation parameters from  $\nu_e$  appearance and  $\nu_\mu$  disappearance  
3056 in nova. *Phys. Rev. Lett.*, 118:231801, Jun 2017.
- 3057 [13] Alan Agresti. *Categorical Data Analysis*. Wiley Series in Probability and Statis-  
3058 tics. Wiley, 2013.
- 3059 [14] A. Aguilar-Arevalo et al. Evidence for neutrino oscillations from the observation  
3060 of anti-neutrino(electron) appearance in a anti-neutrino(muon) beam. *Phys.*  
3061 *Rev.*, D64:112007, 2001.
- 3062 [15] A. A. Aguilar-Arevalo et al. Improved Search for  $\bar{\nu}_\mu \rightarrow \bar{\nu}_e$  Oscillations in the  
3063 MiniBooNE Experiment. *Phys. Rev. Lett.*, 110:161801, 2013.
- 3064 [16] S. Amoruso et al. Study of electron recombination in liquid argon with the  
3065 ICARUS TPC. *Nucl. Instrum. Meth.*, A523:275–286, 2004.
- 3066 [17] C. Anderson et al. The ArgoNeuT Detector in the NuMI Low-Energy beam  
3067 line at Fermilab. *JINST*, 7:P10019, 2012.

- 3068 [18] C. Andreopoulos et al. The GENIE Neutrino Monte Carlo Generator. *Nucl.*  
3069        *Instrum. Meth.*, A614:87–104, 2010.
- 3070 [19] Timofei Bolshakov Andrey Petrov. Java synoptic toolkit. Technical report,  
3071        Sept 2010.
- 3072 [20] M. Antonello, B. Baibussinov, P. Benetti, E. Calligarich, N. Canci, S. Cen-  
3073        tro, A. Cesana, K. Cieslik, D. B. Cline, A. G. Cocco, A. Dabrowska, D. De-  
3074        qual, A. Dermenev, R. Dolfini, C. Farnese, A. Fava, A. Ferrari, G. Fiorillo,  
3075        D. Gibin, S. Gninenko, A. Guglielmi, M. Haranczyk, J. Holeczek, A. Ivashkin,  
3076        J. Kisiel, I. Kochanek, J. Lagoda, S. Mania, A. Menegolli, G. Meng, C. Monta-  
3077        nari, S. Otwinowski, A. Piazzoli, P. Picchi, F. Pietropaolo, P. Plonski, A. Rap-  
3078        poldi, G. L. Raselli, M. Rossella, C. Rubbia, P. Sala, A. Scaramelli, E. Seg-  
3079        reto, F. Sergiampietri, D. Stefan, J. Stepaniak, R. Sulej, M. Szarska, M. Ter-  
3080        rani, F. Varanini, S. Ventura, C. Vignoli, H. Wang, X. Yang, A. Zalewska,  
3081        and K. Zaremba. Precise 3d track reconstruction algorithm for the ICARUS  
3082        t600 liquid argon time projection chamber detector. *Advances in High Energy*  
3083        *Physics*, 2013:1–16, 2013.
- 3084 [21] M. Antonello et al. A Proposal for a Three Detector Short-Baseline Neutrino  
3085        Oscillation Program in the Fermilab Booster Neutrino Beam. 2015.
- 3086 [22] D. Ashery, I. Navon, G. Azuelos, H. K. Walter, H. J. Pfeiffer, and F. W.  
3087        Schlepütz. True absorption and scattering of pions on nuclei. *Phys. Rev. C*,  
3088        23:2173–2185, May 1981.
- 3089 [23] C. Athanassopoulos et al. Evidence for  $\nu(\mu) \rightarrow \nu(e)$  neutrino oscillations  
3090        from LSND. *Phys. Rev. Lett.*, 81:1774–1777, 1998.

- 3091 [24] Borut Bajc, Junji Hisano, Takumi Kuwahara, and Yuji Omura. Threshold  
3092 corrections to dimension-six proton decay operators in non-minimal {SUSY}  
3093  $\text{su}(5)$  {GUTs}. *Nuclear Physics B*, 910:1 – 22, 2016.
- 3094 [25] B. Baller. Trajcluster user guide. Technical report, apr 2016.
- 3095 [26] Gary Barker. Neutrino event reconstruction in a liquid argon TPC. *Journal of*  
3096 *Physics: Conference Series*, 308:012015, jul 2011.
- 3097 [27] BASF Corp. 100 Park Avenue, Florham Park, NJ 07932 USA.
- 3098 [28] R. Becker-Szendy, C. B. Bratton, D. R. Cady, D. Casper, R. Claus, M. Crouch,  
3099 S. T. Dye, W. Gajewski, M. Goldhaber, T. J. Haines, P. G. Halverson, T. W.  
3100 Jones, D. Kielczewska, W. R. Kropp, J. G. Learned, J. M. LoSecco, C. Mc-  
3101 Grew, S. Matsuno, J. Matthews, M. S. Mudah, L. Price, F. Reines, J. Schultz,  
3102 D. Sinclair, H. W. Sobel, J. L. Stone, L. R. Sulak, R. Svoboda, G. Thornton,  
3103 and J. C. van der Velde. Search for proton decay into  $e^+ + \pi^0$  in the imb-3  
3104 detector. *Phys. Rev. D*, 42:2974–2976, Nov 1990.
- 3105 [29] J B Birks. Scintillations from organic crystals: Specific fluorescence and relative  
3106 response to different radiations. *Proceedings of the Physical Society. Section A*,  
3107 64(10):874, 1951.
- 3108 [30] A. Bodek and J. L. Ritchie. Further studies of fermi-motion effects in lepton  
3109 scattering from nuclear targets. *Phys. Rev. D*, 24:1400–1402, Sep 1981.
- 3110 [31] Mark G. Boulay and A. Hime. Direct WIMP detection using scintillation time  
3111 discrimination in liquid argon. 2004.
- 3112 [32] D. V. Bugg, R. S. Gilmore, K. M. Knight, D. C. Salter, G. H. Stafford, E. J. N.  
3113 Wilson, J. D. Davies, J. D. Dowell, P. M. Hattersley, R. J. Homer, A. W. O'dell,

- 3114 A. A. Carter, R. J. Tapper, and K. F. Riley. Kaon-nucleon total cross sections  
3115 from 0.6 to 2.65 gev/ *c. Phys. Rev.*, 168:1466–1475, Apr 1968.
- 3116 [33] W. M. Burton and B. A. Powell. Fluorescence of tetraphenyl-butadiene in the  
3117 vacuum ultraviolet. *Applied Optics*, 12(1):87, jan 1973.
- 3118 [34] CAEN. Caen v1495 data sheet. Technical report, jan 2018.
- 3119 [35] CAEN. Caen v1740 data sheet. Technical report, jan 2018.
- 3120 [36] A. S. Carroll, I. H. Chiang, C. B. Dover, T. F. Kycia, K. K. Li, P. O. Mazur,  
3121 D. N. Michael, P. M. Mockett, D. C. Rahm, and R. Rubinstein. Pion-nucleus  
3122 total cross sections in the (3,3) resonance region. *Phys. Rev. C*, 14:635–638,  
3123 Aug 1976.
- 3124 [37] D. Casper. The nuance neutrino physics simulation, and the future. *Nuclear  
3125 Physics B - Proceedings Supplements*, 112(1-3):161–170, nov 2002.
- 3126 [38] F. Cavanna et al. LArIAT: Liquid Argon In A Testbeam. 2014.
- 3127 [39] A. Cervera, A. Donini, M.B. Gavela, J.J. Gomez Cádenas, P. Hernández,  
3128 O. Mena, and S. Rigolin. Golden measurements at a neutrino factory. *Nu-  
3129 clear Physics B*, 579(1-2):17–55, jul 2000.
- 3130 [40] E. Church. LArSoft: A Software Package for Liquid Argon Time Projection  
3131 Drift Chambers. 2013.
- 3132 [41] ATLAS Collaboration. Observation of a new particle in the search for the  
3133 standard model higgs boson with the ATLAS detector at the LHC. *Physics  
3134 Letters B*, 716(1):1–29, sep 2012.
- 3135 [42] CMS Collaboration. Observation of a new boson at a mass of 125 gev with the  
3136 cms experiment at the lhc. *Physics Letters B*, 716(1):30 – 61, 2012.

- 3137 [43] The LArIAT Collaboration. The liquid argon in a testbeam (lariat) experiment.  
3138 Technical report, In Preparation 2018.
- 3139 [44] Stefano Dell’Oro, Simone Marcocci, Matteo Viel, and Francesco Vissani. Neu-  
3140 trinoless double beta decay: 2015 review. *Advances in High Energy Physics*,  
3141 2016:1–37, 2016.
- 3142 [45] S.E. Derenzo, A.R. Kirschbaum, P.H. Eberhard, R.R. Ross, and F.T. Solmitz.  
3143 Test of a liquid argon chamber with 20 m rms resolution. *Nuclear Instruments  
3144 and Methods*, 122:319 – 327, 1974.
- 3145 [46] Savas Dimopoulos, Stuart Raby, and Frank Wilczek. Proton Decay in Super-  
3146 symmetric Models. *Phys. Lett.*, B112:133, 1982.
- 3147 [47] D. Drakoulakos et al. Proposal to perform a high-statistics neutrino scattering  
3148 experiment using a fine-grained detector in the NuMI beam. 2004.
- 3149 [48] A Ereditato, C C Hsu, S Janos, I Kreslo, M Messina, C Rudolf von Rohr,  
3150 B Rossi, T Strauss, M S Weber, and M Zeller. Design and operation of  
3151 argontube: a 5 m long drift liquid argon tpc. *Journal of Instrumentation*,  
3152 8(07):P07002, 2013.
- 3153 [49] Torleif Ericson and Wolfram Weise. *Pions and Nuclei (The International Series  
3154 of Monographs on Physics)*. Oxford University Press, 1988.
- 3155 [50] A.A. Aguilar-Arevalo et al. The miniboone detector. *Nuclear Instruments and  
3156 Methods in Physics Research Section A: Accelerators, Spectrometers, Detectors  
3157 and Associated Equipment*, 599(1):28 – 46, 2009.
- 3158 [51] Antonio Bueno et al. Nucleon decay searches with large liquid argon TPC de-  
3159 detectors at shallow depths: atmospheric neutrinos and cosmogenic backgrounds.  
3160 *Journal of High Energy Physics*, 2007(04):041–041, apr 2007.

- 3161 [52] A.S. Clough et al. Pion-nucleus total cross sections from 88 to 860 MeV. *Nuclear*  
3162       *Physics B*, 76(1):15–28, jul 1974.
- 3163 [53] B.W. Allardycce et al. Pion reaction cross sections and nuclear sizes. *Nuclear*  
3164       *Physics A*, 209(1):1 – 51, 1973.
- 3165 [54] C Athanassopoulos et al. The liquid scintillator neutrino detector and LAMPF  
3166 neutrino source. *Nuclear Instruments and Methods in Physics Research Section*  
3167       *A: Accelerators, Spectrometers, Detectors and Associated Equipment*, 388(1-  
3168 2):149–172, mar 1997.
- 3169 [55] F. Binon et al. Scattering of negative pions on carbon. *Nuclear Physics B*,  
3170       17(1):168 – 188, 1970.
- 3171 [56] L. Aliaga et al. Minerva neutrino detector response measured with test beam  
3172 data. *Nuclear Instruments and Methods in Physics Research Section A: Ac-*  
3173       *celerators, Spectrometers, Detectors and Associated Equipment*, 789:28 – 42,  
3174 2015.
- 3175 [57] M Adamowski et al. The liquid argon purity demonstrator. *Journal of Instru-*  
3176       *mation*, 9(07):P07005, 2014.
- 3177 [58] P. Vilain et al. Coherent single charged pion production by neutrinos. *Physics*  
3178       *Letters B*, 313(1-2):267–275, aug 1993.
- 3179 [59] R. Acciarri et al. Convolutional neural networks applied to neutrino events  
3180 in a liquid argon time projection chamber. *Journal of Instrumentation*,  
3181 12(03):P03011, 2017.
- 3182 [60] R. Acciarri et al. Design and construction of the MicroBooNE detector. *Journal*  
3183       *of Instrumentation*, 12(02):P02017–P02017, feb 2017.

- 3184 [61] C. E. Aalseth et al.l. DarkSide-20k: A 20 tonne two-phase LAr TPC for direct  
3185 dark matter detection at LNGS. *The European Physical Journal Plus*, 133(3),  
3186 mar 2018.
- 3187 [62] H Fenker. Standard beam pwc for fermilab. Technical report, Fermi National  
3188 Accelerator Lab., Batavia, IL (USA), 1983.
- 3189 [63] H Fesbach. Theoretical nuclear physics: Nuclear reactions. 1992.
- 3190 [64] J. A. Formaggio and G. P. Zeller. From ev to eev: Neutrino cross sections across  
3191 energy scales. *Rev. Mod. Phys.*, 84:1307–1341, Sep 2012.
- 3192 [65] E. Friedman et al. K+ nucleus reaction and total cross-sections: New analysis  
3193 of transmission experiments. *Phys. Rev.*, C55:1304–1311, 1997.
- 3194 [66] V.M. Gehman, S.R. Seibert, K. Rielage, A. Hime, Y. Sun, D.-M. Mei,  
3195 J. Maassen, and D. Moore. Fluorescence efficiency and visible re-emission  
3196 spectrum of tetraphenyl butadiene films at extreme ultraviolet wavelengths.  
3197 *Nuclear Instruments and Methods in Physics Research Section A: Accelerators,*  
3198 *Spectrometers, Detectors and Associated Equipment*, 654(1):116 – 121, 2011.
- 3199 [67] H. Geiger and E. Marsden. On a diffuse reflection of the formula-particles.  
3200 *Proceedings of the Royal Society A: Mathematical, Physical and Engineering*  
3201 *Sciences*, 82(557):495–500, jul 1909.
- 3202 [68] Howard Georgi and S. L. Glashow. Unity of all elementary-particle forces. *Phys.*  
3203 *Rev. Lett.*, 32:438–441, Feb 1974.
- 3204 [69] D.Y. Wong (editor) G.L. Shaw (Editor). *Pion-nucleon Scattering*. John Wiley  
3205 & Sons Inc, 1969.
- 3206 [70] Glassman High Voltage, Inc., Precision Regulated High Voltage DC Power Sup-  
3207 ply.

- 3208 [71] D S Gorbunov. Sterile neutrinos and their role in particle physics and cosmology.  
3209       *Physics-Uspekhi*, 57(5):503, 2014.
- 3210 [72] C. Green, J. Kowalkowski, M. Paterno, M. Fischler, L. Garren, and Q. Lu. The  
3211       Art Framework. *J. Phys. Conf. Ser.*, 396:022020, 2012.
- 3212 [73] S. Hansen, D. Jensen, G. Savage, E. Skup, and A. Soha. Fermilab test beam  
3213       multi-wire proportional chamber tracking system upgrade. June 2014. Interna-  
3214       tional Conference on Technology and Instrumentation in Particle Physics (TIPP  
3215       2014).
- 3216 [74] J. Harada. Non-maximal  $\theta_{23}$  , large  $\theta_{13}$  and tri-bimaximal  $\theta_{12}$  via quark-  
3217       lepton complementarity at next-to-leading order. *EPL (Europhysics Letters)*,  
3218       103(2):21001, 2013.
- 3219 [75] Peter W. Higgs. Broken symmetries and the masses of gauge bosons. *Physical*  
3220       *Review Letters*, 13(16):508–509, oct 1964.
- 3221 [76] P.W. Higgs. Broken symmetries, massless particles and gauge fields. *Physics*  
3222       *Letters*, 12(2):132–133, sep 1964.
- 3223 [77] H J Hilke. Time projection chambers. *Reports on Progress in Physics*,  
3224       73(11):116201, 2010.
- 3225 [78] N. Ishida, M. Chen, T. Doke, K. Hasuike, A. Hitachi, M. Gaudreau, M. Kase,  
3226       Y. Kawada, J. Kikuchi, T. Komiyama, K. Kuwahara, K. Masuda, H. Okada,  
3227       Y.H. Qu, M. Suzuki, and T. Takahashi. Attenuation length measurements of  
3228       scintillation light in liquid rare gases and their mixtures using an improved  
3229       reflection suppresser. *Nuclear Instruments and Methods in Physics Research*  
3230       *Section A: Accelerators, Spectrometers, Detectors and Associated Equipment*,  
3231       384(2-3):380–386, jan 1997.

- 3232 [79] G. Pulliam J. Asaadi, E. Gramellini. Determination of the electron lifetime in  
3233 lariat. Technical report, August 2017.
- 3234 [80] George Jaffé. Zur theorie der ionisation in kolonnen. *Annalen der Physik*,  
3235 347(12):303–344, 1913.
- 3236 [81] C. Jarlskog. A basis independent formulation of the connection between quark  
3237 mass matrices, CP violation and experiment. *Zeitschrift für Physik C Particles  
3238 and Fields*, 29(3):491–497, sep 1985.
- 3239 [82] B J P Jones, C S Chiu, J M Conrad, C M Ignarra, T Katori, and M Toups. A  
3240 measurement of the absorption of liquid argon scintillation light by dissolved ni-  
3241 tragen at the part-per-million level. *Journal of Instrumentation*, 8(07):P07011,  
3242 2013.
- 3243 [83] Benjamin J. P. Jones. *Sterile Neutrinos in Cold Climates*. PhD thesis, MIT,  
3244 2015.
- 3245 [84] Cezary Juszczak, Jarosław A. Nowak, and Jan T. Sobczyk. Simulations from  
3246 a new neutrino event generator. *Nuclear Physics B - Proceedings Supplements*,  
3247 159:211–216, sep 2006.
- 3248 [85] D. I. Kazakov. Beyond the standard model: In search of supersymmetry. In  
3249 *2000 European School of high-energy physics, Caramulo, Portugal, 20 Aug-2  
3250 Sep 2000: Proceedings*, pages 125–199, 2000.
- 3251 [86] Dae-Gyu Lee, R. N. Mohapatra, M. K. Parida, and Merostar Rani. Predic-  
3252 tions for the proton lifetime in minimal nonsupersymmetric  $so(10)$  models: An  
3253 update. *Phys. Rev. D*, 51:229–235, Jan 1995.

- 3254 [87] M A Leigui de Oliveira. Expression of Interest for a Full-Scale Detector Engi-  
3255 neering Test and Test Beam Calibration of a Single-Phase LAr TPC. Technical  
3256 Report CERN-SPSC-2014-027. SPSC-EOI-011, CERN, Geneva, Oct 2014.
- 3257 [88] W. H. Lippincott, K. J. Coakley, D. Gastler, A. Hime, E. Kearns, D. N. McK-  
3258 insey, J. A. Nikkel, and L. C. Stonehill. Scintillation time dependence and pulse  
3259 shape discrimination in liquid argon. *Phys. Rev. C*, 78:035801, Sep 2008.
- 3260 [89] Jorge L. Lopez and Dimitri V. Nanopoulos. Flipped SU(5): Origins and re-  
3261 cent developments. In *15th Johns Hopkins Workshop on Current Problems*  
3262 *in Particle Theory: Particle Physics from Underground to Heaven Baltimore,*  
3263 *Maryland, August 26-28, 1991*, pages 277–297, 1991.
- 3264 [90] Vincent Lucas and Stuart Raby. Nucleon decay in a realistic so(10) susy gut.  
3265 *Phys. Rev. D*, 55:6986–7009, Jun 1997.
- 3266 [91] Ettore Majorana. Teoria simmetrica dell'elettrone e del positrone. *Il Nuovo*  
3267 *Cimento*, 14(4):171–184, apr 1937.
- 3268 [92] Hisakazu Minakata and Alexei Yu. Smirnov. Neutrino mixing and quark-lepton  
3269 complementarity. *Phys. Rev. D*, 70:073009, Oct 2004.
- 3270 [93] M. Mooney. The microboone experiment and the impact of space charge effects.  
3271 2015.
- 3272 [94] E. Morikawa, R. Reininger, P. Gürtler, V. Saile, and P. Laporte. Argon, kryp-  
3273 ton, and xenon excimer luminescence: From the dilute gas to the condensed  
3274 phase. *The Journal of Chemical Physics*, 91(3):1469–1477, aug 1989.
- 3275 [95] FM Newcomer, S Tedja, R Van Berg, J Van der Spiegel, and HH Williams.  
3276 A fast, low power, amplifier-shaper-discriminator for high rate straw tracking  
3277 systems. *IEEE Transactions on Nuclear Science*, 40(4):630–636, 1993.

- 3278 [96] Emmy Noether. Invariant variation problems. *Transport Theory and Statistical*  
3279 *Physics*, 1(3):186–207, jan 1971.
- 3280 [97] I. Nutini. Study of charged particles interaction processes on ar in the 0.2 - 2.0  
3281 GeV energy range through combined information from ionization free charge  
3282 and scintillation light. Technical report, jan 2015.
- 3283 [98] D. R. Nygren. The time projection chamber: A new  $4\pi$  detector for charged  
3284 particles. Technical report, 1974.
- 3285 [99] L. Onsager. Initial recombination of ions. *Phys. Rev.*, 54:554–557, Oct 1938.
- 3286 [100] S. Pascoli, S.T. Petcov, and A. Riotto. Leptogenesis and low energy cp-violation  
3287 in neutrino physics. *Nuclear Physics B*, 774(1):1 – 52, 2007.
- 3288 [101] C. Patrignani et al. Review of Particle Physics. *Chin. Phys.*, C40(10):100001,  
3289 2016.
- 3290 [102] B. Pontecorvo. Neutrino Experiments and the Problem of Conservation of  
3291 Leptonic Charge. *Sov. Phys. JETP*, 26:984–988, 1968. [Zh. Eksp. Teor.  
3292 Fiz.53,1717(1967)].
- 3293 [103] T. Yang R. Acciarri. Investigation of the non-uniformity observed in the wire  
3294 response to charge in lariat run 1. Technical report, February 2017.
- 3295 [104] T. Yang R. Acciarri, M. Stancari. Determination of the electron lifetime in  
3296 lariat. Technical report, March 2016.
- 3297 [105] Martti Raidal. Relation between the neutrino and quark mixing angles and  
3298 grand unification. *Phys. Rev. Lett.*, 93:161801, Oct 2004.
- 3299 [106] Steve Ritz et al. Building for Discovery: Strategic Plan for U.S. Particle Physics  
3300 in the Global Context. 2014.

- 3301 [107] C. Rubbia. The Liquid Argon Time Projection Chamber: A New Concept for  
3302 Neutrino Detectors. 1977.
- 3303 [108] L.M. Saunders. Electromagnetic production of pions from nuclei. *Nucl. Phys.*,  
3304 *B7*: 293-310(1968).
- 3305 [109] Qaisar Shafi and Zurab Tavartkiladze. Neutrino democracy, fermion mass hier-  
3306 archies, and proton decay from 5d su(5). *Phys. Rev. D*, 67:075007, Apr 2003.
- 3307 [110] Sigma-Aldrich, P.O. Box 14508, St. Louis, MO 63178 USA.
- 3308 [111] R. K. Teague and C. J. Pings. Refractive index and the lorentz–lorenz function  
3309 for gaseous and liquid argon, including a study of the coexistence curve near the  
3310 critical state. *The Journal of Chemical Physics*, 48(11):4973–4984, jun 1968.
- 3311 [112] J. Thomas and D. A. Imel. Recombination of electron-ion pairs in liquid argon  
3312 and liquid xenon. *Phys. Rev. A*, 36:614–616, Jul 1987.
- 3313 [113] D.R.O. Morrison N. Rivoire V. Flaminio, W.G. Moorhead. Compilation of  
3314 Cross Sections I:  $\pi^+$  and  $\pi^-$  Induced Reactions. *CERN-HERA*, pages 83–01,  
3315 1983.
- 3316 [114] D.R.O. Morrison N. Rivoire V. Flaminio, W.G. Moorhead. Compilation of  
3317 Cross Sections II:  $K^+$  and  $K^-$  Induced Reactions. *CERN-HERA*, pages 83–02,  
3318 1983.
- 3319 [115] W. Walkowiak. Drift velocity of free electrons in liquid argon. *Nuclear Instru-*  
3320 *ments and Methods in Physics Research Section A: Accelerators, Spectrometers,*  
3321 *Detectors and Associated Equipment*, 449(1-2):288–294, jul 2000.
- 3322 [116] Hermann Weyl. Gravitation and the electron. *Proceedings of the National*  
3323 *Academy of Sciences of the United States of America*, 15(4):323–334, 1929.

- 3324 [117] Colin et al Wilkin. A comparison of pi+ and pi- total cross-sections of light  
3325 nuclei near the 3-3 resonance. *Nucl. Phys.*, B62:61–85, 1973.
- 3326 [118] D. H. Wright and M. H. Kelsey. The Geant4 Bertini Cascade. *Nucl. Instrum.*  
3327 *Meth.*, A804:175–188, 2015.
- 3328 [119] C. S. Wu, E. Ambler, R. W. Hayward, D. D. Hoppes, and R. P. Hudson.  
3329 Experimental test of parity conservation in beta decay. *Phys. Rev.*, 105:1413–  
3330 1415, Feb 1957.
- 3331 [120] N Yahlali, L M P Fernandes, K Gonzlez, A N C Garcia, and A Soriano. Imaging  
3332 with sipms in noble-gas detectors. *Journal of Instrumentation*, 8(01):C01003,  
3333 2013.
- 3334 [121] T. Yanagida. Horizontal symmetry and masses of neutrinos. *Progress of Theo-*  
3335 *retical Physics*, 64(3):1103–1105, sep 1980.